
Compact Antenna Arrays for Mobile Communications

Su-Khiong Yong



A thesis submitted for the degree of Doctor of Philosophy.
The University of Edinburgh.
December 2003



Abstract

Over the past few years, mobile communications has experienced an exponential growth in the number of subscribers. This has driven the need for efficient use of bandwidth to support more users, provides better quality of services and higher data rates for multimedia applications. Smart antenna (SA) technologies emerge as a promising candidate to fulfill these requirements. The main functionality of the SAs is to exploit spatial properties of the channel to mitigate fading, interference and noise. Although SA techniques have received enormous attention, several aspects of these technology have not been fully investigated. This motivates the work reported in this thesis that focuses on the performance analysis of compact antenna arrays (CAAs) spanning from theoretical analysis to simulation of the effect of the antennas and the channel on the performance.

The contributions of this thesis are four fold. Firstly, the implementation of COST 259 directional channel model in terms of a tapped delay line is developed. While the implemented channel model facilitates link level simulation, capacity analysis indicates that the delay spread has relatively small impact as compared to the azimuth spread (AS) on the channel capacity. Secondly, an antenna model which incorporates various antenna effects into the performance study of antenna arrays (AAs) is developed. A comprehensive study of these effects through computer simulations reveal that the use of ideal parameters in the literature always over-predicts the actual system performance. The use of different antenna configurations yield different results with some arrays performing better in certain scenarios than others. Furthermore, a proposed mutual coupling (MC) model explains the conflicting results reported to date in the literature. The overall effect of MC is to reduce the system performance despite lower fading correlation is being obtained between pair of elements when MC is taken into account.

Thirdly, the impact of using different azimuth-of-arrival (AOA) and elevation-of-arrival (EOA) distributions on the performance of various AAs is found to be minimal. The determining factor for the AA performance is the standard deviation of the underlying distribution. Finally, three-dimensional spatial fading correlation (SFC) models for several CAA geometries are developed. The closed-form SFC functions are expressed in terms of AOA, EOA and the geometry of the AA under study. Such closed-form expressions can be used to determine the correlation matrices at both base station and mobile station and thus are important in assisting the capacity analysis of single-input multiple-output and multiple-input multiple-output systems. Furthermore, the developed SFC functions also enable the sensitivity of the AAs to be evaluated through the performance patterns. The results provide invaluable insight that can ultimately assist the design of AA algorithms. An extensive analysis on the array's sensitivity shows that the system performance is more AS dependent than ES while the effect of mean-azimuth-of-arrival and mean-elevation-of-arrival is array dependent. The results also show that the AS is the primary factor affecting antenna correlation and the impact of ES is mainly noticeable at small AS values. Nevertheless, in evaluating the performance of AAs, both AOA and EOA must be taken in account. Capacity analysis also demonstrates the practicability of deploying electromagnetic vector sensor (EVS) and EVS arrays as compact AA receivers.

Acknowledgements

*“When one door closes another door opens;
but we often look so long and so regretfully upon the closed door,
that we do not see the ones which open for us.*

– Alexander Graham Bell (1847-1922)–

A journey of a thousand miles must begin with a single step, and that step for my Ph.D. work required a full determinations and hard work to realise it. I started my Ph.D. in the middle of nowhere with fears and worries. Progressively, I managed to pave my way towards completion of this thesis today. So I would like to take this opportunity to express my sincere thanks and appreciations to those who had played an integral part towards the work reported here, without you this thesis would not be possible.

First of all, I would like to thank my supervisor, Dr. John Thompson, for his invaluable advice, guidance, support and patience throughout the past three years at Edinburgh. It has been a pleasure working under his supervision for which I truthfully appreciate the time and effort he had spent in our discussion and proof-read of my publications and thesis tirelessly over and over again. My thanks also extended to my second supervisor, Prof. Stephen McLaughlin, for his comments and criticisms on the early stage of the work as well as proof-read of the final version of the thesis. I am also in debt to Prof. Peter Grant for giving me the opportunity to join the Signal and System research group that made my stay at Edinburgh a great learning experience in every aspect.

Next, my special thanks go to my sponsor, the Mobile VCE, for the financial support and the industrial experience gained during the past three years though tonnes of work need to be done. My appreciation also goes to industrial coordinator, Dr. Dean Kitchener for his prompt response in approving the publication proposals.

I am in particular grateful to Henrik Asplund of Ericsson Radio Systems in Sweden and Martin Steinbauer of Technical University of Tuwien in Austria (now in Mobikom, Austria) for their kind helps in explaining and clarifying the COST 259 channel models. I also would like to

thank to my fellow colleagues working closely in SASG /IDCOM for the fun and difficult time we had shared together. My friends in Malaysia and my close buddies in Hendon, London who have supported me either directly or indirectly are also gratefully acknowledged. Not to forget the contribution of Matlab Newsgroup that helped me to optimise some of my codes.

I dedicated this thesis to my beloved family for their endless love, care and support. Thanks to my parents forgiveness for my selfishness in pursuing my studies overseas for so many years leaving them alone. Thanks also to my eldest sister, Ginny, brother, Hock Khiong and sister-in-law, Tse Wei for managing various things for me back at home. I also thank my sister, Gillian and brother-in-law, Soon Keat for their hospitalities during my stay in Colchester making me feeling at home. Sorry for not able to attend your wedding ceremony. Of course my thanks also extended to my nephew, Jordan boy, a little baby whose smiles and cries brought me a lot of happiness and joy.

Last but not least, I would like to express my uppermost gratitude to a very special person in my life, Dr. Chia-Chin Chong for encouraging and convincing me to take up this PhD study. You had been with me during the ups and downs for the past three years and your companion has made the journey of my research a wonderful memories. Thank you for your implicit love, care, encouragement, steadfast support and understanding that enabled me to go through many sleepless nights. The technical discussions we have almost everyday on various areas in our research also sparked my inspiration. You make me a man of honour!

Su-Khiong Yong

Edinburgh, Dec 2003.

Contents

Declaration of originality	iii
Acknowledgements	iv
Contents	vi
List of figures	ix
List of tables	xiii
Acronyms and abbreviations	xiv
List of symbols	xvii
1 Introduction	1
1.1 Objective and contributions to knowledge	4
1.1.1 Objective	4
1.1.2 Contributions	4
1.2 Organisation of the thesis	5
2 Principles and background information for antenna and wireless propagation	7
2.1 Review of basic antenna theory	7
2.1.1 Fundamental antenna parameters	7
2.1.2 Classification of antennas	12
2.1.3 Typical mobile antennas	13
2.1.4 Antenna arrays and smart antennas	14
2.1.5 Mutual coupling	15
2.2 Properties of wireless propagation channels	19
2.2.1 Time selectivity	19
2.2.2 Frequency selectivity	21
2.2.3 Time dispersion: delay spread	22
2.2.4 Angle dispersion: angle spread	22
2.2.5 Depolarisation	22
2.3 Review of diversity techniques	23
2.3.1 Angle and pattern diversity	23
2.3.2 Frequency and time diversity	24
2.3.3 Spatial diversity	25
2.3.4 Polarisation diversity	25
2.4 Techniques employing spatial diversity	25
2.4.1 Summation	26
2.4.2 Non-linear optimisation	28
2.4.3 Performance comparison	29
2.5 Correlation, array gain and diversity gain	33
2.6 Summary	35
3 On the implementation of COST 259 channel model	36
3.1 Overview of COST 259 DCM: approach and concept	37
3.2 Channel model: mathematical view	38

3.2.1	Temporal correlation	40
3.2.2	Spatial correlation	44
3.3	Parameter settings	44
3.4	Simulation flow	48
3.5	Simulation results and discussion	51
3.6	Capacity evaluation for antenna arrays	53
3.6.1	Evaluation of channel capacity	54
3.6.2	The impact of delay spread	55
3.6.3	The impact of azimuth spread	57
3.7	Correlation matrices and the relation to the system performance	58
3.7.1	Properties of the correlation matrix and their implications	60
3.7.2	Eigenanalysis: eigenvalue decomposition	61
3.8	Summary	63
4	The effect of antenna parameters on the performance of antenna arrays	64
4.1	The need for antenna modelling	65
4.2	Radiation pattern of an antenna element	65
4.2.1	Short dipole and halfwave dipole	65
4.2.2	Small loop	66
4.2.3	Patch antenna	67
4.3	Type of antenna array	67
4.3.1	Uniform linear array	69
4.3.2	Uniform circular array	69
4.3.3	Uniform Rectangular Array	70
4.3.4	Electromagnetic vector sensor	72
4.3.5	An array of EVS	73
4.3.6	Radiation pattern of an antenna array with identical elements	74
4.4	Mutual coupling	74
4.5	Number of antennas and antenna spacing	79
4.6	Performance analysis on antenna parameters	79
4.6.1	The effect of antenna element pattern	79
4.6.2	The effect of types of antenna array	80
4.6.3	The effect of mutual coupling	82
4.6.4	The effect of antenna spacing and number of antenna elements	87
4.7	Summary	88
5	The impact of angle of arrival distribution on the performance of antenna arrays	91
5.1	Statistical angle-of-arrival distributions	91
5.2	The impact of azimuth-of-arrival distribution	93
5.3	The impact of elevation-of-arrival distribution	97
5.4	Summary	97
6	3-Dimensional spatial fading correlation models	100
6.1	Introduction	101
6.2	Closed-form spatial fading correlation models	102
6.2.1	ULA, UCA and URA	102
6.2.2	EVS	103

6.2.3	Arrays of EVS	104
6.3	Analytical results	105
6.4	Sensitivity analysis	110
6.4.1	Effect of MAOA and AS	111
6.4.2	Effect of MEOA and ES	113
6.4.3	Effect of AS and ES	114
6.4.4	Effect of MAOA and MEOA	118
6.5	Implications of the performance patterns	119
6.6	Capacity analysis for MIMO systems	121
6.7	Summary	126
7	Conclusions and future work	127
7.1	Conclusions and summary of results	127
7.2	Future work	128
A	Generation of correlated Gaussian random variables	131
B	Computation of path loss of first cluster	132
C	Radiation Patterns	134
C.1	The ULA with isotropic elements	134
C.2	The UCA with Isotropic	135
C.3	The URA with isotropic elements	136
C.4	The ULA with HW dipoles	137
C.5	The UCA with HW dipoles	138
C.6	The URA with HW dipoles	139
D	Derivation of closed-form spatial fading correlation for ULA, UCA and URA	140
D.1	Closed-form SFC for ULA	140
D.2	Closed-form SFC for UCA	142
D.3	Closed-form SFC for URA	142
E	Derivation of closed-form spatial fading correlation for EVS	144
F	Derivation of closed-form spatial fading correlation for EVS arrays	147
F.1	Closed-form SFC for ULA-EVS	148
F.2	Closed-form SFC for UCA-EVS and URA-EVS	150
G	Original publications	152
G.1	Journal papers	152
G.2	Conference papers	152
G.3	MVCE internal reports	153
G.4	COST 273 submissions	154
	References	178

List of figures

2.1	The output of the trace represents the polarisation state of the wave.	11
2.2	An arbitrary AA where each element is referenced to the origin of the coordinate system.	16
2.3	Mechanism for MC and the effect to the radiation pattern.	17
2.4	Illustration of path loss, large scale and small scale fading [69].	20
2.5	The concept of diversity combining with the two independent Rayleigh fading signals at Doppler frequency 100Hz.	24
2.6	Multi-user scenario using an AA receiver with ZF combiner.	27
2.7	The performance of MRC in a completely correlated Rayleigh fading channel. .	30
2.8	The performance of MRC in a completely uncorrelated Rayleigh fading channel.	31
2.9	The performance comparison between ZF and MRC.	32
2.10	The effect of different INR levels using MMSE on the system performance. . .	33
2.11	The performance of JD for $M = 4$ and varying number of users.	34
2.12	Array gain and diversity gain.	35
3.1	Multiple TDL model.	40
3.2	The frequency response of a 4 th order IIR filter at 100MHz maximum doppler frequency.	41
3.3	The generation of the fading signal.	42
3.4	Output of the filter for the first 1000 samples and the normalised level crossing rate.	42
3.5	Distribution of the envelope of the fading signal and the Rayleigh pdf fit. . . .	43
3.6	The location of local cluster and distant clusters.	45
3.7	Ratio of L_1/L as a function of distance between BS and MS.	47
3.8	An illustration of the instantaneous PDP for two clusters case.	49
3.9	The distinction of azimuth of arrival for the local and distant clusters.	50
3.10	Channel response of an omni-directional antenna 1 in the GTU at velocity 100km/h and antenna spacing $\lambda/2$	51
3.11	Channel response of an omni-directional antenna 2 in the GTU at velocity 100km/h and antenna spacing $\lambda/2$	52
3.12	Average PDP for the GTU normalised by to the first arrival path.	52
3.13	Average power azimuth spectrum for the GTU normalised by to the 0° MAOA.	53
3.14	The cdf for the DS values simulated in the COST 259 GTU channel model. . .	55
3.15	The capacity ccdf for $S_{50\%T}$ at SNR 0, 3, 6, 18 and 21dB for one mobile location with 180° AS.	56
3.16	The capacity ccdf of three DS values for different number of antennas at 21dB SNR for one mobile location with 180° AS.	56
3.17	The overall channel capacity ccdf of the three DS values for different number of antennas at 21dB SNR averaged over 1000 mobile locations with 180° AS. .	57
3.18	The capacity ccdf of three AS values for different number of antennas at 21dB SNR for one mobile location.	58

3.19	The overall channel capacity ccdf of the three AS values for different number of antennas at 21dB SNR averaged over 1000 mobile locations.	59
4.1	A HD and its radiation pattern.	66
4.2	A patch antenna and its radiation pattern.	68
4.3	A M-element ULA oriented in x-y plane with antenna spacing d	69
4.4	A M-element UCA oriented in x-y plane with circumference spacing d	70
4.5	A M-element URA oriented in x-y plane with antenna spacings d_x and d_y	71
4.6	An EVS consists of three electrically identical short dipoles and three magnetically identical small loops which are co-located and orthogonally oriented.	72
4.7	Mutual resistance and reactance of the centre fed HW dipole antennas located side-by-side as a function of the antenna spacing.	76
4.8	Magnitude of the coupling matrix elements for HD elements of the ULA at 0.5λ antenna spacing.	77
4.9	Magnitude of the coupling matrix elements for HD elements of the UCA at 0.5λ antenna circumference spacing.	78
4.10	Magnitude of the coupling matrix elements for HD elements of the URA at 0.5λ antenna spacings for d_x and d_y	78
4.11	The BER performance comparison of 4-element ULA with different antenna elements associated with ES. No MC is assumed.	80
4.12	The BER performance comparison of 4-element ULA with different antenna elements associated with AS. No MC is assumed.	81
4.13	The target SNR performance with $M=4$ antennas showing the comparison between ULA, UCA and URA under different ES at varying AS with 0° MAOA and 90° MEOA. No MC is assumed.	82
4.14	The target SNR performance with $M=4$ antennas showing the comparison between ULA, UCA and URA under different ES at varying AS with the 90° MEOA and 0° MAOA. No MC is assumed.	83
4.15	The target SNR performance with $M=4$ antennas showing the comparison between ULA, UCA and URA under different AS at varying MAOA with 60° ES and 90° MEOA. No MC is assumed.	83
4.16	The absolute received power versus antenna spacing for no MC, MC without normalisation and MC with normalisation at 0dB SNR.	84
4.17	The BER versus antenna spacing for no MC and MC with normalisation at 0dB SNR.	85
4.18	The distribution of power associated with elements $R(1,1)/R'(1,1)$ and $R(1,2)/R'(1,2)$ for a 2×2 correlation matrix.	86
4.19	The distribution of spatial correlation associated with elements $R(1,2)/R'(1,2)$ for a 2×2 correlation matrix.	86
4.20	The corresponding BER performance for $M=2$ antennas versus MAOA at various antenna spacings.	88
4.21	The target SNR for 0.01 BER with $M=4$ antennas versus antenna spacing for ULA, UCA and URA.	89
4.22	The BER performance for 2,4 and 8 diversity branches using HD. URA (circle), ULA (asterisk), 90° MAOA (solid) and 0° MAOA (dashed).	89

5.1	The statistical distribution for the uniform, Gaussian and Laplacian angle-of-arrival.	93
5.2	The MAOA, AS, MEOA and ES in spherical coordinates with uniform distributions in AOA and EOA.	94
5.3	The SFC comparison for the ULA, UCA and URA at 90° MAOA, 0° ES and 90° MEOA for different AS values.	95
5.4	The SFC comparison for the ULA, UCA and URA at 0° MAOA, 0° ES and 90° MEOA for different AS values.	96
5.5	The SFC comparison for the ULA, UCA and URA at 0° MAOA, 0° AS and 90° MEOA for different AS values.	98
6.1	SFC at various AS and ES values with 90° MEOA and MAOA for the ULA and ULA-EVS.	106
6.2	SFC at various AS and ES values with 90° MEOA and MAOA for the UCA and UCA-EVS.	107
6.3	SFC at various AS and ES values with 90° MEOA and MAOA for the URA and URA-EVS.	107
6.4	SFC between elements (m,n) of the EVS versus AS for 45° MAOA, 90° MEOA and 0° ES.	109
6.5	SFC between elements (m,n) of the EVS versus ES for 90° MAOA, 90° MEOA and 0° and 30° AS.	109
6.6	SFC between elements (m,n) of the EVS versus MEOA and versus MAOA for 30° AS and ES.	110
6.7	The target SNR as a function of MAOA and AS for EVS.	112
6.8	The target SNR as a function of MAOA and AS for ULA-EVS.	112
6.9	The target SNR as a function of MAOA and AS for URA-EVS.	113
6.10	The target SNR as a function of ES and MEOA for EVS.	114
6.11	The target SNR as a function of MEOA and ES for URA-EVS.	115
6.12	The target SNR as a function of AS and ES for EVS.	116
6.13	The target SNR as a function of AS and ES for ULA-EVS.	116
6.14	The target SNR as a function of AS and ES for URA-EVS.	117
6.15	The target SNR as a function of AS and ES for URA.	117
6.16	The target SNR as a function of MAOA and MEOA for EVS.	118
6.17	The target SNR as a function of MAOA and MAOA for ULA-EVS.	119
6.18	The target SNR as a function of MAOA and MAOA for URA-EVS.	120
6.19	The performance comparison between ULA, UCA, URA and EVS as a function of AS (0° ES) and ES (0° AS) at 90° MAOA and MEOA.	122
6.20	The performance comparison between ULA-EVS, UCA-EVS and URA-EVS as a function of AS (0° ES) and ES (0° AS) at 90° MAOA and MEOA.	123
6.21	The performance comparison at 10° ES and 90° MAOA and MEOA between ULA, UCA and URA.	124
6.22	The performance comparison at 10° ES and 90° MAOA and MEOA between ULA-EVS, UCA-EVS and URA-EVS.	125
C.1	The radiation pattern for the 4-element isotropic ULA with 0.5λ antenna spacing in 3-D, and with cuts through the z-x plane, x-y plane and y-z plane.	134

C.2	The radiation pattern for the 4-element isotropic UCA with 0.5λ antenna spacing in 3-D, and with cuts through the z - x plane, x - y plane and y - z plane.	135
C.3	The radiation pattern for the 4-element isotropic URA with 0.5λ antenna spacing in 3-D and with cuts through the z - x plane, x - y plane and y - z plane.	136
C.4	The radiation pattern for the 4-HW dipoles ULA with 0.5λ antenna spacing in 3-D and with cuts through the z - x plane, x - y plane and y - z plane.	137
C.5	The radiation pattern for the 4-HW dipoles UCA with 0.5λ circumference antenna spacing in 3-D and with cuts through the z - x plane, x - y plane and y - z plane.	138
C.6	The radiation pattern for the 4-HW dipoles URA with 0.5λ antenna spacing for d_x and d_y in 3-D and with cuts through the z - x plane, x - y plane and y - z plane. .	139

List of tables

2.1	General assumptions.	33
E.1	Result of integration for I_{ab} and K_{ab}	146

Acronyms and abbreviations

3-D	three-dimensional
3G	third generation
AA	antenna array
AF	array factor
AOA	azimuth-of-arrival
AS	azimuth spread
BER	bit error rate
BPSK	binary phase shift keying
BS	base station
CAA	compact antenna array
ccdf	complementary cumulative distribution function
cdf	cumulative distribution function
CIR	channel impulse response
DCM	directional channel model
DMI	direct matrix inversion
DS	delay spread
EMF	electromotive force
EOA	elevation-of-arrival
EP	external parameter
EPL	excess path loss
ES	elevation spread
EVD	eigenvalue decomposition
EVS	electromagnetic vector sensor
GP	global parameter
GSM	Global System for Mobile Communications
GTU	general typical urban
HD	halfwave dipole
i.i.d.	independent identical distributed
IIR	infinite impulse response

INR	interference plus noise ratio
ISI	inter symbol interference
JD	joint detection
LMS	least mean square
LOS	line-of-sight
LP	local parameter
MAOA	mean-azimuth-of-arrival
MC	mutual coupling
MEOA	mean-elevation-of-arrival
MIMO	multiple-input-multiple-output
MININEC	mini numerical electromagnetics code
MLSE	maximum likelihood sequence estimation
MMSE	minimum mean square error
MOM	method of moment
MPC	multipath component
MRC	maximum ratio combining
MS	mobile station
NEC	numerical electromagnetics code
NLOS	non-line-of-sight
PAS	power azimuth spectrum
pdf	probability density function
PDP	power delay profile
PDS	power delay spectrum
PES	power elevation spectrum
rms	root mean square
RLS	recursive least square
RE	radio environment
RV	random variable
SFC	spatial fading correlation
SIMO	single-input-multiple-output
SINR	signal-to-interference plus noise ratio
SNR	signal to noise ratio
SV	steering vector

SVD	singular value decomposition
TDL	tapped delay line
TV-CIR	time-variant channel impulse response
TV-DCIR	time-variant directional channel impulse response
TV-DVCIR	time-variant directional vector channel impulse response
UCA	uniform circular array
ULA	uniform linear array
URA	uniform rectangular array
XPD	cross polar discrimination
ZF	zero forcing

List of symbols

$\mathbf{a}(\varphi, \theta)$	steering vector in the direction φ and θ
$\mathbf{a}_{EAA}(\Theta)$	steering vector for electromagnetic vector sensor arrays
$\mathbf{a}_{LOS}(\varphi, \theta)$	steering vector for the LOS component in the direction φ and θ
\mathbf{B}	magnetic field vector
B_d	Doppler frequency
C	channel capacity
C^{ab}	$\cos^a(x) \cos^b(x)$
C_j	j^{th} cluster
C_i	cosine integral
\mathbf{d}	users's signal vector
d_u	output signal of the combiner
d	antenna spacing for antenna array
d_{eff}	effective antenna spacing
d_x	antenna spacing between array element parallel to the x -axis
d_y	antenna spacing between array element parallel to the y -axis
d_{CO}	cut off distance
d_{MS-BS}	distance between base station and mobile station
D	directivity
\mathbf{E}	electric field vector
$f(\varphi, \theta)$	normalised radiation pattern
f_d	Doppler frequency
f_{dmax}	maximum Doppler frequency
f_s	sampling frequency
$g_{nm}(t)$	input of the spatial shaping filter or output of the temporal filter
\mathbf{h}	channel vector
$h_m(t, \tau, \Omega)$	time-variant directional channel impulse response of the m^{th} antenna
$h(t, \tau)$	time-variant channel impulse response
h_{BS}	BS height
h_B	average building height

$\mathbf{h}[k, n]$	discrete channel impulse response
$\mathbf{h}(t, \tau, \Omega)$	time-variant directional channel impulse response
\mathbf{H}	channel matrix
$\mathbf{H}(f)$	channel transfer vector
$H(s)$	transfer function for filter
I_{ab}	integral of $\sin^a(\varphi) \cos^b(\varphi)$
\mathbf{I}	identity matrix
\mathbf{J}	electric current density
J	minimum difference between received signal and possible sequence
J_k	Bessel function of k^{th} order
\mathbf{k}	propagation vector in the direction of incoming signal
k_w	wave propagation number
K_r	rank of a matrix
K	rice factor
K_0	narrowband K-factor
K_{ab}	integral of $\sin^a(\theta) \cos^b(\theta)$
L	total number of multipath components
L_i	cluster path loss for i^{th} cluster
L_{add}	path loss for additional clusters
m_c	mean number of clusters
\mathbf{M}	magnetic current density
M	number of antennas
M_T	number of transmit antennas
N_R	number of receive antennas
N	number of users
N_{cl}	number of clusters
$N_{cl,min}$	minimum number of clusters
N_{LS}	number of local clusters
N_{tap}	number of taps
$p(\varphi)_u$	uniform probability density function
$p(\varphi)_g$	Gaussian probability density function
$p(\varphi)_l$	Laplacian probability density function
$P(\cdot)$	Poisson distribution

P_e	theoretical probability error
P_i	shadowing of i^{th} cluster
$P_i(\tau)$	power delay profile of the i^{th} cluster
$P_i(\varphi)$	power azimuth spectrum of the i^{th} cluster
$P_i(\theta)$	power elevation spectrum of the i^{th} cluster
$P_i(\tau, \varphi)$	power azimuth-delay spectrum of the i^{th} cluster
P	total power radiated
P_{dir}	power of direct component
P_{LOS}	probability of line-of-sight
\mathbf{r}_m	vector position of element m relative to origin
r	radius of a uniform circular arrays
\mathbf{R}	spatial correlation matrix
\mathbf{R}_R	correlation matrix for receiver
\mathbf{R}_T	correlation matrix for transmitter
\mathbf{R}_{BS}	correlation matrix for BS
\mathbf{R}_{MS}	correlation matrix for MS
\mathbf{S}	received voltage vector without mutual coupling
S_i	sine integral
S^{ab}	$\sin^a(x) \sin^b(x)$
$S_{\varphi,i}$	azimuth spread of cluster i
$S_{\tau,i}$	delay spread of cluster i
$S_{10\%\tau}$	10 percentile of the DS
$S_{50\%\tau}$	50 percentile of the DS
$S_{90\%\tau}$	90 percentile of the DS
T	time resolution of the tap
T_m	multipath spread
\mathbf{U}	unitary matrix
$U(\varphi, \theta)$	radiation intensity
U_m	maximum radiation intensity
U_{ave}	average radiation density
\mathbf{V}	received voltage vector with mutual coupling
W_k	weight for k^{th} antenna
\mathbf{W}	weight matrix

$x!$	x factorial
\mathbf{y}	received signal vector
Z	geometry of the antenna array
\mathbf{Z}	impedance matrix
Z_L	load impedance
Z_{ij}	impedance between element i and j
\mathbf{Z}_{norm}	normalised impedance matrix
α	amplitude
β	phase shift
δ	Dirac delta function
Δ_θ	elevation spread
Δ_φ	azimuth spread
$(\Delta f)_c$	coherence bandwidth
$(\Delta t)_c$	coherence time
$(\Delta f)_s$	signal bandwidth
$(\Delta t)_s$	symbol duration
η	polarisation phase difference
γ	auxiliary polarisation
ε	amplitude
$\Gamma(\cdot)$	Gamma function
λ	wavelength
λ_k	k^{th} eigenvalue
Λ	diagonal matrix of its real-valued-eigenvalues
μ	phase shift between successive element along the x -axis
ν	phase shift between successive element along the y -axis
$\rho(x,y)$	complex correlation for variables x and y
σ^2	noise variance
σ_k	k^{th} singular value
τ_θ	tilt angle
τ	delay
τ_{1,D_R}	delay when the power of cluster 1 drops below $D_R(dB)$
θ	elevation-angle-of -arrival
θ_0	mean-elevation-of-arrival

Θ	spatial vector parameter
φ	azimuth-angle-of -arrival
φ_0	mean-azimuth-of-arrival
$E\{ \cdot \}$	expectation operation
$[\bullet]$	dot product
$[\cdot]^T$	transposition operation
$[\cdot]^H$	Hermitian transpose operation
$(\cdot)^{-1}$	inverse matrix
$[\cdot]^*$	complex conjugate operation
\Im	imaginary part
\Re	real part
\otimes	Kronecker multiplication operator
$\binom{b}{a}$	b select a
$\det(\cdot)$	determinant
$\arctan(\cdot)$	arc tangent
$ \cdot $	absolute operation
\overline{X}	mean value of X
$\delta(\cdot)$	Dirac delta function
$diag(\cdot)$	diagonal of the matrix
$\exp(\cdot)$	exponential function
$max(\cdot)$	maximum value
$sinc(\cdot)$	sinc function
$vec(\cdot)$	maps a matrix to vector by stacking the columns of the matrix

Chapter 1

Introduction

The migration of mobile communication from second to third generation (3G) or beyond entails high data rate communication, a reliable link at anytime and anywhere as well as better quality services [1, 2]. To be able to satisfy these demands, adaptive antenna arrays (AAs) can be employed at both base station (BS) and mobile station (MS) to improve the overall system performance [3–7]. The research on the application of AAs at the BS has been active over the past few years as there are less implementation constraints [8]. Recently, the use of AAs at the MS has been given attention with the idea that the compact AAs could be mounted at the back of the user terminals [8–11]. This new application faces a number of challenges. Firstly, the limitation in the physical size of the mobile limits the number of antenna elements that can be mounted on the units. Secondly, the lack of understanding of the impact of propagation conditions from the perspective of the MS. Thirdly, an appropriate signal processing algorithm for the AAs in mobile requires careful design which must take into account the performance and complexity requirements of the terminals.

In broader terms, the limitation of the size of the MS will impact directly on the performance of an AA. Various antenna specific effects such as antenna patterns, AA configurations, mutual coupling (MC), etc. will have a significant impact on the array's performance and must be adequately characterised. Unfortunately, little work has been reported in the literature that comprehensively investigates their impact on the system performance. It is a common practice to assume the antenna elements used are isotropic. The use of this ideal antenna which radiates equally in all directions simplifies the analysis and yields a better performance than is obtained when more practical antennas are used. Furthermore, the AAs used in the literature are typically in uniform linear configuration. It is well known that the uniform linear array (ULA) performs better in broadside than in endfire conditions. However, the performance of other AAs such as uniform circular arrays (UCA) and uniform rectangular arrays (URA) has not been adequately investigated. Due to the geometry of the arrays, the array performance can vary significantly under different channel conditions. In order to obtain the overall array performance, an extensive analysis on a particular array configuration is generally required and thus

precludes many practical approaches. Though MC has been theoretically and experimentally investigated, the study of the effect of MC in the system performance is not fully understood. A number of conflicting studies have been reported in the literature examining the impact of MC. It was shown that the performance of adaptive AAs in the presence of MC degraded significantly as compared to the case of no MC [12, 13]. However, [14, 15] show that MC decreases the correlation of the received signal between antenna elements. Hence, to accurately evaluate the system performance of AA, the effect of MC must be fully modelled.

Since the functionality of the AA is mainly based on the exploitation of the spatial properties of the multipath channel, it is imperative to gain a good understanding of the influence of angular parameters on the performance of AA. In general, the angular domain comprises both the azimuth-of-arrival (AOA) and elevation-of-arrival (EOA). Different statistical probability density functions (pdfs) have been deployed to model the AOA and EOA of the multipath components (MPCs) that arrive at the MS. The AOA statistics have been extensively investigated for both indoor and outdoor environments whereby uniform, Gaussian and Laplacian pdfs have been proposed in [16], [15] and [17] respectively. On other hand, the EOA has received little attention and is usually modelled as a uniform or Laplacian pdf as suggested in [11]. Most of the work reported in the literature derives a spatial fading correlation (SFC) for a particular AA and AOA distribution assuming the elevation is contained in the horizontal plane only. For instance, [18] derived a closed-form SFC in uniform AOA for the ULA; [19] derived a closed-form SFC in Laplacian AOA for the UCA and [15] derived a closed-form SFC in Gaussian AOA for the ULA. A more unified approach proposed by [20] studies the SFC for the ULA in the uniform, Gaussian and Laplacian AOA pdfs using a geometrical based channel model. In addition, an approximate SFC expression averaged over all possible azimuth orientations of the MS is derived in [21]. The SFC in this case is computed based on uniform distribution within an azimuth range parameterised by angular spread $0 \leq \Lambda \leq 1$. In [22], an attempt is made to derive a simple generalised equation for the SFC using the three AOA pdfs discussed. Unfortunately, the generalised SFC is only applicable for small azimuth spread (AS) and mean-azimuth-of-arrival (MAOA) close to 0° . Furthermore, the approximated SFC which is derived based on Gaussian distribution tends to over predict the correlation value for Laplacian distributions at higher correlation, and under predict for uniform distributions at lower correlation. Recent work in [23] derived the SFC for each of the distributions for ULA by taking clustering into account. Simplification of the SFC analysis can be achieved as [24] demonstrated mathematically that the impact of AOA pdfs is insignificant and what matters is the AS. Furthermore, [24] also shows

that many AOA statistics obtained through measurements yield Laplacian distribution of the nominal AOA. However, the derivation is limited to the ULA case and it assumes the array has a beamwidth much wider than the AS.

While the results in these works are important for diversity studies, they are mainly limited to the azimuth plane only. Aulin [25] extended the classical Clarke model [26] by incorporating a three-dimensional (3-D) approach. Aulin assumed that the AOA is uniformly distributed over $[0, 2\pi]$ while the EOA is non-uniformly distributed around the horizontal plane. The SFC is expressed in terms of an integral of a Bessel function of the first kind of zero order. Apart from Aulin, several 3-D models have also been reported recently [27, 28]. Teal [27] presented a model analysis approach which claimed that it allows closed-form expressions for the SFC to be obtained for arbitrary scattering distribution functions. Unfortunately, the model is limited to the case of the ULA and the result for the 3-D case is only expressible in terms of some integrals¹. On the other hand, Mohasseb [28] proposed a 3-D spatio-temporal simulation model for the ULA (both vertical and horizontal arrays) which is useful for space-time coding. The major shortcoming of this geometrically based model is computational inefficiency whereby scatterers are needed to be deployed tailored to the specific channel parameters.

None of the above work yields expressions in closed-form that relate different parameters associated with AOA, EOA and the geometry of the AA so that the SFC can be easily evaluated. Such a closed-form expression is needed to simplify the analyses of the impact of these parameters on the system performance particularly for systems employing smart antenna technology. To date, there also exists no generalised SFC function that describes the SFC between element pairs of a given AA for a given distribution in both AOA and EOA domains.

Significant degradations in performance can be observed in scenarios with small AS but significant elevation spread (ES) if only AOA is considered. This is due to the fact that the performance of the handset AAs is also dependent on the effect of EOA since the handset could be randomly oriented [29]. Moreover, recent measurement results have also demonstrated the practical significance of EOA. In particular, [30] showed that about 65% of the energy was incident with elevation² larger than 10° above the horizontal while [31] reported that about 90% of the energy was incident with elevations between 0° and 40° . Interestingly, [32] reported an average ES of 9° for several environments ranging from indoor to outdoor while [33] mea-

¹Though two-dimensional cases are reducible to closed-form.

²The measurement results reported here define the elevation angle with respect to the azimuth plane.

sured values of 70.6° for the AS and 28.8° for the ES with Laplacian power spectra in vertical polarisation for the indoor-to-outdoor environment.

Another assumption that is commonly adopted in the literature is the isotropic scattering at the MS. Despite being widely used, recent measurement results in [30–35] demonstrate that it is not always true to assume isotropic scattering at the MS, particularly in dense urban areas with street dominated environments (where the canyon effect is significant) and for outdoor-indoor cases. Moreover, in AA terminal receivers, the beamforming algorithm itself will determine the effective angle spread that is being observed [36].

1.1 Objective and contributions to knowledge

1.1.1 Objective

Based on the problems addressed above, a number of possible solutions are generated which form the motivation of the work reported here. The main objective of this thesis is to study in detail the main constraints on the application of compact arrays and to describe how such constraints can be modelled and incorporated from the perspective of antenna and channel parameters. In this regard, 3-D SFC models are developed which facilitate the study of the impact of antenna parameters and channel conditions on the system performance, hence, permitting the study of the trade-offs between the associated channel and antenna parameters in the development of compact arrays. The work reported here can be used to identify optimised parameters for specific scenarios so that system performance can be maximised. The developed SFC models can also be used to determine the correlation matrices at both transmitter and receiver in multiple-input multiple-output (MIMO) systems.

1.1.2 Contributions

Several contributions regarding the performance analysis of the AAs from the perspective of antenna and channel issues are addressed in this thesis. The main contributions of this work can be summarised as:

- The implementation of the COoperation européenne dans le domaine de la recherche Scientifique et Technique (COST) 259 channel model using a tapped delay line (TDL) is reported which facilitates link level simulations for AA system [37, 38].

- An antenna model that incorporates various antenna effects into the performance study of AAs systems is developed. In particular, the proposed MC model can explain the apparently conflicting claims reported in the literature [39, 40].
- It is shown that the impact of using different AOA and EOA distributions on the performance of different AAs is insignificant. The key parameter for system performance is the standard deviation of the underlying distribution [41].
- 3-D SFC models for ULA, UCA, URA, electromagnetic vector sensor (EVS) and EVS arrays are developed. The closed-form SFC functions are expressed in terms of AOA, EOA as well as the geometry of the AA under consideration. The closed-form SFC expressions can be used to determine the correlation matrices at both the BS and MS for capacity analysis [42–45].
- An extensive analysis to determine the sensitivity of the AAs over all possible angles is carried out. This gives the invaluable insights into the array's performance for many scenarios. Such a performance pattern can assist the design of AA algorithms by exploiting the characteristics of the AA in advance [46].
- The practicability of introducing a MIMO receiver for MS using EVS and EVS arrays over traditional arrays is demonstrated. The EVS and EVS arrays offer several advantages in terms of their capability to exploit multipath richness, reduced dependency on the angular of arrival as well as the capability to yield higher performance for a given increase in antenna spacing [46].

1.2 Organisation of the thesis

The rest of the thesis is structured in chapters as follows:

Chapter 2

This chapter presents an overview of the relevant information in the area of antenna and wireless propagation. Some fundamental properties of the antenna and propagation channel are highlighted. A number of techniques that can be employed to enhance system performance by means of diversity are revisited. This is followed by investigating the tradeoff between the performance and complexity for the various combining algorithms used in spatial diversity receivers.

Chapter 3

This chapter outlines the implementation of the COST 259 macrocell channel models. Major channel effects are discussed and incorporated into existing channel models with certain modifications and assumptions. Channel capacity analysis of the implemented channel model is presented to study the impact of delay spread (DS) and AS. The capacity results reveal that the impact of the AS is more significant than the DS. The importance of correlation matrix and eigenvalue decomposition (EVD) techniques is also discussed.

Chapter 4

This chapter presents an antenna model that incorporates various antenna effects into the performance study of AA systems. The various antenna parameters that affect the array performance are first identified and described. This is followed by a comprehensive study of the antenna effects by means of computer simulation. The important result obtained in this chapter is that the MC causes fading decorrelation which in principle leads to performance gain, but this is compensated by the effect of signal cancellation that reduces the received power. The overall effect of MC is to reduce the system performance.

Chapter 5

This chapter investigates the impact of the AOA and EOA distributions on the performance of different AA topologies. Several typical pdfs for AOA and EOA are studied. The analysis shows that the actual distribution for the AOA and EOA is not a primary concern, but instead the associated AS and ES values are the key parameters that determine the performance.

Chapter 6

This chapter derives closed-form expressions for the SFC functions of various AAs in a 3-D multipath channel. The SFCs are expressed in terms of the AOA and EOA as well as the geometry of the AA under consideration. Verification is carried out through computer simulation. The application of the developed SFCs are highlighted. In particular, the importance and dependency of the angular parameters on the system performance is demonstrated by the developed performance pattern. Capacity analysis for MIMO systems employing various AA configurations for different channel conditions is also presented.

Chapter 7

In the final chapter, some concluding remarks are presented and possible future work is described.

Chapter 2

Principles and background information for antenna and wireless propagation

The performance of wireless communication systems depends strongly on various factors, particularly the antennas that are used and the propagation channel encountered. Thus, it is vital to gain a good understanding on the area of antennas and propagation so that their impact on the system performance can be studied. This chapter presents an overview of the principles and background to the area of antennas and wireless propagation which form the basis of this thesis. The rest of the chapter is structured as follows: Section 2.1 briefly reviews some of the basic but important antenna theories that assist in understanding the concept of antenna as a source of communication. The properties of various groups of antennas and AAs are also outlined; Section 2.2 discusses some important properties of wireless propagation channel associated with selectivity and dispersion; Section 2.3 revisits a number of diversity techniques that can be used to enhance the system performance based on the exploitation of the channel and antenna; Section 2.4 gives an overview of the number of techniques that employing spatial diversity. The tradeoff between the performance and complexity of these techniques are also compared in this section; Section 2.5 outlines and explains a number of commonly used terms in the context of AAs. Finally, Section 2.6 summarises the chapter.

2.1 Review of basic antenna theory

2.1.1 Fundamental antenna parameters

This section aims to give an overview and definition for some fundamental antenna parameters. These parameters are widely used in the antenna community to describe the characteristics and performance of an antenna. Due to large number of parameters, attention is only focused on those that will be used in this thesis as given as follows:

1. Radiation patterns: how to evaluate a radiation field?

The radiation pattern of an antenna is defined as a mathematical function or graphical representation of the electromagnetic waves emitted by the antenna as a function of space coordinates. In general, the radiation pattern of a radiating element (antenna) can be mathematically expressed by invoking Maxwell's equations. The derivation of far field radiation patterns for antennas such as a short dipole and a halfwave dipole (HD) have been demonstrated in many antenna textbooks [47–50] and will not be further described here. Instead, general guidelines for radiation pattern evaluation are summarised as follows where the electric and magnetic current density are specified as \mathbf{J} (in A/m^2) and \mathbf{M} (in V/m^2) respectively:

1. Determine a magnetic vector potential \mathbf{A} due to \mathbf{J} using

$$\mathbf{A} = \frac{\mu_0}{4\pi} \iiint_V \mathbf{J} \frac{e^{-jk_w r_d}}{r_d} dv' \quad (\text{wb/m}) \quad (2.1)$$

where the scalar μ_0 is the permeability of free space, scalar r_d is referred as a distance between the source and the observation point in meter, the term V represents the integral over the volume and scalar k_w signifies the wave propagation number given by $2\pi/\lambda$ where λ is the wavelength.

2. Determine the electric field, \mathbf{E} from the vector \mathbf{A} . For a z directed line source¹ $I(z')$, under far field conditions, \mathbf{A} can be simplified to

$$\mathbf{A} = \hat{\mathbf{z}} \frac{\mu_0}{4\pi} \int I(z') \frac{e^{-jk_w r_d}}{r_d} dl' \quad (2.2)$$

where $\hat{\mathbf{z}}$ is the unit vector in the z -direction. Then the vector \mathbf{E} is given by

$$\mathbf{E} = -j\omega\mathbf{A} \quad (\text{V/m}) \quad (2.3)$$

3. Determine the magnetic field \mathbf{B} from vector \mathbf{E} . Using the plane wave relation where the vectors \mathbf{B} and \mathbf{E} are perpendicular to each other and to the direction of propagation, \mathbf{B} is then given by,

$$\mathbf{B} = \frac{1}{\mu_0} \times \mathbf{E} \quad (\text{A/m}) \quad (2.4)$$

¹Unless otherwise specified, the antenna used in this thesis is assumed to be z -oriented (directed) i.e. in parallel to the z -axis

where \times denotes the cross product. Similarly, the far field radiation due to magnetic source \mathbf{M} can be determined in a similar manner by first computing electric vector potential \mathbf{F} [47].

2. Radiation intensity

Radiation intensity is defined as the power radiated from an antenna per solid angle expressed as

$$U(\varphi, \theta) = U_m |f(\varphi, \theta)|^2 \quad (2.5)$$

where the scalars φ and θ are the azimuth and elevation angles respectively. The term U_m is the maximum radiation intensity given as $U_m = U(\varphi_{max}, \theta_{max})$ and $f(\varphi, \theta)$ is the normalised radiation pattern in the direction of maximum intensity signified by $(\varphi_{max}, \theta_{max})$. It is straightforward to obtain the total power radiated by an antenna in space by

$$P = \int_0^{2\pi} \int_0^\pi U(\varphi, \theta) \sin(\theta) d\varphi d\theta \quad (2.6)$$

where $\sin(\theta) d\varphi d\theta$ is the element of solid angle in spherical co-ordinates. Thus, the average radiation density is given by

$$U_{ave} = \frac{P}{4\pi} \quad (2.7)$$

3. Directivity

The directivity, D , is an important parameter for an antenna, which is defined as the ratio of the radiation intensity in a given direction from the antenna to the radiation intensity averaged over all directions [47–49]. The average intensity is equal to the total power radiated by the antenna divided by 4π . However, if the direction is not specified, maximum direction radiation intensity is assumed. Mathematically, D is given by

$$D(\varphi, \theta) = \frac{U(\varphi, \theta)}{U_{ave}} \quad (2.8)$$

Substituting (2.5) and (2.7) into (2.8) gives

$$D(\varphi, \theta) = \frac{4\pi |f(\varphi, \theta)|^2}{\int_0^{2\pi} \int_0^\pi |f(\varphi, \theta)|^2 \sin(\theta) d\varphi d\theta} \quad (2.9)$$

4. 3dB beamwidth

The 3dB beamwidth is defined as the angular separation of the points where the power

drops by half relative to the maximum [47–49]. This parameter describes the resolution of an antenna to differentiate two closely located radiating objects. The sidelobe level of an antenna can also be qualitatively determined whereby large beamwidth corresponds to low directivity.

5. Polarisation

In this thesis, a plane wave propagation is assumed where the electric and magnetic fields lie in planes that are perpendicular to each other. The polarisation of a plane wave can be characterised by the electric field traced out with respect to time at a fixed observation point. The traces generated can be generally described by using a polarisation ellipse as shown in Figure 2.1(a) [51, 52]. The scalar γ is the auxiliary polarisation angle by which the electric field component in the y direction, E_y , leads the electric field component in the x direction, E_x given by

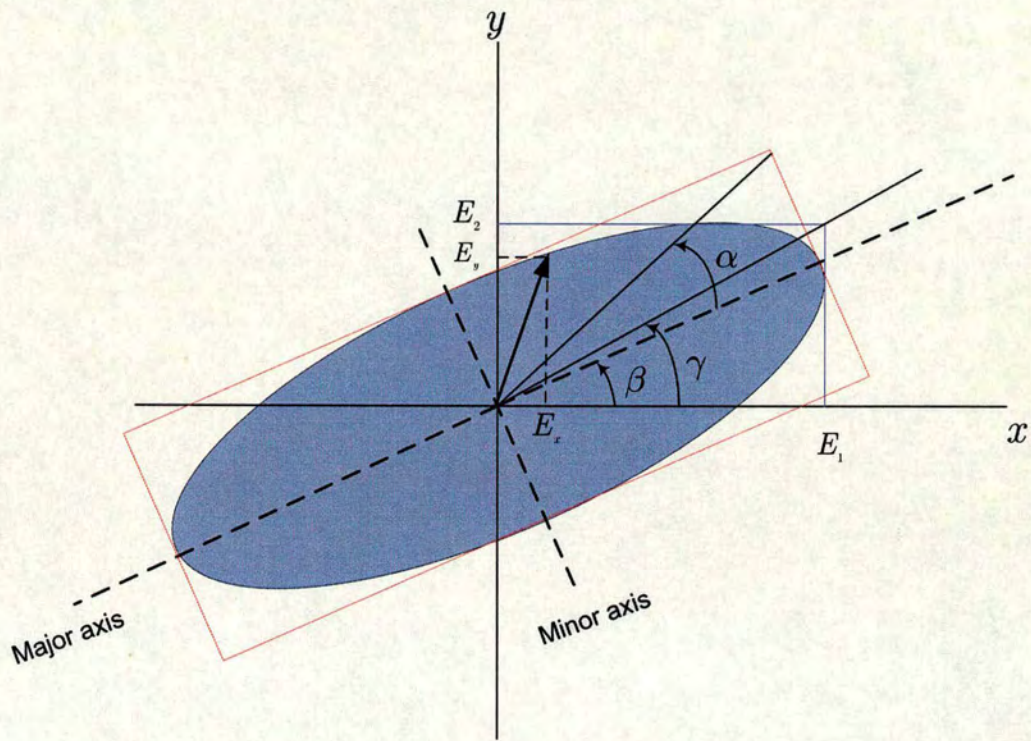
$$\gamma = \tan^{-1} \left(\frac{E_2}{E_1} \right), \quad 0^\circ \leq \gamma \leq 90^\circ \quad (2.10)$$

where E_1 and E_2 are the amplitude of the linearly polarised wave in the x and y direction respectively. The scalar η ($-180^\circ \leq \eta \leq 180^\circ$) is the polarisation phase difference. Another way to describe wave polarisation is using the Poincaré representation where the scalars τ_θ ($0^\circ \leq \tau_\theta \leq 180^\circ$), tilt angle² and ϵ are introduced. The scalar ϵ is given by

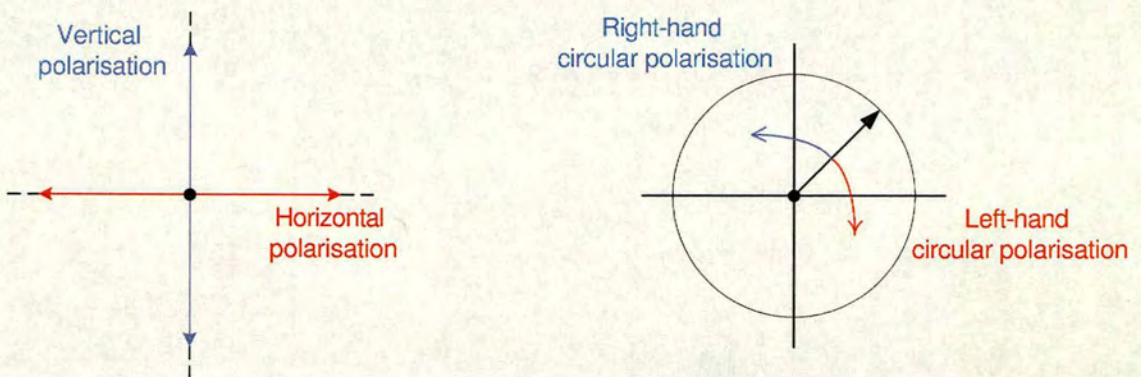
$$\epsilon = \tan^{-1} \left(\frac{1}{\mp AR} \right), \quad -45^\circ \leq \epsilon \leq 45^\circ \quad (2.11)$$

where AR is the axial ratio of the ellipse defined as the ratio of the major axis to the minor axis. Note that a set of parameters γ and η or ϵ and τ is sufficient to characterise the polarization state of a electromagnetic wave. Knowing the value of one of the set, allows the other set to be easily evaluated. Linear and circular polarisation are special cases of the elliptical polarisation as depicted in Figure 2.1(b). A linear polarised wave occurs when $\eta = 0$ (or $AR = \infty$). For vertical polarisation, $E_1 = 0$ while for horizontal polarisation $E_2 = 0$. A 45° linear polarisation is produced when $E_1 = E_2$. For circular polarisation, $\eta = \pm 90^\circ$ ($AR = 1$) and $E_1 = E_2$ which the positive sign signifies the left circularly polarised and vice versa. Examples of antennas that produce linear and circular polarisation are dipole and helix antennas. The discussion so far is only concentrated on

²Tilt angle is defined as the angle between the positive x -axis and the major axis.



(a) Elliptical polarisation.



(b) Linear and circular polarisation.

Figure 2.1: The output of the trace represents the polarisation state of the wave.

deterministic polarisations. In practice, the transmitted signal can have a random polarisation due to the reflection and scattering of different MPCs that make up the signal. This causes a difference in power between the vertical and horizontal polarised components at the receiver.

2.1.2 Classification of antennas

Antennas can be categorised into several classifications based on their function, size and frequency of operation.

1. Electrically small antennas

The term small refers to the physical size being much less than a wavelength. This type of antenna is one of the simplest and commonly used antenna for many applications. The operating frequency of the electrically small antenna is in the range of very high frequency and below. Due to its simplicity, a mathematical framework can possibly be developed more easily than for other complex antennas for the purpose of theoretical analysis. Some basic properties of the electrical small antennas include very low directivity, low input resistance, high input reactance and low radiation intensity. Short dipole, small loop and monopole are examples of this group of antennas.

2. Resonant/wire antennas

This type of antenna is also simple and relatively easy to analyse. It has low to moderate gain with broad main beam and input impedance close to being a real value. The operating frequency of resonant antennas are from high frequency to the GHz range but with a narrow bandwidth. HDs and microstrip/patch antennas are examples of resonant antennas.

3. Broadband antennas

This term broadband refers to the higher operating bandwidth of this type of antenna compared to the resonant ones. Broadband antennas offer acceptable performance in terms of pattern, gain and impedance whereby these parameters are approximately constant over the wide range of frequency. The basic properties of the broadband antenna include low to moderate constant gain, and real input impedance. Spiral, helical and log periodic dipole arrays are examples of broadband antennas.

4. Aperture antennas

The term aperture reflects that this type of antenna has an opening through which propagating waves can flow into the waveguide. The aperture is usually several wavelengths long. The basic properties of aperture antennas include moderate bandwidth, high gain and the gain increased with frequency. Typically used in aircraft and spacecraft applications, horn and reflector are examples of aperture antennas.

2.1.3 Typical mobile antennas

Apart from the halfwave dipole, patch antenna, loop and monopole, some typically used antennas in the mobile communications are briefly reviewed .

1. Quarter wavelength monopole (Whip)

By applying the principle of image theory with a ground plane of infinite size [53], a monopole antenna can be obtained. If a ground plane is placed at the centre of a dipole with the lower part of the dipole removed, a monopole antenna is formed. The handset case can be used as the ground plane of this type of antenna. Since the effective length is half of the HD, we expect the input impedance is reduced by half of that found in the dipole counterpart i.e. about $(36 + j21.3)\Omega$. The radiation only takes place in the upper part of the ground plane; therefore double the directivity of a similar dipole i.e. 3.28 is obtained. The radiation patterns of monopole antennas depend on the type of ground plane used. This type of antenna is suited to mobile communication because of its small physical size.

2. Helix

A helix antenna is an example of a broadband antenna. Basically, the helix consists of a conducting wire wound in the form of screw thread under a ground plane. The important parameters associated with helix is the number of turns, diameter and spacing between each turn as well as the pitch angle, defined as the inverse tangent of the ratio between successive turn spacing and the circumference of the helix. Depending on the pitch angle, the helix can be reduced to either a loop antenna or a linear straight wire. The radiation characteristics of the antenna can be varied by adjusting its geometrical properties compared to the wavelength [47]. The input impedance is strongly dependent on the pitch angle and the size of the conducting wire [47]. Circular and linear polarisation can be achieved using a helix since it has an elliptical polarisation in the general case [49]. The

common modes of operation for helix are normal mode and axial mode. Other types of helix antennas are bifilar and quadrifilar helix [54].

3. Planar inverted-F antenna

A planar inverted-F antenna (PIFA) is one of the most compact patch-type antennas and was originally called open microstrip antennas. The usage of this type of antenna is becoming increasingly popular. The PIFA antenna literally looks like the letter 'F' lying on its side with the two shorter sections providing feed and ground points and the 'tail' providing the radiating surface. The main advantage of PIFA is its compact size as compared to the square patch antenna and thus it can easily be incorporated into wireless handsets. PIFA has a very good bandwidth capability [29]. Apart from that, embedded PIFAs has less requirement for a separate dielectric carriage, which normally degrades the efficiency of the antenna. In general, PIFA antennas require the use of a ground plane, which is usually the cellular phone circuit board ground plane. PIFAs make good embedded antennas in that they exhibit a somewhat omnidirectional pattern and can be made to radiate in more than one frequency band [54].

2.1.4 Antenna arrays and smart antennas

As mobile technology advances, many applications (such as tracking and interference rejection) require more flexible and powerful antenna systems with specific characteristics that a single antenna is not capable of providing. Such a limitation can be overcome by means of arranging the antenna elements in certain electrical and geometrical configuration to form an AA. In an interference rejection application for example, one can use AAs to form a beam (with high gain/directivity) directed towards the desired user while simultaneously forming nulls to the interfering users. Furthermore, for tracking applications, the beam of the underlying antenna systems (algorithm) must be able to follow the user as they move along a given trajectory. The use of AAs in these scenarios is termed as spatial filtering or array beamforming, which have received significant attention in wireless communication systems employing space division multiple access.

Two main areas of research can be found in the literature namely array synthesised and adaptive beamforming (smart antennas). In general, adaptive arrays outperform synthesised arrays in performance since the adaptive processing is based on statistically optimum processing while the synthesised array has a fixed array response to a random time varying fading channel. The

fixed weight³ synthesised array is easier to implement in the mobile terminals due to its low complexity. This helps in reducing the cost and processing power required at the user terminal. Part of the work in this thesis involved in investigating fixed weight synthesis arrays and the response of the arrays to various channel conditions and antenna parameters. The basic concepts and terminologies (such as directivity, 3dB beamwidth and radiation pattern) for AAs remain the same as the single antenna case. However, parameters needing further attention are the steering vector (SV)⁴ and the array manifold of the AA. A SV is the response of the AA to the incoming signal that relates the phase of the signal at each of the antenna elements with respect to a reference element usually located at the origin of the coordinate system. In general, the SV for an AA with arbitrary element positions as shown in Figure 2.2 is given by the response of each antenna element to the incoming signals i.e.

$$\mathbf{a}(\varphi, \theta) = \left[a_1(\varphi, \theta), a_2(\varphi, \theta), \dots, a_M(\varphi, \theta) \right]^T \quad (2.12)$$

where the superscript $[\cdot]^T$ represents the transpose. The response of each antenna element of the AA can be determined by considering the direction cosine which represents the spatial distance of the antenna element m with respect to the reference element. Thus, each element of the SV in (2.12) is given by

$$\begin{aligned} a_m(\varphi, \theta) &= e^{-j\mathbf{k}_w \cdot \mathbf{r}_m} \\ &= e^{-j\frac{2\pi}{\lambda}(x_m \cos \theta \cos \varphi + y_m \cos \theta \sin \varphi + z_m \sin \theta)} \end{aligned} \quad (2.13)$$

where \mathbf{r}_m is the vector position of element m relative to the origin and \mathbf{k}_w is the propagation vector given by $|\mathbf{k}_w| = 2\pi/\lambda$ in the direction of signal propagation. The operator $[\cdot]$ denotes the dot product. Finally, the array manifold is a set of SVs calculated over all values of θ and φ .

2.1.5 Mutual coupling

The discussion so far assumes that the element terminal currents are proportional to their excitations and the current distribution for each element in the array is identical. In practical AAs,

³One can obtain a desired pattern without signal weighting by appropriately arranging the array in a specific configuration.

⁴The term array factor (AF) is used interchangeably with SV in this thesis although some authors define them slightly differently.

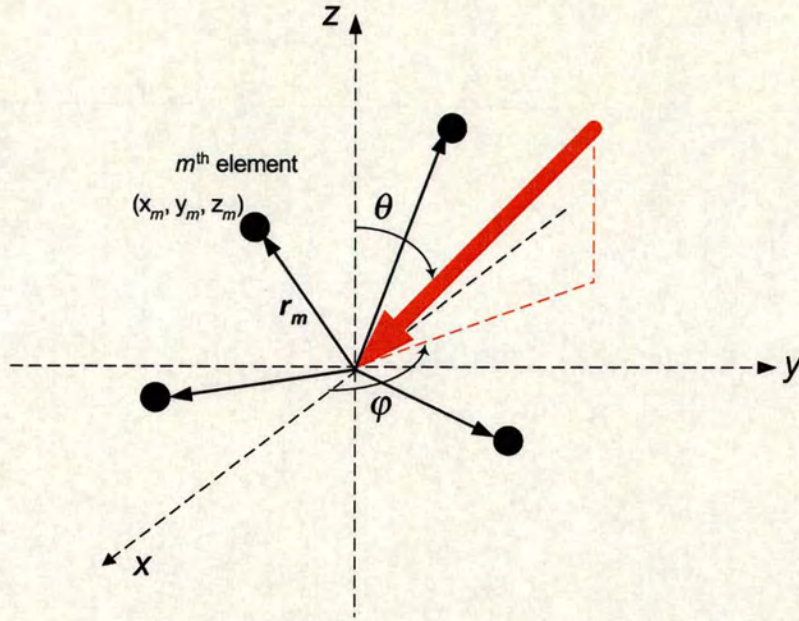


Figure 2.2: An arbitrary AA where each element is referenced to the origin of the coordinate system.

the elements of the array interact with each other. This alters the actual current distributions and impedances from what the theory would predict if the elements were isolated in space. The complex interaction is termed as MC and is particularly significant when antenna elements are in close proximity. Therefore, MC serves as one of the most important effects in the study of compact AAs. The effect of MC is mainly due to three major sources as can be envisaged in Figure 2.3 i.e.

1. Direct coupling due to closely spaced array elements (red line).
2. Indirect coupling due to scattering from nearby objects (blue line).
3. Feed network coupling that interconnect the elements in the array (green line).

In this thesis, the effect of the indirect and network couplings are ignored since their contributions are relatively small compared to the direct coupling. Moreover, the indirect coupling is environment dependent while the feed network coupling can be minimised by proper impedance matching between elements. In general, the MC depends on

1. Radiation pattern of the elements.

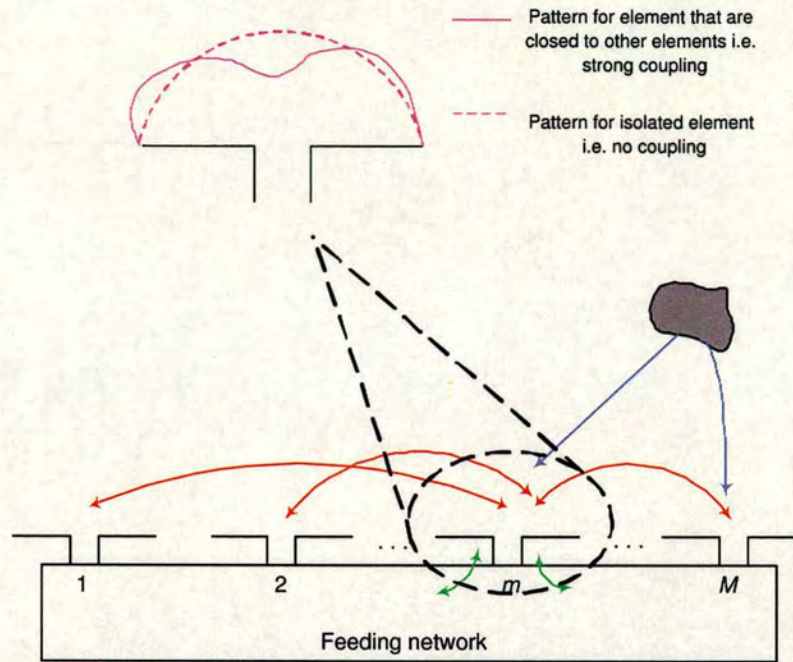


Figure 2.3: Mechanism for MC and the effect to the radiation pattern.

2. Inter-element spacing.
3. Orientation of the elements.
4. Feeding current/current distribution.

An effective way to describe the presence of MC (or to compensate for MC effects) in the array signal processing community is through the use of a coupling matrix [14, 55]. The coupling matrix relates the active element patterns of the individual elements in the presence of the array environment to the idealised, free-standing element patterns [56]. To evaluate the coupling matrix which consists of self and mutual impedances, several methods ranging from the simple to the complex can be employed. The impedance of an antenna depends on the factors such as its geometry, closeness to other objects, method of excitation and frequency of operation. Due to the complex geometries of the antennas, only a limited number of practical antennas have been investigated analytically while many others need to be determined experimentally. The three commonly used methods are through the induced electromotive force (EMF) method, the method of moment (MOM) and measurements. Each of these methods will be briefly revisited with focus on their strengths and limitations.

1. Induced EMF method

This classical method is easier and more computationally efficient as compared to the MOM and measurement methods described below. However, this method is limited to few antenna geometries such as straight wire, arrays in side by side, collinear and parallel echelon configurations [47, 49]. The mathematical tractability of this method leads to closed-form solutions that facilitate antenna analysis.

2. Method of Moment

MOM is one of the numerical methods for solving complex integral equations by reducing them to a system of simpler linear equations [57]. This method is based on the weighted residual technique by first establishing a set of trial solution functions with one or more variables. The residuals are measured by the difference between the trial and the true solutions. The variable parameters are determined such that a best fit of the trial functions can be obtained based on minimisation of the residuals. Using this method, more practical antenna configurations can be examined and the assumptions of uniform/sinusoidal current distribution that are normally used in the induced EMF method described above can be extended to a more generalised case. However, this powerful method comes at the expense of mathematical complexities which is a time consuming process to develop, implement and validate the software. Fortunately, many general purpose MOM programs are readily available and thus aid in development of new software. Numerical Electromagnetics Code (NEC) and Mini Numerical Electromagnetics Code (MININEC) are the two popular non-commercial software used by antenna engineers [58–60].

3. Experiment/Measurement method

This is a costly alternative to the former two methods and involves determining the actual array response using field measurements. This method is normally used when the numerical approach becomes difficult and also to validate theoretical results. Recently, many measurements were conducted [56, 61, 62] to obtain a compensation matrix for MC. This is important to calibrate AAs so that accurate results can be obtained particularly for parameter estimation.

In this thesis, the induced EMF method is employed due to its simplicity. Note that for the AA configurations considered in this thesis, closed-form expressions can be derived using the induced EMF approach with accuracy comparable to the MOM.

2.2 Properties of wireless propagation channels

In a wireless propagation channel, the transmitted signals arrive at the receiver via different propagation paths (multipath) as a result of scattering, reflection or diffraction [63, 64]. Each of the MPCs arrives at the receiver with a distinct attenuation (amplitude), phase shift, propagation delay, angle of arrival as well as Doppler frequency. The governing propagation mechanisms can be explained as follows:

- Scattering occurs when the propagating wave impinges upon an object whose dimension is small with respect to the carrier wavelength, for example trees and lamp posts. The resulting waves are scattered in many directions.
- In contrast, reflection occurs when the propagating waves impinge upon a smooth object with a large dimension compared to the wavelength. The resulting waves are deflected from their original direction.
- Diffraction occurs when the propagation path is obstructed by either a dense body with dimensions that are large compared to wavelength or a surface that has sharp irregularities. Diffracted waves arrive at the receiver even though there is non-line-of-sight (NLOS) path between transmitter and receiver.

All of the three phenomena cause propagation signal power losses and fluctuations [65] termed as path loss and fading respectively. Path loss is defined as the ratio of the received and transmitted power that describes the attenuation of the median power as a function of distance travelled. On the other hand, fading describes the selectivity of the channel either with respect to time, frequency and space [66–68]. A thorough understanding of these terms is essential in modelling the mobile radio channel. In the following subsections, the time and frequency selectivity of the channel are distinguished where the terms slow, fast, flat and frequency selective fading are discussed. Key parameters such as AS and DS and the associated pdfs that characterise the channels are then briefly explained.

2.2.1 Time selectivity

The time selectivity of a channel is a result of MS movement or the movement of the channel itself (surrounding objects). The time selectivity of the channel can be further classified to fast

fading (small scale fading) and slow fading (large scale fading/shadowing) as illustrated from Figure 2.4.

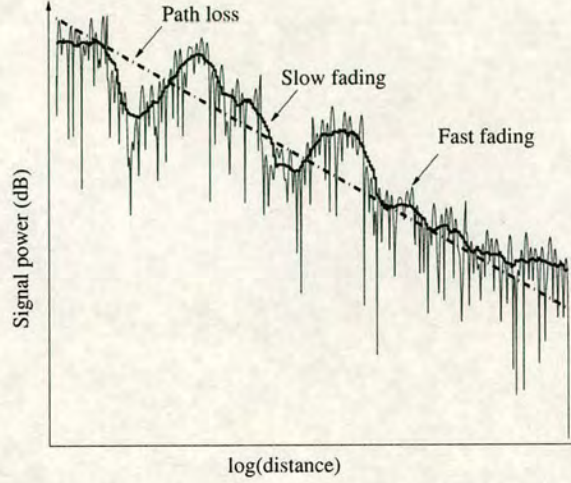


Figure 2.4: Illustration of path loss, large scale and small scale fading [69].

Slow-fading signifies the average signal power received over a large area (few tens of wavelengths) due to the dynamic evolution of propagation paths whereby new paths arise and old paths disappear. The signal envelope is normally found to be log-normal distributed.

Fast fading is caused by the multipath signals that arrive at the receiver with random phases that add constructively or destructively. It causes rapid changes in signal amplitude over a small distance travelled ($< 10\lambda$). For a simple model, the distance between the successive maxima and minima is typically on the order of half a wavelength [65]. In this thesis, the focus will be given to small scale fading only since this effect is the most important in determining the performance of receiver architectures. Three widely used distributions to describe the statistics of the received signal's envelope in fast fading are :

1. Rayleigh fading where an infinite number of MPCs with equal amplitude and uniformly distributed phases is assumed and there is no line-of-sight (LOS) condition between the transmitter and receiver. By central limit theorem, the sum of these waves will give a complex normal distribution.
2. Rician fading when there is a dominant incoming wave i.e. LOS component or strong specular component. It will reduce to the case of Rayleigh fading where no LOS is

present.

3. Nakagami fading where the severity of the fading can be controlled. Rayleigh and Rician fading can be modelled as special cases of Nakagami fading.

The rapidity of the fast fading of the channel is related to the velocity of the MS which can be quantified by the coherence time, $(\Delta t)_c$ and the Doppler spread, B_d of the channel. The scalar $(\Delta t)_c$ measures how fast the channel is changing with time. In other words, it is a measure of the expected duration over which the channel response is invariant. On the other hand, B_d is the range of values of frequency over which the Doppler power spectrum is non zero. Assuming a signal with symbol duration $(\Delta t)_s$ (or equivalently signal bandwidth $(\Delta f)_s$), fast fading occurs when $(\Delta t)_s$ has a similar value to $(\Delta t)_c$ or equivalently if B_d greater than $(\Delta f)_s$. In fact, Doppler effects are the frequency domain manifestation of time domain fast fading. The most widely accepted Doppler power spectrum is the Clark Doppler spectrum⁵ which assumes that the scatterers are uniformly distributed around the MS and all the signal paths are incident at the MS in the same plane [26, 70, 71].

2.2.2 Frequency selectivity

The time dispersion of a channel is a result of the different propagation path lengths. Hence, the received signal is delayed in time. The amount of delay introduced by the multipath channel causes the transmitted signal to undergo either flat or frequency selective fading. The frequency selectivity of the channel is quantified by coherence bandwidth, $(\Delta f)_c$ and multipath spread, T_m of the channel. The scalar $(\Delta f)_c$ is a measure of the range of frequencies over which the channel is considered flat where all signal components are subject to equal gain and linear phase. It also determines the maximum bit rate that can be supported by the channel without equalisation or using orthogonal frequency division multiplexing.

Flat fading occurs if the $(\Delta f)_c$ is greater than the $(\Delta f)_s$. Hence, the $(\Delta t)_s$ is much greater than the T_m of the channel. This type of channel is also referred to as a narrowband channel. Partial waves from all scatterers are superimposed so that the influence of a particular scatterer is not distinguished. The flat fading channel is always modelled as multiplicative fading whereby the transmitted signal is multiplied by a random value with a Rayleigh or Rice distributed envelope [72].

⁵Also known as Jakes Doppler spectrum or classical Doppler spectrum.

Frequency selective channel occurs if the $(\Delta f)_c$ is smaller than the $(\Delta f)_s$ and the $(\Delta t)_s$ is smaller than the T_m of the channel. This type of channel is also referred as a wideband channel. Hence, significant inter symbol interference (ISI) is observed at the receiver. This type of channel is non-multiplicative.

2.2.3 Time dispersion: delay spread

The time dispersion of the wireless channel can be characterised by investigating the power delay profile (PDP) or delay power density spectrum. The PDP describes the expected received power for different delays. A widely accepted PDP is given by an exponentially decaying function. A number of parameters are used to characterise the PDP and the most commonly used is the root mean square (rms) DS defined as the second central moment of the PDP. Stronger information can be interpreted from the rms DS since it takes both the relative power and delay into account. Furthermore, the rms DS is inversely proportional to the coherence bandwidth and thus provides an indication of the nature of the ISI. Some typical DS values obtained from measurements for various environments are listed in [73].

2.2.4 Angle dispersion: angle spread

The angle dispersion of the wireless channel can be described by the power angle spectrum⁶. Analogous to the PDP, PAS describes the expected received power for different azimuth angles. A number of distributions has been proposed for PAS for BS and MS: uniform [18], Gaussian [15], Laplacian [74] and the n^{th} power of a cosine function [75]. PES on the other hand, is typically taken into consideration in microcells and picocells. They are usually modelled as: Laplacian [11] or a one sided exponential function [76]. The corresponding parameters for angular dispersion are the rms AS and rms ES. Some typical AS values obtained from measurements for various environments are also listed in [73].

2.2.5 Depolarisation

The depolarisation effect due to the channel can be conveniently described by the cross polar discrimination (XPD) value of the channel. The parameter expresses the ratio of the received

⁶Power angle spectrum composed of a power azimuth spectrum (PAS) and a power elevation spectrum (PES).

power for vertical polarised antenna to that for its horizontal counterpart [29]. Measurement results [77, 78] reveal that the XPD value ranges from 0 dB to 18 dB, where 6 dB is typically found in urban environment. For simplicity, it will be assumed that in this thesis, the XPD value is set to unity but results can also be generalised to study different XPD values.

2.3 Review of diversity techniques

To overcome the problems of signal fading, the statistical behavior of the fading through time, frequency and spatial variation of the channel can be exploited through diversity techniques. The concept of diversity is to reduce performance degradations as a result of multipath fading by providing more than one transmission or receive channel/branch. For effective diversity reception, two criteria must be fulfilled [72]. First, the impairments on the separate channels are preferably independent or sufficiently decorrelated so that simultaneous severe signal degradations are unlikely. Secondly, the mean received power level for each individual signal at the diversity systems should be similar (or close to each other)⁷. Otherwise, the performance is dominated by the strong signal and the diversity concept becomes meaningless even though the signals are decorrelated. Similarly, if the time-varying propagation channel effects on the individual channels are highly correlated, the benefit provided by diversity reception is very limited as the signals will be in deep fades at the same time. The concept of diversity is illustrated in Figure 2.5 where it can be clearly seen that diversity combining gives a better received signal as there is high probability that only one signal at maximum is in a deep fade at any time. Several classes of diversity reception are used in wireless communications such as spatial, polarisation, angle, pattern, time and frequency diversities. Among the diversity techniques available, spatial and polarisation diversities show great promise to improve system performance from the MS perspective. Hence, this thesis is focussed on spatial and polarisation diversity while the other techniques are only briefly discussed.

2.3.1 Angle and pattern diversity

Angle diversity is a general technique used to configure antennas for signal detection coming from different angle paths. On the other hand, pattern diversity samples the incoming signals

⁷Note that a 5 to 6 dB difference in power only gives a 1dB loss in SNR for dual diversity and this corresponds to a correlation value of 0.7.

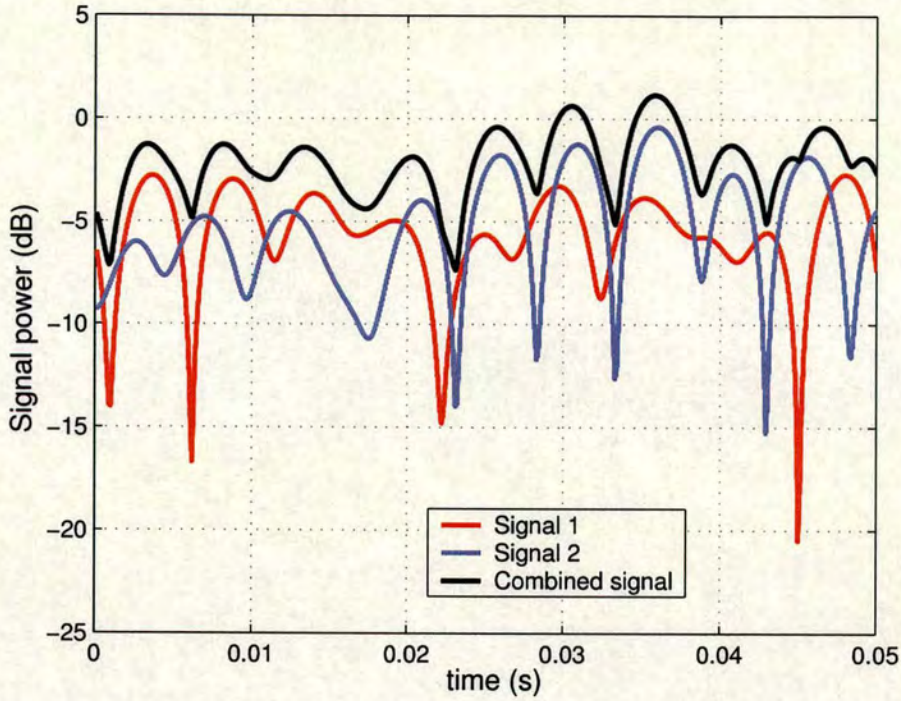


Figure 2.5: *The concept of diversity combining with the two independent Rayleigh fading signals at Doppler frequency 100Hz.*

in different ways. This can be achieved by using different types of adjacent antennas. With different antenna patterns, the probability of simultaneously experiencing deep fade conditions at all antennas is reduced.

2.3.2 Frequency and time diversity

Frequency diversity is a technique that selects transmission frequencies based on the channel behavior to provide multiple uncorrelated copies of the same signal to the receiver. The same signal is transmitted over different carrier frequencies. In contrast, time diversity exploits the time varying nature of the signal impairments to retransmit information at suitable time intervals. The key here is that signals should be retransmitted at time intervals larger than the reciprocal of the signal fading rate. This is to ensure adequate decorrelation between successive transmissions. For both techniques, only one antenna is needed at both transmit and receive ends. However, they are generally inefficient; frequency diversity utilises more radio spectrum while time diversity reduces the effective data rate.

2.3.3 Spatial diversity

Spatial diversity relies on the provision of two or more spatially separated propagation paths by employing more than one receiver (receiver spatial diversity) or transmitter (transmit spatial diversity). This technique does not introduce an efficiency loss (in fact a gain is added which is described in later Section 2.5). However, more hardware and computationally complex software are needed, particularly at the receiver. The decorrelation of the received signals depend on the nature of the scatterers and the inter-element spacing. Measurements show that, a separation of at least 0.5λ and 10λ are needed to obtain two uncorrelated signals at the MS and BS respectively. In addition, isotropic scattering usually gives better spatial diversity than the non-isotropic case for a given antenna configuration.

2.3.4 Polarisation diversity

Polarisation diversity is the reception of a signal on two mutually orthogonal polarisations, with or without transmission in the same two polarisations. Although the technique is limited to two diversity channels, no additional frequency spectrum is needed and a single dual polarised antenna can be deployed instead of separate space diversity antennas. The performance of this technique is very dependent on the depolarisation effects of the channel as both reflection and diffraction can rotate the polarisation of the scattered wave. Extensive measurements in urban, sub-urban, rural, outdoor-to-indoor and indoor [8] show that vertical and horizontal polarised signals at the MS are generally uncorrelated. Unfortunately, the horizontal (cross-polarised) component typically has lower power than the vertical (co-polar) component when the transmitted signal is vertically polarised and thus reducing the gain [8, 77–79].

2.4 Techniques employing spatial diversity

Having described the sources of fading and various diversity techniques that are applicable, we now examine several diversity combining techniques for spatial diversity. Proper combining of multiple signals will greatly reduce the severity of fading and ensure reliable communication. There are three major groups of combining techniques:

- Selection (switching, scanning, selection).

- Summation (equal gain, maximum ratio, optimum combining)⁸.
- Non-linear optimisation (joint detection, maximum likelihood sequence estimation).

The first group is characterised as a single branch being selected to yield the active output with maximum signal to noise ratio (SNR) at a time. It is simple and cheap to implement. Selection based on switched beam or sectorisation is widely used in current cellular systems. In contrast, the second and third group involve weighting and summing all branch signals to form the output signal. In the next section, a concise discussion for summation using maximum ratio combining (MRC), zero forcing (ZF) and minimum mean square error (MMSE) as well as non-linear technique using joint detection (JD) are discussed with focus on their properties and complexity.

2.4.1 Summation

1. Maximum ratio combining

In this technique, the received signals are adjusted both in magnitude and phase by the weights in the combining filter to maximise the SNR at the output of the linear combiner [6, 80]. The weighting applied to each diversity branch is adjusted independently but simultaneously from other branches according to the SNR at that branch. MRC gives the best statistical reduction in fading of any known linear diversity combiner. This is due to the fact that the SNR at the output is the sum of the SNR at the individual branches. The received signal at k^{th} branch, y_k and the output of the MRC combiner, d_u are given by

$$d_u = \sum_k^M W_k^H y_k \quad (2.14)$$

$$y_k = h_k u + n \quad (2.15)$$

$$W_k^H = h_k^H \quad (2.16)$$

where $[\cdot]^H$ represents the Hermitian or complex conjugate. The transmitted signal, u is corrupted by the channel effects characterised by h_k , while W_k is the associated weight of the k^{th} antenna element. In the presence of noise only, the performance of an MRC

⁸Selection and summation techniques can be implemented either as predetection or postdetection combining. In predetection, each received signal is cophased at the IF frequency and combined before detection. On the other hand, postdetection combines the signals after detection at the baseband level.

array is optimal. However, when time delayed multipath or interference is taken into consideration, the performance of MRC degrades significantly. This is because MRC does not have the capability to reject interference. References [67, 81] examined the bit error rate (BER) for various modulation schemes when using MRC in a Rayleigh fading channel.

2. Zero forcing

In a ZF combiner, the combiner coefficients W are chosen to remove undesired interference leaving only the desired signal. This technique assumes the channel characteristic is known or estimated from the pilot bits. Hence, distortion introduced by the channel or interference signals to the desired signal can be compensated by the inverse of the channel coefficients. Figure 2.6 shows a multi-user channel model with M antennas and N users. The output of the ZF combiner is given by

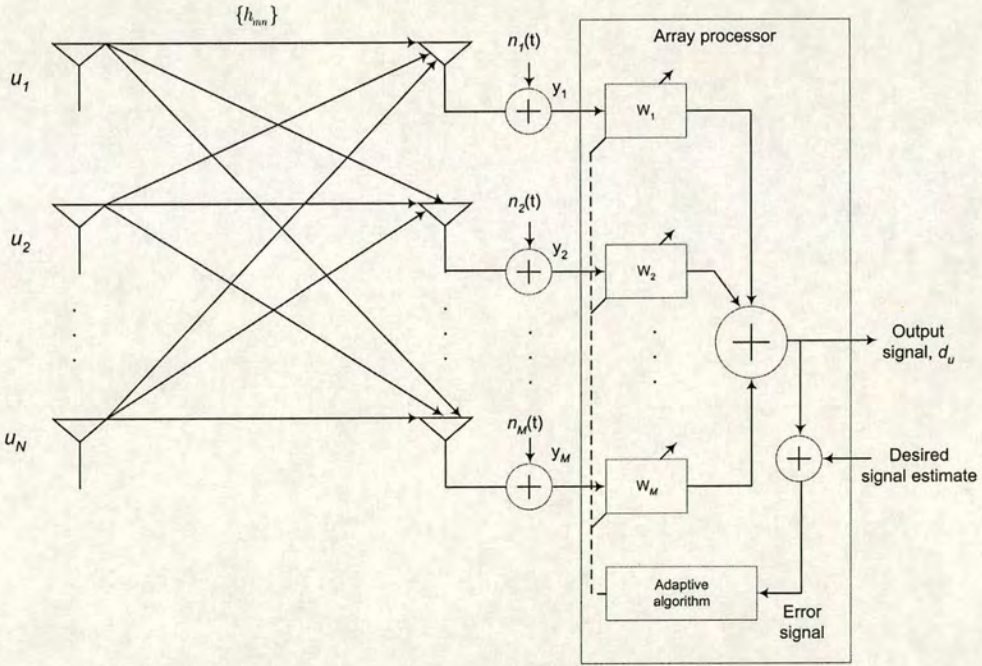


Figure 2.6: Multi-user scenario using an AA receiver with ZF combiner.

$$\mathbf{d}_u = \mathbf{W}^H \mathbf{y} \quad (2.17)$$

$$\mathbf{y} = \mathbf{H}\mathbf{u} + \mathbf{n} \quad (2.18)$$

$$\mathbf{W}^H = (\mathbf{H}^H \mathbf{H})^{-1} \mathbf{H}^H \quad (2.19)$$

where \mathbf{d}_u is an estimate of the users' signal vector, \mathbf{y} is a received signal vector corrupted by the channel effects characterised by \mathbf{H} as given in (2.18). The matrix \mathbf{W} is a weight matrix for the antenna elements and $(\cdot)^{-1}$ is the inverse matrix operation. Note that ZF always performs worse than the MMSE solution [81].

3. Minimum mean square error

In this technique, the combiner implements the Wiener solution directly or an approximation to it [72]. Basically, the optimum combiner maximises the signal-to-interference plus noise ratio (SINR) instead of SNR in the MRC case [82, 83]. The equation that governs the output of the MMSE combiner is given exactly by (2.17) but the corresponding weight matrix is modified by additional terms given by

$$\mathbf{W}^H = (\mathbf{H}^H \mathbf{H} + \sigma^2 \mathbf{I})^{-1} \mathbf{H}^H \quad (2.20)$$

where σ^2 and \mathbf{I} are noise variance and identity matrix respectively. The ability of optimum combining to handle interference and multipath makes it more robust in mobile environments. Several algorithms to implement the optimum combiner have been investigated [81, 83, 84]. These algorithms are least mean square (LMS), recursive least square (RLS) and direct matrix inversion (DMI). LMS is simple to implement with its low complexity in both software and hardware. However, the rate of convergence of the LMS in general is relatively slow [85, 86]. RLS is relatively insensitive to the eigenvalue spread of the system as compared to the LMS. Therefore, it improves the convergence rate but increases the complexity of the adaptive signal processing [86]. DMI is also more complex than the LMS but it speeds up the convergence as well as circumventing the dependency of convergence rate on eigenvalue distribution of the system.

2.4.2 Non-linear optimisation

1. Joint detection/ Maximum likelihood

This algorithm enables the detection and estimation of all the cochannel users' signals based on the channel differences between them. These differences allow the receiver to make an accurate decision in extracting the desired user signal. The equation that governs

the selection of the best sequence is based on the maximum likelihood principle given by

$$J = \arg \min_k \left\{ (\mathbf{y} - \mathbf{y}_k)^H (\mathbf{y} - \mathbf{y}_k) \right\} \quad (2.21)$$

$$\mathbf{y}_k = \boldsymbol{\alpha} \mathbf{U}_k \quad (2.22)$$

where \mathbf{y}_k is one possible sequence of the transmitted signals and the scalar J is the value of k that gives the minimum difference between received signal and the possible transmitted sequences. It has been shown that the number of users that can be supported by JD can well exceed the number of antennas. Furthermore, to optimise the performance, JD requires power control to keep the users power about the same level. As the number of users increases, the performance of JD degrades relatively slowly as compared to MMSE combining. Thus, for any number of users, JD outperforms MMSE combining [87]. Obviously, this technique greatly improves system capacity and spectrum efficiency [88]. Nevertheless, the computational complexity will increase exponentially with the number of users. In ISI channels, a modified maximum likelihood detector called the maximum likelihood sequence estimation (MLSE) can be used. The single user MLSE is widely used in time division multiple access systems to combat ISI [89].

2.4.3 Performance comparison

Link-level simulations have been developed for the combining methods described in Subsection 2.4.1 and 2.4.2 to evaluate their performance in a flat Rayleigh fading channel, where the amplitudes of the channel coefficients stored in the matrix, \mathbf{H} are Rayleigh distributed. These simulations are based on binary phase shift keying (BPSK) modulation with a receiver AA. In all cases, it is assumed that estimates of all users' channel coefficients are available at the receiver. Different numbers of antenna elements (2,4,8 and 16 elements) in the receiver are used to investigate the performance improvement over a single antenna. The simulation results can be summarised as follows:

1. The performance of MRC in a correlated fading channel

The first simulation investigated the performance gain of a receiver array using MRC. In addition, the angle spread of the channel is assumed to be small enough to ensure the signal at antenna elements are completely correlated with each other. Therefore, the channel amplitude is the same at the multiple antenna elements. At the receiver end,

the received signal, $y_k(t)$ is weighted by the complex conjugate of the complex channel coefficients, h_k^H before summing with other branches received signals. Mathematically, the output signal, $d_u(t)$ using the MRC combining circuit is given by (2.14). Single and multiple antennas are considered in this simulation and the performance of each case is compared. It is clear from Figure 2.7 that the use of multiple antennas at the receiver can improve the system performance substantially over the single antenna case. In general, M antenna elements can provide $10\log_{10}M$ dB improvement in SNR over the single antenna case known as array gain.

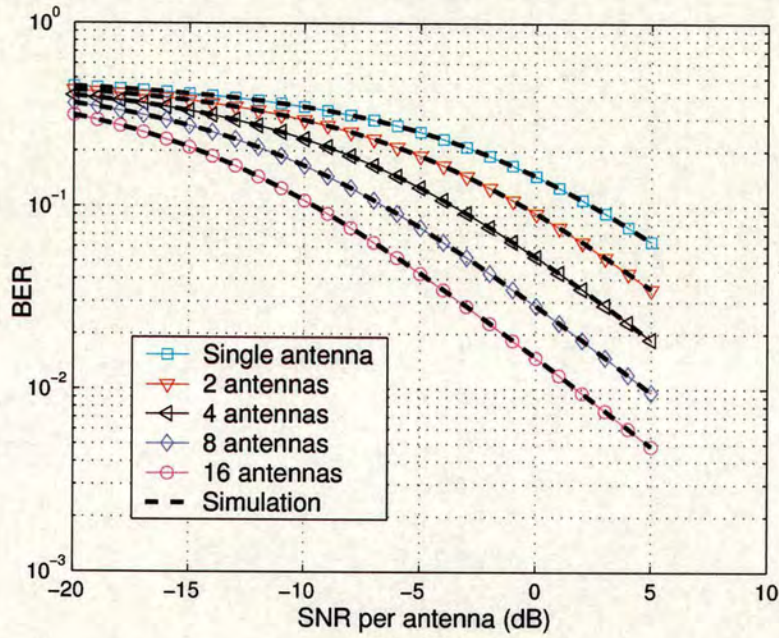


Figure 2.7: The performance of MRC in a completely correlated Rayleigh fading channel.

2. The performance of MRC in an uncorrelated channel

In this simulation, the assumptions made in case 1 are changed to multiple independent Rayleigh fading channels between the transmitter and each antenna element. This means that, each of the elements will experience different amplitudes h_k . This generates a completely uncorrelated fading signal at each of the array element, a situation which would occur with large angle spread. Again, MRC is used to weight the output signals from each branch before being combined. The output signal is given exactly by the same equation in the previous simulation. Single and multiple antennas are considered in this simulation and the performance are compared in Figure 2.7. The performance presented in the

completely uncorrelated case is far better than the in the case of completely correlated case as shown in Figure 2.8. This suggests that the importance of uncorrelated fading at the antenna elements in the implementation of diversity combining technique.

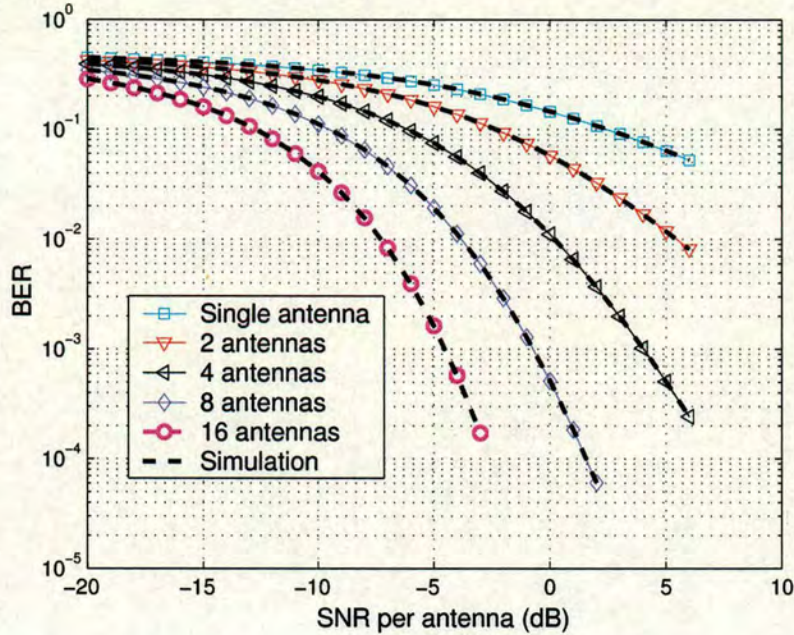


Figure 2.8: The performance of MRC in a completely uncorrelated Rayleigh fading channel.

3. The performance of ZF in an uncorrelated channel

In this simulation, a multi-user scenario is considered. The signal transmitted from the n^{th} user to the m^{th} antenna element experiences different channel coefficients, h_{mn} . Thus a set of $M \times N$ channel coefficients are produced which can be represented in a matrix. In this simulation, M is assumed to be greater than N . In addition, the power of all the interferers is assumed to be equal and hence the interference plus noise ratio (INR) associated with each interferer is the same. The output signal matrix can be determined through (2.18). With these assumptions, it can be shown that the performance of ZF for M antennas and N users is equivalent to MRC with $M-N+1$ antennas and no interferers as suggested by [81]. The performance for different combination of number of users and antenna elements is shown in Figure 2.9. The results obtained agree with the theoretical predictions. For instance for $M = 6$ and $N = 3$ the BER curve overlaps with the BER curve for 4 antennas case using MRC.

4. The performance of MMSE in an uncorrelated channel

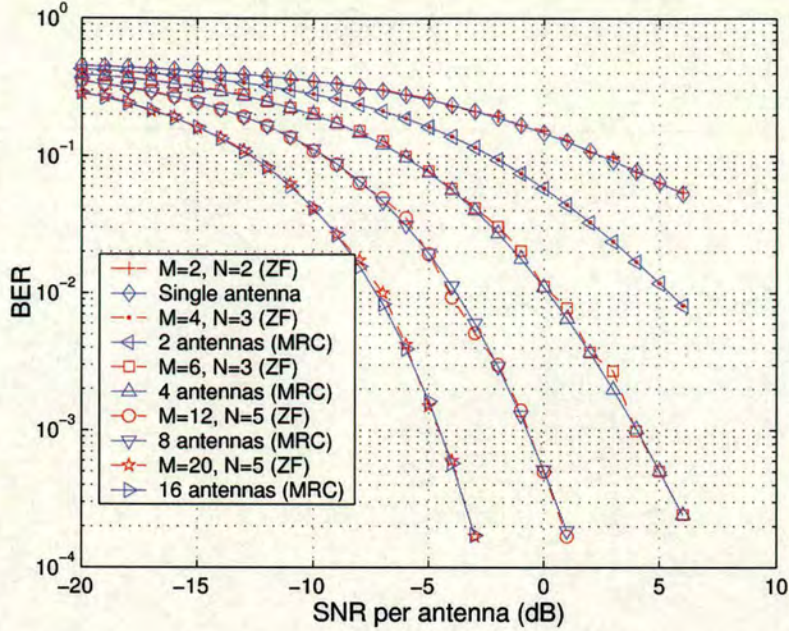


Figure 2.9: The performance comparison between ZF and MRC.

This simulation is an extension to the case of ZF by using the MMSE combiner. The effect of power level of the interferers is examined where the desired user has power level different from the interferers. However, the power level of the interferers remains the same. Again, a set of $M \times N$ channel coefficients is generated and can be represented in a matrix. Different levels of INR are used in the simulation to verify the effect on the system performance. Comparison is made with the ZF case. Also, in this simulation M is assumed to be greater than or equal to N . Clearly from Figure 2.10, ZF serves as an upper bound on BER performance and represents infinity INR in dB. As the INR level drops, system performance improves gradually.

5. The performance of joint detection in an uncorrelated channel

This simulation uses the JD algorithm which generates all possible sequences of the users' signals. Thus, for BPSK modulation and with N users, a total of 2^N possible sequences are needed. These sequences are then used to test the received signal from all the users on bit-by-bit basis. The sequence which yields the minimum error function is selected and this sequence is an estimate of the desired signal as given by (2.21). From Figure 2.11, it is obvious that this method outperforms MMSE combining for any array sizes. More interestingly, even when the number of interferers is greater than the number

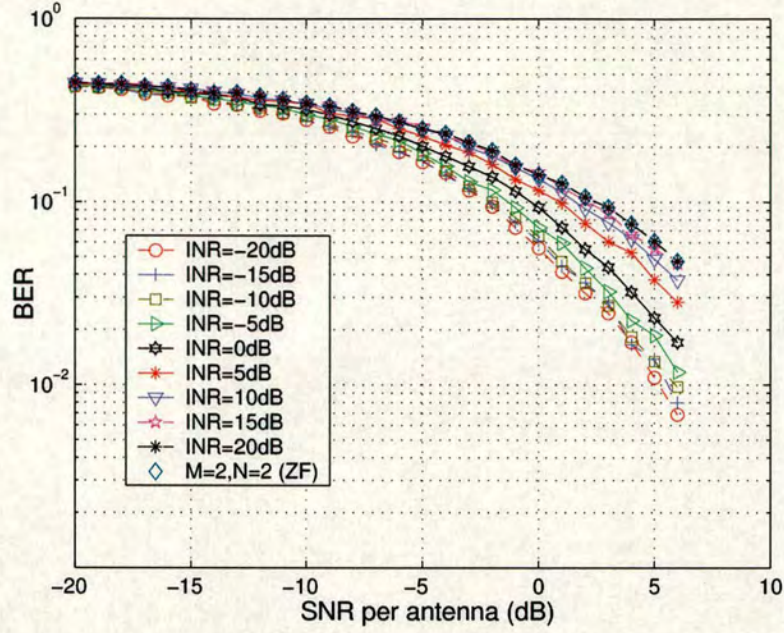


Figure 2.10: The effect of different INR levels using MMSE on the system performance.

of antennas, JD is still capable of producing acceptable performance to a certain extent, depending on the number of users and the severity of the channel effects.

In the rest of the thesis, unless otherwise specified, the analysis in this thesis uses the general assumptions listed in table 2.1.

Simulation assumptions	
Modulation	BPSK
Combining method	MRC
Channel estimation	Ideal channel estimation

Table 2.1: General assumptions.

2.5 Correlation, array gain and diversity gain

In this section, several important parameters employing AA technology are revised:

Correlation is a means of comparing two signals. A number of definitions for correlation appear in the literature such as complex, power and envelope correlation. Unless otherwise

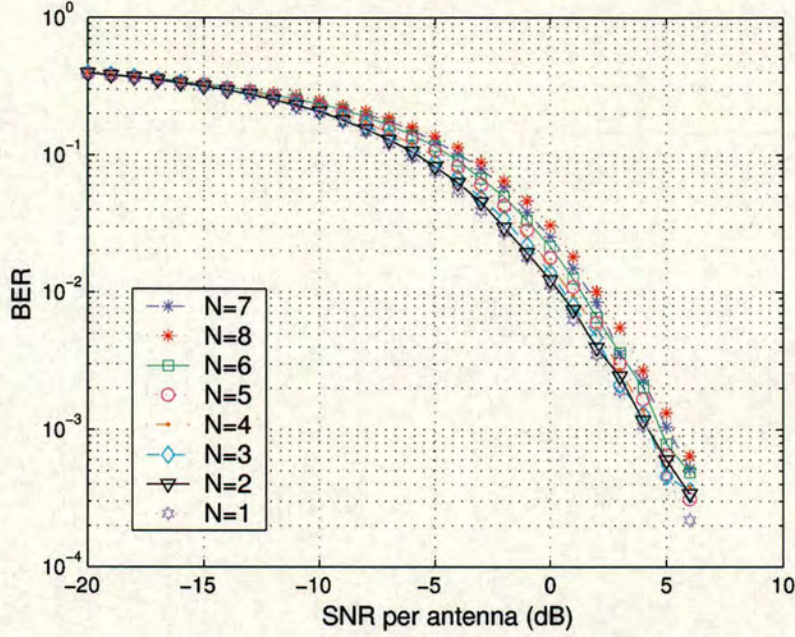


Figure 2.11: The performance of JD for $M = 4$ and varying number of users.

specified, the term correlation used in this thesis is referred as complex correlation (or cross correlation). The complex correlation for variables x and y is defined as

$$\rho_{(x,y)} = \frac{E\{(y - \bar{y})(x - \bar{x})^*\}}{\sqrt{E\{(y - \bar{y})^2\}E\{(x - \bar{x})^2\}}} \quad (2.23)$$

where the $E[\cdot]$ and superscript $*$ denote the expectation and complex conjugate respectively. The scalars \bar{x} and \bar{y} are the mean values for variables x and y respectively. The complex correlation with phase and amplitude information is essential for channel modelling employing AA systems.

Array gain is the average signal power of the combined signal relative to the individual average signal powers from element to element. Referring to Figure 2.12, 3dB of array gain is measured. Note that the array gain is the same irrespective of the BER at which the array gain is taken (same slope in BER performance).

Diversity gain is used to quantify the benefit offered by the diversity technique in reducing signal power variations due to fading effects. It specifies the decrease in SNR that can be achieved to meet a given performance criterion relative to the SNR that would be required

without diversity. The diversity gain is signified by the changing in BER performance slope which measure 5dB at a BER of 2×10^{-2} according to Figure 2.12.

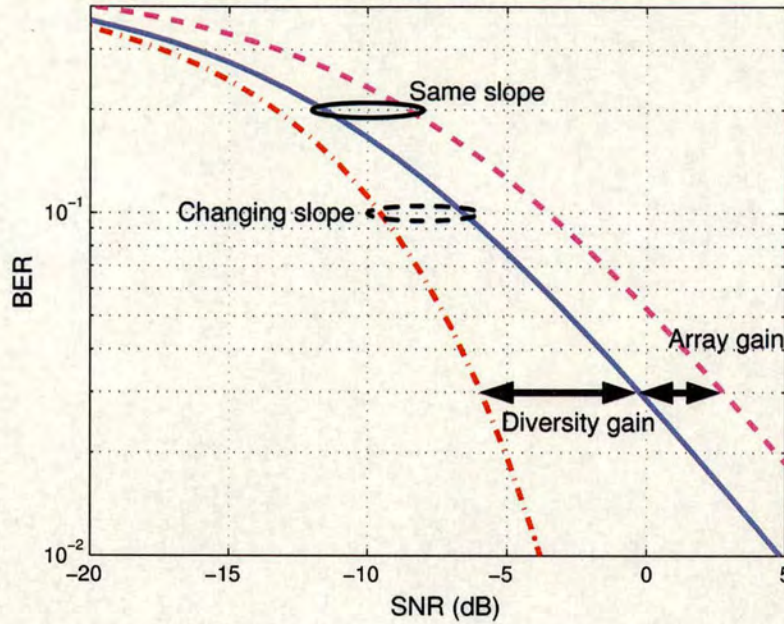


Figure 2.12: Array gain and diversity gain.

Diversity order is the number of independently fading signal paths between transmitter and receiver. In general, it depends on the number of transmit and receive antennas as well as the propagation channel.

2.6 Summary

In this chapter, background information required for system performance analysis from the antenna and propagation stand points was presented. The basic antenna theory and properties of propagation channel were briefly reviewed. A number of diversity techniques, methods of implementation and fundamental parameters was also discussed. As a whole, this chapter has outlined the scope and paves the way for the remainder of the thesis. In the next chapter, we outline the implementation of a realistic channel model and carry out a capacity analysis of it.

Chapter 3

On the implementation of COST 259 channel model

Channel modelling is one of the most important areas in mobile communication systems. A realistic channel model which resembles closely the real propagation environment is imperative for reliable wireless system design and system performance evaluation. Over the last few years, adaptive, directional AAs have received significant attention for capacity improvement [5, 36]. This has driven the need for directional channel models to develop and optimise the concept of AAs for future mobile communication. This chapter outlines the implementation of the COST 259 macrocell channel models. Major channel effects are discussed and incorporated into existing channel models with certain modifications and assumptions.

The rest of the chapter is organised as follows: In section 3.1, an overview of the COST 259 directional channel model (DCM) will be described. A mathematical framework is developed in Section 3.2 to assist the channel implementation using a TDL model. The temporal correlation of the channel is achieved by filtering complex Gaussian white noise with the frequency response of the required Doppler spectrum. On the other hand, the spatial correlation of the channel is realised by invoking the canonical Gaussian approach. In Section 3.3, parameter settings are presented which form the basis of the simulation flow in Section 3.4. This is done by randomly locating the geometrical positions of the MS, BS, local and distant clusters. Hence, various parameters which describe the characteristics of the clusters of the radio environment (RE) under study can be determined. Simulation results are discussed in Section 3.5. In Section 3.6, the capacity evaluation of the implemented channel is performed with emphasis given to studying the impact of the DS and AS. The relationship of the covariance matrices to the system performance is revisited in Section 3.7 to gain invaluable insight for the work reported in the rest of this thesis. Finally, the chapter is summarised in Section 3.8

3.1 Overview of COST 259 DCM: approach and concept

The COST 259 DCMs are the evolution of the well-known COST 207 channel models (also known as Global System for Mobile Communications (GSM) models) [90] by incorporating directional information as well as clustering of the MPCs. Unlike the COST 207 model which is limited to macrocells and omni-directional antennas, the COST 259 DCM has several advantages over some of the current spatial channel models. The COST 259 DCM can be considered as one of the most “complete” wideband directional models to date. Most of the parameters or results were validated by extensive measurements. It is highly topographically dependent, as it covers all three major cell types: macro, micro and pico-cell. Hence, the COST 207 model is treated as a special propagation scenario that can be found within the COST 259 models. The backward compatibility of the COST 259 DCM is vital in allowing comparisons with earlier work [91]. Unfortunately, the COST 259 DCM is very complex and some of the parameters are not yet fully defined, particularly for the microcell and picocell. Moreover, the channel impulse cannot be fully described by a set of equations that relate various important parameters such as DS, AS and XPD values.

To generalise the various environments, the COST 259 DCM defined a 3-level structure that consists of cell types, radio environments (REs) and propagation scenarios [76]. In the first level, three cell types have been identified namely, macrocells, microcells and picocells. For each cell type, a number of REs can be specified. For instance, macrocell has four different REs namely general typical urban (GTU), general rural area, general bad urban and general hilly terrain. Within a particular RE, we can find a whole class of propagation constellations that exhibit similar or typical features that can be related to the surroundings. The topographical features of a RE are characterised by the external parameters (EPs) such as frequency band, BS and MS height, BS-MS distance, building height, etc. The propagation conditions of a particular RE are characterised by a set of pdfs and/or statistical moments called global parameters (GPs) which are typically extracted from measurements. Sets of EPs and GPs for different REs can be obtained from [11]. Therefore, a given RE consists of a number of propagation scenarios defined as local parameters (LPs) whose statistical properties are governed by a set of GPs. The LP (also referred to as random realisations) consists of parameters such as total number of MPCs L , amplitude α , delay τ , angle-of-arrival θ and φ . These random realisations are important to generate realistic versions of the channel impulse response (CIR) for Monte Carlo simulations. For simulation purposes, we look at the parameter settings and simulation flow,

taking the macrocell GTU case as a specific example, and identify the steps involved to generate random realisations [37]. This process can be extended to any other RE. The COST 259 report does not specify a particular implementation method and to the best knowledge of the author, the only implementation that has been published is in terms of geometrical stochastic channel models [92]. Here, we present it in terms of a TLD model.

3.2 Channel model: mathematical view

A discrete channel model is used to characterise the channel where each MPC is considered to be a plane wave arriving from a discrete direction at a discrete time. In the COST 259 channel model, the dispersion of the channel in the temporal and angular domains as “seen” from the multiple antennas can be described by the time-variant directional vector channel impulse response (TV-DVCIR) [11, 16, 93]. Hence, for a single-input-multiple-output (SIMO) system, the TV-DVCIR between a transmitter and M receivers is given by

$$\mathbf{h}(t, \tau, \varphi, \theta) = \begin{bmatrix} h_1(t, \tau, \varphi, \theta), & h_2(t, \tau, \varphi, \theta), & \dots, & h_M(t, \tau, \varphi, \theta) \end{bmatrix}^T \quad (3.1)$$

where $[\cdot]^T$ denotes the transpose. The scalar $h_m(t, \tau, \varphi, \theta)$ is the time-variant directional channel impulse response (TV-DCIR) of the m^{th} receiver antenna and can be expressed as

$$h_m(t, \tau, \varphi, \theta) = \sum_{l=1}^L h(t_l, \tau_l, \varphi_l, \theta_l) \quad (3.2)$$

Equation (3.2) shows that the TV-DCIR is the superposition of L MPCs where each of the MPCs has a distinct τ , φ and θ . Taking the clustering¹ effect into account, the MPCs that arrive at about the same delay and angle of $h(t_l, \tau_l, \varphi_l, \theta_l)$ in (3.2) for $l=1, 2, \dots, L$ can be grouped into $J \leq L$ disjoint clusters C_1, C_2, \dots, C_J where each class has $N_J \geq 1$ MPCs and

$$\sum_{j=1}^J N_j = L \quad (3.3)$$

¹The clustering of the MPCs can be interpreted as clusters of scatterers that reflect scattered waves on their way from the transmitter to the receiver [91].

Hence, (3.2) can be rewritten as

$$h_m(t, \tau, \varphi, \theta) = \sum_{j=1}^J \sum_{n \in c_j} h(t_n, \tau_n, \varphi_n, \theta_n) \quad (3.4)$$

In order to implement a TDL channel model, a time-variant channel impulse response (TV-CIR), $h(t, \tau)$ is needed. Theoretically, $h(t, \tau)$ can be obtained by integrating $h(t, \tau, \varphi, \theta)$ weighted by antenna pattern, $f(\varphi, \theta)$, over direction [11] i.e.

$$h(t, \tau) = \int_{\varphi} \int_{\theta} f(\varphi, \theta) h(t, \tau, \varphi, \theta) d\varphi d\theta \quad (3.5)$$

In practice, $h(t, \tau)$ can be expressed into two independent components that carry temporal and spatial information as

$$\begin{aligned} h(t, \tau) &= \sum_{l=1}^L \varepsilon_l e^{j(\beta_l + 2\pi f_{d_l} t)} \cdot \delta(\tau - \tau_l) \cdot a_m(\varphi_l, \theta_l) \\ &= \sum_{l=1}^L \underbrace{\alpha_l(t) \cdot \delta(\tau - \tau_l)}_{\text{Temporal info.}} \cdot \underbrace{a_m(\varphi_l, \theta_l)}_{\text{Spatial info.}} \end{aligned} \quad (3.6)$$

where β_l , f_{d_l} and ε_l are the phase shift, Doppler shift and amplitude of the l^{th} multipath respectively. The $a_m(\varphi_l, \theta_l)$ is the array response for the m^{th} element due to the l^{th} multipath given by

$$a_m(\varphi_l, \theta_l) = e^{-jk(x_m \cos \theta_l \cos \varphi_l + y_m \cos \theta_l \sin \varphi_l + z_m \sin \theta_l)} \quad (3.7)$$

The temporal information, $\varepsilon_l e^{j(\beta_l + 2\pi f_{d_l} t)} \cdot \delta(\tau - \tau_l)$ can be grouped into $\alpha_l(t) \cdot \delta(t - \tau)$ which can be implemented by two fundamental methods namely the “sum of sinusoids” [70] and the “filtering approach” [16, 94]. The former are usually more limited by the degree of accuracy and computational speed as compared to the latter² [95]. Thus, the method of filtering approach to generate fading signals will be discussed in Section 3.2.1. Similarly, the spatial information can be incorporated into the model through the canonical Gaussian approach [94, 96, 97] as will be described in Section 3.2.2. The $h(t, \tau)$ obtained can be applied to a multiple (antenna) TDL as depicted in Figure 3.1.

Note that all the variables of the TV-DCIR can vary with time, position and velocity of the

²Strictly speaking, the computational speed does depend on the application, for example in GSM model where burst-by-burst processing can be performed, the sum of sinusoids method will be more computational efficient.

user. However, for a movement of less than some 10λ , the number of MPCs, angle of arrival, (φ_l, θ_l) , Doppler shift, delay and path loss are approximately constant. In our implementation, we ignore the effect of large scale fading, user mobility and thus the transitions between REs and cell types. The channel model described here is only valid for short time interval or small mobile displacement.

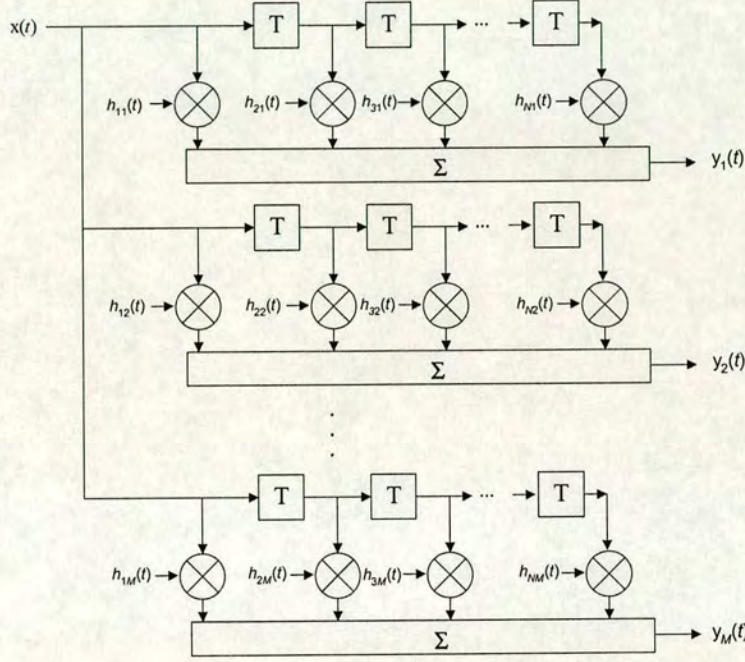


Figure 3.1: Multiple TDL model.

3.2.1 Temporal correlation

In this section, the generation of the fading signal using a filtering approach is presented. This can be realised by filtering complex white Gaussian noise with infinite impulse response (IIR) or finite impulse response filters. To obtain a reasonable result with low computational effort, a fourth order IIR filter is chosen which consists of two cascaded second order filters [98]. A more accurate but more complex, higher order filter can be found in [99]. The transfer function of the fourth order IIR filter is given by

$$H(s) = \frac{1}{(s^2 + \sqrt{2}s + 1)} \frac{1}{(s^2 + 0.02s + 1)} \quad (3.8)$$

and the corresponding frequency response of the filter for $f_{dmax} = 100\text{Hz}$ is shown in Figure 3.2.

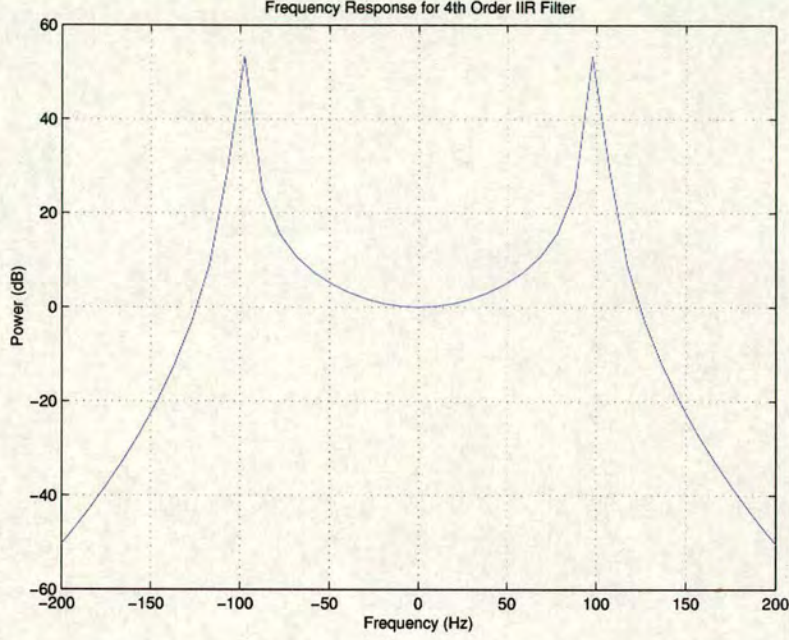


Figure 3.2: The frequency response of a 4th order IIR filter at 100MHz maximum doppler frequency.

The filter is then transformed to the z -domain by using the bilinear transformation with an appropriate sampling frequency f_s . The choice of f_s must be at least twice the Doppler frequency of the channel under consideration to ensure the Nyquist criterion is met. Since the Doppler frequency of the channel would be expected to be much lower than that of the channel bandwidth, the fading signal can be assumed to be stationary over a number of transmitted symbols. First, complex Gaussian white noise is passed through the IIR filter before the dominant coherent path (if any) with Rice factor K is added to the filter output as depicted in Figure 3.3. The sum of these components is then linearly interpolated to increase the rate to match that of the time resolution of the tap, T , i.e. the inverse of the system bandwidth. The final output, $g_{nm}(t)$ is then applied to the spatial shaping filter described in Section 3.2.2. Note that, for each of the taps of the antennas, a new independent set of fading signals is generated. This gives a matrix \mathbf{G} of size $N_{tap} \times M$ whose entries correspond to the outputs $g_{nm}(t)$. An example of the output of the filter $g_{nm}(t)$ is shown in Figure 3.4(a) and the level crossing rate for the generated fading signal is shown in Figure 3.4(b). The distribution of the filter output is plotted in Figure 3.5. It is evident that the Rayleigh pdf fitted well to the output envelope distribution.

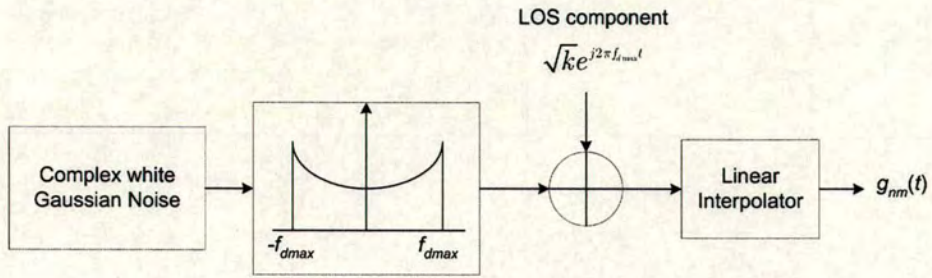
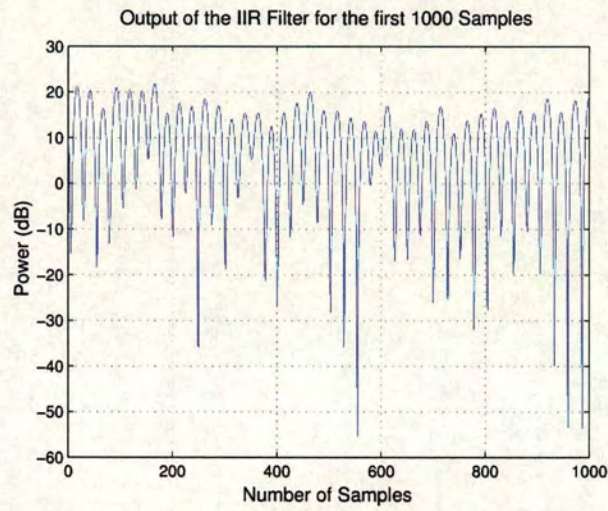
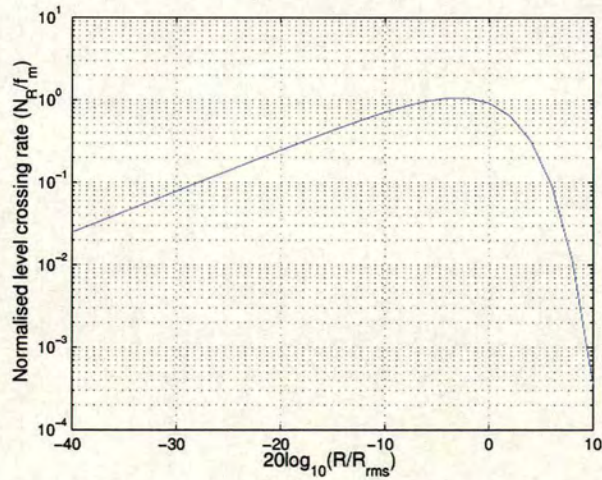


Figure 3.3: The generation of the fading signal.



(a) Envelope Fading



(b) Normalised Level Crossing Rate

Figure 3.4: Output of the filter for the first 1000 samples and the normalised level crossing rate.

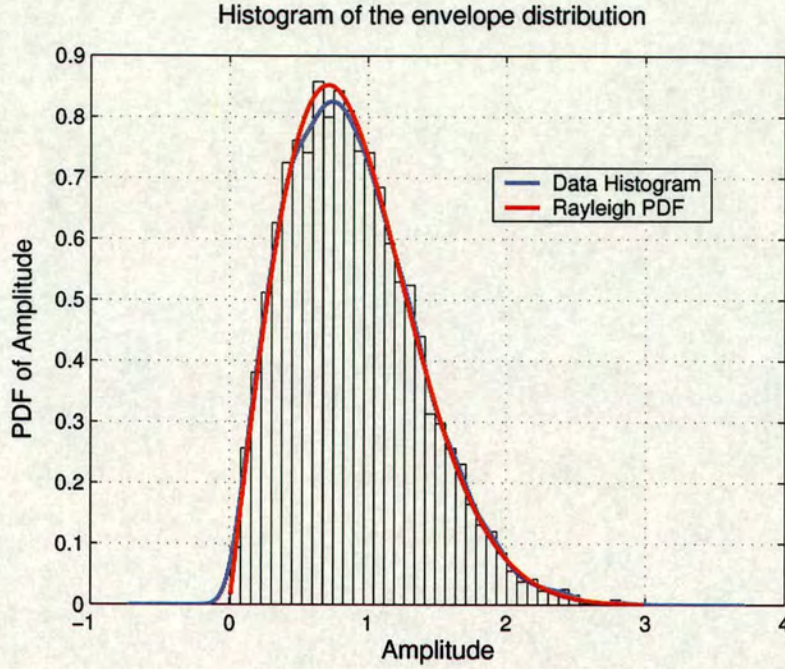


Figure 3.5: Distribution of the envelope of the fading signal and the Rayleigh pdf fit.

Also, the LOS component K can be modelled using probability of occurrence of LOS [100] given as

$$P_{LOS} = \begin{cases} \frac{(h_{BS} - h_B)}{h_{BS}} \cdot \frac{d_{CO} - d}{d_{CO}} & d < d_{CO} \text{ and } h_{BS} > h_B \\ 0 & d > d_{CO} \text{ or } h_{BS} < h_B \end{cases} \quad (3.9)$$

where h_{BS} , h_B and d_{CO} are the BS height, average building height and cut off distance respectively. With (3.9), one can characterise how often the LOS component occurs in a given RE and for a given distance between BS and MS. The LOS only indirectly affects the K -factor which can be determined using the following procedures:

1. Determine the occurrence of LOS i.e. if P_{LOS} is greater than zero.
2. Compute the excess path loss (EPL) given by (B.1) in Appendix B.
3. Determine the narrowband K -factor, K_0 from (B.2) in Appendix B.
4. The power of direct component, $P_{dir} = P_1 10^{\frac{K_0}{10}}$ where P_1 is the power of the first cluster.
5. Applying the power of the direct component to the output of the filter as shown in Figure 3.3.

The reason for the indirect modelling procedure described above is that measurements results show that Ricean and Rayleigh fading do appear in both NLOS and LOS conditions respectively. However, on average Ricean fading is more likely to occur in LOS while Rayleigh fading is more likely to occur in NLOS. The model captures this behaviour nicely.

3.2.2 Spatial correlation

The directional information of the channel is incorporated into the model by using the canonical Gaussian approach as proposed in [96, 97]. According to this approach, the spatial property of the channel at a particular delay can be described by specifying the spatial correlation matrix \mathbf{R}_n which is calculated using the SV $\mathbf{a}(\varphi_l, \theta_l)$ of the array under study. This approach assumes Rayleigh fading at each antenna and a SV for the LOS path is added in the case of Ricean fading [96]. Hence, at a particular delay tap, a spatial correlation matrix is generated as follows

$$\mathbf{R}_n = \sum_{l=1}^L \alpha_l^2 \mathbf{a}(\varphi_l, \theta_l) \mathbf{a}^H(\varphi_l, \theta_l) \quad (3.10)$$

where n is the tap number and α_l is the amplitude of the l^{th} MPC. The matrix \mathbf{R}_n represents the mean power and cross correlations at each tap. Furthermore, by studying \mathbf{R}_n , the envelope correlation given by the squared magnitude of the complex signal correlation can be explicitly formed [94]. Observing the envelope correlation enables us to determine the possible benefit of applying diversity combining techniques at the MS. The matrix \mathbf{R}_n is then further decomposed into its unitary eigenvalues and eigenvectors using eigenvalue decomposition (EVD) [101]. The application of the canonical Gaussian approach not only simplifies the channel implementation but also enables us to use different AA geometries in the design of compact antenna arrays (CAAs). This allows us to include the impact of antenna effects such as MC and antenna patterns in the system performance analysis as will be demonstrated in Chapter 4.

3.3 Parameter settings

To simulate the COST 259 GTU channel model, the following steps are used to generate random realisations based on the EPs and GPs given in [11]³. Note that the procedures described

³For an updated and more extensive description of all the relevant processes and parameters, readers are referred to [102, 103]. These references contains several modifications of the initial publication [11] for which the work

here are also applicable to other macrocell REs.

1. Firstly, the number of clusters, N_{cl} is determined as

$$N_{cl} = N_{cl,min} + P(m_c) \quad (3.11)$$

where $P(m_c)$ denotes the Poisson distribution with m_c the mean number of the additional clusters. In principle, the distribution of the number of clusters is determined by the dynamic appearance/disappearance resulting from visibility region concepts [104, 105]. However, the Poisson distribution is a very good approximation to the concept of virtual cell deployment in macrocells.

2. The number of additional clusters (if $N_{cl} > 1$) determined in step 1 is placed uniformly in space [92] with maximum circle radius 3km. So, the position of additional clusters (coordinates) can be determined by assuming the BS is at the (0, 0) point.
3. The position of MS is randomly placed with MS-BS distance, d_{MS-BS} is a random variable (RV) with mean 500m and bounded in the range $50m < d_{MS-BS} < 1000m$. Assuming that the BS is at the centre point (0, 0) then the position of MS is in the locus of the circle as illustrated in Figure 3.6.

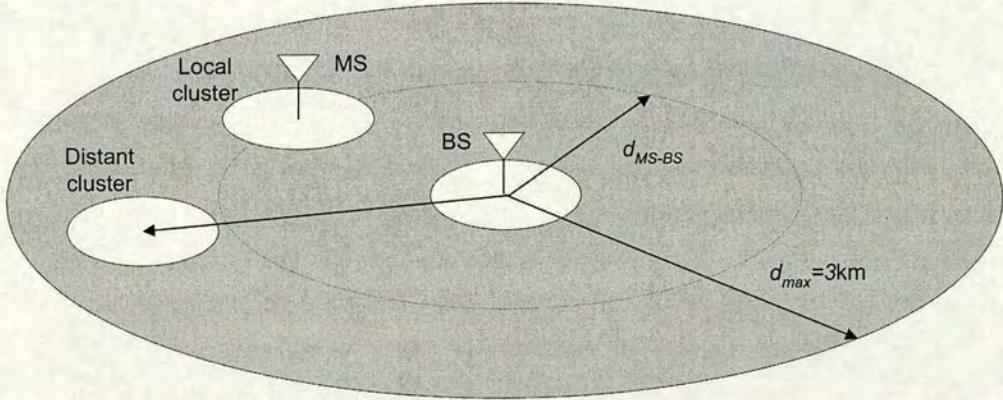


Figure 3.6: The location of local cluster and distant clusters.

4. For the local cluster, $N_{LS} = 50$ local scatterers are placed uniformly distributed within the local cluster circle with radius 100m centred at MS position determined in step 3.

reported in this thesis is based on.

This allows us to distinguish the location of the MS and the scatterers local to the MS.

5. Assuming single bounce (single scattering), the delay and direction of arrival (azimuth) due to each scatterer are computed by using a simple ray tracing method. The average cluster delay and average cluster azimuth are computed. This gives τ_i and φ_i for $i = 1$, i.e. local cluster delay and local cluster azimuth respectively.
6. With the position of the additional clusters (which is represented by a single point in Cartesian) obtained in step 2, the average cluster delay and average cluster azimuth can be computed using [11],

$$\tau_i = \frac{\left(\left| \vec{x}_{BS} - \vec{x}_{cl,i} \right| + \left| \vec{x}_{cl,i} - \vec{x}_{MS} \right| \right)}{c} \quad (3.12)$$

$$\varphi_i = \arg(\vec{x}_{cl,i}) - \arg(\vec{x}_{MS}) \quad (3.13)$$

where \vec{x}_{BS} , \vec{x}_{MS} and $\vec{x}_{cl,i}$ represent the position of the BS, MS and i^{th} cluster while c is the speed of light. This gives τ_i and φ_i for $i = 2, \dots, N_{cl}$.

7. With the data obtained in step 5 and 6, the shadowing of each cluster, P_i [dB], DS of each cluster, $S_{\tau,i}$ [s] and AS of each cluster $S_{\varphi,i}$ [deg] can be computed using the following equations [11].

$$P_i[dB] = 9X - L_i \quad (3.14)$$

$$S_{\tau,i}[s] = 0.4\mu s \cdot d_i^{0.5} \cdot 10^{\frac{2 \cdot Z}{10}} \quad (3.15)$$

$$S_{\varphi,i}[deg] = 10 \cdot 10^{\frac{2Y}{10}} \quad (3.16)$$

where X , Y and Z are normal RVs with zero mean, unit variance, and correlation coefficients $\rho_{xy} = -0.75$, $\rho_{yz} = 0.5$ and $\rho_{zx} = -0.75$. This model is based on [106] with the modifications by [104, 107]. The generation of these RVs is explained in Appendix A. Also $d_i = \tau_i c$ and is expressed in km. The quantity L_i is cluster path loss and can be written as follows

$$L_i = L_1 + L_{add}[dB] \quad (3.17)$$

$$L_{add} = U(0, 20) + (\tau_i - \tau_0)/\mu s [dB] \quad (3.18)$$

where L_1 is the path loss of the first cluster and L_{add} is the path loss of additional cluster(s). Also, $U(a, b)$ signifies a uniform distribution between a and b . The scalar

$\tau_0 = d_{MS-BS}/c$. The computation of L_1 is very intricate and is given in Appendix B. The narrowband attenuation of the COST 259 models computed should agree with the COST 231 Hata-Okumura or Walfisch-Ikegami models depending on the RE under study. Figure 3.7 shows the ratio of the path loss for the cluster one to the global path loss predicted by COST 231 Walfisch-Ikegami model. For the three random realisations considered, it can be seen that the path loss for cluster one is always less than that of the global path loss and thus satisfies the conditions of (B.6). Furthermore, as in the case of realisation one where the ratio L_1/L is close to unity, the number of clusters is one. On the other hand, the number of clusters for realisation two and three are greater than one since the difference between L_1 and L is accounted for by the additional clusters.

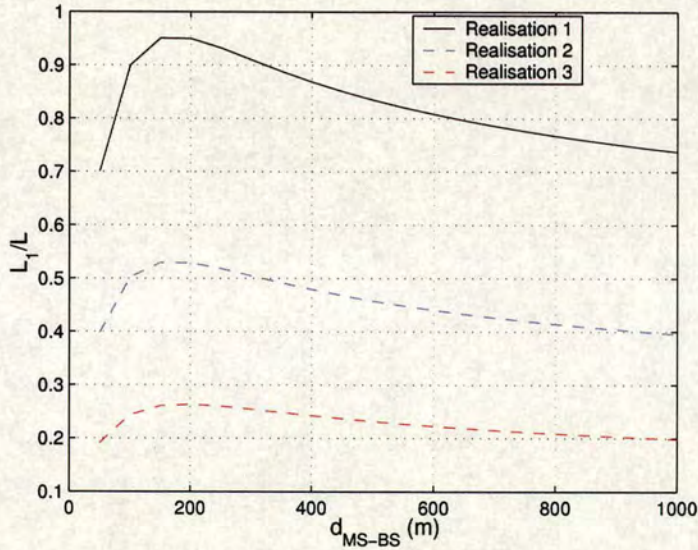


Figure 3.7: Ratio of L_1/L as a function of distance between BS and MS.

8. With the set of data $\{P_i, S_{\tau,i}, S_{\varphi,i}, \tau_i \text{ and } \varphi_i\}$ determined by steps 1 to 7, the characteristics of the clusters in terms of their position, spread, power and shape can be determined. In general, clusters have exponential decay in delay, Laplacian shape in azimuth, φ and elevation, θ . Mathematically, the distributions are

$$P_i(\tau) = e^{\frac{-\tau}{S_{\tau,i}}} \quad (3.19)$$

$$P_i(\varphi) = e^{-\sqrt{2} \left| \frac{\varphi}{S_{\varphi,i}} \right|} \quad (3.20)$$

$$P_i(\theta) = e^{-\sqrt{2} \left| \frac{\theta}{S_{\theta,i}} \right|} \quad (3.21)$$

9. The cluster's joint power azimuth-delay spectrum, $P_i(\varphi, \tau)$ in a macrocell with elevation $\theta_i = 0$ can be expressed as

$$P_i(\tau, \varphi) = \frac{1}{1 - e^{-\frac{\sqrt{2}\pi}{S_{\varphi,i}}}} \cdot \frac{1}{\sqrt{2}S_{\tau,i}S_{\varphi,i}S_{\theta,i}} \cdot e^{\frac{-\tau}{S_{\tau,i}}} \cdot e^{-\sqrt{2} \left| \frac{\varphi}{S_{\varphi,i}} \right|} \quad (3.22)$$

The index i is valid for $i > 1$ i.e. for cluster 2, 3,...

10. For the GTU case in macrocells with one cluster, it is found that $P(\varphi, \tau)$ can be decomposed as $P(\tau, \varphi) = P(\varphi)P(\tau)$ [74] where $P(\varphi)$ and $P(\tau)$ are the PAS and power delay spectrum (PDS) within the cluster (intra cluster). On the other hand, when the number of clusters are more than one, this decomposition is not necessarily valid. However, the joint power azimuth-delay spectrum of each single cluster, $P_i(\tau, \varphi)$ can always be decomposed as $P_i(\varphi, \tau) = P_i(\varphi)P_i(\tau)$. This relation is important in channel modelling taking clustering effects into account.
11. The pdfs of the delay and azimuth are found to be exponential and uniform for the first cluster and exponential and Gaussian for the far clusters.
12. With the pdfs obtained in step 11, RVs for delay and azimuth can be generated and thus joint power azimuth-delay spectrum can be characterised for each cluster.

3.4 Simulation flow

1. With the parameters obtained in Section 3.3, the dynamic range, $D_R(\text{dB})$, say 20dB below the strongest path is set and thus number of delay taps (or delay bins) required can be determined (see Figure 3.8).

$$\text{Power}_i(\tau) = \exp \left(\frac{\tau_i - \tau}{S_{\tau,i}} \right) \quad (3.23)$$

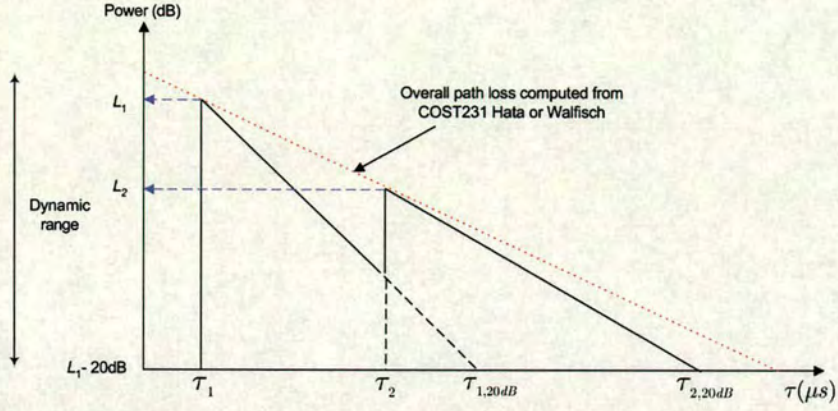


Figure 3.8: An illustration of the instantaneous PDP for two clusters case.

Take the logarithm on both sides

$$\text{Power}_i(\tau) [dB] = 10 \log_{10} \exp \left(\frac{\tau_i - \tau}{S_{\tau,i}} \right) \quad (3.24)$$

Let us define $\tau_{1,D_R dB}$ to be the delay when the power level drops below $D_R dB$ for cluster 1 such that $\text{Power}_i(\tau) = -D_R dB$. Rearranging terms of (3.24) to give

$$\begin{aligned} \tau_{1,D_R dB} &= \tau_1 - S_{\tau,1} \ln(10^{\text{Power}_1(\tau) [dB]/10}) \\ &= \tau_1 - S_{\tau,1} \ln(10^{-D_R/10}) \end{aligned} \quad (3.25)$$

Thus the total numbers of taps required are

$$\text{Total taps for cluster 1} = \tau_{1,D_R dB} \times BW \quad (3.26)$$

where BW is the bandwidth of the system. For example, in the universal mobile telecommunications system, BW is given by 3.84 MHz. Similarly, this is done to cluster 2, 3 and so on depending on their occurrences.

2. For each cluster, a sufficiently large number of MPCs (> 100) for each delay tap is generated with uniform azimuth distribution for the 1st cluster and Laplacian distribution for any additional clusters. This can be envisaged as shown in the Figure 3.9.
3. For each of the delay taps, a spatial correlation matrix is generated according to (3.10). The correlation matrix obtained is normalised by dividing the number of multipath before

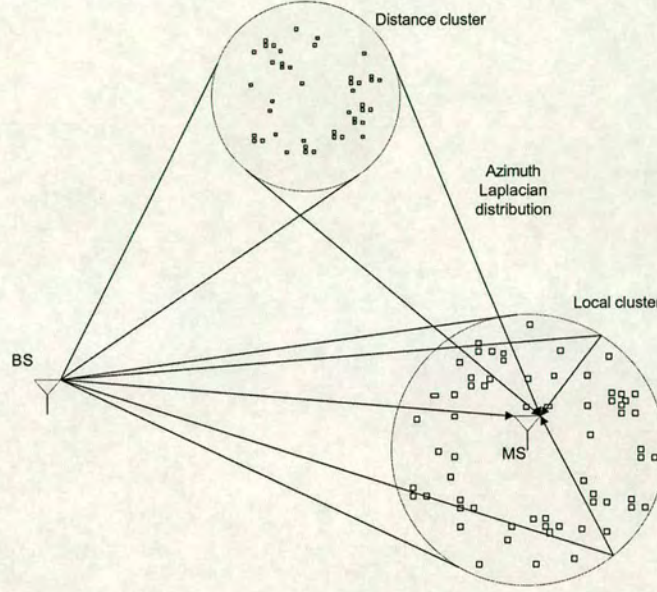


Figure 3.9: The distinction of azimuth of arrival for the local and distant clusters.

multiplying \mathbf{R}_k with the power of the delay taps up to the preset dynamic range i.e.

$$\bar{\mathbf{R}}_k = \frac{1}{L} (\mathbf{R}_k \times \text{Power}(\tau)) \quad (3.27)$$

4. Obtain the matrix \mathbf{U}_k of its unitary eigenvectors and diagonal matrix $\mathbf{\Lambda}_k$ of its real-valued-eigenvalues by

$$\bar{\mathbf{R}}_k = \mathbf{U}_k \mathbf{\Lambda}_k \mathbf{U}_k^H \quad (3.28)$$

The discrete TV-CIR, $\mathbf{h}[k, n]$ is synthesised by

$$\mathbf{h}[k, n] = \sqrt{P_i} \mathbf{U}_k \mathbf{\Lambda}_k^{\frac{1}{2}} \mathbf{g}_k[n] \quad (3.29)$$

where P_i is shadowing of the corresponding cluster and $\mathbf{g}_k[n]$ is fading generated using the filtering approach. The scalar n represents the discrete time and $\mathbf{g}_k[n]$ is the size M vector of independent complex Gaussian samples.

5. Also, the Rician component can be added to the model based on the probability of LOS as described in the Section 3.2.1. This will be a scaled SV of the LOS path, $a_{LOS}(\varphi, \theta)$.

3.5 Simulation results and discussion

The $\mathbf{h}[k, n]$ obtained can be used as time variant coefficients of the multiple TDL Model. Figure 3.10 and 3.11 show the channel responses of antenna one and two in a macrocell GTU environment with carrier frequency 2GHz. The speed of the mobile is approximately 100km/h, which corresponds to a maximum Doppler frequency of 200Hz. Due to the spatial separation between the two antennas, the TV-CIR of the two antennas are different even though they share the same joint power delay azimuth spectrum. This suggests the use of the diversity techniques at the receiver where we observe that there are times when the signal at antenna one fades whilst the signal at antenna two is at an acceptable level. In addition, severe fading with several deep fades occurring within 10ms can be clearly identified. However, at lower antenna spacing such as $\lambda/4$, the two antennas exhibit high correlation which degrades the diversity performance (this can be shown by the correlation matrix of the corresponding entries). To demonstrate

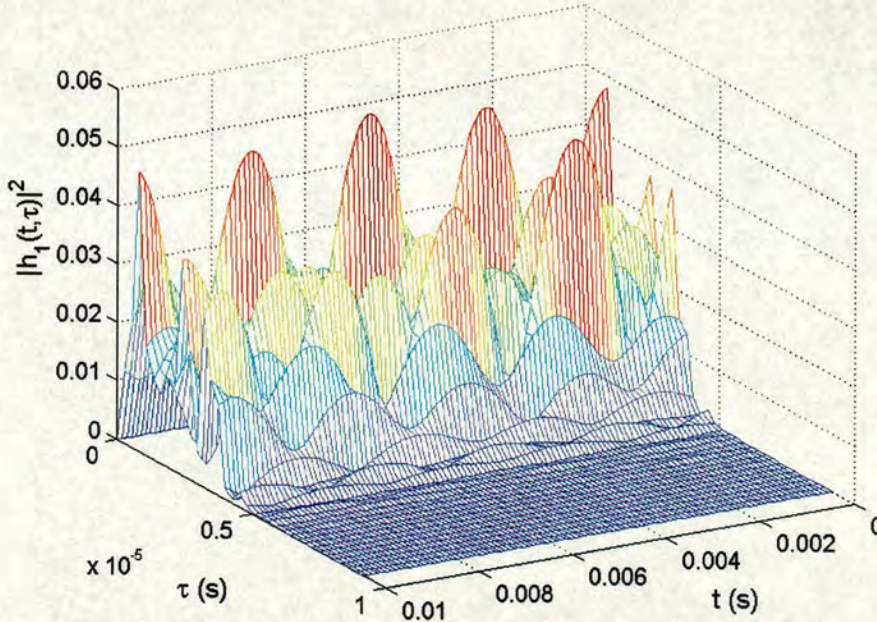


Figure 3.10: Channel response of an omni-directional antenna 1 in the GTU at velocity 100km/h and antenna spacing $\lambda/2$.

the validity of the channel model implementation, the average PDS and PAS of the GTU channel normalised with respect to first arrival path and MAOA are plotted in Figure 3.12 and 3.13 respectively. It can be observed that the average PDS of the COST 259 GTU is dominated by the first cluster corresponding to the scattering around the MS. The contribution of the additional clusters is only noticeable at longer delay with much lower power than the first cluster

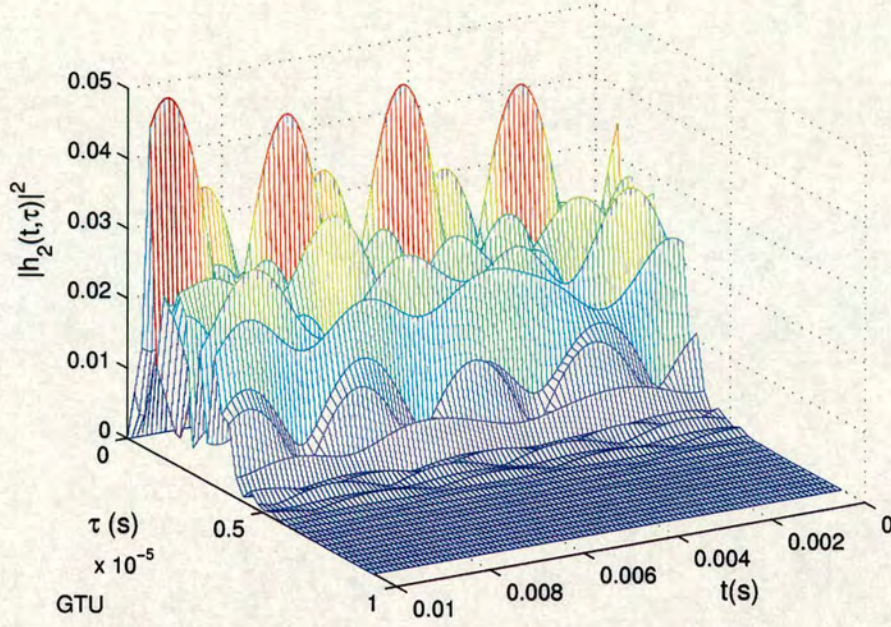


Figure 3.11: Channel response of an omni-directional antenna 2 in the GTU at velocity 100km/h and antenna spacing $\lambda/2$.

Average power delay profile (global) for GTU RE normalised by first arrival path

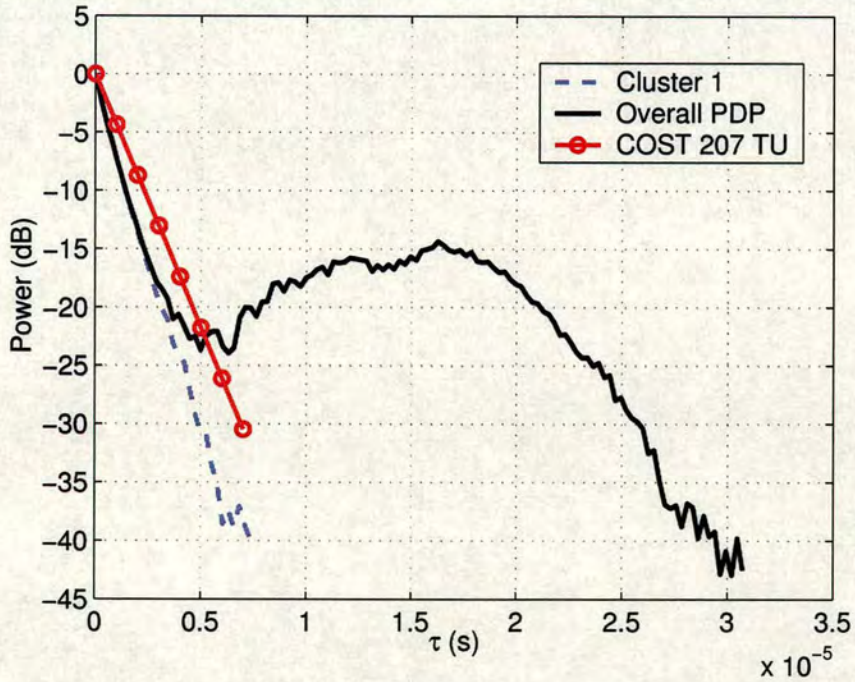


Figure 3.12: Average PDP for the GTU normalised by to the first arrival path.

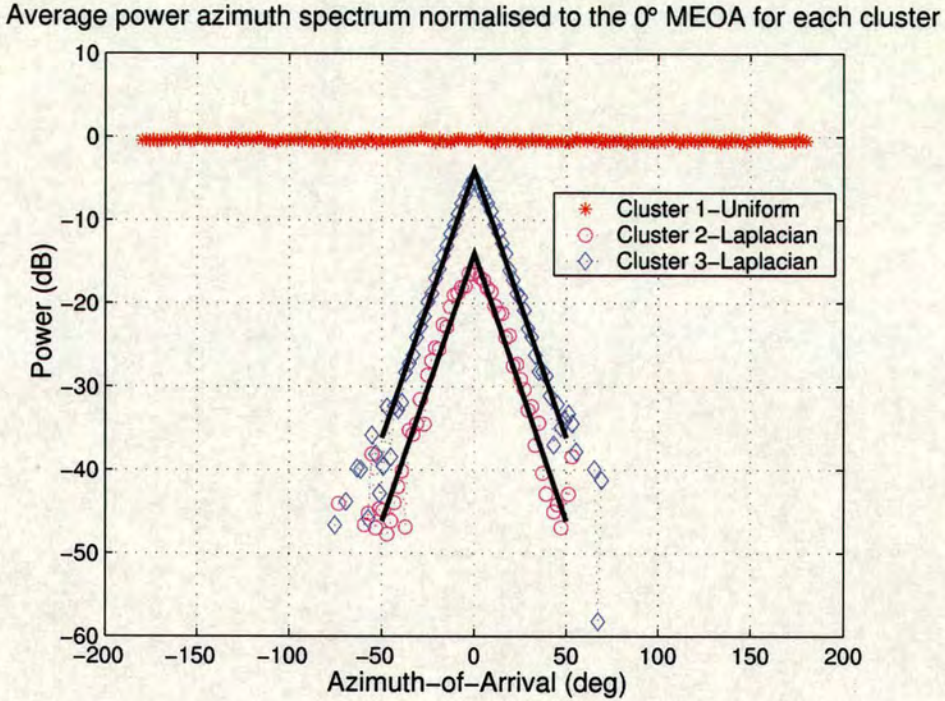


Figure 3.13: Average power azimuth spectrum for the GTU normalised by to the 0° MAOA.

since the occurrence of distance clusters is limited in the GTU case. A comparison is also made with the COST 207 TU model where both curves show some degree of agreement particularly in the region where first cluster is significant. Note that COST 207 channel model is a special case of the COST 259 DCM. The simulated average PAS in Figure 3.13 also agrees well with the PAS described in [11] where the first cluster is uniform in shape and the additional clusters are Laplacian in shape.

3.6 Capacity evaluation for antenna arrays

A number of studies have been reported which show that enormous capacity can be achieved through the use of multiple antennas at both side of the transmitters and receivers [108, 109]. Most of the work reported assumes that the fades between antenna elements are independently and identically Rayleigh distributed. However, in real propagation environments, such “ideal” conditions do not always hold [110]. Therefore, a more realistic channel model is crucial in the capacity evaluation. In this section, the capacity evaluation for multiple antenna receivers using the COST 259 GTU channel model implemented previously is investigated. The capacity of

the channel is evaluated by means of Monte Carlo simulation using a SIMO configuration at various channel conditions associated with DS and AS. These investigations allow us to assess and identify the dominant factors on the system performance associated with different channel conditions.

3.6.1 Evaluation of channel capacity

In general, the channel capacity depends on the type of channel model, channel realisations, noise as well as transmitted signal power under study. For a SIMO system with M receiver antennas, the CIR can be generated based on the location of clusters as described in Section 3.3 to 3.4. Hence, the entries of the channel transfer vector, $\mathbf{H}(f)$ can be determined. Assuming that the SNR and $\mathbf{H}(f)$ are known at the receiver, the channel capacity of a frequency selective channel can be computed by integrating over the utilised bandwidth [111] i.e.

$$C = \frac{1}{BW} \int_{BW} \log_2 [1 + SNR \mathbf{H}^H(f) \mathbf{H}(f)] df \quad (\text{bits/s/Hz}) \quad (3.30)$$

Equation (3.30) reveals that the channel capacity depends on a random channel vector for each realisation. Thus, a complementary cumulative distribution function (ccdf) is usually plotted to characterise the channel capacity.

In order to study the effect of propagation delay, three DS corresponding to 10, 50 and 90 percentiles of the DS of the COST 259 GTU RE are considered. These values can be obtained from the cumulative distribution function (cdf) as shown in Figure 3.14 where simulation is performed over 10,000 mobile locations. It is found that the $S_{10\%T}$, $S_{50\%T}$ and $S_{90\%T}$ are given by $0.166\mu s$, $0.289\mu s$ and $0.472\mu s$ respectively. In the COST 259 model, the AS for the first cluster is 180° . However, when directional AAs are to be deployed, the effective AS seen from the receiver will no longer be isotropic [21, 36]. Hence, to investigate the effect of different AS values, the AS is set to fixed values 5° , 30° and 90° respectively. Note that the three DS/AS values considered here represent low, moderate and high DS/AS values for the macrocell propagation channel. Furthermore, in the case of the GTU RE, it is appropriate to assume that the capacity contribution from additional clusters is negligible since the power level of each additional cluster is much lower than that for the local cluster surrounding the mobile [38]. In Section 3.6.2, simulations are performed at three DS values over 1000 MS locations with the AS value fixed at 180° as described in [37]. Similarly, in Section 3.6.3, the effect of AS is studied by performing the same simulation at three AS values but with the DS

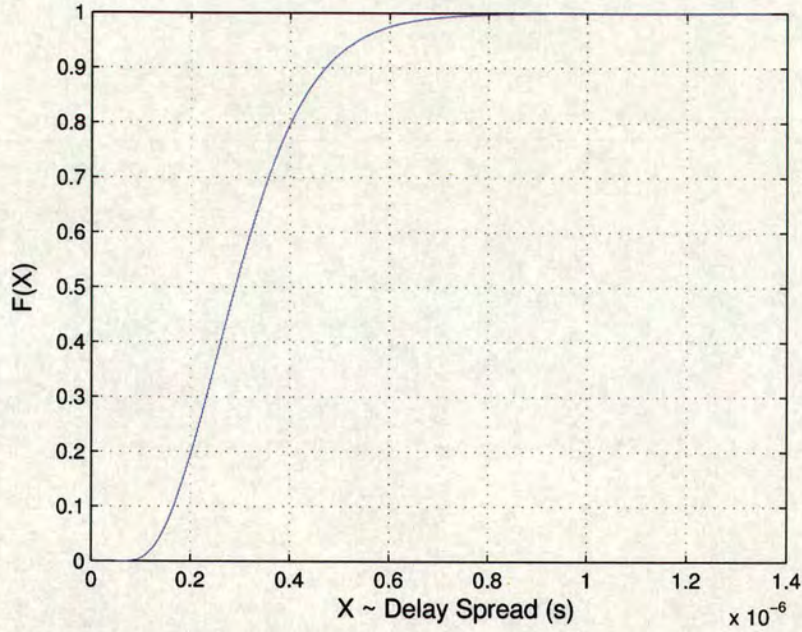


Figure 3.14: The cdf for the DS values simulated in the COST 259 GTU channel model.

value changing according to the simulation steps in [37].

3.6.2 The impact of delay spread

In general, the capacity of the channel increases as the SNR and the number of antennas increase as demonstrated in Figure 3.15 for one mobile location (one realisation) at $S_{50\%T}$. It can be observed that the capacity increases approximately by 1bps/Hz as the number of antennas used is doubled. Similar improvement in capacities can be observed as the SNR increases by 3dB. Due to the same DS value being used, the channel variation as seen from the slope of the capacity ccdf is small. There is some increase in slope gradient when we go from 2 to 4 antennas, but there is little additional diversity benefit beyond this number of antennas. The effect of the DS on the channel capacity is shown in Figure 3.16 for different number of antennas at a SNR of 21dB in one mobile location. The capacities corresponding to these DS values are about the same but the channel variations are clearly indicated from the slopes of the ccdf plot. Note that smaller channel variation corresponds to a steeper capacity slope. This suggests that as the DS decreases, the channel variation increases which leads to lower capacity for a given outage probability. To obtain a reasonable statistic on the overall channel capacity, the simulation is extended over 1000 mobile locations around the cell size of the GTU RE. The results obtained

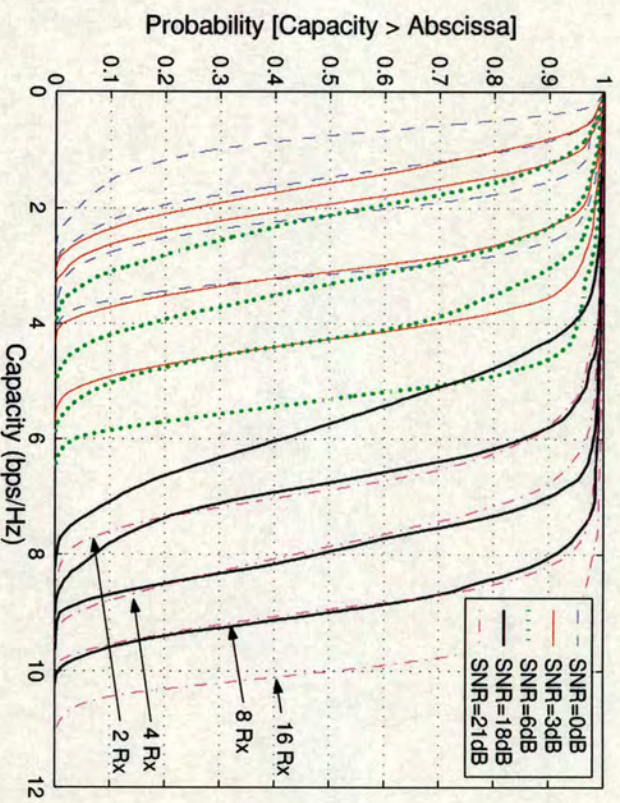


Figure 3.15: The capacity cdf for $S_{50\%T}$ at SNR 0, 3, 6, 18 and 21dB for one mobile location with 180° AS.

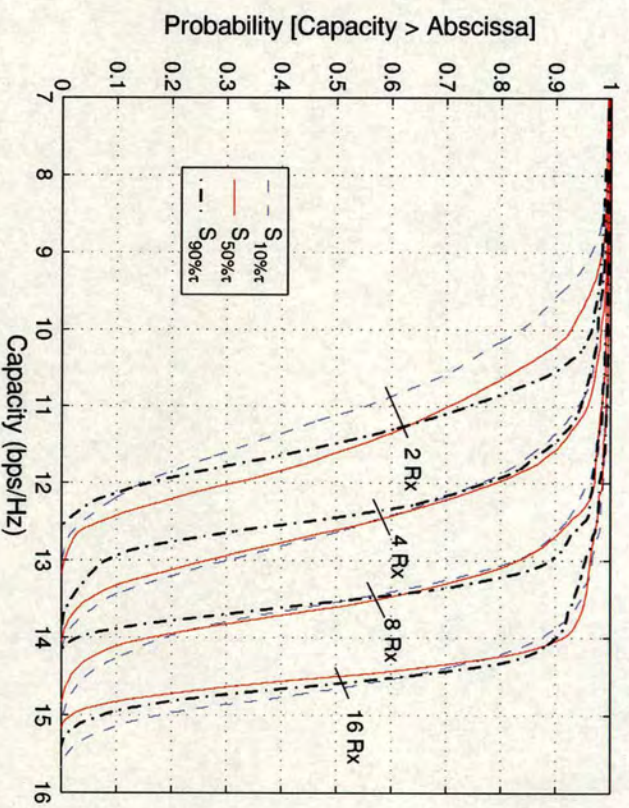


Figure 3.16: The capacity cdf of three DS values for different number of antennas at 21dB SNR for one mobile location with 180° AS.

are then averaged over the number of mobile locations as shown in Figure 3.17. As can be seen, the capacity corresponding to different DS values are approximately equal. Improvements in capacity from low to higher DS values can only be identified in the case of 2 and 4 received antennas. The observations in this section show that the diversity benefit of the DS saturates as the DS increases and so the diversity benefit is most notable for low diversity order systems.

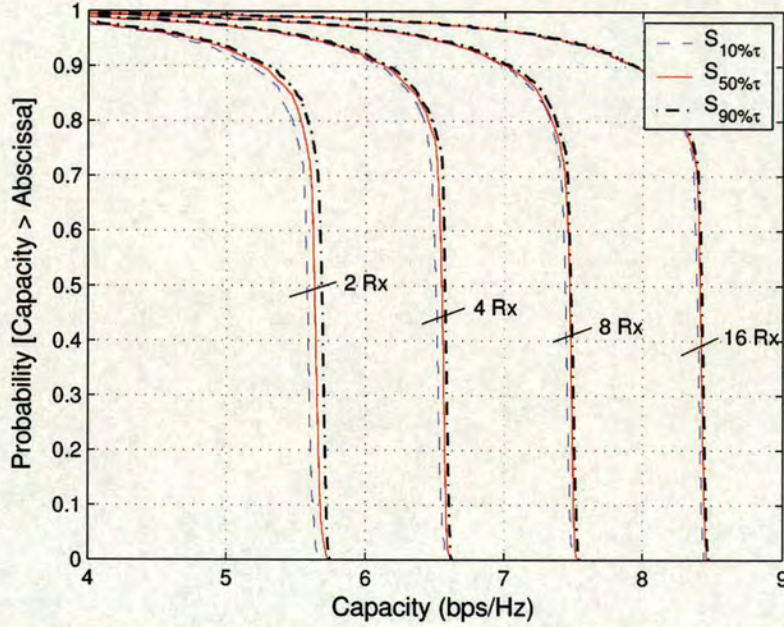


Figure 3.17: The overall channel capacity cdf of the three DS values for different number of antennas at 21dB SNR averaged over 1000 mobile locations with 180° AS.

3.6.3 The impact of azimuth spread

In order to have a clearer impression of the impact of AS on the system capacity, the capacities for the three AS values are compared in Figure 3.18. It is obvious that higher capacity can be achieved with higher AS values for a given outage probability. It is also observed that the channel variation decreases as the AS increases which leads to the higher capacity. This is expected as large AS values provide more uncorrelated paths for AAs to fully exploit spatial diversity. In addition, as the number of antennas increases from 2 to 16, the slope of the corresponding cdf curve also increases. The above observations suggest that spatial diversity is a promising way to increase system capacity, particularly when in an environment with large AS values. For the overall channel capacity, the simulation is again extended to 1000 mobile

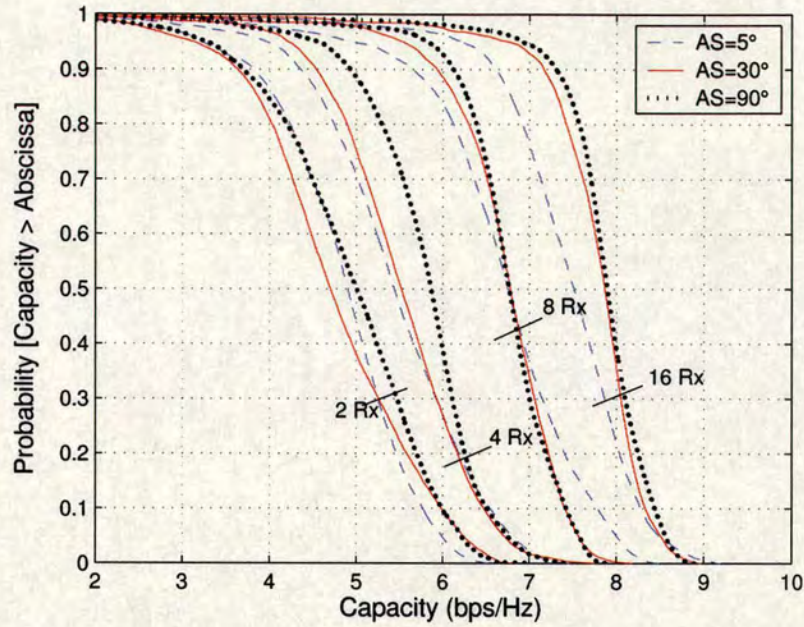


Figure 3.18: The capacity cdf of three AS values for different number of antennas at 21dB SNR for one mobile location.

locations and averaging is performed. It is evident from Figure 3.19 that large AS values lead to higher capacity. Some increase in the overall capacity can be seen when AS increases from 5° to 30° . Full spatial diversity corresponding to 180° in AS is also simulated to demonstrate the significance of the AS. As opposed to the case of the DS, an increase in capacity from low to higher AS values can be identified for all the number of antennas used in the simulations. The channel capacities corresponding to the AS values of 90° and 180° are comparable to each other as the performance of the AA saturates at high AS values [42].

3.7 Correlation matrices and the relation to the system performance

It has been demonstrated in Section 3.6 that the prime determinant of the system performance of a wideband system is the AS (spatial domain). The DS on the other hand is an important effect that can degrade the system performance. It can cause ISI which can be overcome by equalisation, though this is beyond the investigation on this thesis. It is worth mentioning that in the absence of delay, the values of the elements of the correlation matrix is strongly dependent on the properties of the incoming multipath waves. As will be shown in chapter 6,

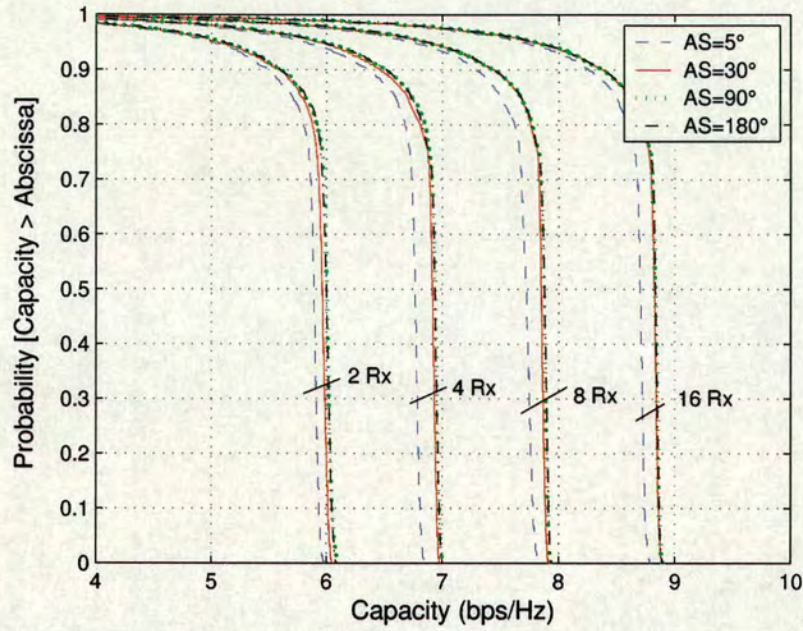


Figure 3.19: *The overall channel capacity cdf of the three AS values for different number of antennas at 21dB SNR averaged over 1000 mobile locations.*

the system performance is strongly dependent on the angular spreading of the incoming wave as well as the mean incidence angle in both azimuth and elevation domains. Should these parameters change, the spatial correlation changes accordingly. It is well-known that higher angle spread values result in a better performance (and vice versa) since large angle spread provides more uncorrelated paths. This relationship can be described mathematically using a correlation matrix. For a given scenario, the spatial characteristics of the channel are fully captured by the spatial correlation matrix. Since the correlation matrix plays a key role in the performance analysis of a system employing AAs, it is important to understand its fundamental properties and their implications.

3.7.1 Properties of the correlation matrix and their implications

For a M receive antenna system⁴ the associated correlation matrix is of size $M \times M$ given by

$$\mathbf{R} = E[\mathbf{h}\mathbf{h}^H] = \begin{bmatrix} R_{11} & R_{12} & \cdots & R_{1M} \\ R_{21} & R_{22} & \cdots & R_{2M} \\ \vdots & \vdots & \ddots & \vdots \\ R_{M1} & R_{M2} & \cdots & R_{MM} \end{bmatrix} \quad (3.31)$$

where \mathbf{h} is the channel vector and the element R_{mn} represents the correlation between antenna m and n while R_{nn} represents the correlation of the antenna n with itself (which is always one). For complex-valued channels, \mathbf{R} is a Hermitian matrix whose the elements $R_{mn} = R_{nm}^*$. In the special case of real value channels, \mathbf{R} is a symmetric matrix [86].

A number of implications can be deduced from \mathbf{R} . To enumerate this further, let us consider few correlation matrices correspond to several measurement results reported in [112] and the simulation results obtained from the previous section as examples. In particular, the following scenarios/environments are adopted:

1. A microcell environment where the BS (receiver) is elevated approximately 5.7m in height and located 300m away from the indoor MS (transmitter). The PAS at the BS is Laplacian distributed with $AS = 20^\circ$ and antenna spacing 3λ . The PAS at the MS is uniformly distributed with $AS = 180^\circ$ and antenna spacing 0.4λ . The spatial correlation matrices for both cases are given as [112]

$$\mathbf{R}_{BS,3\lambda} = \begin{bmatrix} 1.00 & 0.41 & 0.08 & 0.02 \\ 0.41 & 1.00 & 0.41 & 0.08 \\ 0.08 & 0.41 & 1.00 & 0.41 \\ 0.02 & 0.08 & 0.41 & 1.00 \end{bmatrix}; \mathbf{R}_{MS,0.4\lambda} = \begin{bmatrix} 1.00 & 0.09 & 0.05 & 0.03 \\ 0.09 & 1.00 & 0.09 & 0.05 \\ 0.05 & 0.09 & 1.00 & 0.09 \\ 0.03 & 0.05 & 0.09 & 1.00 \end{bmatrix} \quad (3.32)$$

2. A macrocell environment where the BS (transmitter) is elevated to 15m height and located 500m away from the outdoor MS (receiver) in average. The PAS at the MS is uniformly distributed. The spatial correlation matrices for antenna spacings 0.25λ and

⁴Assuming identical elements i.e. each element has the same radiation pattern.

1λ are evaluated with $AS = 180^\circ$ and $AS = 5^\circ$ respectively, are given as

$$\mathbf{R}_{MS,0.25\lambda} = \begin{bmatrix} 1.00 & 0.46 & 0.38 & 0.32 \\ 0.46 & 1.00 & 0.46 & 0.38 \\ 0.38 & 0.46 & 1.00 & 0.46 \\ 0.32 & 0.38 & 0.46 & 1.00 \end{bmatrix}; \mathbf{R}_{MS,1.0\lambda} = \begin{bmatrix} 1.00 & 0.95 & 0.80 & 0.57 \\ 0.95 & 1.00 & 0.95 & 0.80 \\ 0.80 & 0.95 & 1.00 & 0.95 \\ 0.57 & 0.80 & 0.95 & 1.00 \end{bmatrix} \quad (3.33)$$

Referring to (3.32), the \mathbf{R}_{MS} has a much lower correlation value than the corresponding \mathbf{R}_{BS} for a given set of antennas. Even though the spacing for the BS is much larger than the MS, the small AS reduces the overall correlation value. For the macrocell case, similar changes in correlation with respect to the AS and antenna spacing can be observed. The 0.25λ spacing with high AS results in a lower correlation than the case with 1λ spacing but with small AS. Note that the correlation matrix only represents an “incomplete” picture of the real propagation conditions as one cannot determine if the lower/higher correlation has arisen from the channel conditions (angle spread or angle-of-arrival) or the antenna itself (eg spacing and geometry). However, the system performance under such conditions can be studied through an eigenanalysis of the underlying correlation matrix.

3.7.2 Eigenanalysis: eigenvalue decomposition

Eigenanalysis is usually carried out through singular value decomposition (SVD) and EVD [109]. Both methods are used to diagonalise a matrix and evaluate the corresponding singular values and eigenvalues. The number of subchannel(s) between the BS and MS can be determined by using either SVD of the channel vector, \mathbf{h} (for SIMO) and channel matrix, \mathbf{H} (for MIMO) or performing EVD of the instantaneous correlation matrix, \mathbf{R} given as $\mathbf{R} = \mathbf{h}\mathbf{h}^T$ (for SIMO) and $\mathbf{R} = \mathbf{H}\mathbf{H}^T$ (for MIMO). The two decomposition methods can be summarised for both SIMO and MIMO systems as follows:

1. SIMO with N_R receivers

- SVD decomposes the channel vector \mathbf{h} of size $N_R \times 1$ to

$$\mathbf{h} = \mathbf{U}\mathbf{\Sigma}\mathbf{V}^H \quad (3.34)$$

where \mathbf{U} is unitary matrix, $\mathbf{\Sigma}$ is a vector with N_R elements $\{\sigma_1, 0, \dots, 0\}$ and \mathbf{V} is

scalar of value 1 or -1.

- EVD decomposes the matrix \mathbf{R} as

$$\mathbf{R} = \mathbf{h}\mathbf{h}^T = \mathbf{U}\mathbf{\Lambda}\mathbf{U}^H \quad (3.35)$$

where \mathbf{U} is unitary matrix while $\mathbf{\Lambda} = \text{diag}(\lambda_1, 0, \dots, 0)$.

Clearly the number of subchannels in SIMO systems is one signified by the single non zero singular value, σ_1 or single non zero eigenvalue, λ_1 which are related by $\sigma_1^2 = \lambda_1$.

2. MIMO system with N_R receiver and M_T transmitters

- SVD decomposes the channel matrix \mathbf{H} of size $N_R \times M_T$ to

$$\mathbf{H} = \mathbf{U}\mathbf{\Sigma}\mathbf{V}^H \quad (3.36)$$

where \mathbf{U} and \mathbf{V} are unitary matrices while $\mathbf{\Sigma} = \text{diag}(\sigma_1, \dots, \sigma_K)$ with elements $\{\sigma_1 \geq \sigma_2 \geq \dots \geq \sigma_K\}$.

- EVD

$$\mathbf{R}_{MS} = \mathbf{H}\mathbf{H}^T = \mathbf{U}\mathbf{\Lambda}\mathbf{U}^H \quad \text{or} \quad \mathbf{R}_{BS} = \mathbf{H}^T\mathbf{H} = \mathbf{V}\mathbf{\Lambda}\mathbf{V}^H \quad (3.37)$$

where \mathbf{U} is unitary matrix while $\mathbf{\Lambda} = \text{diag}(\lambda_1, \dots, \lambda_K)$ with the elements $\{\lambda_1 \geq \lambda_2 \geq \dots \geq \lambda_K\}$.

Thus for MIMO systems, applying the SVD or EVD enable us to estimate K_r parallel subchannels where the scalar K_r is the rank of the matrix given by $K_r = \text{rank}(\mathbf{H}) \leq \min(M_T, N_R)$ or $K_r = \text{rank}(\mathbf{R}) \leq \min(M_T, N_R)$ [109]. Each subchannel is associated with a singular value, σ_k or eigenvalue, λ_k which signifies the power gain of that subchannel. Again, the singular value and eigenvalue are related by $\sigma_k^2 = \lambda_k$.

The degree of correlation and decorrelation of the channel can be qualitatively described by the number of eigenvalues. A large number of approximately equal eigenvalues represents a situation where the link between the transmit and receive antennas are uncorrelated and vice versa. Usually, in a rich scattering environment (high AS at both BS and MS) a number of strong eigenvalues (orthogonal subchannels) are available between the link. On the other hand, if the correlation level is high, as for the case when the lesser eigenvalues are weak, it is not

possible to distinguish a large number of orthogonal subchannels. A MIMO system can be reduced to a SIMO configuration in a pin-hole [113] or keyhole [114] scenario with only one subchannel. To describe the SFC between two antennas separated in space at the BS or MS, one can refer to the correlation matrix, \mathbf{R} whereby the elements m and n of the \mathbf{R} , R_{mn} signifies the SFC at antenna m and n .

Since the correlation matrix is a Hermitian matrix (for complex values) and symmetry matrix (for real value), the use of the EVD is sufficient to extract the eigenvalues and thus will be used throughout in this thesis. This method forms the basis for the simulation and derivation of the theoretical results. The potential gain from applying diversity concepts is strongly dependent on the correlation coefficients between the antenna elements. It is worth mentioning that the effects of various antenna parameters are not explicitly incorporated in the analysis. In Chapter 4, these limitations are relaxed by considering EOA, different types of antenna element and AA on the system performance.

3.8 Summary

This chapter has presented the implementation of the COST 259 channel model in a macrocell environment using a TDL approach. The approaches and concepts used in modelling COST 259 are described in detail to ensure the correct parameter settings. Simulation procedures are outlined to identify the modelling steps involved. While the channel model facilitates link level simulations for AA systems, the associated capacity analysis demonstrated that AS is the primary determinant to the system performance. The channel variation decreases more rapidly in the case of increasing AS values than in the case of increasing DS values. Furthermore, increasing the number of antennas used permits the available spatial diversity to be exploited more effectively. Hence, the relationship between the system performance and the spatial diversity is established based on the spatial correlation matrix. In the next chapter, the effect of various antenna parameters on the performance of AAs are investigated.

Chapter 4

The effect of antenna parameters on the performance of antenna arrays

This chapter presents a simple antenna model that incorporates various antenna effects into the performance study of the AA systems. This is particularly important as little work has been reported that comprehensively investigates the system performance from the perspective of antenna parameters. The developed antenna model can facilitate the study of the impact of antenna parameters on the system performance. The aims of this chapter are two fold. Firstly, to study in detail the main constraints on the application of CAAs and to describe how such constraints can be modelled and incorporated into the system performance evaluation. Secondly, to study the trade-offs between these parameters in the development of handset AA by considering a 3-D multipath propagation model that permits both AOA and EOA to be taken into account. Thus, the optimised antenna parameters under specific scenarios without considering practical implementation issues can be determined. Our analysis shows that different antenna elements and arrays yield different performance which is more favourable in some cases than others. Furthermore, MC causes fading decorrelation which in principle leads to performance gain, but this is compensated by the effect of signal cancellation that reduces the overall received power. The “effective” result is that MC degrades the system performance.

The rest of the chapter is organised as follows, Section 4.1 highlights the motivation of considering antenna modelling. Section 4.2 briefly describes the properties of various antenna elements that are commonly used in wireless communication with emphasis given to their radiation patterns. Section 4.3 considers several AAs and describes the associated SV which is an important parameter that characterises the radiation pattern of the AA under study. Section 4.4 outlines the MC model for different AAs by treating the M elements of the AA as an $M + 1$ terminal linear bilateral network. Section 4.5 discusses the effect of inter element spacing and number of antenna elements. Section 4.6 analyses the impact of all the antenna parameters considered on the system performance. Finally, Section 4.7 concludes this chapter.

4.1 The need for antenna modelling

Apart from the channel effects, to enable a complete performance evaluation of CAAs, the impact of the antenna effects on the system performance must be adequately characterised. These antenna effects include MC, antenna patterns and orientation as well as different AA configurations. This section explains how to develop such an antenna model, a topic which is ignored by most of the researchers in the studies of the capacity improvement introduced by multiple-element antennas. (see [115] and references therein). Most of the work reported in the literature assumes that the elements of the adaptive AAs are isotropic. This ideal antenna, which radiates the power uniformly over a sphere, is unrealistic but provides a benchmark for more practical antennas to be assessed. Therefore, it is important to investigate the effects of the antenna element patterns on the array performance. Different types of antenna elements yield different radiation patterns [47–49]. However, these radiation patterns are usually not sufficiently directive in some applications such as tracking and interference suppression. In this regard, multiple antennas are employed. The required pattern can be changed by appropriately adjusting the current amplitudes and phases between the elements based on the algorithm employed. This is referred to as an adaptive antenna or smart antenna. In order to maximise the performance of AAs one can sufficiently separate the antenna elements at the BS and MS so that a large diversity order versus fading can be achieved. While this does not present a significant problem at the BS, accommodating more antennas on the MS introduces several constraints for practical implementation. In such a scenario, the antenna elements are in close proximity and the effect of MC becomes significant, an effect that must be taken into consideration.

4.2 Radiation pattern of an antenna element

A number of antenna types that are commonly used in mobile communication will be reviewed with the focus on their properties.

4.2.1 Short dipole and halfwave dipole

The HD is one of the most widely used antennas [47–49] and is depicted in Figure 4.1. Measurements show that the current distribution of a HD is approximately sinusoidal with maximum value at the centre of the dipole. The normalised radiation pattern of a short dipole and HD

oriented in the z -axis are given by (4.1) and (4.2) respectively

$$f(\varphi, \theta)_{SD} = \sin(\theta) \quad (4.1)$$

$$f(\varphi, \theta)_{HD} = \frac{\cos\left(\frac{\pi}{2} \cos \theta\right)}{\sin \theta} \quad (4.2)$$

It can be seen from Figure 4.1(b) that the radiation pattern for the short dipole and HD

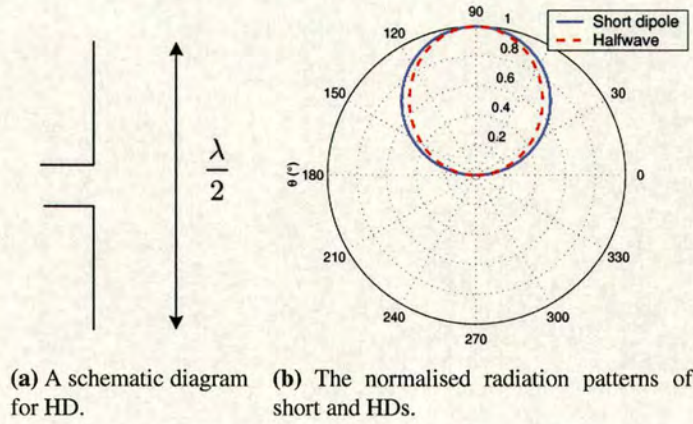


Figure 4.1: A HD and its radiation pattern.

are almost identical. The main advantage of HD is it resonates at approximately zero input impedance. This reduces the need for tuning to achieve the conjugate impedance match [48]. At the resonant frequency, the input impedance is about 73Ω . This antenna has omni-directional coverage in azimuth. In addition, the elevation beamwidth and directivity of this antenna are 78° and 1.64 respectively.

4.2.2 Small loop

Loop antennas can take many different forms such as rectangle, circle, triangle, etc. The overall length of this type of antenna is typically on the order of $\lambda/10$ [47]. They are relatively inefficient and are normally used in receiving mode. However, they are more robust in an interfering and multipath channel since they are more immune to noise [47]. The loop antennas can be placed either horizontally or vertically. The radiation pattern and directivity of the small loop antennas with any shape is similar to the short electric dipole i.e. $\sin(\theta)$ and $\frac{3}{2} \sin^2(\theta)$. This can be proved by principle of duality or deriving the fields of the small loop directly. The input impedance of the loop antenna depends on several factors such as number of loops, types

of wire used, shapes of the loop, current distribution etc. Hence, the input impedance and directivity of loop antennas are usually determined from a computer simulation program.

4.2.3 Patch antenna

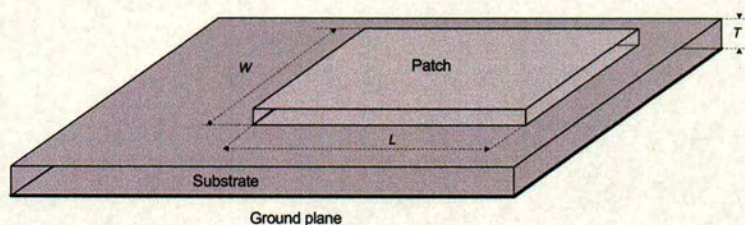
As with loop antennas, patch antennas can also take many different shapes but the most widely used are rectangular, circular and thin strip patch. They can be integrated into a flat and compact size using printed circuit technology. Apart from being light weight and having a low production cost, patch antennas are versatile in terms of resonant frequency, polarisation and input impedance. However, they have a low radiation efficiency and very narrow bandwidth. Figure 4.2 shows a patch antenna (microstrip) with dimension $W \times L \times T$. The thickness of the substrate, T is very thin i.e. $T \ll \lambda$. The length, L is on the order of $\lambda/2$ while the width, W is selected to give suitable radiation resistance (usually 50Ω). Patch antennas can be created with linear or circular polarisation while the radiation pattern is designed in such a way that maximum is at normal to the patch. The normalised radiation pattern of the patch antenna is given as

$$f(\varphi, \theta)_{PA} = \{\sin \theta \sin(X) \sin(Z) / (XZ)\} \times \cos(kL \sin \theta \sin \varphi / 2) \quad (4.3)$$

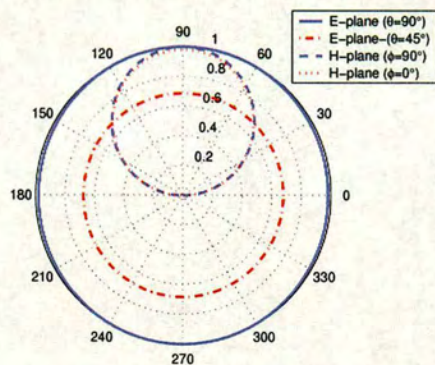
where $X = 0.5kT \sin \theta \cos \theta$ and $Z = 0.5kW \cos \theta$. As seen in Figure 4.2(b), the radiation decreases as the elevation angle moves away from the horizontal plane while the radiation remains approximately unchanged as the azimuth angle changes.

4.3 Type of antenna array

As discussed in the Section 3.3 on parameter settings, we see that different AA configurations can be adapted into the channel models by specifying its associated SV. Recall from Chapter 2, the SV of an AA with arbitrary elements is given by (2.12) and (2.13). Combining (2.12) and (2.13), the SV of the ULA, UCA and URA can be derived. In this thesis, several types of AAs are considered namely: ULA, UCA, URA, EVS and array of EVS.



(a) A schematic diagram for patch antenna.



(b) The normalised radiation patterns of patch for different E-plane and H-plane.

Figure 4.2: A patch antenna and its radiation pattern.

4.3.1 Uniform linear array

A ULA is one of the most commonly encountered AAs in the literature and has been widely used in current BS systems [5, 36]. Theoretically, the azimuthal coverage of the ULA is restricted to 180° due to an ambiguity in determining the AOA. In practice the azimuthal coverage is further limited in 120° due to the practical difficulties in AOA measurement. A ULA with M antenna elements is illustrated in Figure 4.3. Taking the first element as a reference and using isotropic antenna elements, the SV of the ULA is given by

$$\mathbf{a}(\varphi, \theta)_{ULA} = \left[1, e^{j2\pi d \cos \varphi \sin \theta / \lambda}, \dots, e^{j2\pi d(M-1) \cos \varphi \sin \theta / \lambda} \right]^T \quad (4.4)$$

where d is the antenna element spacing.

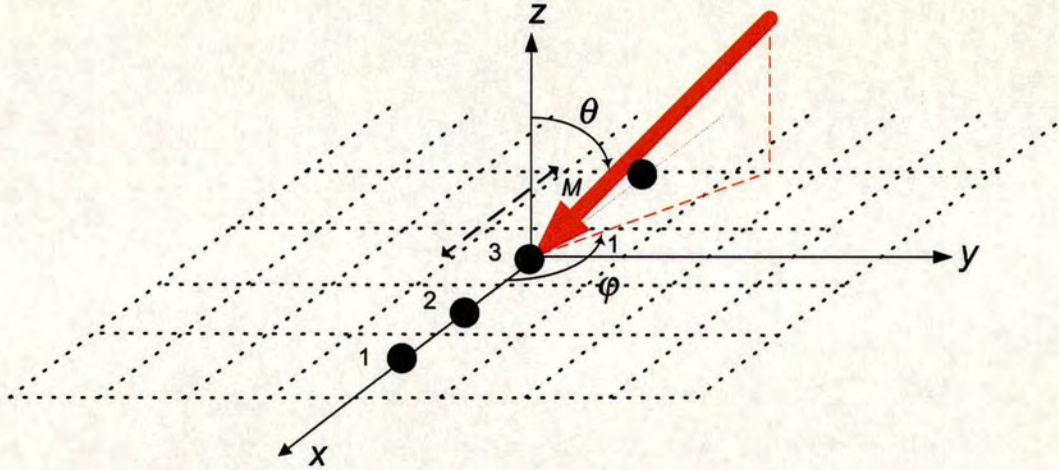


Figure 4.3: A M -element ULA oriented in x - y plane with antenna spacing d .

4.3.2 Uniform circular array

A UCA is used to provide 360° azimuthal coverage as compared to the 180° in the case of ULA [116]. They also outperform the ULA by being able to provide information in the elevation angle. However, the accuracy of elevation information that can be resolved is dependent on its element radiation pattern. A UCA is parameterised by a number of elements M , radius of the UCA r and circumferential spacing between adjacent elements d . Taking the centre of the UCA

as a reference point and using isotropic antenna elements, the SV of the UCA is given by

$$\mathbf{a}(\varphi, \theta)_{UCA} = \left[e^{j\zeta \cos(\varphi - \psi_0)}, e^{j\zeta \cos(\varphi - \psi_1)}, \dots, e^{j\zeta \cos(\varphi - \psi_{M-1})} \right]^T \quad (4.5)$$

where $\psi_n = 2\pi r n / M$ and $\zeta = 2\pi r \sin \theta / \lambda$.

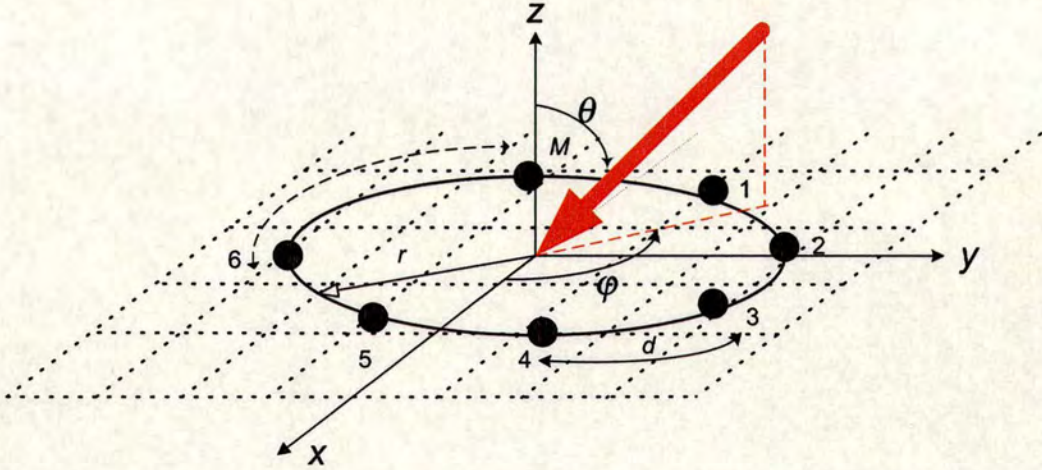


Figure 4.4: A M -element UCA oriented in x - y plane with circumference spacing d .

4.3.3 Uniform Rectangular Array

A URA is capable of providing 3-D coverage of the source information and hence is widely used in direction finding applications [117]. A URA with $P \times N$ elements located in the x - y plane with the origin as a reference point is shown in Figure 4.10. The spacing between the array elements parallel to the x -axis and y -axis are denoted by d_x and d_y respectively. The azimuth and elevation angles of a source are specified by the direction of cosines with respect to the x - and y -axis respectively i.e. $\cos(\varphi) \sin(\theta)$ and $\sin(\varphi) \sin(\theta)$. Thus, the phase shifts between the successive elements along the x and y -axis are given by

$$\mu = 2\pi d_x \cos \varphi \sin \theta / \lambda \quad (4.6)$$

$$v = 2\pi d_y \sin \varphi \sin \theta / \lambda \quad (4.7)$$

By treating all the elements in each column along the x -axis as a ULA and assuming that the

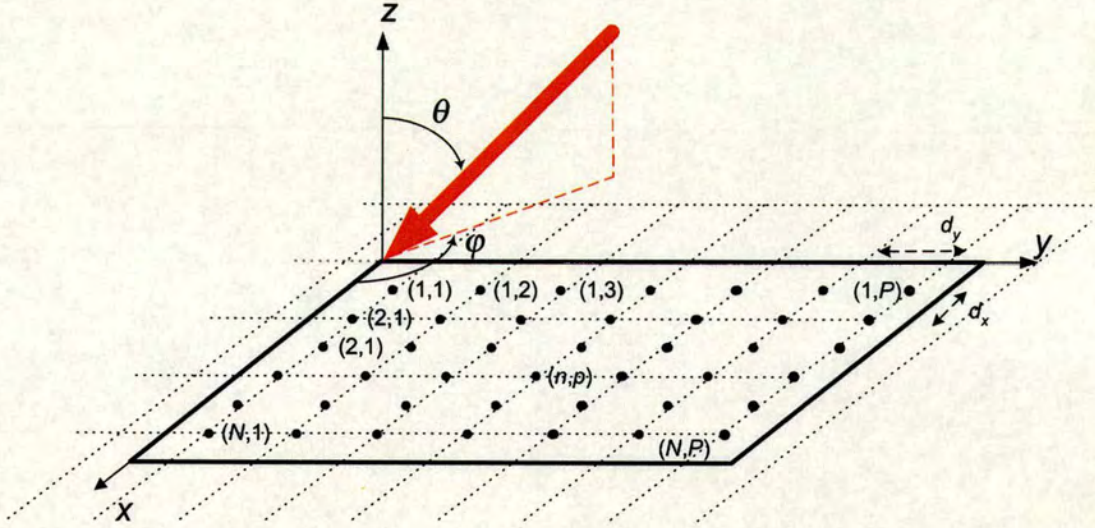


Figure 4.5: A M -element URA oriented in x - y plane with antenna spacings d_x and d_y .

reference point is taken at the origin, the associated SV for each column n is given by

$$\mathbf{a}_N(\mu) = [1, e^{j\mu}, \dots, e^{j(N-1)\mu}]^T \quad (4.8)$$

Similarly, by treating all the elements in each row along the y -axis as a ULA, the SV for each row p is given by

$$\mathbf{a}_P(v) = [1, e^{jv}, \dots, e^{j(P-1)v}]^T \quad (4.9)$$

By combining the two SVs, we obtain the steering matrix for the URA which is given by

$$\mathbf{a}(\varphi, \theta)_{URA} = \text{vec}(\mathbf{a}_N(\mu)\mathbf{a}_P^T(v)) \quad (4.10)$$

The operator $\text{vec}(\cdot)$ maps an $N \times P$ matrix to an $NP \times 1$ vector by stacking the columns of the matrix. The operator returns a SV for the URA as

$$\begin{aligned} \mathbf{a}(\varphi, \theta)_{URA} = & [1, e^{jv}, \dots, e^{j(P-1)v}, e^{j\mu}, e^{j(v+\mu)}, \dots, e^{j[\mu+(P-1)v]}, \\ & \dots, e^{j(N-1)\mu}, \dots, e^{j[(N-1)\mu+(P-1)v}]^T \end{aligned} \quad (4.11)$$

4.3.4 Electromagnetic vector sensor

The AAs discussed so far are scalar sensors which only provide measurement of one component of the electric or magnetic field. An EVS on the other hand, is capable of measuring three electric fields, \mathbf{E} and three magnetic fields, \mathbf{B} at a point in space while occupying a small volume whose constituent dimensions are on the order of less than half a wavelength. The exploitation of these fields is possible due to the three electrically identical short dipoles and three magnetically identical small loops which are co-located and orthogonally oriented as depicted in Figure 4.6. EVS offer several advantages [118] over the traditional AAs:

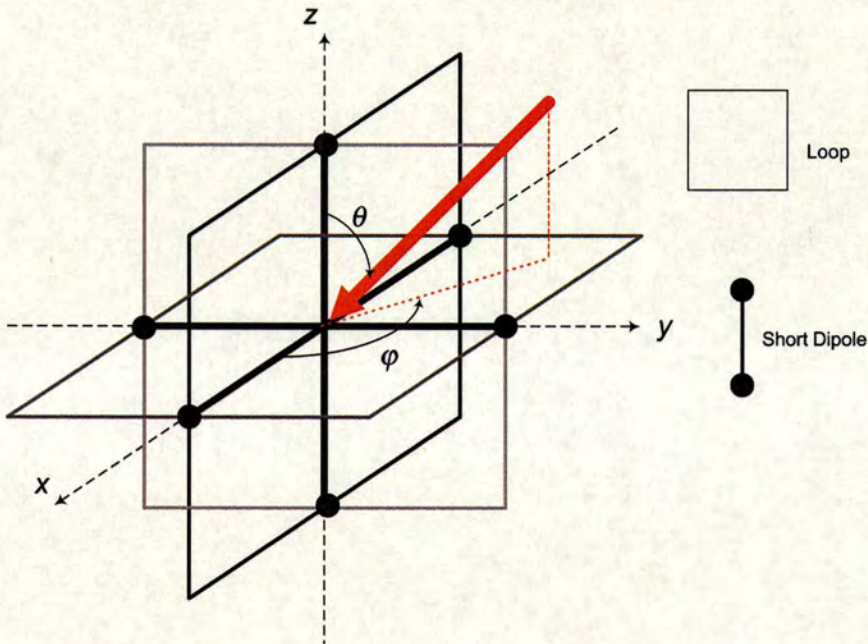


Figure 4.6: An EVS consists of three electrically identical short dipoles and three magnetically identical small loops which are co-located and orthogonally oriented.

- Capable of performing high resolution 3-D direction of arrival estimation and beamforming.
- Close to isotropic response.
- Compact size.

Though, the EVS has been widely used for direction finding applications [119, 120], recent results [121] show that EVS can be applied to mobile communication systems whereby the use

of polarization diversity can provide capacity improvement over a conventional dual-polarised system. The SV of an EVS¹ can be obtained by considering an incident source of an electromagnetic wave which can be defined as [123].

$$\begin{aligned} \mathbf{a}_{EVS}(\Theta) &= [\mathbf{E}^T \mathbf{B}^T]^T = \Psi(\theta, \varphi) \Omega(\gamma, \eta) \\ &= \begin{bmatrix} \cos \theta \cos \varphi & -\sin \varphi \\ \cos \theta \sin \varphi & \cos \varphi \\ -\sin \theta & 0 \\ -\sin \varphi & -\cos \theta \cos \varphi \\ \cos \varphi & -\cos \theta \sin \varphi \\ 0 & \sin \theta \end{bmatrix} \begin{bmatrix} \sin \gamma e^{j\eta} \\ \cos \gamma \end{bmatrix} \end{aligned} \quad (4.12)$$

where $\Theta = [\theta, \varphi, \gamma, \eta]^T$ is the spatial vector parameter. A transmitted signal with well defined polarisation will be randomly depolarised after passing through a radio channel [29]. Thus, unless otherwise specified, it is assumed for the rest of the analysis that the signals arriving at the receiver are randomly polarised with γ and η uniformly distributed over $[0, \pi/2]$ and $[-\pi, \pi]$, respectively.

4.3.5 An array of EVS

Due to the compact structure of the EVS, it is possible to arrange multiple EVSs in an array configuration so that higher performance can be achieved. When multiple EVSs are located at different places with certain arrangements like the ULA, URA or UCA, the resultant SV for the array of EVS, $\mathbf{a}_{EAA}(\Theta)$ is given by

$$\mathbf{a}_{EAA}(\Theta) = \mathbf{a}_{EVS}(\Theta) \otimes \mathbf{a}_{UAA}(\theta, \varphi) \quad (4.13)$$

where \otimes is the Kronecker multiplication operator and $\mathbf{a}_{UAA}(\theta, \varphi)$ is the SV of the AA under study. For instance, $\mathbf{a}_{UAA}(\theta, \varphi)$ could be the SV given in (4.4), (4.5) and (4.11). When multiple EVSs are located in an array configuration, an extra dimension is added to the system via spatial diversity as the spatial phase factor is now included in the overall SV.

¹Note that, unlike the ULA, UCA and URA, the EVS SV has no spatial phase factors [122] due to the orthogonal and co-located components.

4.3.6 Radiation pattern of an antenna array with identical elements

When the antenna elements are arranged to form an AA, the power gain as well as the directivity can be improved. The overall radiation pattern of an array is determined by the type of element used, the spatial positions and orientation of the elements as well as the current that feeds the elements. For an AA with identical elements, the overall radiation pattern can be derived from the principle of pattern multiplication [47–49] defined as the product of the array factor² (AF) and individual elemental pattern i.e.

$$f(\theta, \varphi) = \text{single element pattern} \times AF \quad (4.14)$$

For example, a ULA using two HW dipoles located in the x -axis with the dipole axis parallel to the z -axis, the normalised radiation characteristic for the single HW dipole is changed from (4.2) to

$$f(\theta, \varphi) = \underbrace{\frac{\cos\left(\frac{\pi}{2} \cos \theta\right)}{\sin \theta}}_{\text{elemental pattern of halfwave dipole}} \times \underbrace{\left[\cos \left(\frac{kd \sin \theta \cos \varphi + \delta}{2} \right) \right]}_{\text{Array factor}} \quad (4.15)$$

where δ is the phase shift. The AF is a function of the array geometry, inter-element spacing, number of antenna elements as well as the relative magnitude and phase between the elements. The AF is always symmetrical about the axis of the array while element patterns are not necessary symmetrical but depend on the types of antenna elements used (e.g. dipole, patch etc). In our analysis, we assume the elements are spaced equally and each element is fed with equal amplitude and phases. Thus, for a given spacing d , magnitude and phase shift, the radiation pattern will solely depend on the geometry/configuration of the array. Appendix C shows a series of radiation patterns for the ULA, UCA and URA using different types of antenna elements. Different patterns can be adjusted by controlling the spacing, magnitude and phase shift.

4.4 Mutual coupling

The modelling of MC in ULAs with HDs³ has been discussed in detail in [12, 14, 15] where an expression that relates the output voltages, current and mutual impedance of the element is first developed. By treating the M antenna elements as an $M+1$ terminal linear bilateral network, an

²AF is another form of writing the SV but in a compact format.

³The axes of the HD are oriented along the vertical z -axis.

impedance matrix \mathbf{Z} that consist of self and mutual impedance is formed. This approach is valid for any antenna provided the corresponding impedances can be calculated. The relationship that governs the received voltage vector without coupling S_m and the one with coupling V_m is then given by

$$\begin{bmatrix} 1 + \frac{Z_{11}}{Z_L} & \frac{Z_{12}}{Z_L} & \dots & \frac{Z_{1M}}{Z_L} \\ \frac{Z_{21}}{Z_L} & 1 + \frac{Z_{22}}{Z_L} & \dots & \frac{Z_{2M}}{Z_L} \\ \vdots & \vdots & \ddots & \vdots \\ \frac{Z_{M1}}{Z_L} & \frac{Z_{M2}}{Z_L} & \dots & 1 + \frac{Z_{MM}}{Z_L} \end{bmatrix} \begin{bmatrix} V_1 \\ V_2 \\ \vdots \\ V_M \end{bmatrix} = \begin{bmatrix} S_1 \\ S_2 \\ \vdots \\ S_M \end{bmatrix} \quad (4.16)$$

where Z_{ij} and Z_L denote the impedance between the antenna elements i and j , and the load impedance respectively. The scalar Z_{ij} for $i \neq j$ is the mutual impedance of antenna elements i and j . On the other hand, Z_{ij} for $i = j$ is the self impedance. Equation (4.16) can be written in matrix form as

$$\begin{aligned} \mathbf{Z}_{eq} \mathbf{V} &= \mathbf{S} \\ \mathbf{V} &= \mathbf{Z}_{eq}^{-1} \mathbf{S} \end{aligned} \quad (4.17)$$

where \mathbf{Z}_{eq}^{-1} denotes the inverse matrix of \mathbf{Z}_{eq} and $\mathbf{Z}_{eq} = (\mathbf{Z} + Z_L \mathbf{I})/Z_L$. The matrix \mathbf{I} is the size M identity matrix. Note that \mathbf{Z}_{eq} is always non-singular i.e. \mathbf{Z}_{eq}^{-1} always exists. Most of the analysis of adaptive AA assumes the element spacing is such that the MC is negligible and the matrix \mathbf{Z}_{eq} becomes diagonal. The matrix \mathbf{Z}_{eq} characterises the array and is independent of the channel in which the array operates.

Consider centre fed HW dipoles in the ULA configuration oriented along the z -axis. The corresponding mutual impedance between two isolated elements m and n located side-by-side in space, $Z_{mn} = R_{mn} + jX_{mn}$, can be deduced from the method of induced EMF [47, 49] where

$$R_{mn} = 30[2C_i(u_0) - C_i(u_1) - C_i(u_2)] \quad (4.18)$$

$$X_{mn} = 30[2S_i(u_0) - S_i(u_1) - S_i(u_2)] \quad (4.19)$$

where C_i and S_i are the cosine and sine integral given as

$$\begin{aligned} C_i &= -\int_x^\infty \frac{\cos y}{y} dy \\ S_i &= \int_0^x \frac{\sin y}{y} dy \end{aligned} \quad (4.20)$$

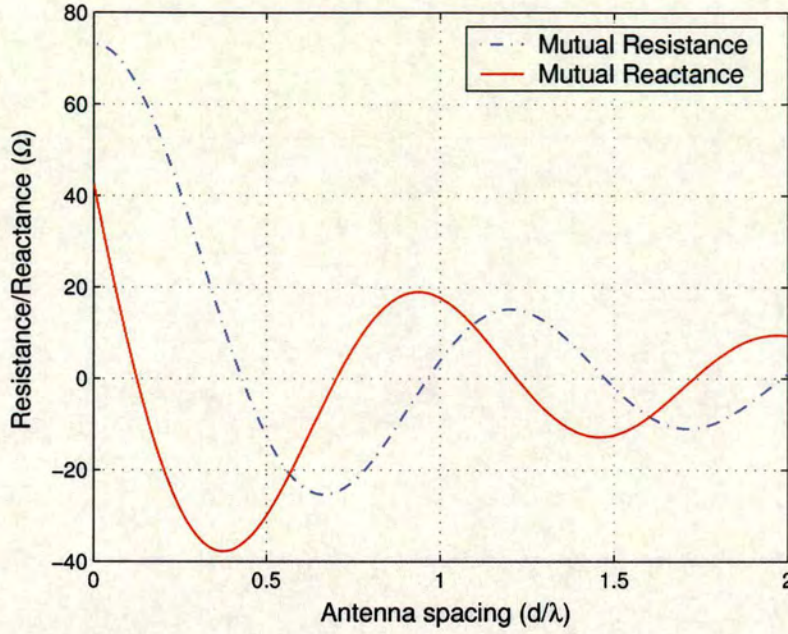


Figure 4.7: Mutual resistance and reactance of the centre fed HW dipole antennas located side-by-side as a function of the antenna spacing.

and

$$\begin{aligned} u_0 &= kd_{eff} \\ u_1 &= k \left(\sqrt{d_{eff}^2 + l^2} + l \right) \\ u_2 &= k \left(\sqrt{d_{eff}^2 + l^2} - l \right) \end{aligned} \quad (4.21)$$

The scalar $d_{eff} = d|m - n|$ with d is the spacing between adjacent antennas. We extend the same modelling approach to the case of the UCA and URA by assuming that the antennas have been relocated into circular and rectangular positions, and treating each pair of the antennas in the array as a two element ULA. It can be shown that for the UCA configuration, the scalar d_{eff} is given by

$$d_{eff} = r\sqrt{2(1 - \cos \vartheta)} \quad (4.22)$$

where $\vartheta = 2\pi|m - n|/M$ and $r = Md/2\pi$. Similarly for the case of URA, the d_{eff} is given by

$$d_{eff} = \begin{cases} d|p_m - p_n| & \text{if } p_m - p_n \neq 0 \text{ \& } q_m - q_n = 0 \\ d|q_m - q_n| & \text{if } q_m - q_n \neq 0 \text{ \& } p_m - p_n = 0 \\ \sqrt{(d|p_m - p_n|)^2 + (d|q_m - q_n|)^2} & \text{if } p_m - p_n \neq 0 \text{ \& } q_m - q_n \neq 0 \end{cases} \quad (4.23)$$

where p_m and q_m signify the coordinate of the m elements in the cartesian coordinates. Figures 4.8 to 4.10 show the magnitude of the coupling matrix elements for HD elements of the ULA, UCA and URA cases. Notice that the density of the coupling matrix is mostly concentrated at the adjacent elements corresponding to the main diagonal. As the distance between successive adjacent elements increases, the magnitude of coupling matrix decreases. In addition, the matrix entries along each subdiagonal are symmetrical about the main diagonal. Comparing these MC density figures, it can be observed that the UCA is more sensitive to the MC effects (i.e. with highest coupling power) since UCA has higher resultant d_{eff} distance⁴ between antenna elements as compared to the ULA and URA configurations. The URA on the other hand has the more edge elements than the ULA is thus more sensitive to the impact of MC. In practice, particularly for direction application, the ULA and URA are calibrated by placing a passive (dummy) antenna to balance the MC caused by the edge elements [124, 125].

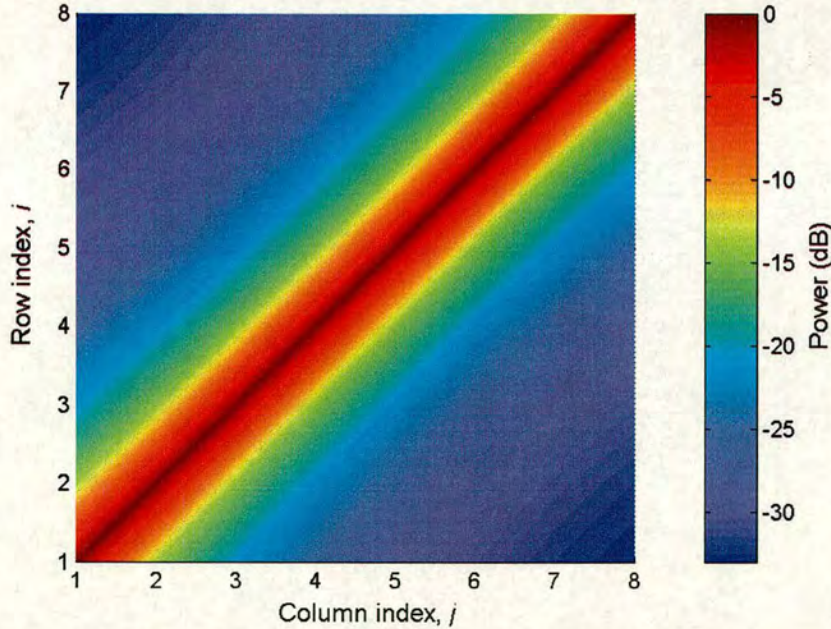


Figure 4.8: Magnitude of the coupling matrix elements for HD elements of the ULA at 0.5λ antenna spacing.

We now introduce a normalisation constant given by the maximum value of the diagonals of the matrix \mathbf{Z}_{eq} i.e. $\max(\text{diag}(\mathbf{Z}_{eq}))$ [39, 40]. The normalised coupling matrix of the conventional

⁴Some authors define the antenna spacing for the UCA in terms of the radius of the UCA which yields higher d_{eff} as compared to our case and thus gives lower coupling power.

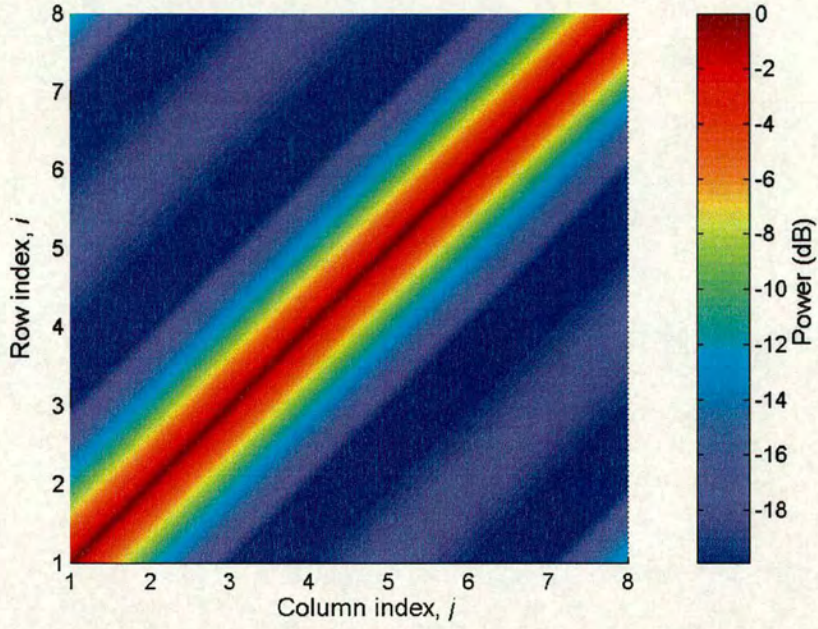


Figure 4.9: Magnitude of the coupling matrix elements for HD elements of the UCA at 0.5λ antenna circumference spacing.

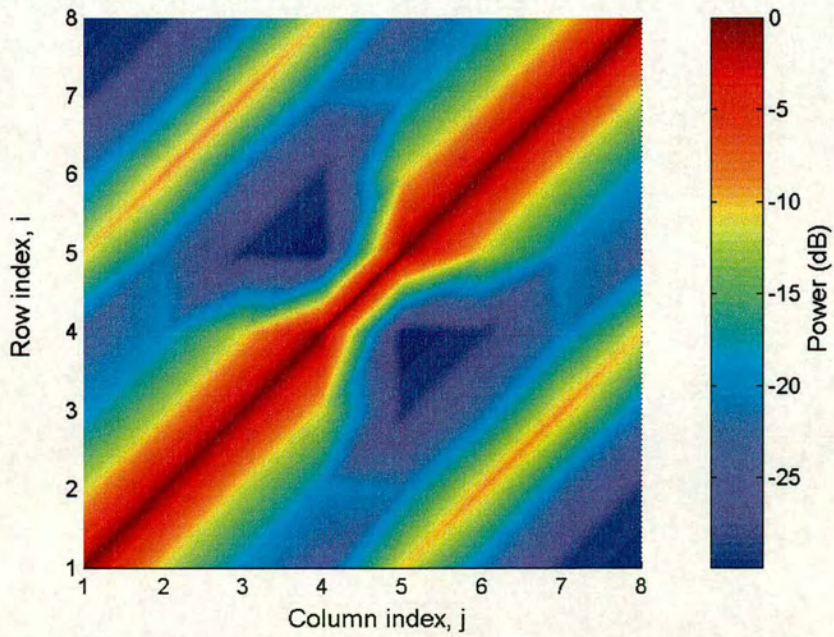


Figure 4.10: Magnitude of the coupling matrix elements for HD elements of the URA at 0.5λ antenna spacings for d_x and d_y .

model given by

$$\mathbf{Z}_{norm} = \mathbf{Z}_{eq} / \max(\text{diag}(\mathbf{Z}_{eq})) \quad (4.24)$$

This normalisation allows a direct comparison of performance with the SV equations, e.g. (4.4) as will be demonstrated in Section 4.6.3. The MC modelling can be generalised to other orientations of the elements of the arrays using two additional configurations namely collinear and parallel in echelon configurations. For modelling MC using other elements such as patch antennas, interested readers are referred to [126] and references therein. Note that the principle is the same but the mutual and self impedances need to be evaluated for the type of antenna element used.

4.5 Number of antennas and antenna spacing

In order to optimise the performance gain, a large diversity order is generally required. However, for a given terminal size, increasing the number of antenna elements will reduce the spacing and increase the fading correlation. Thus, the best compromise between spacing and number of elements must be found.

4.6 Performance analysis on antenna parameters

4.6.1 The effect of antenna element pattern

We consider the BER performance for a 4-element ULA associated with 60° mean-elevation-of-arrival (MEOA) and 0° MAOA for varying ES and AS values. Three types of antenna elements are considered for the ULA namely isotropic, HD and patch antenna with 0.5λ antenna spacing. At low SNR, the performance difference between ES values of 10° and 60° (see Figure 4.11) and AS values of 10° and 60° (see Figure 4.12) for the three element types are negligible but increases gradually at higher SNR. The results can be justified by comparing the directivity for the isotropic, HD and patch elements of the ULA given by 4, 8.4 and 20.3 respectively. Since directivity represents the ability of the antennas to focus energy in a particular direction, the antennas corresponding to higher directivity with AOA off the target direction will have low performance gain. Conversely, low directivity antennas perform well even under large AOA as the energy is captured over a larger range of angles of arrival. High directivity AAs can be applied to interference rich environments whereby interference can be suppressed by steering a

narrow beam pattern toward the desired users while simultaneously forming a null toward other users. Comparing Figure 4.11 and 4.12, it is observed that the performance improvement

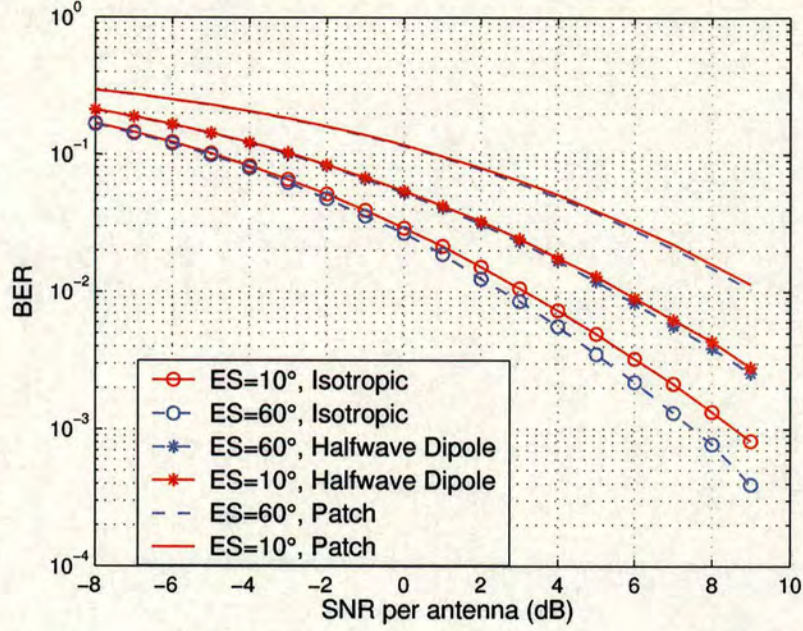


Figure 4.11: The BER performance comparison of 4-element ULA with different antenna elements associated with ES. No MC is assumed.

is greater when the AS increases as compared to the ES. For instance, to achieve BER of 0.01, there is only a minor reduction in the required SNR when increasing the ES from 10° to 60° for all types of antenna elements. However, it can be observed that a 3dB gain can be achieved when the AS is increased from 10° to 60° for the case of isotropic and HD antennas. This suggests that all three antenna element types perform better under AS rich than ES rich environments. Thus, the horizontally oriented element would be expected to outperform the vertically oriented counterpart [127–129].

4.6.2 The effect of types of antenna array

In general, the performance in term of the required target SNR to achieve a 0.01 BER of the three arrays improves as the AS increases. For most of the cases in Figure 4.13, the ULA outperforms the UCA and URA except at low MAOA values ($< 30^\circ$). At a low MAOA, the elements of the ULA are approximately parallel to the direction of the incoming signals and thereby increase the correlation of the received signals at each of the antenna elements. In

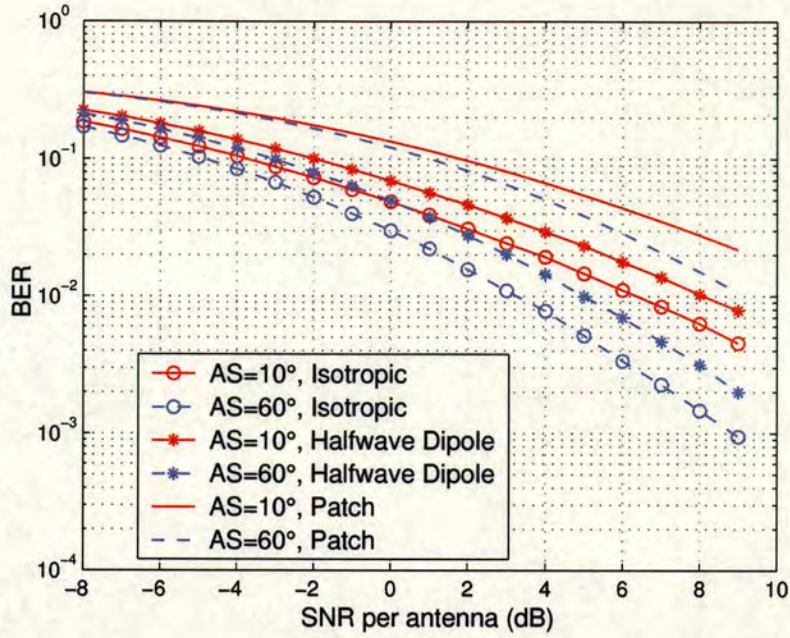


Figure 4.12: The BER performance comparison of 4-element ULA with different antenna elements associated with AS. No MC is assumed.

contrast, for the UCA and URA, only two of the antenna elements are in parallel to the incoming signals while the other two are perpendicular. Thus, the UCA and URA perform better than ULA in this case. The performance of ULA improves to the maximum as the MAOA moves from endfire (0°) to broadside⁵ (90°). Figure 4.14 shows the performance comparison between the three arrays for different ES again with varying AS. In general, the performance of the three arrays improves as the ES increases. This makes the required target SNR drop accordingly. Also, for a given ES, the performance of the array improves as the AS of the incoming signal increases. At an ES less than or equal to 30° , the UCA and URA outperform the ULA. For higher ES values, the ULA outperforms the UCA and URA at low AS values up to 30° and beyond this AS value, the performance of these arrays start to converge. Figure 4.15 shows the performance comparison versus MAOA under different AS with ES at 60° . In this specific instance of the ULA, we note that at zero AS, the performance gets worse as MAOA goes from 0° to 90° . However, as the AS increases, the performance now improves as MAOA goes from 0° to 90° . Thus, the AS effect is more important than that of the MAOA. Furthermore, the

⁵Note that, unlike in [130] which defined broadside as 0° measured from the axis perpendicular to the ULA's axis, broadside is defined as 90° and 0° angle is referred as endfire in this thesis since the AOA is measured from the positive x -axis where the array's axis lies. Both definitions yield the same results provided they are used consistently throughout the analysis.

performance of the UCA and URA are comparable to each other under many scenarios as the pattern gain for both arrays with four antennas looks very similar⁶.

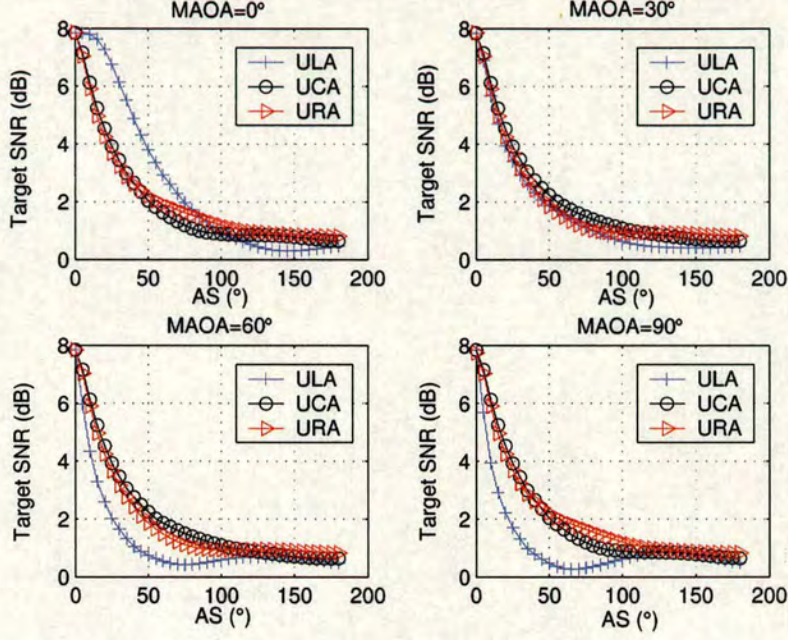


Figure 4.13: The target SNR performance with $M=4$ antennas showing the comparison between ULA, UCA and URA under different ES at varying AS with 0° MAOA and 90° MEOA. No MC is assumed.

4.6.3 The effect of mutual coupling

In this section, we first demonstrate the applicability of the normalisation process introduced in (4.24) and then study the effect of MC in detail. It can be clearly seen from Figure 4.16 that without normalisation, there is always a power reduction even at spacings when MC is insignificant. However, with normalisation, the received power converges to the case of non-MC at higher spacings where the effect of MC can be generally neglected. The power loss due to our proposed MC model in Figure 4.16 is 3dB with reference to the no MC case. This is justified as maximum power transfer occurs (where half of the power is transferred) since the load impedance used is the complex conjugate of the antenna impedance.

Furthermore, the BER performance as shown in Figure 4.17 also reflects the fact that applying

⁶Note that four element UCA and URA have a similar geometry but the antenna spacing for the UCA is measured as a circumference distance between adjacent antennas.

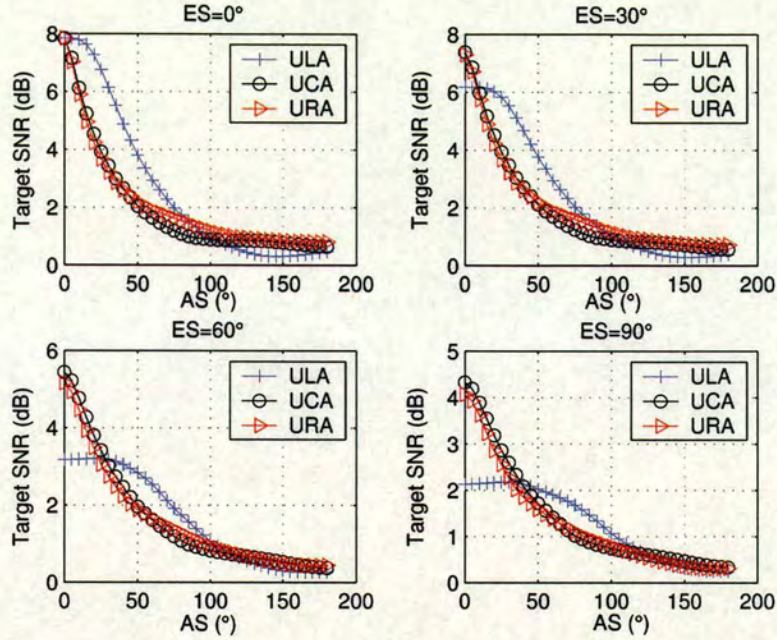


Figure 4.14: The target SNR performance with $M=4$ antennas showing the comparison between ULA, UCA and URA under different ES at varying AS with the 90° MEOA and 0° MAOA. No MC is assumed.

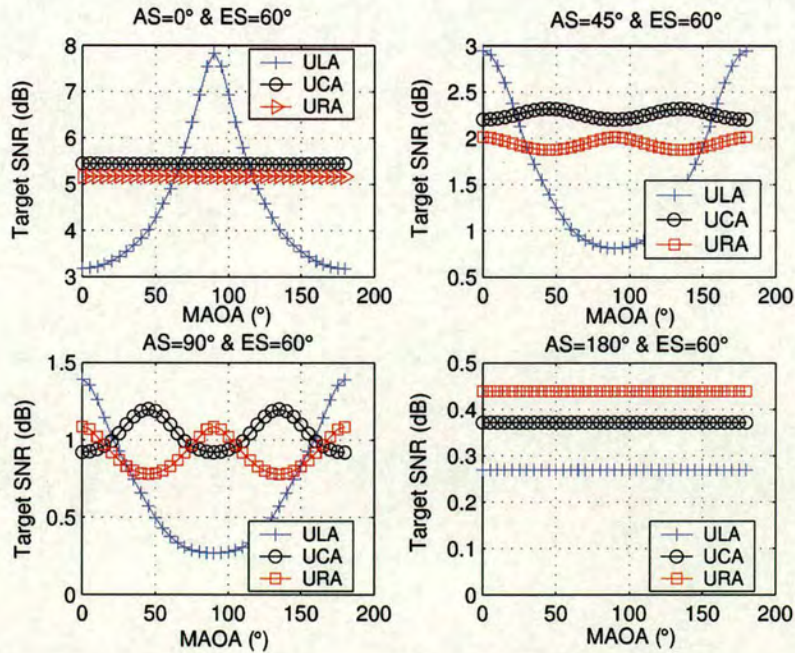


Figure 4.15: The target SNR performance with $M=4$ antennas showing the comparison between ULA, UCA and URA under different AS at varying MAOA with 60° ES and 90° MEOA. No MC is assumed.

the normalisation process allows a direct comparison of the effects of MC on the performance. For reference, the BER performance for a single antenna is plotted where there is no MC effect. As the number of antennas increases, we observe that the effects of MC become significant and the degradation in BER performance is more apparent for the case of $M=4$ antennas than the $M=2$ antennas case. As the antenna spacing increases, the BER performance shows improvement towards to the case of no MC: at spacings of 0.5λ and above, the effect of MC is seen to be insignificant. Using the MC model developed in Section 4.4, we demonstrated

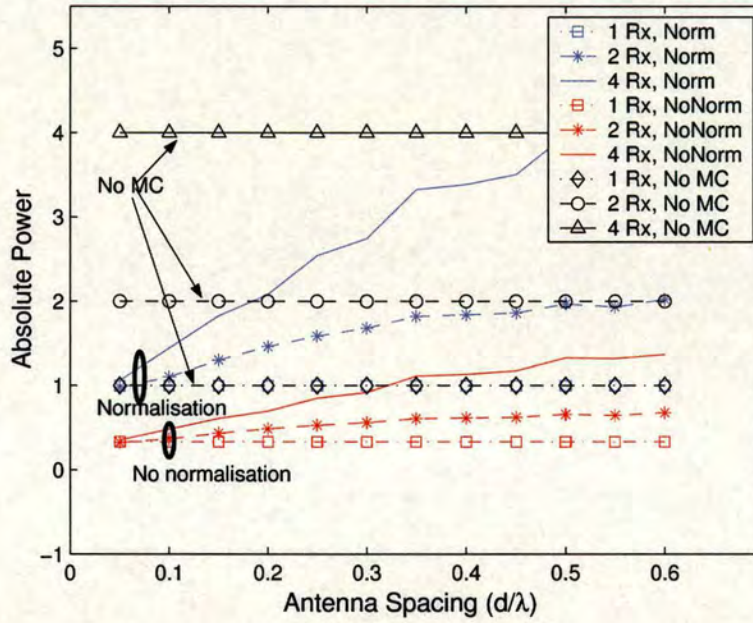


Figure 4.16: The absolute received power versus antenna spacing for no MC, MC without normalisation and MC with normalisation at 0dB SNR.

in [39] that for all types of AA under consideration, the effects of MC are apparent when the antenna separation is small ($< 0.5\lambda$). In [39], the curves of spatial correlation (between element 1 and 2) versus AS with and without MC can be clearly distinguished. As the antenna spacing increases to 0.5λ , the effect of MC decreases significantly, so that the curves with and without MC are almost overlapping. This suggests that the effect of MC can in fact decorrelate the received signal between the antenna elements due to pattern diversity which has dominant effect over spatial diversity at low antenna spacing [131]. The pattern diversity arises due to the fact of overlapping radiation patterns when the antennas are in close proximity. To gain further insight on the effect of MC, let us examine the covariance matrices with no MC, given by $\mathbf{R} = E[\mathbf{h}\mathbf{h}^H]$, and with MC, given by $\mathbf{R}' = E[\mathbf{Z}_{norm}^{-1}\mathbf{h}\mathbf{h}^H(\mathbf{Z}_{norm}^{-1})^H]$. Let us consider

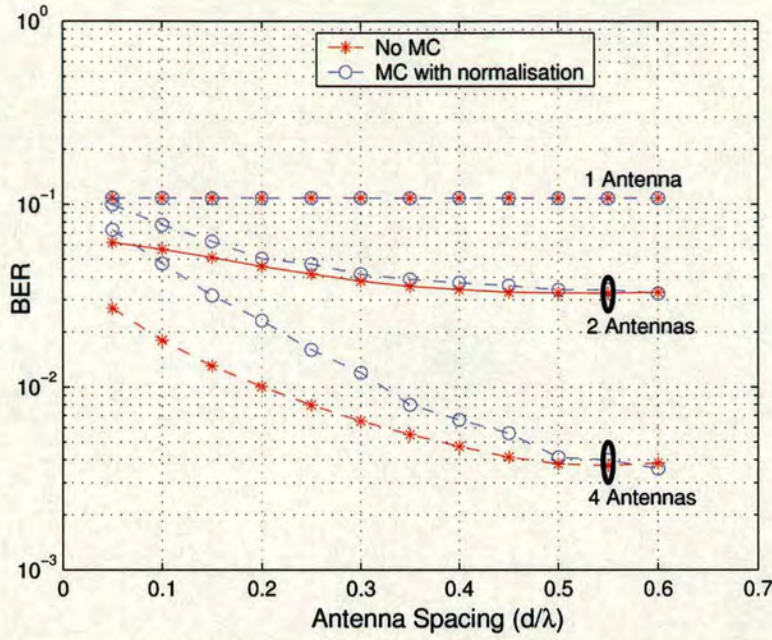


Figure 4.17: The BER versus antenna spacing for no MC and MC with normalisation at 0dB SNR.

the case with two receive antennas at 60° AS, 0° ES, 90° MEOA and 0dB SNR. Figure 4.18 and 4.19 show the distribution of the absolute value for the diagonal and off diagonal elements of the 2×2 correlation matrices over the MAOA. Note that, the diagonal terms of \mathbf{R} (and \mathbf{R}') denoted by $R(1,1)$ and $R(2,2)$ (and equivalently $R'(1,1)$ and $R'(2,2)$) indicate the received power at the antenna one and two respectively. Similarly, the off-diagonal terms of \mathbf{R} (and \mathbf{R}') signified by $R(1,2)$ and $R(2,1)$ (and equivalently $R'(1,2)$ and $R'(2,1)$) represent the cross correlation between the two received antennas. Figure 4.18 shows that in the case of no MC, the received power in the two antennas is equal regardless of the antenna spacing between the two antennas. On the other hand, when MC is taken into account, there is a power difference between the two receive antennas due to the pattern diversity. For all the spacings considered, the received power in the second antenna is almost unchanged, regardless of the MAOA. However, the first antenna experiences significant changes in power whereby at the small spacing (0.1λ), the received power decreases as the MAOA increases. On the other hand, the received power increases as the MAOA increases at higher spacing. It can also be identified that significant power reduction occurs as the antenna spacing is reduced from 1 to 0.1λ . At high spacing, even with MC taken into account, the average power of the two antennas almost converges to the case of no MC which demonstrates that the modified model behaves in a sensible fashion. It is

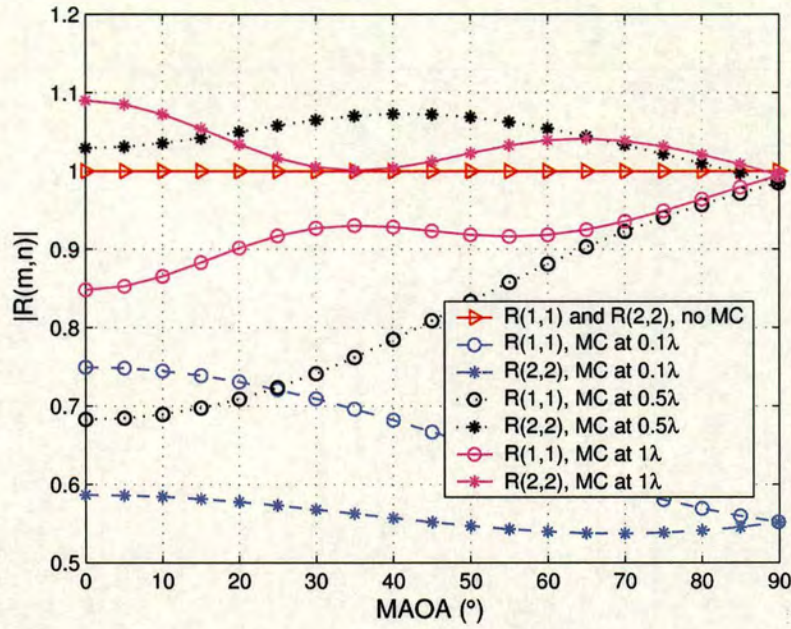


Figure 4.18: The distribution of power associated with elements $R(1,1)/R'(1,1)$ and $R(1,2)/R'(1,2)$ for a 2×2 correlation matrix.

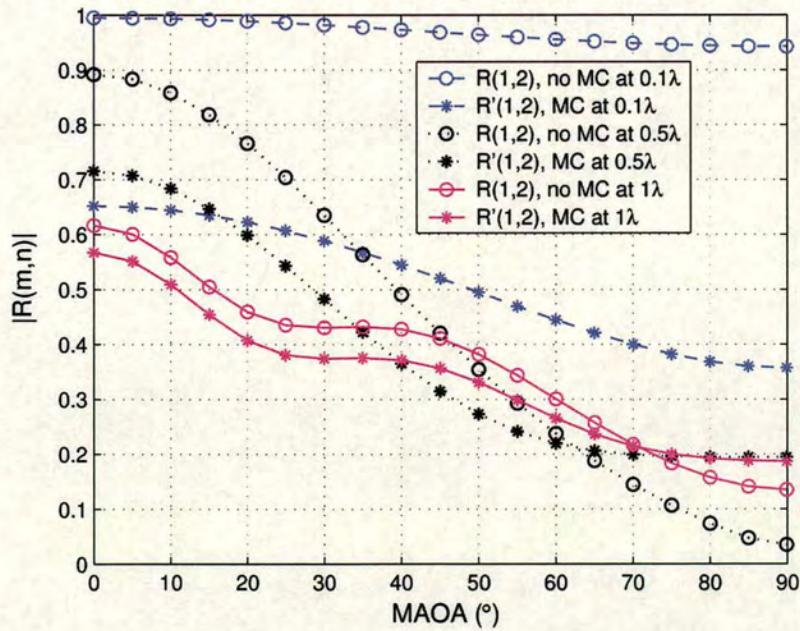


Figure 4.19: The distribution of spatial correlation associated with elements $R(1,2)/R'(1,2)$ for a 2×2 correlation matrix.

shown in Figure 4.19 that the correlation for the case of MC ($R'(1, 1)$ and $R'(2, 2)$) is always lower than the case of no MC. However, only at small spacing (0.1λ) is the correlation vastly different between the MC and no MC cases. At large spacing (1λ), the correlations for these two cases are almost identical.

Based on the observations in Figure 4.18 and 4.19, two effects due to the presence of MC can be highlighted. Firstly, MC reduces the overall received power compared to the no MC case. The reduction in power is particular apparent at small spacing but becomes less significant as the antenna spacing increases. Secondly, MC also reduces correlation between antenna elements. Again, this effect is only significant at small spacing. These two effects combined can explain the apparently conflicting claims as reported in [12–15, 132]. The lower correlation (due to the presence of MC at small spacing) in theory yields a better performance. However, this is now compensated by the reduction in the overall received power. The resultant effect is to reduce the system performance as illustrated in Figure 4.20. It can be observed that the BER performance for the MC is always worse than the corresponding no MC case. These results agree with many experimental results reported such as [133, 134]. However, the performance difference between these two cases is only significant at low antenna spacings and gradually reduces as the antenna spacing increases. It is vital to point out that the two element array with MC taken into account still outperforms the single antenna case with a significant margin though there is a performance degradation due to MC.

4.6.4 The effect of antenna spacing and number of antenna elements

At low AS, large antenna spacings are necessary to obtain diversity gain and minimise the required target SNR, as shown in Figure 4.21. It is observed that the system performance saturates as the antenna spacing goes beyond 4λ . This indicates that the application of CAA becomes difficult in scenarios where the incident power is confined to a limited angular range from two opposite directions (called the canyon effect) and without LOS to the MS [30]. For large AS (60°), an additional 2dB in SNR is needed to achieve the target BER as the antenna spacing is reduced from 0.5 to 0.1λ . Increasing antenna spacing beyond 0.5λ under large AS does not provide further improvement which indicates that the concept of CAA can be well applied in indoor environments where the AS is expected to be high [135].

Figure 4.22 shows the BER performance comparison for 2,4 and 8 antennas for the ULA and URA at 30° AS in endfire and broadside conditions. As the MAOA varies from 0° to 90° in a

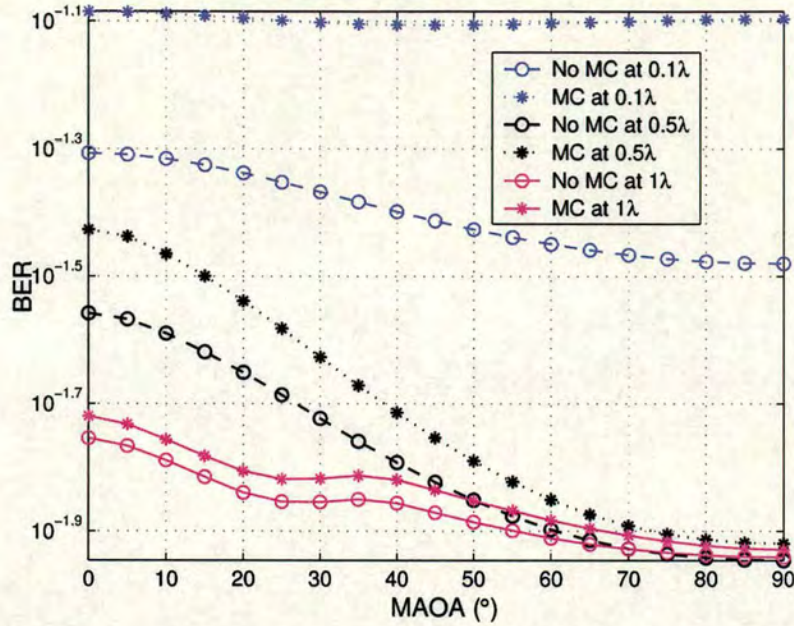


Figure 4.20: The corresponding BER performance for $M=2$ antennas versus MAOA at various antenna spacings.

4 element ULA, the system performance improves considerably. Since the URA is in general not sensitive to changes in the MAOA, there is no improvement that can be noted in the case of the URA. However, a small performance difference can be observed in the case of 8 antenna URA. This is due to the orientation of the URA which essentially consists of two 4-receiver antenna ULA located parallel to the x -axis. Hence, the performance of the URA lies between the performance of the ULA at 0° and 90° MAOA respectively. The use of large diversity order may not be justified in practice. Implementation and marketing issues such as complexity, weight, battery life and size of the MS need to be taken into account and this is beyond the scope of the investigation in this thesis. Interested readers are referred to [136] and references therein for further details.

4.7 Summary

This chapter has investigated the impact of different antenna parameters associated with the type of antenna elements, type of arrays, MC, inter-element spacing and number of antennas. This allowed the study of the trade-offs between these parameters in the development of the CAA. The parameters are modelled and incorporated into the system performance evaluation

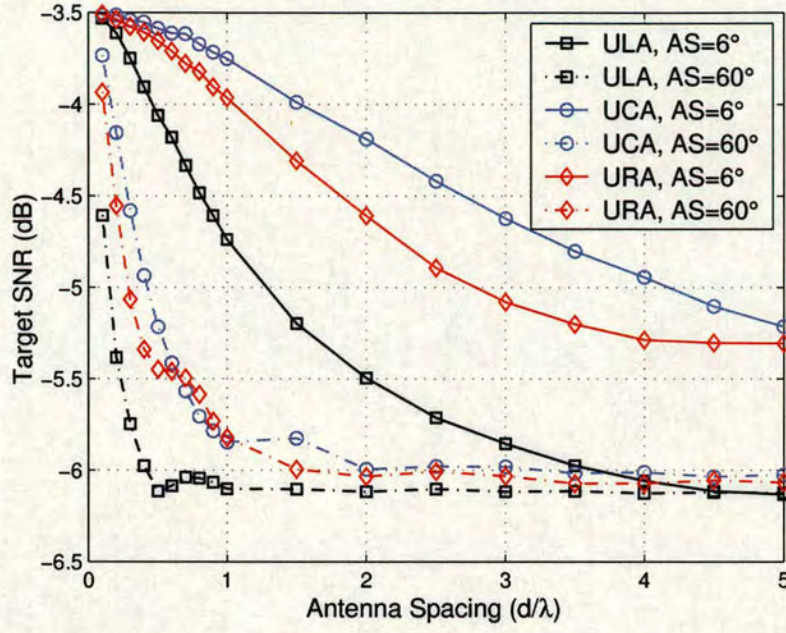


Figure 4.21: The target SNR for 0.01 BER with $M=4$ antennas versus antenna spacing for ULA, UCA and URA.

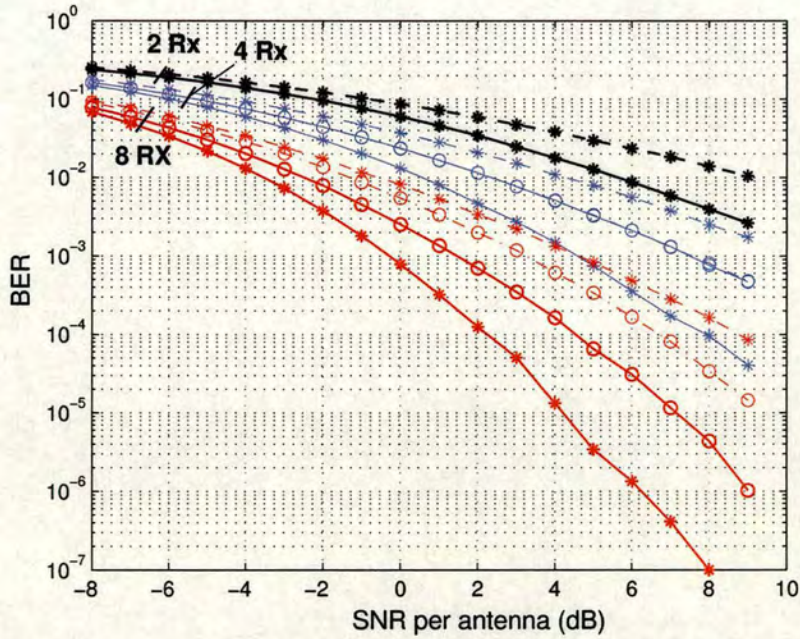


Figure 4.22: The BER performance for 2, 4 and 8 diversity branches using HD. URA (circle), ULA (asterisk), 90° MAOA (solid) and 0° MAOA (dashed).

under some specific channel conditions to demonstrate the significance of the antenna parameters. It has found that different antenna elements and arrays yield different performance which is more favourable in some cases than others. In addition, we have also showed that for all AAs under consideration, MC can decorrelate the received signal particularly at low antenna spacing. The performance gain due to the lower correlation is however compensated for by a signal cancellation effect that reduces the received power. The overall effect of MC is to reduce the system performance. The application of the CAA is shown to be practical in indoor environments but be difficult in low angle spread scenarios such as caused by the canyon effect. This in turn requires a larger antenna spacing to achieve the target BER or more antenna elements need to be crammed into the MS to give better performance. Having described the impact of antenna parameters on the system performance, in the next chapter, we study the impact of angle-of-arrival distribution.

Chapter 5

The impact of angle of arrival distribution on the performance of antenna arrays

This chapter studies the impact of the angle-of-arrival distribution on the performance of different AA architectures. The SFC of the AA under study for different statistical pdfs that are commonly encountered in the modelling of angle-of-arrival for both AOA and EOA are examined and analysed. The main objective of this chapter is to study in more detail the impact of using different AOA and EOA pdfs on the SFCs of the ULA, UCA and URA. This investigation allows us to determine the significance of the different pdfs in comparison to the angle of arrival parameters. Secondly, to study the importance of EOA with respect to AOA on the SFC of the AAs. This investigation is important as the system performance of the handset AAs are also dependent on the effect of the multipath elevation since the handset could be oriented in any direction [137]. Furthermore, measurement results have also shown that about 65% of the energy was incident with elevation larger than 10° [30]. By studying the SFCs which serve as a figure of merit in the performance analysis of AAs, they can provide a useful measure for comparing diversity systems. Our results show that the impact of using different AOA and EOA pdfs on SC is insignificant. The key parameter for system performance is the standard deviation of the underlying pdfs. This chapter is organised as follows, Section 5.1 discusses the numerous statistical distributions that are available in the literature. The impact of AOA and EOA distributions on the SFC for different AAs are discussed in Sections 5.2 and 5.3 respectively. Finally in Section 5.4, some concluding remarks will be made.

5.1 Statistical angle-of-arrival distributions

A number of statistical pdfs have been deployed to model the AOA and EOA of the MPCs that arrive at the MS. The typical pdfs that describe the AOA statistics are the uniform, Gaussian and Laplacian distribution. On other hand, the EOA is commonly modelled as a uniform or

Laplacian pdf. Most of the work reported in the literature derives a SFC for a particular angle-of-arrival distribution and AA. To date, there exists no generalised SFC function that describes the SFC between element pairs of a given AA as well as for a given distribution in both AOA and EOA domains. Despite [24] demonstrated mathematically that the impact of AOA pdfs on the ULA is insignificant and what matters is the AS, it is not clear whether this result can be equally applied to EOA domain as well as other AA topologies. Hence, to allow a flexible analysis on the study of the impact of angle-of-arrival distribution for the various AAs, we instead determine the SFC through computer simulations.

It is worth pointing out some important properties relating to the different pdfs for both AOA and EOA in the spherical coordinates system. The MAOA, φ_0 and MEOA, θ_0 are measured from the positive x - and z -axis respectively as depicted in Figure 5.2. Numerous definitions of the AS and ES are available in the literature such as [15, 18, 19, 32, 66]. In this thesis, unless otherwise specified, the definition of the AS and ES follows that of Salz and Winters in [18] and is depicted in Figure 5.2. It must be emphasised that the actual definitions of the AS and ES are not of primary concern provided that they are used consistently in the thesis. This means that, we will obtain the same results whether we use of the definition of Salz and Winters or those [15, 19, 32, 66] provided that the definitions of the AS and ES are adjusted accordingly.

A uniform AOA distribution¹ is expressed as

$$p(\varphi)_u = \begin{cases} \frac{1}{2\Delta} & ; -\Delta_\varphi + \varphi_0 \leq \varphi \leq \Delta_\varphi + \varphi_0 \\ 0 & ; \text{otherwise} \end{cases} \quad (5.1)$$

where $2\Delta_\varphi$ is the maximum deviation of the AS from the MAOA, φ_0 . A truncated Gaussian AOA distribution is given by

$$p(\varphi)_g = \frac{\kappa_g}{\sqrt{2\pi}\sigma_g} e^{-\frac{(\varphi-\varphi_0)^2}{2\sigma_g^2}}, (-\pi + \varphi_0 \leq \varphi \leq \pi + \varphi_0) \quad (5.2)$$

where the scalars σ_g and κ_g signify the standard deviations of the Gaussian distribution and normalisation constant to make (5.2) a pdf. Similarly, the Laplacian AOA distribution is given by

$$p(\varphi)_l = \frac{\kappa_l}{\sqrt{2}\sigma_l} e^{-\frac{\sqrt{2}|\varphi-\varphi_0|}{\sigma_l}}, (-\pi + \varphi_0 \leq \varphi \leq \pi + \varphi_0) \quad (5.3)$$

¹Equivalently the following definition is also applicable for the EOA except that the angle range for the EOA is limited to $0 \leq \theta < 180^\circ$.

where σ_l and κ_l are the standard deviations and normalisation constants to make (5.3) a pdf. The corresponding statistical distributions for the three cases are illustrated in Figure 5.1 where

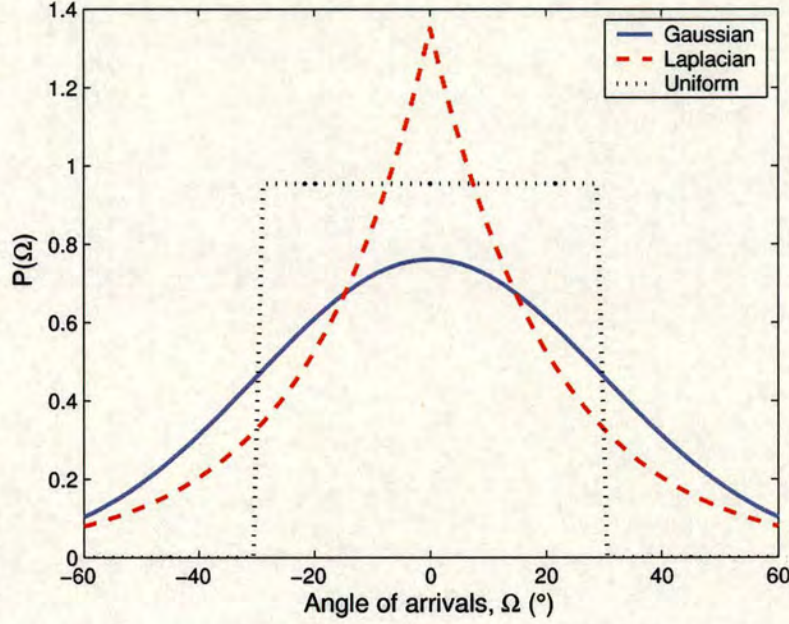


Figure 5.1: *The statistical distribution for the uniform, Gaussian and Laplacian angle-of-arrival.*

the shape for each case can be clearly identified. To allow a consistent comparison, the AS is assumed for the moment to be the standard deviation of the underlying pdfs. For the uniform distribution the standard deviation is given by $\frac{\Delta_\varphi}{\sqrt{3}}$. Unless otherwise specified, the SFC is computed between antenna elements 1 and 2, $\rho_{(1,2)}$ for the cases of the ULA and UCA, while $(1,1)$ and $(2,2)$, $\rho_{(1,1,2,2)}^2$ for the case of the URA is used.

5.2 The impact of azimuth-of-arrival distribution

In order to study the impact of AOA distributions, simulations are performed for the ULA, UCA and URA with 0° ES. Two specific MAOAs (90° and 0°) are considered for varying AS values as shown in Figure 5.3 and 5.4. By studying both figures, we observe that for a given AS, the SFCs for the three AOA pdfs have a similar pattern (i.e. when one increases/decreases the others follow suit). Furthermore, as the AS increases, the SFC decreases very rapidly

²The notation (n_1, p_1, n_2, p_2) represents the elements at cartesian coordinates (n_1, p_1) and (n_2, p_2) .

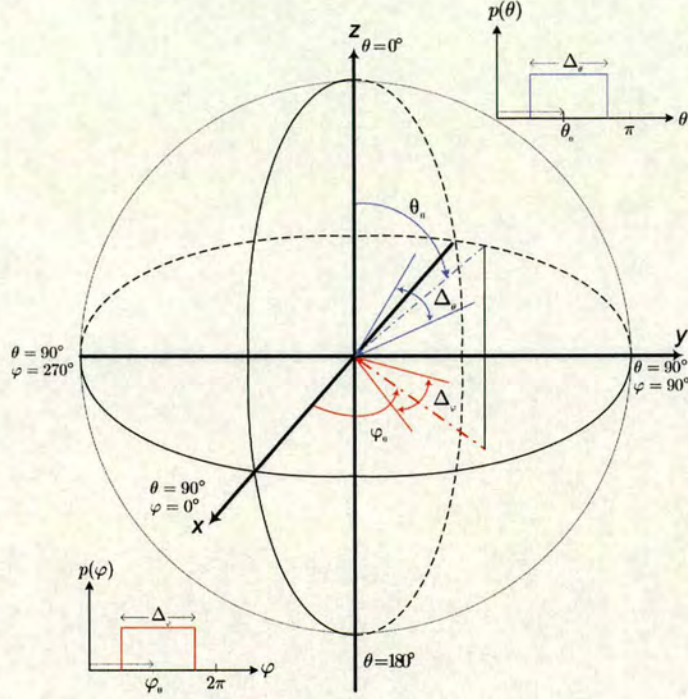
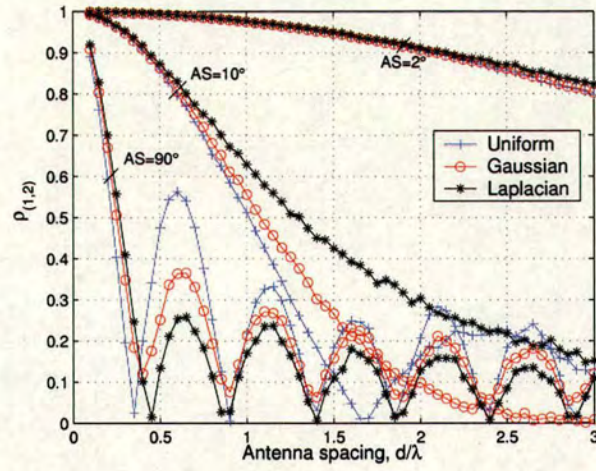


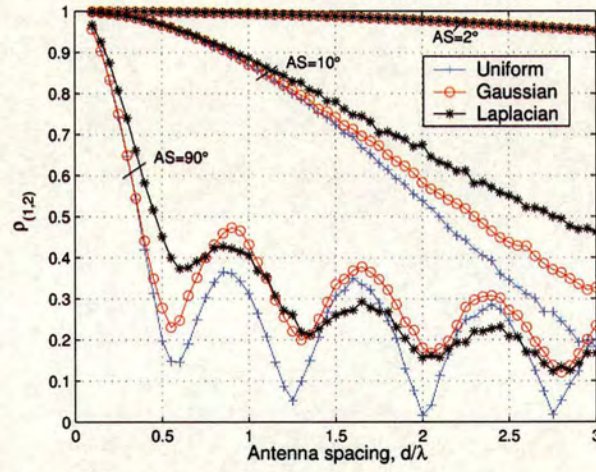
Figure 5.2: The MAOA, AS, MEOA and ES in spherical coordinates with uniform distributions in AOA and EOA.

from 2° to 10° to 90° respectively. This suggests that the important parameter of the SFC as a function of antenna spacing is the standard deviation of the pdf and not the type of pdf under consideration. Although, the impact of different pdfs on the SFC can be regarded as small, it is observed that the uniform and Laplacian pdfs have the lowest and highest SFCs respectively while the Gaussian case is the intermediate one. The uniform pdf has more paths located further away from the MAOA than the case of Laplacian and Gaussian pdfs where most of the paths are incident close to the MAOA. Thus, the small SFC difference between Gaussian and Laplacian can be justified from their symmetry properties and similar general shape. The main discrepancy between them is the much heavier tail and higher density at the peak of the Laplacian as compared to the Gaussian pdf [138]. The above observation can be understood by analogy to Doppler spread. The standard deviation of the Doppler determines the level crossing rate and average fade duration of the fading signal, though different AOA pdf will result in different Doppler power spectra for the fading signal [70].

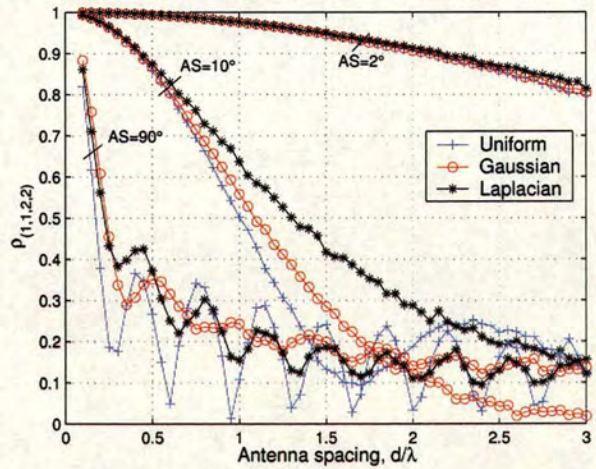
Changing the MAOA from 90° to 0° increases the SFC for the ULA significantly for a given AS. Since the MAOA is now in the endfire condition, the SFC is expected to be very high (≈ 1)



(a) ULA

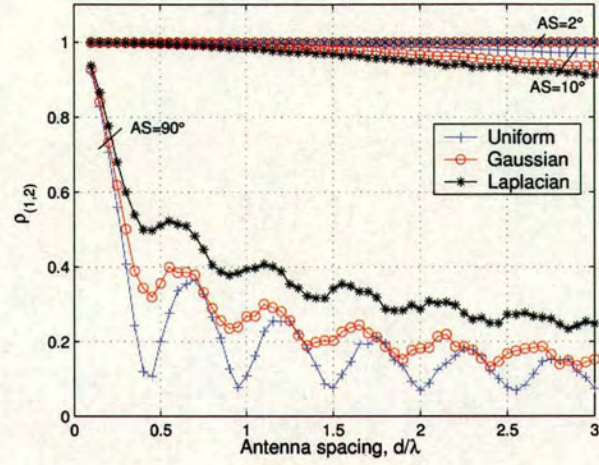


(b) UCA

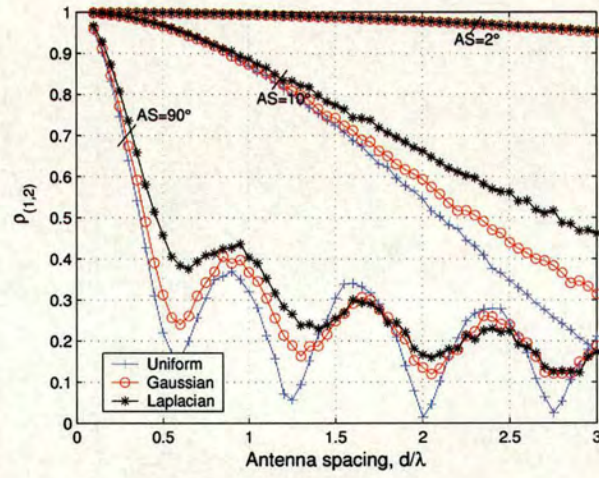


(c) URA

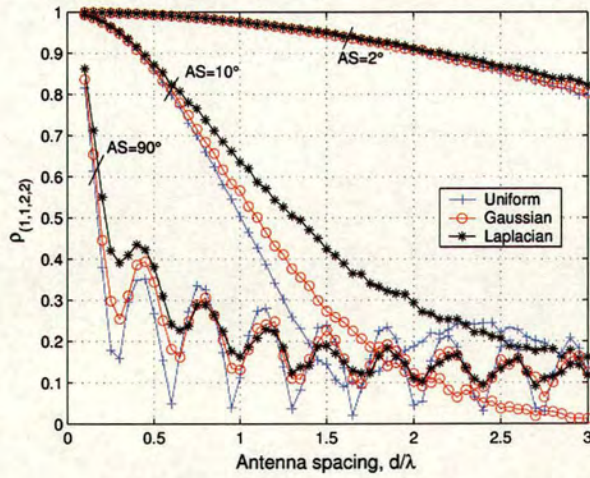
Figure 5.3: The SFC comparison for the ULA, UCA and URA at 90° MAOA, 0° ES and 90° MEOA for different AS values.



(a) ULA



(b) UCA



(c) URA

Figure 5.4: The SFC comparison for the ULA, UCA and URA at 0° MAOA, 0° ES and 90° MEOA for different AS values.

particularly for a small AS values and will only gradually increase as the AS increases. On the other hand, the SFC for UCA and URA remains approximately unchanged. This is due to the orientation of the array for which the element pairs of interest “see” the same MAOAs. Despite changing the AOA parameters, the SFCs for the three AOA distributions show close resemblance at least in considering the diversity performance [139]. There is no significant difference when one considers the correlation value between for example 0.5 and 0.7 in a diversity system though in practice lower correlation value is preferable.

5.3 The impact of elevation-of-arrival distribution

In this section, we extend our analysis to the case of EOA [41] which has not received much attention in the literature. For the case of EOA, similar analyses are performed to investigate the impact of using different EOA pdfs on SFC. Figure 5.5 shows the SFC of different arrays under three EOA pdfs at 0° MAOA. Under this specific condition, the impact of the EOA and AOA on the SFC can be compared by observing Figure 5.4 and 5.5 where the AS and ES are the only changing variables. Our analysis demonstrates that in general, angle spread in azimuth leads to a lower SFC than the equivalent spread in elevation. In addition, the reduction in SFC due to increasing ES seems to be less rapid than that for the AS. If the MAOA is changed to 90° , similar observations are expected for the case of the UCA and URA. Nevertheless, the SFC of the ULA will be at value one. For the same reasoning as in the azimuth domain, uniform and Laplacian pdfs in EOA have the lowest and highest correlation in all cases. Again the SFC and hence performance of the AAs is dependent on the ES and not the type of EOA pdf under consideration. However, it can be observed that, the difference in SFC between the three pdfs are more noticeable in the case of EOA than AOA. This is owe to the fact that the pattern gain at 0° or 180° EOAs is zero as shown in Appendix C.

5.4 Summary

This chapter has investigated the impact of both the AOA and EOA on the SFC of different AA architectures. As shown in the analysis, the impact of using different AOA and EOA pdfs on SFC is insignificant for all the arrays considered. On the other hand, the key parameter to the system performance is the standard deviation of the underlying pdfs. Therefore, in the remainder of the thesis, we restrict our attention to uniform distributions. Our results also

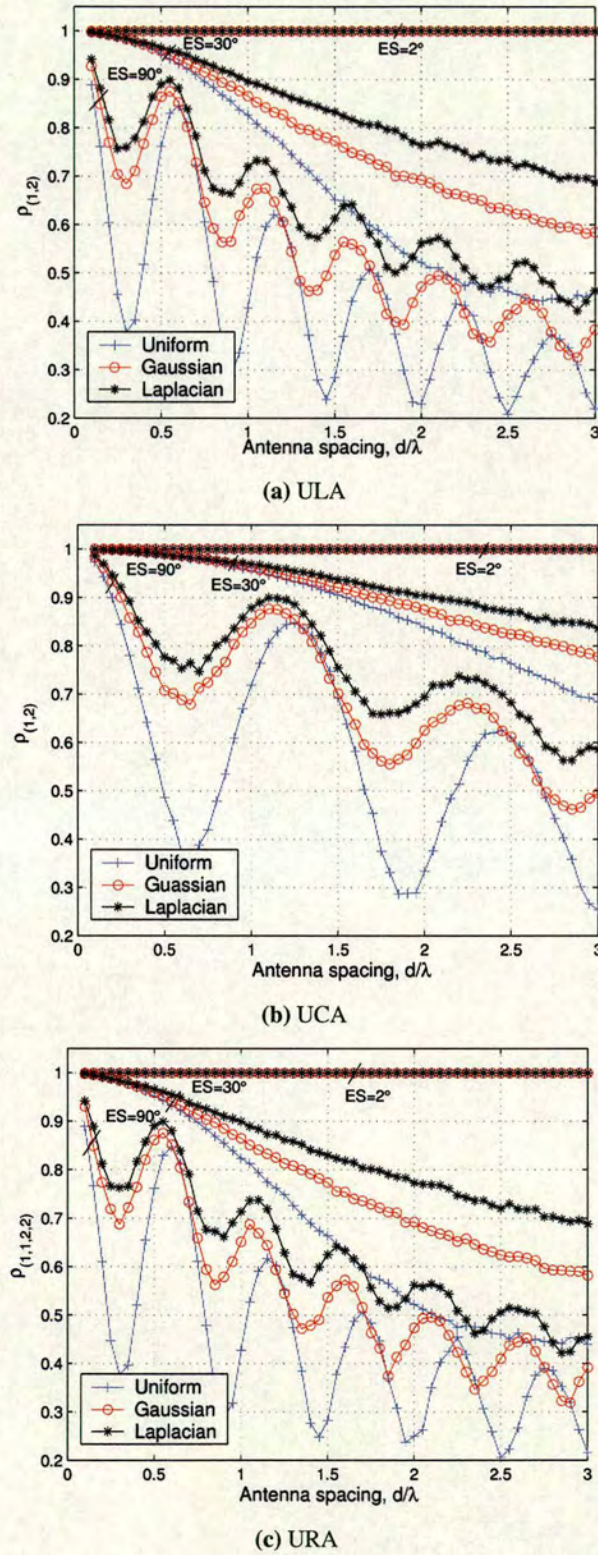


Figure 5.5: The SFC comparison for the ULA, UCA and URA at 0° MAOA, 0° AS and 90° MEAO for different AS values.

demonstrate that the effect of AS on SFC is more significant than that of ES. In the next chapter, 3-D SFC models for the CAAs under consideration are developed using a uniform distribution to facilitate the performance analysis.

Chapter 6

3-Dimensional spatial fading correlation models

In this chapter, closed-form expressions for the SFC functions of AAs in a 3-D multipath channel are derived. The SFCs are expressed in terms of the AOA and EOA as well as the geometry of the AA under consideration. Verification is achieved by means of computer simulation where excellent agreement is shown between the theoretical and simulation results. The developed SFCs can be used to investigate the importance and dependency of the angular parameters associated with MAOA, AS, MEOA and ES on the system performance. Our analysis shows that in general, the system performance is more AS dependent than ES while the impact of MAOA and MEOA is array dependent. However, it must be emphasized that in evaluating the performance of AAs, both azimuth and elevation angle must be taken into consideration. Furthermore, the SFCs can also be used to determine the correlation matrix at both the transmitter and receiver for capacity evaluation in MIMO systems. Finally, our investigation also shows the feasibility of deploying EVS and EVS arrays as a MIMO receiver.

The aims of this chapter are three fold. Firstly, to develop SFC models for various CAAs which can be applied to determine the correlation matrix at both the transmitter and receiver in MIMO systems for capacity evaluation. Secondly, to study in detail the importance and dependency of the angular parameters parameterised by the MAOA, AS, MEOA and ES to the SFC. By evaluating the performance patterns as a function of two of the parameters, the sensitivity of the system performance to these parameters can be determined. Thirdly, to compare the capacity performance of different CAAs under the same channel conditions. This is crucial in selecting types of compact receivers used in different applications and radio environments. The rest of the chapter is organised as follows: Section 6.1 gives a quick overview of the importance and development of the SFC for AAs; Section 6.2 derives the closed-form expression for the SFC functions in terms of AOA, EOA, antenna spacing and antenna geometry; Section 6.3 presents some analytical results to verify the developed close-formed expressions; Section 6.4 analyses the sensitivity of the AAs through the performance patterns; Section 6.5 deduces some

important implications from the performance patterns; Section 6.6 performs capacity analysis for MIMO systems employing the AAs under investigation; Section 6.7 concludes this chapter.

6.1 Introduction

AAs are one of the most promising candidates for capacity and signal quality enhancement in wireless communications systems. Since the functionality of the AA is mainly based on the exploitation of the spatial properties of the multipath channel, it is a pre-requisite to have a better knowledge on how the angular parameters influence the performance of AA. Recall from Chapter 1 that many prior works expressed the SFC functions for different AAs in various AOA pdfs. In this chapter, we consider the impact of both the AOA and the EOA on the SFC, as many measurement results have demonstrated the practical significance of EOA in addition to AOA to the performance of AAs (see Chapter 1). Employing multiple antennas at the MS for MIMO techniques introduces a number of difficulties as described Chapter 1. Therefore, several candidate CAA configurations are considered in this thesis. In this regard, the EVS emerges as a promising alternative to the ULA, UCA and URA. Due to the compact structure of the EVS, it is possible to arrange multiple EVS in an array configuration so that higher performance can be achieved. Hence, it is imperative to study the SFC between the elements of the CAA as the capacity of a MIMO channel and diversity gain are very dependent on the fading correlation between antenna elements [110, 139]. In addition, the results obtained in this chapter can be used to derive the theoretical probability of error P_e performance of the CAA as shown in [42]. In the next section, the mathematical framework toward the closed-form SFC expressions is established.

6.2 Closed-form spatial fading correlation models

6.2.1 ULA, UCA and URA

For the ULA, UCA and URA¹, the SFC between antennas at positions n and m is defined as

$$\begin{aligned}\rho_{(m,n)} &= \frac{E\{(h_m - \bar{h}_m)(h_n - \bar{h}_n)^*\}}{\sqrt{E\{(h_m - \bar{h}_m)^2\}E\{(h_n - \bar{h}_n)^2\}}} \\ &= \frac{\int_{\theta} \int_{\varphi} a_n(\varphi, \theta) a_m^*(\varphi, \theta) p(\varphi, \theta) \sin(\theta) d\theta d\varphi}{\sqrt{\int_{\varphi} \int_{\theta} |a_n(\varphi, \theta)|^2 \sin(\theta) p(\varphi, \theta) d\theta d\varphi \int_{\varphi} \int_{\theta} |a_m(\varphi, \theta)|^2 \sin(\theta) p(\varphi, \theta) d\theta d\varphi}} \quad (6.1)\end{aligned}$$

where $a_n(\varphi, \theta)$ is the n^{th} entry of $\mathbf{a}(\varphi, \theta)$. The term $\sin(\theta)$ appears in (6.1) because the integral is carried out in spherical coordinates. The scalar $p(\varphi, \theta)$ is the joint pdf of the angles-of-arrival of the MPC. We assume that the AOA and EOA are independent of each other, thus the function $p(\varphi, \theta)$ can be decomposed to $p(\varphi)p(\theta)$ [11, 74]. We concentrate our analysis on uniform AOA and EOA distributions since Chapter 5 showed that the key parameter for the system performance is the standard deviation of the angle spread of the MPC and not the type of pdf under investigation. As described in Chapter 5 and [18], the AOAs of the MPCs are uniformly distributed over the range of angles $[\varphi_0 - \Delta_{\varphi}, \varphi_0 + \Delta_{\varphi}]$ where Δ_{φ} and φ_0 are the AS and MAOA (see Figure 5.2). Similarly, the EOAs of the MPCs are uniformly distributed over $[\theta_0 - \Delta_{\theta}, \theta_0 + \Delta_{\theta}]$ where Δ_{θ} and θ_0 are the ES and MEOA respectively (see Figure 5.2). As shown in the Appendix D, the real and imaginary parts of the $\rho_{(m,n)}$ for the cases of the ULA, UCA and URA can be expressed:

$$\begin{aligned}\Re[\rho_{(Z(m,n))}] &= \frac{1}{\text{sinc}(\Delta_{\theta}) \sin(\theta_0)} \left\{ \sum_{k=0}^{\infty} \sum_{l=0}^k \frac{(-1)^{2k+1+l} Z^{2k}}{2^{4k} (k!)^2} \binom{2k+1}{l} \text{sinc}[(2k+1-2l)\Delta_{\theta}] \times \right. \\ &\quad \sin[(2k+1-2l)\theta_0] + 2 \sum_{k=1}^{\infty} \sum_{l=0}^{\infty} \sum_{p=0}^{k+l} \frac{(-1)^{k(A+1)+2l+p+1}}{l! \Gamma(2k+l+1)} \times \\ &\quad \text{sinc}(2k\Delta_{\varphi}) \cos(2kB) \left(\frac{Z^{2(k+l)}}{2^{4(k+l)}} \right) \binom{2(k+l)+1}{p} \times \\ &\quad \left. \text{sinc}\{[2(k+l-p)+1]\Delta_{\theta}\} \sin\{[2(k+l-p)+1]\theta_0\} \right\} \quad (6.2)\end{aligned}$$

¹For the URA, the SFC is denoted by $\rho_{(Z(m,p,n,q))}$ where (m,p) and (n,q) are the coordinates of the elements as depicted in Figure 4.5.

$$\begin{aligned}
 \Im[\rho_{(Z(m,n))}] = & \frac{2}{\text{sinc}(\Delta_\theta) \sin(\theta_0)} \sum_{k=0}^{\infty} \sum_{l=0}^{\infty} \frac{(-1)^{Ak+l}}{l! \Gamma(2k+l+2)} \left(\frac{Z}{2}\right)^{2(k+l)+1} \text{sinc}[(2k+1)\Delta_\varphi] \times \\
 & \cos^D[(2k+1)\varphi_0] \sin^E[(2k+1)\alpha] \left\{ \frac{1}{2^{2(k+l+1)}} \binom{2(k+l+1)}{k+l+1} + \right. \\
 & \sum_{p=0}^{k+l} \frac{(-1)^{k+l+1+p}}{2^{2(k+l)+1}} \binom{2(k+l+1)}{p} \\
 & \left. \text{sinc}[2(k+l+1-p)\Delta_\theta] \cos[2(k+l+1-p)\theta_0] \right\}
 \end{aligned} \tag{6.3}$$

where $\Gamma(x)$ is the gamma function, $\text{sinc}(x) = \sin(x)/x$ and variables A, B, D, E and Z take different values according to whether the array geometry is the ULA, UCA or URA. For the ULA, $A = 1, B = \varphi_0, D = 1, E = 0$ and $Z = k_w d(m - n)$. For the UCA and URA, $A = 0, B = \alpha, D = 0$ and $E = 1$. As defined in Appendix D.2, for the case of the UCA, $Z = \sqrt{Z_1^2 + Z_2^2}$ with $Z_1 = k_w r[\cos \psi_m - \cos \psi_n]$ and $Z_2 = k_w r[\sin \psi_m - \sin \psi_n]$. Similarly as defined in Appendix D.3, for the case of the URA, $Z = \sqrt{Z_x^2 + Z_y^2}$ with $Z_x = k_w(n - m)d_x$ and $Z_y = k_w(p - q)d_y$ [43]. For all the AAs considered, summation over 50 terms for k and l is sufficient to achieve accuracy up to 6 decimal places when comparing the closed-form expressions with numerical integration of (6.1).

6.2.2 EVS

In order to include the polarization domain, (6.1) is modified to become

$$\begin{aligned}
 \rho_{(p,q)} = & \frac{\int_{\varphi} \int_{\theta} \int_{\gamma} \int_{\eta} a_p(\Theta) a_q^*(\Theta) p(\Theta) \sin(\theta) d\varphi d\theta d\gamma d\eta}{\sqrt{\int_{\varphi} \int_{\theta} \int_{\gamma} \int_{\eta} |a_p(\Theta)|^2 p(\Theta) \sin(\theta) d\varphi d\theta d\gamma d\eta}} \times \\
 & \frac{1}{\sqrt{\int_{\varphi} \int_{\theta} \int_{\gamma} \int_{\eta} |a_q(\Theta)|^2 p(\Theta) \sin(\theta) d\varphi d\theta d\gamma d\eta}}
 \end{aligned} \tag{6.4}$$

By making the assumptions of random polarisation mixing i.e. $p(\gamma)$ and $p(\eta)$ are uniformly distributed over the range $[0, \pi/2]$ and $[-\pi, \pi]$ respectively, it can shown in Appendix E and [44, 45] that the SFC between the components (p, q) of the EVS can be expressed in closed-form as

$$\rho_{(p,q)} = \frac{\mathbf{M}_1(p, q) + \mathbf{M}_2(p, q)}{\sqrt{\Phi_p \Phi_q}} \tag{6.5}$$

where $\mathbf{M}_1(p, q)$, $\mathbf{M}_2(p, q)$, Φ_p and Φ_q are the result of the integration of the terms $\Psi_{1,p}\Psi_{1,q}$, $\Psi_{2,p}\Psi_{2,q}$, $\Psi_{1,p}^2 + \Psi_{2,p}^2$ and $\Psi_{1,q}^2 + \Psi_{2,q}^2$ over spherical coordinates, respectively. The scalars $\Psi_{1,q}$ and $\Psi_{2,q}$ are the q^{th} entry of the first and second columns of 6×2 matrix $\Psi(\theta, \varphi)$ in (4.12). The closed-form expression of 6×6 matrices \mathbf{M}_1 , \mathbf{M}_2 and 6×1 vector Φ are given in Appendix E. Equation (6.5) can be generalised to take different XPD value into account. This can be achieved by appropriately scaling the matrices \mathbf{M}_1 and \mathbf{M}_2 to represent the power difference between the vertical and horizontal polarisations. For a given XPD value, the scaling factors can be computed by first determining the range of the integration for the variable γ .

6.2.3 Arrays of EVS

For EVS in array configurations, it can be shown in Appendix F that the SFC between component p of the m^{th} EVS and component q of the n^{th} EVS is given by

$$\rho(Z(m, n, p, q)) = \frac{\Upsilon(Z(m, n, p, q))}{\sqrt{N(Z(m, n, p, q))}} \quad (6.6)$$

where $\Upsilon(Z(m, n, p, q))$ is given by (6.7) and (6.8) for the cases of ULA and UCA/URA² respectively.

$$\begin{aligned} \Upsilon(Z(m, n, p, q)) = & G_2 \left\{ \sum_{k=0}^{\infty} \frac{(-1)^k}{(k!)^2} \left(\frac{Z}{2} \right)^{2k} \left(R_{a_1 a_2 00} S_{b_1 b_2 b_3 00} + R_{c_1 c_2 00} S_{d_1 d_2 d_3 00} \right) + \right. \\ & \sum_{k=0}^{\infty} \sum_{l=1}^{\infty} \frac{(-1)^{k+l}}{l! \Gamma(2k+l+1)} \left(\frac{Z}{2} \right)^{2(k+l)} \left(R_{a_1 a_2 a_3 0} S_{b_1 b_2 0 b_4 0} + R_{c_1 c_2 c_3 0} S_{d_1 d_2 0 d_4 0} \right) \\ & + j2 \sum_{k=0}^{\infty} \sum_{l=0}^{\infty} \frac{(-1)^{k+l}}{l! \Gamma(2k+l+2)} \left(\frac{Z}{2} \right)^{2(k+l)+1} \times \\ & \left. \left(R_{a_1 a_2 0 a_4} S_{b_1 b_2 0 0 b_5} + R_{c_1 c_2 0 c_4} S_{d_1 d_2 0 0 d_5} \right) \right\} \end{aligned} \quad (6.7)$$

²Note for the EVS in URA configuration, the SFC is denoted as by $\Upsilon(Z(m, r, n, s, p, q))$ where (m, r) and (n, s) are the coordinates of the EVS elements while (p, q) signify the relevant components of the EVS.

$$\begin{aligned}
 \Upsilon_{(Z(m,n,p,q))} = G_2 & \left\{ \sum_{k=0}^{\infty} \frac{(-1)^k}{(k!)^2} \left(\frac{Z}{2} \right)^{2k} \left(U_{a_1 a_2 00} S_{b_1 b_2 b_3 00} + U_{c_1 c_2 00} S_{d_1 d_2 d_3 00} \right) + \right. \\
 & 2 \sum_{k=0}^{\infty} \sum_{l=1}^{\infty} \frac{(-1)^l}{l! \Gamma(2k+l+1)} \left(\frac{Z}{2} \right)^{2(k+l)} \left(U_{a_1 a_2 a_3 0} S_{b_1 b_2 0 b_4 0} + U_{c_1 c_2 c_3 0} S_{d_1 d_2 0 d_4 0} \right) \\
 & + j 2 \sum_{k=0}^{\infty} \sum_{l=0}^{\infty} \frac{(-1)^l}{l! \Gamma(2k+l+2)} \left(\frac{Z}{2} \right)^{2(k+l)+1} \times \\
 & \left. \left(U_{a_1 a_2 0 a_4} S_{b_1 b_2 0 b_5} + U_{c_1 c_2 0 c_4} S_{d_1 d_2 0 d_5} \right) \right\} \quad (6.8)
 \end{aligned}$$

The functions R_{tuvvw} , S_{tuvwx} and U_{tuvw} are the results of integration of (6.9) to (6.11) respectively as shown in Appendix F:

$$R_{tuvvw} = \int_{\varphi_0 - \Delta_\varphi}^{\varphi_0 + \Delta_\varphi} \cos^t(\varphi) \sin^u(\varphi) \cos^v(2k\varphi) \cos^w[(2k+1)\varphi] d\varphi \quad (6.9)$$

$$S_{tuvwx} = \int_{\theta_0 - \Delta_\theta}^{\theta_0 + \Delta_\theta} \cos^t(\theta) \sin^u(\theta) \sin^{v(2k+1)}(\theta) \sin^{w[2(k+l)+1]}(\theta) \sin^{x[2(k+l+1)]}(\theta) d\theta \quad (6.10)$$

$$U_{tuvw} = \int_{\varphi_0 - \Delta_\varphi}^{\varphi_0 + \Delta_\varphi} \cos^t(\varphi) \sin^u(\varphi) \cos^v[(2k(\varphi + \xi))] \sin^w[(2k+1)(\varphi + \xi)] d\varphi \quad (6.11)$$

It is straightforward to show that the denominator, $N_{(m,n,p,q)}$ reduces to the denominator of (6.5).

6.3 Analytical results

In this section, some analytical results for each of the AAs are presented and compared with simulation results to verify the developed closed-form SFC expressions. Due to many different possible combinations, only a single result is presented here for each AA and thus it does not represent the overall AA response. This constraint is relaxed in Section 6.4 and 6.6 to allow the performance of AAs to be assessed more thoroughly. For all cases, simulations are performed over 3 million channel realisations to compute the correlation values. The results obtained show excellent agreement with the theoretical results and thus validate the derived expressions. Figure 6.1 to Figure 6.3 show the SFC between element (1,2) for the case of ULA and UCA, element (1,1,2,2) for the URA and its corresponding EVS array. Thereafter, we refer the corresponding EVS array as an array of EVS in ULA, UCA and URA configurations

(denoted by ULA-EVS, UCA-EVS and URA-EVS) with reference to the ULA, UCA and URA respectively.

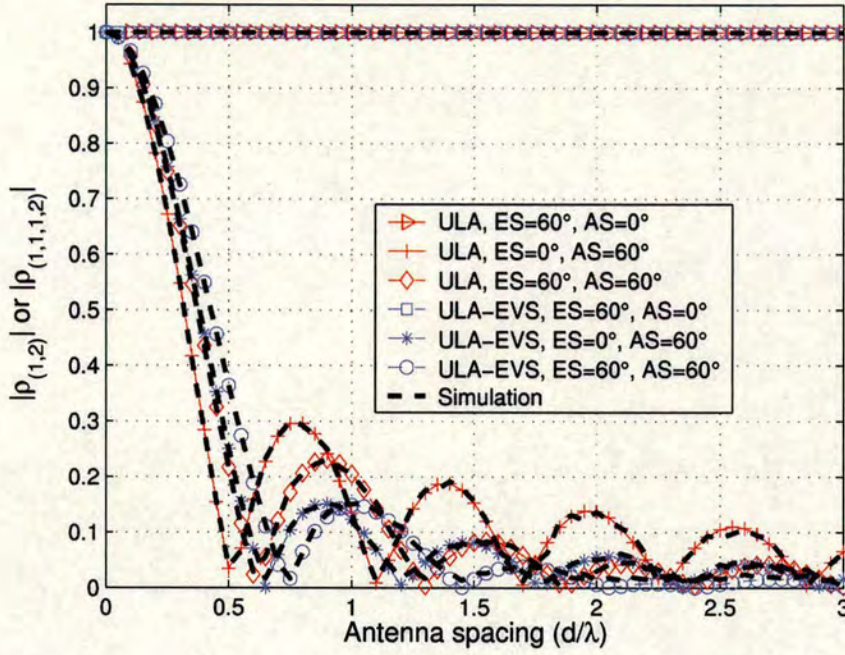


Figure 6.1: SFC at various AS and ES values with 90° MEOA and MAOA for the ULA and ULA-EVS.

For all cases, the SFC decreases as the antenna spacing or the AS increases. Similarly, the SFC also decreases as the ES increases except for the case of ULA configuration where the effect of ES is negligible. However, it is noted that this is only true for this specific 90° MAOA (broadside condition). In this case, each element of the array experiences the same relative phase since the paths contributing to the received signal at the array arrive perpendicular to the array direction. For other MAOAs, the impact of ES must be taken into consideration. It can also be observed that, there are zero crossing points in the case of the ULA configurations where the first zero occurs approximately at $d/\lambda \approx 30/AS$ [18]. The effect of increasing ES in this case tends to move the zero crossing point to antenna spacings higher than 0.5λ . When the MAOA deviates from 90°, the zero crossing points disappear and higher spacing is required to achieve the same correlation value as for the case of 90° MAOA. In contrast, the SFC of the case of UCA and URA do not have zero crossing points for any values of the angle of arrival. Furthermore, the SFC of the EVS array has a very similar shape to that of the corresponding isotropic array except that the oscillations in the SFC decay more rapidly as the antenna spacing increases.

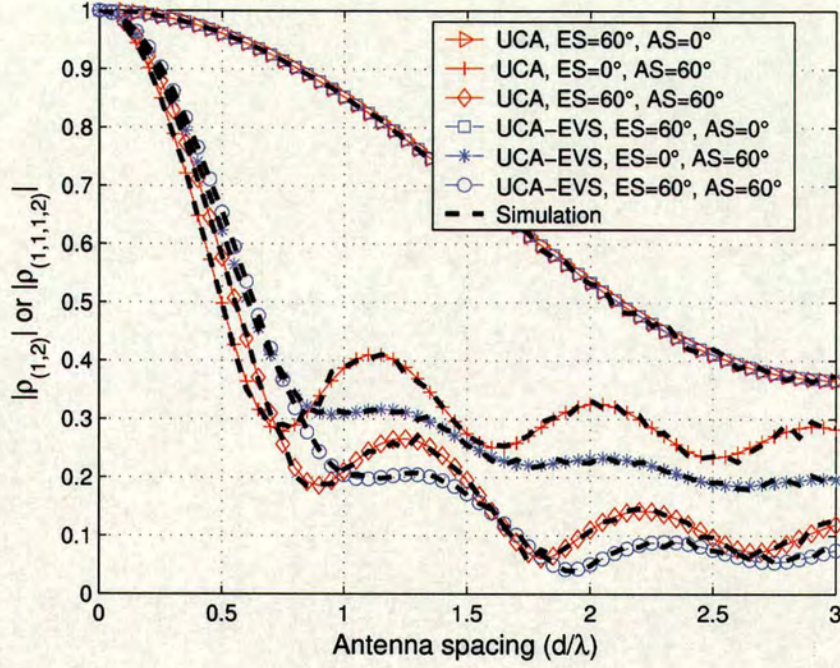


Figure 6.2: SFC at various AS and ES values with 90° MEOA and MAOA for the UCA and UCA-EVS.

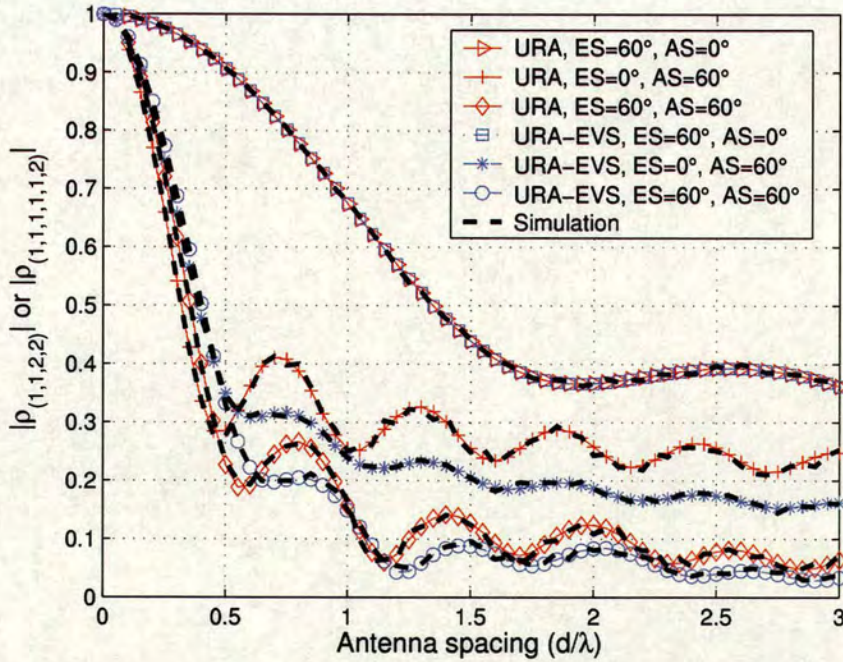


Figure 6.3: SFC at various AS and ES values with 90° MEOA and MAOA for the URA and URA-EVS.

The SFC for the case of the single EVS has been presented in [44, 45]. The SFC corresponds to different components of EVS under varying AS and ES values are shown in Figure 6.4 and 6.5. As expected, when the AS and ES increase, the SFC decreases. Recall from Chapter 4 (Section 4.3.4) that the EVS consists of three electrically identical short dipoles and three magnetically identical small loops which are co-located and orthogonally oriented. The response from each dipole is proportional to the electric field component along the direction of the dipole. Similarly, the response from each small loop is proportional to the magnetic field which is parallel to the normal of the loop. Furthermore, for transverse plane waves in space, the electrical and magnetic components are perpendicular to each other and orthogonal to the direction of wave propagation [51]. The above properties can be used to justify the results obtained for the EVS in this section. For instance, the first four component pairs i.e. (1,6), (2,6), (3,4) and (3,5)³ in Figure 6.4 have the same correlation as the AS changes but the reduction in correlation is slower for the last two component pairs i.e. (1,2) and (4,5). This is because the first group measures the correlation between electric and magnetic field sensitive components while the second one measures the correlation between two electric field sensitive components. The component pairs (1,2) and (4,5) which measure the (E_x, E_y) and (B_x, B_y) have the same response under this channel condition where the electric and magnetic field are incident on the dipole and loop in a similar manner.

Figure 6.5 shows SFC versus ES for EVS elements (1,6), (2,6), (3,4), (3,5), (1,2) and (4,5). By comparing with Figure 6.4, the SFC reduces more rapidly when the AS increases than for the ES. Figure 6.6 shows the SFC versus MAOA and MEOA for various components of the EVS. As the MEOA moves from 0° to 90° , the SFC for element pairs (3,2), (5,6), (1,5) and (2,4) decreases significantly. However, the SFC for element pair of (1,6) and (3,4) increases slightly. For the case of the MAOA, the element pair of (2,6) and (3,5) appear to have an opposite effect to the (1,6) and (3,4). In other words as the SFC of (2,6) reduces it increases for (1,6) and vice versa. The SFC of (1,2) and (4,5) is symmetrical about MAOA 45° . The developed closed-form SFC for various AAs are important for several applications. In the next two sections, two major applications relating to sensitivity and capacity analysis are addressed in Section 6.4 and 6.6 respectively.

³Note that other component pairs which are not shown in the figure have zero correlation except for the autocorrelation of one element with itself.

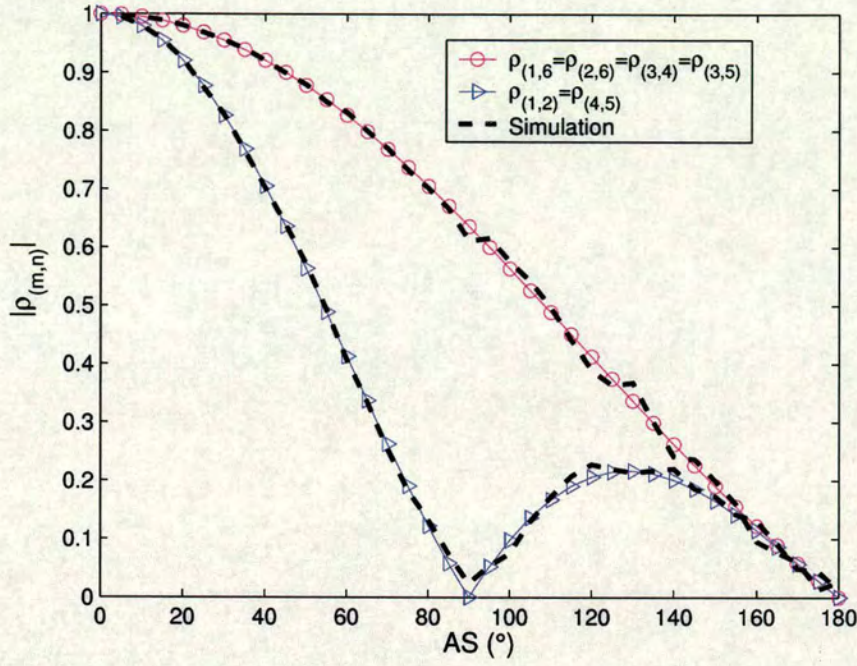


Figure 6.4: SFC between elements (m,n) of the EVS versus AS for 45° MAOA, 90° MEOA and 0° ES.

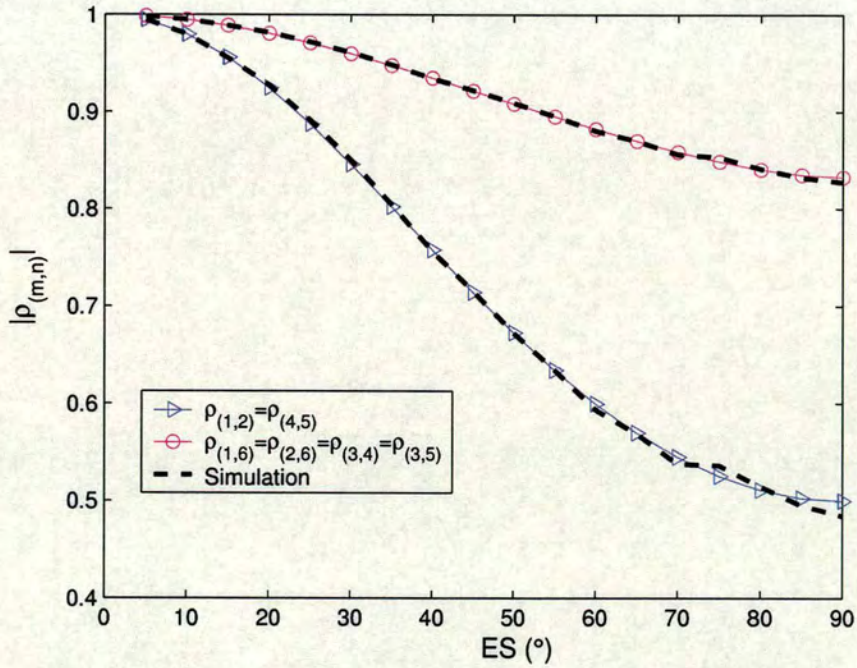


Figure 6.5: SFC between elements (m,n) of the EVS versus ES for 90° MAOA, 90° MEOA and 0° and 30° AS.

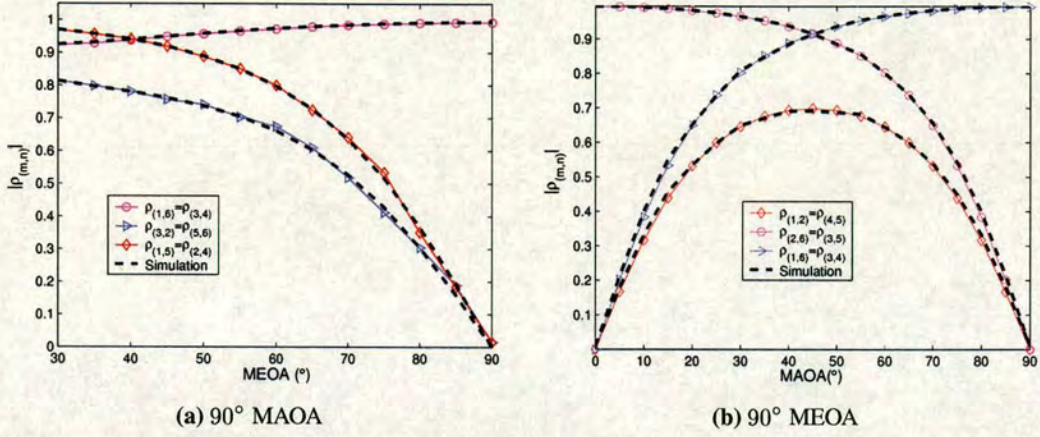


Figure 6.6: SFC between elements (m,n) of the EVS versus MEOA and versus MAOA for 30° AS and ES.

6.4 Sensitivity analysis

Depending on the elements of interest and angle-of-arrival, the SFC can differ significantly from one element pair to another even under the same channel conditions. Hence, the general characteristics of the array's sensitivity to different channel parameters cannot be fully represented by one correlation value. In order to allow the array's sensitivity to be investigated, several parameter sets associated with MAOA, AS, MEOA and ES are considered. To examine the importance and dependency of the above parameters on the system performance, two of the parameters are examined at a time while keeping the other two fixed. The results are reported in terms of the SNR required to achieve a target P_e for BPSK modulation. The P_e can be computed using the EVD of the spatial correlation matrix, \mathbf{R} as shown in [42] and is given by [67]

$$BER = \frac{1}{2} \sum_{k=1}^M \pi_k \left[1 - \sqrt{\frac{\bar{\lambda}_k}{1 + \bar{\lambda}_k}} \right] \quad (6.12)$$

$$\pi_k = \prod_{\substack{i=1 \\ i \neq k}}^M \frac{\bar{\lambda}_k}{(\bar{\lambda}_k - \bar{\lambda}_i)} \quad (6.13)$$

where λ_k is the diagonal matrix of eigenvalues obtained using EVD of correlation matrix $\mathbf{R} = \mathbf{U}\mathbf{\Lambda}\mathbf{U}^H$. In our analysis, unless otherwise specified, the number of receive antennas (isotropic elements), antenna spacing and the target P_e are fixed at 4, 0.5λ and 0.01. It should be noted that the analysis is equally applicable to any number of antennas and spacing under any channel conditions. Four parameter sets are examined to study their impact on the system

performance. The investigation on the parameter set MAOA-AS in Subsection 6.4.1 has been reported such as in [15, 18]. We then examine three additional parameter sets which have yet to be reported in the literature, namely MEOA-ES, AS-ES and MAOA-MEOA in Subsection 6.4.2 to 6.4.4, respectively. The results for the case of ULA, UCA and URA under these parameter sets have been presented in [42, 140] and will therefore be briefly discussed in this thesis. Readers are referred to [42, 140] for detailed discussions. Hence, we mainly focus on the results for the single EVS and EVS arrays.

6.4.1 Effect of MAOA and AS

The performance sensitivity of the ULA, UCA and URA⁴ to the MAOA and AS are shown in [42] where the performance of the ULA, UCA and URA is AS dependent while the effect of MAOA is array dependent. The ULA is very sensitive to changes in MAOA whereby the reduction in performance is more rapid in the broadside region (around 90° and 270°) than in the endfire region (around 0° and 180°). However, the performance of the UCA and URA are generally independent of MAOA. The sensitivity of a single EVS to changes in MAOA-AS is illustrated in Figure 6.7. The performance pattern appears to be the same as that of the UCA/URA where the performance improves with increasing AS but is insensitive to changes in MAOA. The EVS arrays exhibit very close performance patterns to their corresponding isotropic array configurations (see [42]) as shown in Figure 6.8 to 6.9. For the ULA-EVS, at low AS ($< 10^\circ$), the required target SNR is high irrespective of the MAOA values. However, as the AS increases, the reduction in target SNR is more rapid in the broadside region than in the endfire region. As the AS increases to a large value ($> 80^\circ$), the performance of the ULA-EVS saturates irrespective of the MAOA. Unlike the ULA-EVS, the performance of the UCA-EVS or URA-EVS is insensitive to changes of MAOA as shown in Figure 6.9. Nonetheless, their performance is highly sensitive to the AS of the incoming signal. By studying Figure 6.7 to 6.9, one notes that as the AS increases, significant improvements occur in target SNR. On the other hand, only small changes can be observed in target SNR as the MAOA changes except the for the ULA-EVS. This suggests that the system performance is AS dependent while the effect of MAOA is again array dependent.

⁴Note that the four element UCA and URA have a similar geometry but the former is 0.1λ less than the latter in spacing, thus we would expect a very similar performance pattern for these two configuration. See also Appendix C which demonstrated that the four element UCA and URA have almost identical radiation patterns.

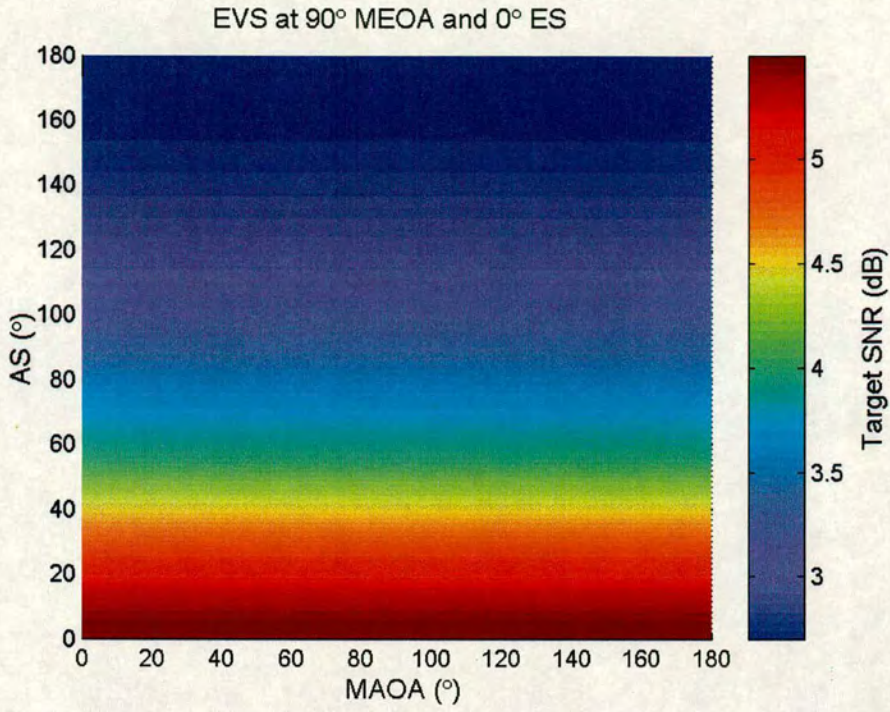


Figure 6.7: The target SNR as a function of MAOA and AS for EVS.

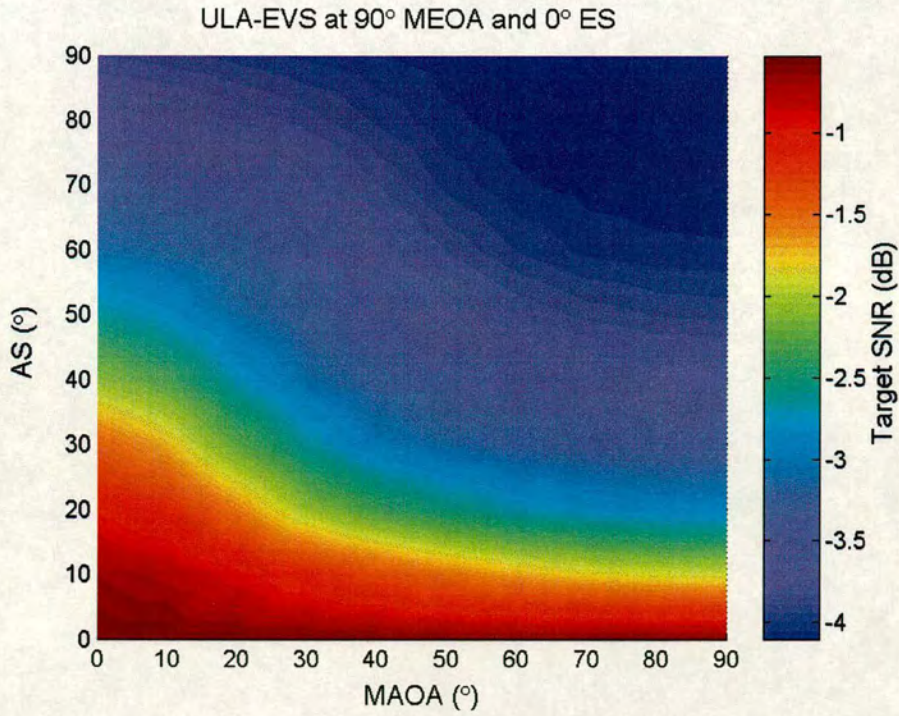


Figure 6.8: The target SNR as a function of MAOA and AS for ULA-EVS.

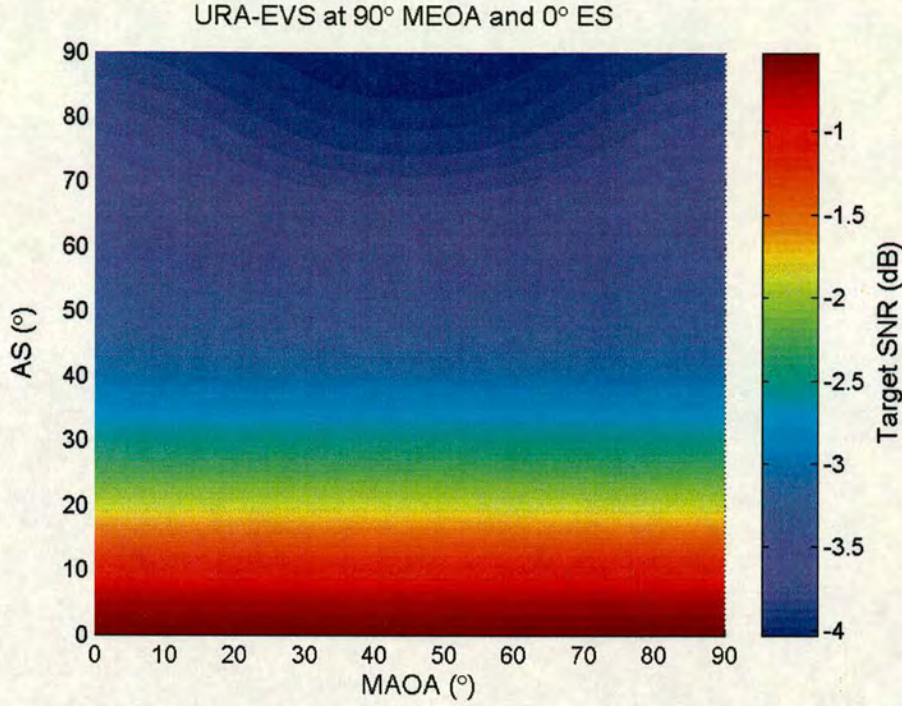


Figure 6.9: The target SNR as a function of MAOA and AS for URA-EVS.

6.4.2 Effect of MEOA and ES

In this parameter set, it is found that the ULA, UCA and URA have a similar performance patterns where the arrays are more sensitive to the effect of ES than the MEOA. The impact of MEOA is relatively small (in the order of 1-2dB) as compared to the impact of ES (in the order of 4dB) for the ULA. The single EVS has a similar performance pattern in Figure 6.10 as for varying AS and MAOA shown in Figure 6.7. Again, the single EVS is relatively insensitive to changes to MEOA while the performance improves as the ES increases. However, one can note that in Figure 6.10 the single EVS tends to perform slightly better in 90° MEOA than for other elevation angles. Furthermore, the reduction in target SNR in both Figure 6.7 and 6.10 are approximately equal as AS and ES increases up to 60°. The performance of the three EVS arrays also have a similar pattern to their corresponding isotropic AA configurations [42]. As shown in Figure 6.11 for the case of URA-EVS, the higher target SNR values are concentrated at the horizontal plane corresponding to 90° MEOA. In addition, the performance is symmetrical about this MEOA value because the radiation patterns for MEOAs below/above 90° are mirror images of each other. For a given ES, the performance improves slightly as the MEOA deviates from the 90°. On the other hand, for a given MEOA, the performance

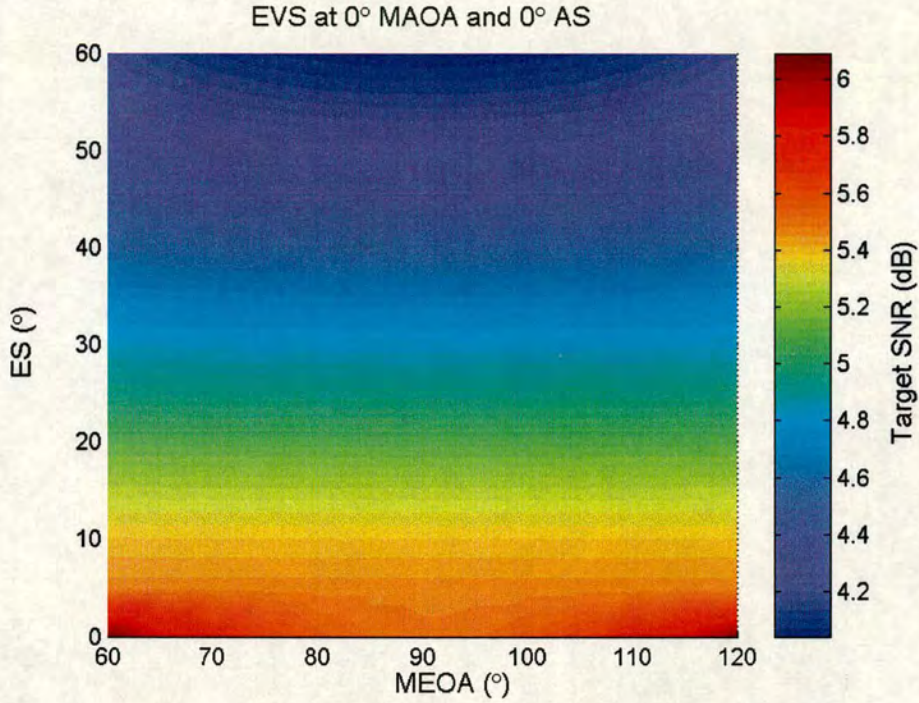


Figure 6.10: *The target SNR as a function of ES and MEOA for EVS.*

improves significantly as the ES increases. The above observations highlight the importance of ES as compared to MEOA in system performance. Unlike the MAOA, the behaviour of all the three EVS array types is similar when the MEOA is changed. However, the performance changes with respect to the MEOA are somewhat less rapid than the case of ULA-EVS.

6.4.3 Effect of AS and ES

The impact of AS and ES on the performance of the ULA is dependent on the MAOA. This dependency is stronger at endfire where the impact of both AS and ES is equally important. The dependency vanishes gradually as the MAOA moves towards the broadside condition where the ES has no impact on the ULA performance [42]. However, the impact of AS remains significant. For the UCA and URA, the performance of the system is more dependent on AS than ES.

Unlike the case of the UCA and URA, the impact of the AS and ES on the single EVS can be considered equally important for AS/ES values $< 60^\circ$. For instance, the AS value required to achieve a given target SNR value for 0.01 BER is approximately equal to the corresponding

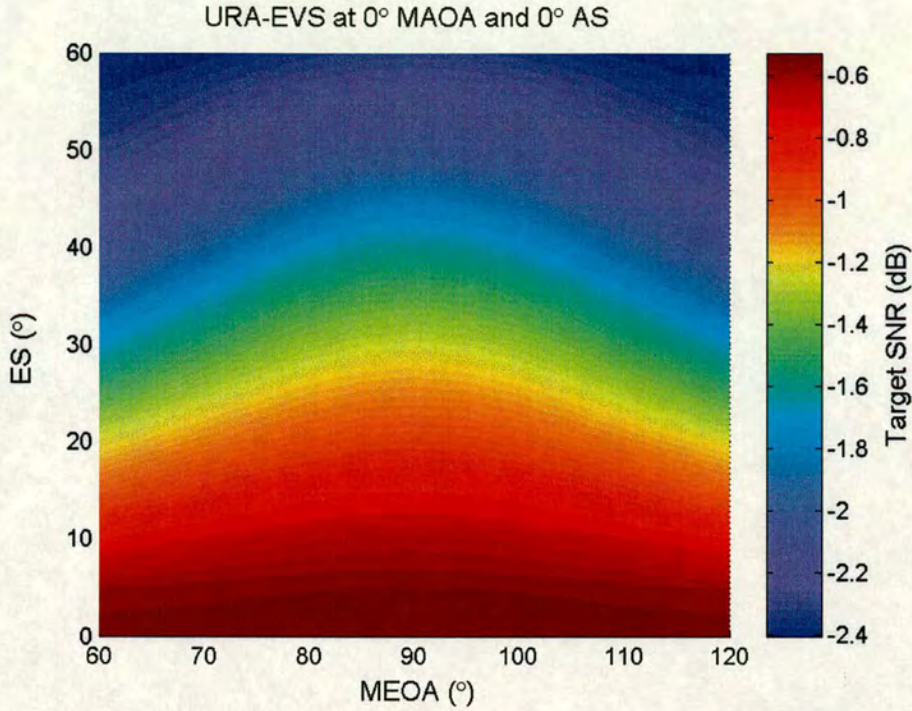


Figure 6.11: *The target SNR as a function of MEOA and ES for URA-EVS.*

ES value as can be seen from the changes in colour density in both AS and ES direction in Figure 6.12. However, when AS/ES exceeds 60° , the AS has a larger impact on the system performance than the equivalent ES values. The performance of ULA-EVS in Figure 6.13 exhibits similar pattern to the ULA [42]. It can be seen that the impact of AS and ES are considered equally important at low angle spread but as the angle spread increases the impact of AS tends to be more significant. On the other hand, the impact of the AS is more pronounced than that of ES for the cases of the UCA-EVS and URA-EVS. One can observe from Figure 6.14 the URA-EVS's sensitivity to the AS whereby the required AS value to achieve the target SNR is approximately half of the corresponding ES value. Comparing to the UCA and URA (where only little performance gain can be obtained at low AS even with high ES values in Figure 6.15) with its corresponding EVS arrays, the EVS arrays provide better gain for the MPCs that arrive in elevation domain while simultaneously maintaining the performance in the azimuth domain.

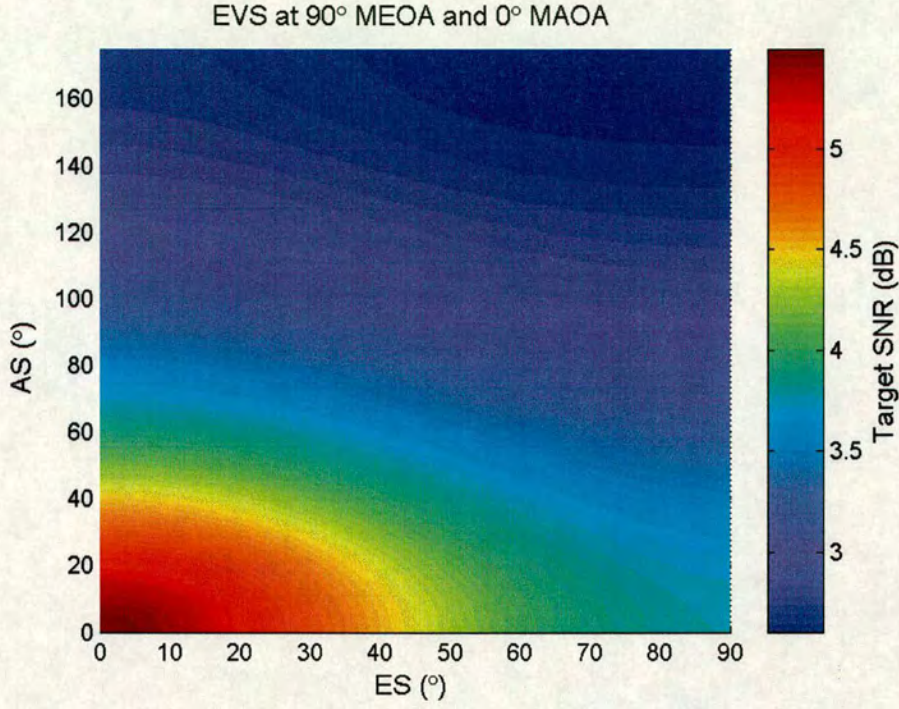


Figure 6.12: The target SNR as a function of AS and ES for EVS.

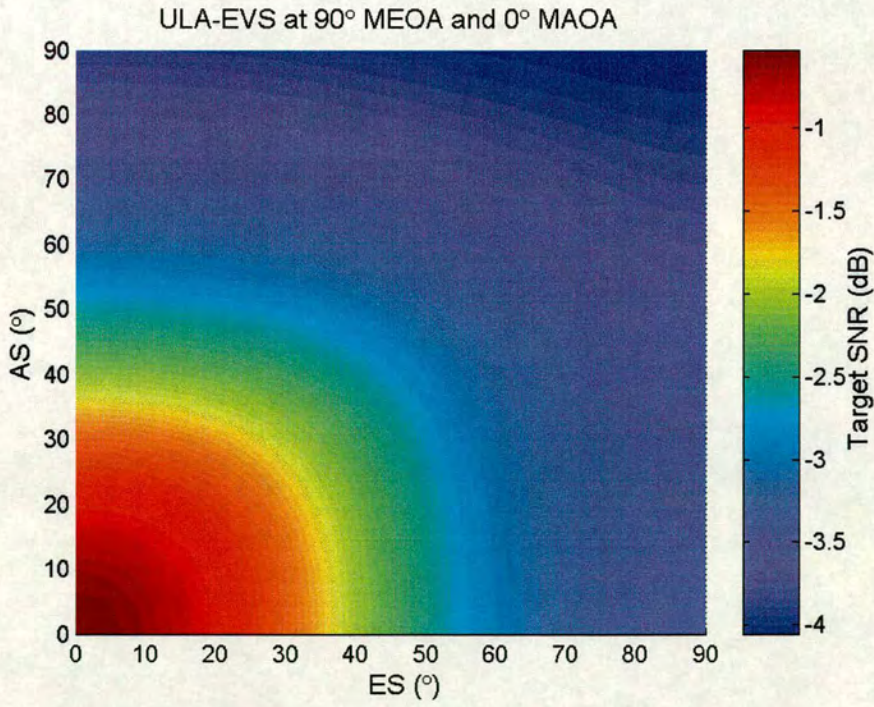


Figure 6.13: The target SNR as a function of AS and ES for ULA-EVS.

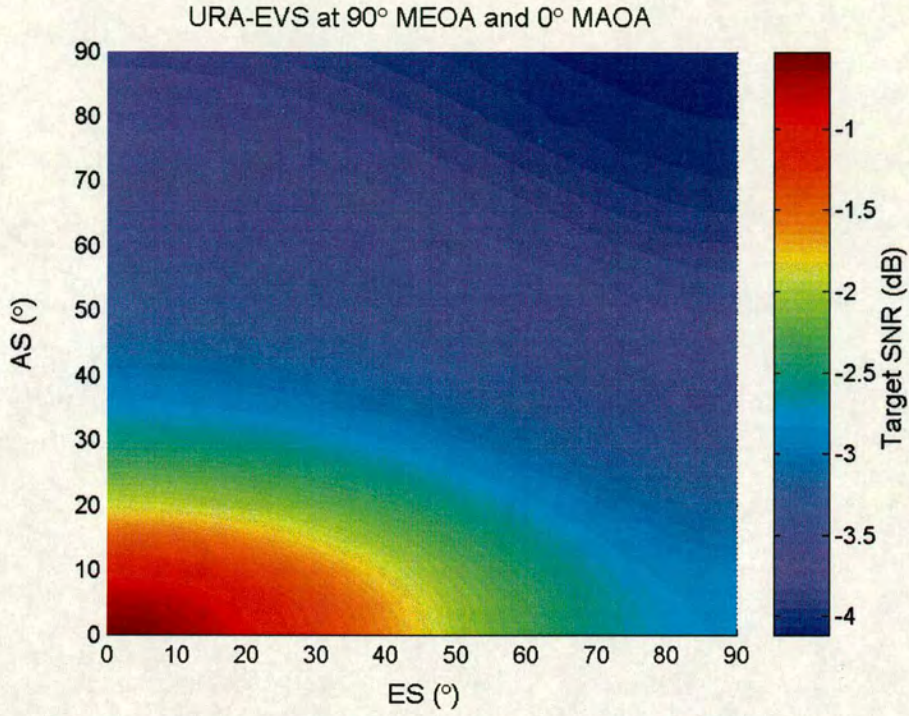


Figure 6.14: The target SNR as a function of AS and ES for URA-EVS.

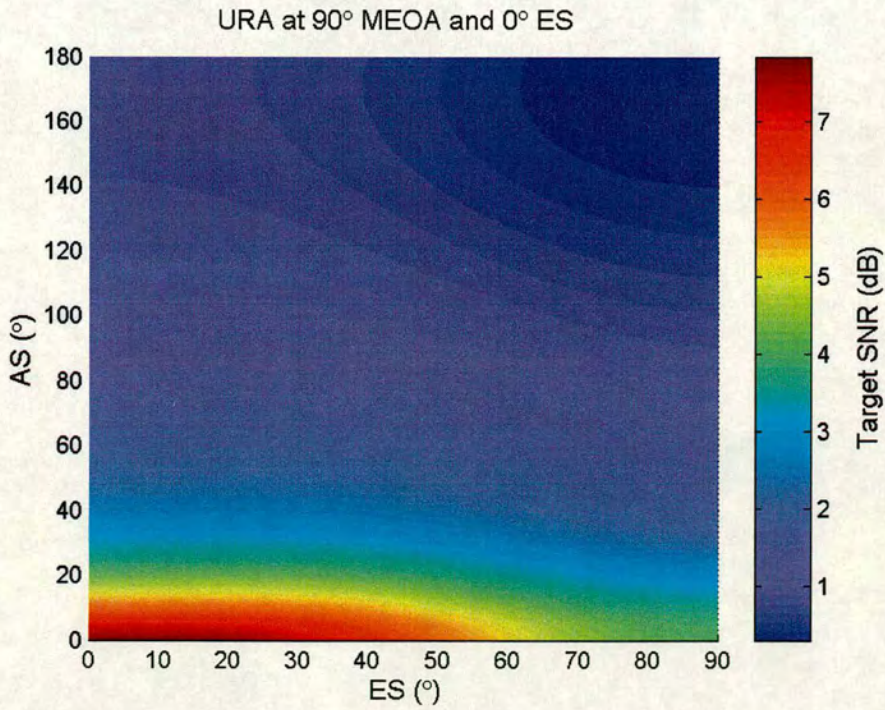


Figure 6.15: The target SNR as a function of AS and ES for URA.

6.4.4 Effect of MAOA and MEOA

When the AS and ES are non-zero, the ULA is sensitive to changes in the MAOA and MEOA whilst the UCA and URA are more sensitive to variations in the MEOA than to the MAOA [42]. It is also apparent that the performance variation due to changes in MAOA/MEOA are comparatively small compared to changes in AS and ES. The effect of MAOA-MEOA on the performance of the single EVS is shown in Figure 6.16. It can be observed that the single EVS is in general insensitive to both parameters where only small fraction of dB (in the order of 0.3dB) in performance difference is observed as the MEOA changes. The MAOA on the other hand has no impact on the single EVS performance. The ULA-EVS is sensitive to the changes

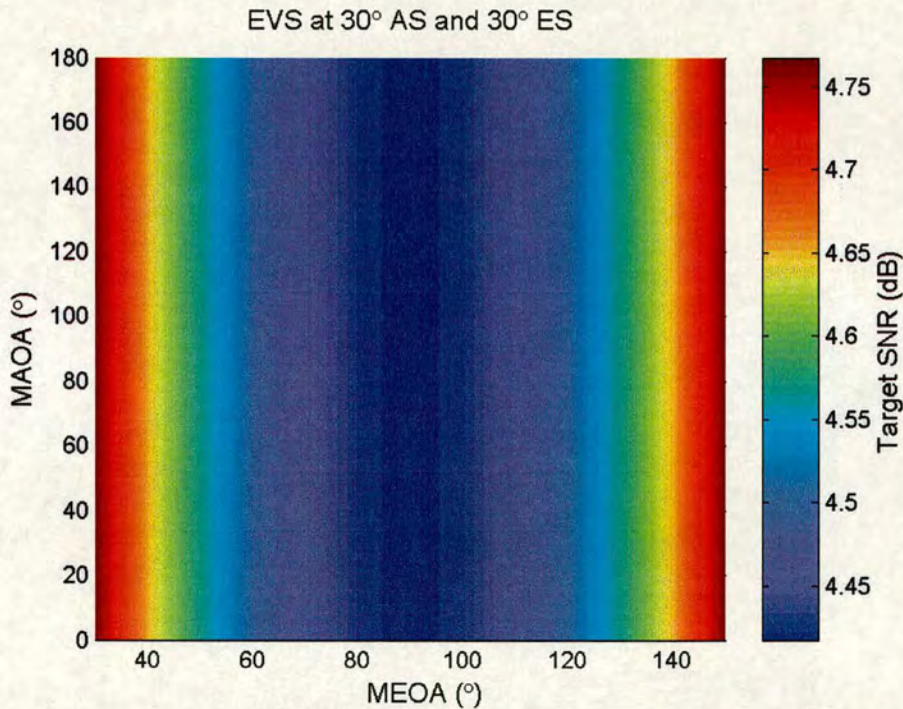


Figure 6.16: *The target SNR as a function of MAOA and MEOA for EVS.*

in MAOA due to the linear configuration as shown in Figure 6.17. The performance pattern is almost identical to the ULA in [42]. In particular, the highest and lowest target SNR regions can be identified in endfire and broadside conditions with 90° MEOA. As the MEOA deviates from 90° , the target SNR decreases and increases by a fraction of a dB in the endfire and broadside regions respectively. However, one can see that the performance around the broadside region for the ULA-EVS spans a larger area than the ULA counterpart. The performance of the UCA-EVS and URA-EVS has a similar pattern (not shown) with higher target SNR concentrated at

the horizontal plane and independent of the MAOA values as shown in Figure 6.18. Notice that the changes in target SNR under this parameter set is comparatively small. Hence, we conclude that the effect of the MEOA and MAOA on the system performance is negligible. In addition, we found that the ULA-EVS is sensitive to both parameters whilst the UCA-EVS and URA-EVS are generally insensitive to MEOA and MAOA.

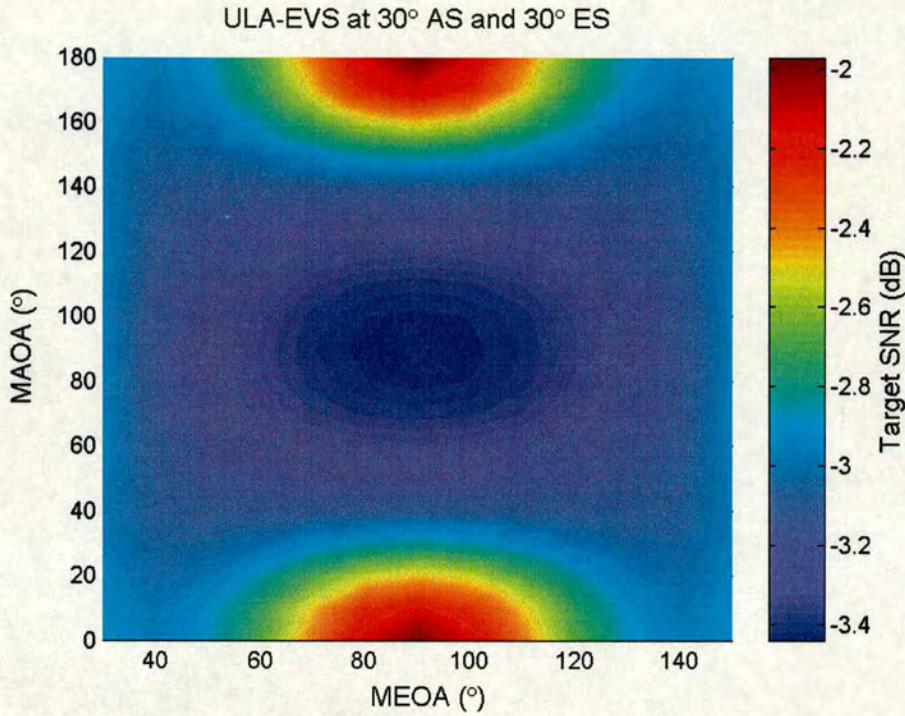


Figure 6.17: The target SNR as a function of MAOA and MAOA for ULA-EVS.

6.5 Implications of the performance patterns

In this section, several important implications that can be extracted from the performance patterns presented in Section 6.4 are provided. These implications can be useful in selecting types of AA used in different REs and applications so that system performance can be optimised.

MAOA vs AS The effect of MAOA is array dependent where in particular the ULA is found to perform best in the broadside and poorest in the endfire region. Thus, it is beneficial to orient the ULA in such a way that the receive and transmit directions are mostly distributed in broadside condition where the ULA has better resolution. On the other hand,

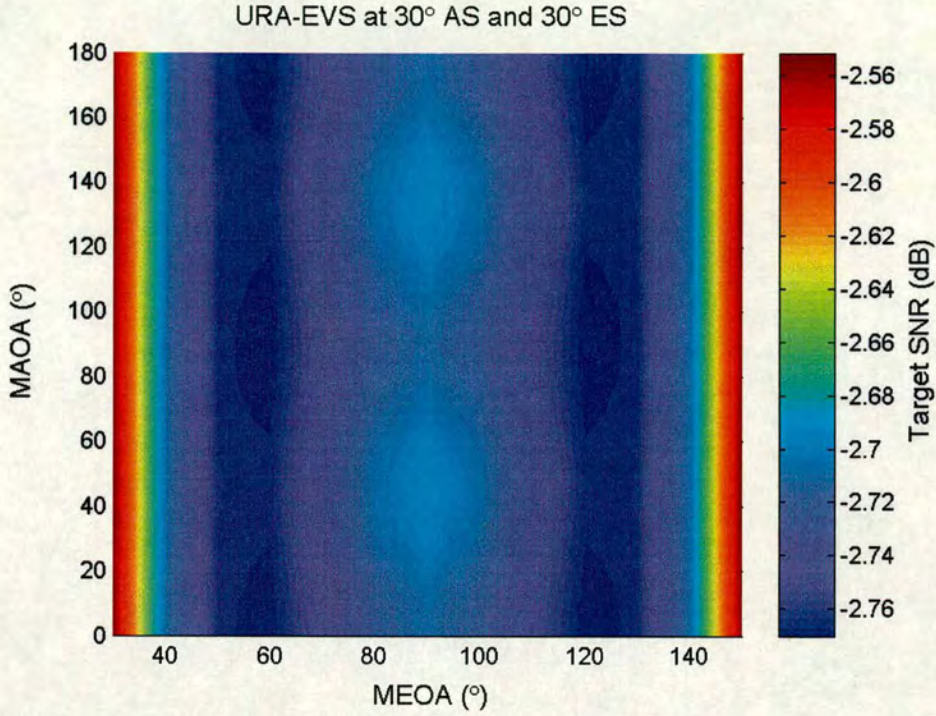


Figure 6.18: *The target SNR as a function of MAOA and MEOA for URA-EVS.*

the UCA and URA which are insensitive to the MAOA can be deployed without requiring details of the general direction distribution of the users. However, for the isotropic scattering assumption where the AS is 180° , the use of different AA or EVS array configurations is expected to give no difference in performance as it tends to saturate at high AS values irrespective of the MAOA.

MEOA vs ES In an elevation rich but azimuth limited environment, it is advantageous to slightly tilt the AAs such that the MEOA is not close to the horizontal plane (i.e. 90° MEOA). The random orientation of a typical MS which averages the performance over a given MEOA range will therefore help in improving the performance of the AAs.

AS vs ES From the performance patterns, it can be identified that the impact of AS is more significant than ES for the traditional arrays while the response to the ES is improved for the EVS and EVS arrays. Therefore, in the scenario where the AS is small but with significant ES (such as in the canyon effect), the EVS and EVS arrays can be employed instead of traditional arrays to maximise the gain due to multipath that arrives with large ES.

MEOA vs MAOA Since the performance change due to the MAOA and MEOA is relatively small (except for the ULA configuration), the performance of the deployed AAs are not very much affected by this parameter set. However, the dependency on the MEOA is reduced from maximum for the UCA/URA; to intermediate for a single EVS; to minimum EVS arrays. For the ULA, it depends on the MAOA whereby the dependency is stronger in the endfire than in the broadside region.

6.6 Capacity analysis for MIMO systems

In this section, we compare the performance of the compact arrays discussed so far to illustrate the efficacy of these compact arrays under various scenarios. As Section 6.4 showed that the key parameters to the system performance are the AS and ES of the MPC, we focus on the capacity analysis of the CAAs under these two parameters using the derived closed-form expressions in the Section 6.2. Consider a MIMO system with N_R receive antennas and M_T transmit antennas, with the well-known independent identical distributed (i.i.d.) assumption for which the fades between pairs of transmit-receive antennas are statistically independent and identically Rayleigh distributed. With equal power at each transmit antenna [108, 141], the channel capacity is given by

$$C = \log_2 \left[\det \left(\mathbf{I}_{N_R} + \frac{SNR}{M_T} \mathbf{H} \mathbf{H}^H \right) \right] \quad \text{bits/sec/Hz} \quad (6.14)$$

where \mathbf{H} is an i.i.d. $N_R \times M_T$ channel matrix whose (n_R, m_T) entry describes the channel responses from transmit antenna m_T to receive antenna n_R . The i.i.d. assumption does not hold for most practical cases particularly in systems where CAAs are deployed. In such a system, the matrix \mathbf{H} is no longer i.i.d. due to the effect of antenna SFC and the channel capacity is modified according to [142]

$$C = \log_2 \left[\det \left(\mathbf{I}_{N_R} + \frac{SNR}{M_T} \mathbf{R}_R \mathbf{H} \mathbf{R}_T \mathbf{H}^H \right) \right] \quad \text{bits/sec/Hz} \quad (6.15)$$

where the size $N_R \times N_R$ matrix \mathbf{R}_R and size $M_T \times M_T$ matrix \mathbf{R}_T signify the correlation matrices of the receive and transmit AAs. We assume that the transmit antennas are separated sufficiently far apart (as found in most existing BS) so that \mathbf{R}_T becomes the (scaled) identity matrix even under small angle spread scenarios. We apply the \mathbf{R}_R matrices obtained from the previous section for the various AAs to (6.15) and use the following simulation parameters: 4

transmit antennas, 4 receive antennas⁵, 0.5λ antenna spacing, 20dB SNR and 90° MAOA and MEOA.

Generally, it can be observed from Figure 6.19 that increasing the AS leads to higher capacity values for all the AAs. However, the capacity results tend to saturate at higher AS ($> 90^\circ$) values. A similar trend is also observed for the case of increasing ES except for the ULA. For all the isotropic arrays, the impact of the ES on the capacity is less pronounced than that of AS. For instance, with the same AS and ES at 60° , the UCA records capacities of 18 and 12 bits/s/Hz respectively. Furthermore, the ULA outperforms the UCA and URA under broadside conditions for most AS values. The capacity of the ULA reaches the upper capacity bound given by the i.i.d. case at higher AS. Considering the attainable capacity for the single EVS

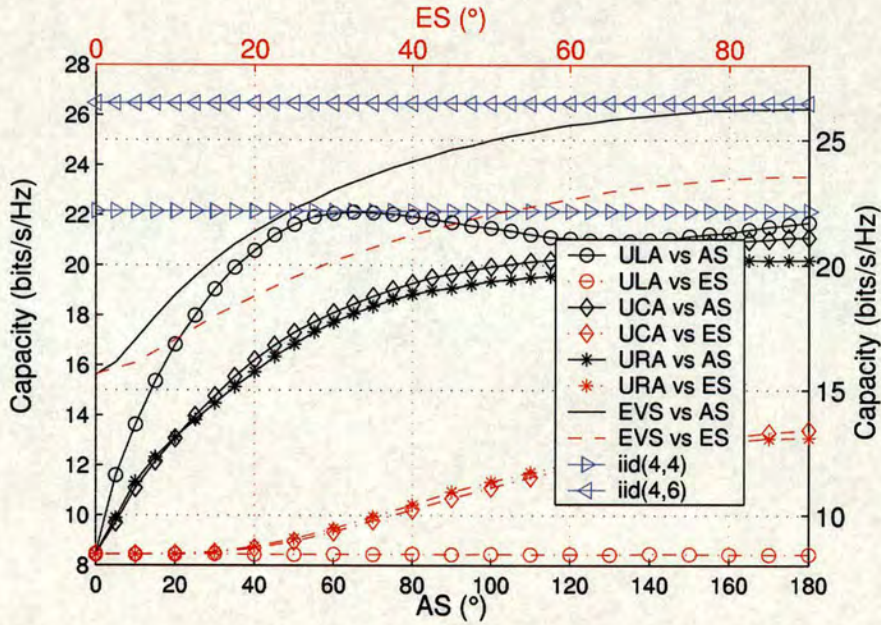


Figure 6.19: The performance comparison between ULA, UCA, URA and EVS as a function of AS (0° ES) and ES (0° AS) at 90° MAOA and MEOA.

in Figure 6.19 illustrates that the single EVS outperforms the isotropic arrays for all cases. Such a performance gain arises not only from the two additional receive components but is also achieved through polarization diversity where ideal polarization mixing is assumed. In fact, the EVS can exploit a given value of AS or ES more efficiently than the isotropic arrays while providing a very compact structure (though the EVS does occupy a 3-D space). This signifies

⁵ A single EVS is referred as a single sensor which consists of 6 antenna elements.

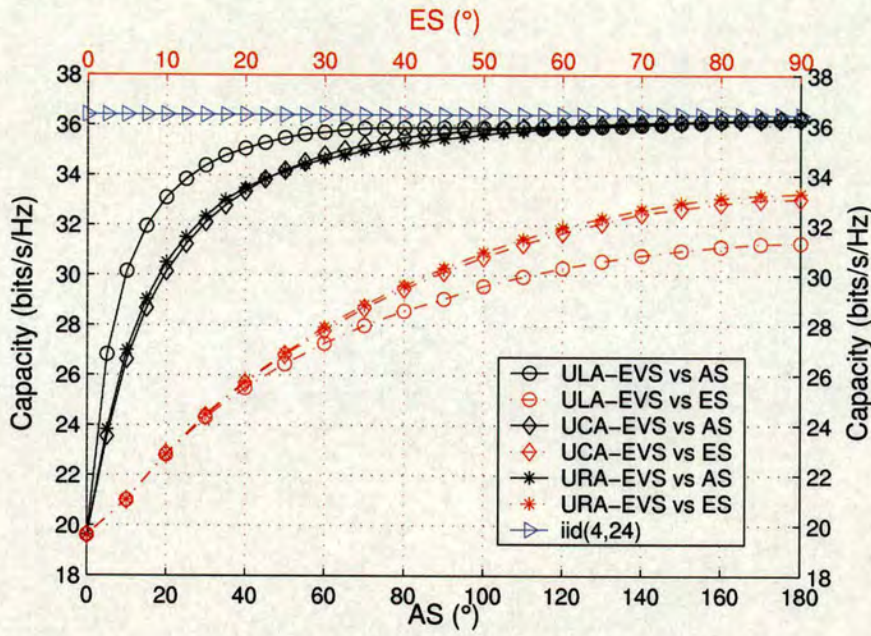


Figure 6.20: The performance comparison between ULA-EVS, UCA-EVS and URA-EVS as a function of AS (0° ES) and ES (0° AS) at 90° MAOA and MEOA.

the importance of the EVS as an alternative to conventional arrays for MIMO deployment. It is interesting to note that for a given ES, the single EVS has a comparable performance to the equivalent AS. The capacity for the EVS could reach the i.i.d. (4,6) case when both AS and ES are at their maximum i.e. isotropic scattering.

For the EVS arrays, increasing the AS and ES also results in higher capacities and the impact of AS is also more significant than the ES as illustrated in Figure 6.20. The capacities of all the EVS arrays saturate at higher AS and ES and are expected to reach the i.i.d. case in the isotropic scattering scenario. Comparing Figure 6.19 and 6.20, the capacity gradient of all isotropic arrays as a function of increasing AS or ES is less steep than for the corresponding EVS arrays. For instance, the average capacity for the three isotropic arrays improves from 8.5 to 16.1 bits/s/Hz as compared to the EVS arrays which changes from 19.6 to 33.0 bits/s/Hz when the AS increases from 0 to 30° . This observation highlights the capability of the EVS arrays to exploit the spatial diversity very effectively and thus it can be very advantageous in small angle spread scenarios. Furthermore, one can also observe that the angle-of-arrival dependency for the ULA configuration is significantly reduced when using the EVS as the ULA element.

It is apparent from Figure 6.21 and 6.22 that the channel capacities degrade significantly as the antenna spacing is reduced. When the antenna spacing is constrained to a lower value, the spatial correlation increases since each antenna “sees” the same MPCs. To gain some insights on the effect of antenna spacing, a comparison is made with reference to the angular parameters since it is well-known that the AS has a significant impact of the system performance. To allow consistent and fair comparison, the capacities are computed under varying AS (with 0.5λ antenna spacing) and antenna spacing (with 30° AS), respectively. All the other parameters are fixed as previously, specifically, the MAOA, MEOA, ES, SNR are fixed at 90° , 90° , 10° and 20dB, respectively. The results are depicted in Figure 6.21 for the ULA, UCA and URA and Figure 6.22 for the EVS-arrays where the following observations can be made:

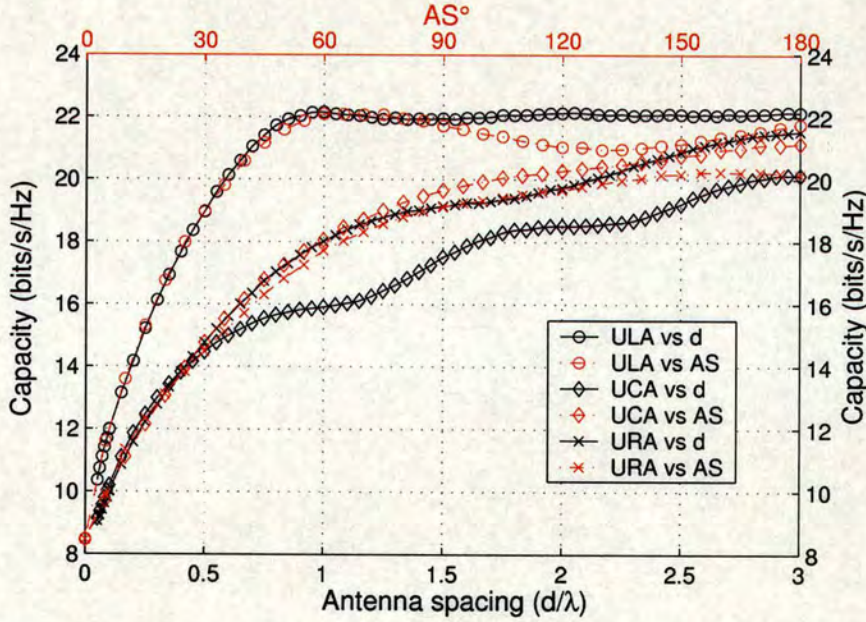


Figure 6.21: The performance comparison at 10° ES and 90° MAOA and MEOA between ULA, UCA and URA.

1. The capacity curves versus spacing and versus AS intersect at $d = 0.5\lambda$ and $AS = 30^\circ$. This is expected given the same simulation settings.
2. Under the channel conditions considered, at spacings less than 0.5λ and AS less than 30° , there exists close relationship between the effect of AS and antenna spacing. It can be clearly identified from Figure 6.21 that the effect of reducing the antenna spacing from 0.5λ to 0.1λ is essentially equivalent to decreasing the AS from 30° to 10° for the

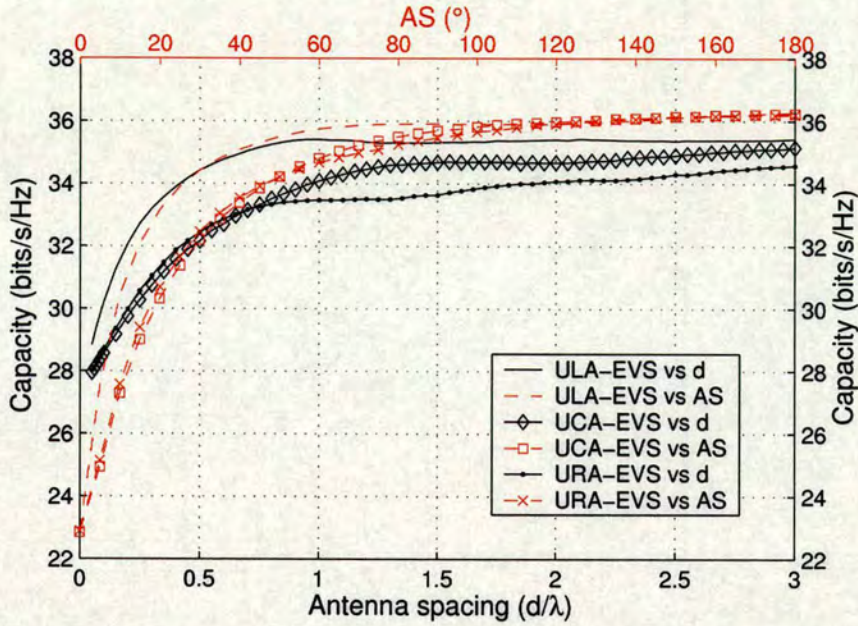


Figure 6.22: The performance comparison at 10° ES and 90° MAOA and MEOA between ULA-EVS, UCA-EVS and URA-EVS.

case of ULA, UCA and URA. Beyond this spacing and AS, the impact of antenna spacing become less apparent than the AS though at higher spacing and AS both capacities saturate.

3. For the case of EVS arrays, the effect of increasing antenna spacing leads to higher absolute capacity gains than the isotropic array, though the percentage gain is somewhat less than the percentage capacity increment for its corresponding isotropic array. In addition, it is evident from Figure 6.22 that the EVS array is more sensitive to changes in AS than the spacing between its elements. Though the capacity for $d < 0.5\lambda$ is higher than AS $< 30^\circ$, the capacity is degraded more severely when AS is reduced from 30° to 0° (corresponding to an average capacity reduction of 10.2bit/s/Hz) than reducing the antenna spacing from 0.5λ to 0.1λ (corresponding to average capacity reduction of 5.4 bits/s/Hz). However, the capacity is higher when AS $> 30^\circ$ than $d > 0.5\lambda$ which demonstrates that EVS arrays can be compactly arranged for a given mobile terminal size.

6.7 Summary

In this chapter, closed-form expressions for the SFC function for different AAs namely ULA, UCA, URA, EVS, ULA-EVS, UCA-EVS and URA-EVS have been derived. These SFC functions are expressed in terms of the MAOA, AS, MEOA, ES, antenna spacing and geometry of the array under study. Verification is achieved by means of computer simulations where excellent agreement is found between theoretical and simulation results. Furthermore, the impact of different channel conditions for four parameter sets on the system performance was investigated. The importance and dependency of the parameters under study can be determined from the performance patterns where it is found that the impact of AS and ES are of particular interest. On the other hand, the impact of MAOA and MEOA are generally insignificant to the system performance but this does depend on the type of array under investigation. It must be emphasized that both AOA and EOA must be taken into account so that an accurate performance analysis of the AA can be performed. The properties of the EVS which is insensitive to the both MAOA and MEOA make it a very robust receiver array that works well under many scenarios as well as offering small physical size for MIMO deployment. Furthermore, EVS arrays offer several advantages over conventional arrays in terms of its potential to exploit multipath richness, reduced dependency on the angle-of-arrival as well as the capability to yield higher performance for a given increase in antenna spacing. Finally, the developed SFC can also be used to determine the correlation matrix at both the transmitter and receiver of a MIMO system in order to analyse the effect of correlation on channel capacity.

Chapter 7

Conclusions and future work

This thesis has contributed to a detailed analysis of compact antenna receivers for CAA deployments in terms of antenna and channel parameters. This concluding chapter summarises the key results from different chapters and describe how such results can influence future development of compact receivers. Possible future research areas to exploit the current results are also proposed.

7.1 Conclusions and summary of results

The COST 259 macrocell channel model is implemented in terms of a TDL. The concepts and approaches are mainly based on the COST 259 modelling frame work with some modifications and new assumptions. A detailed simulation flow is outlined to help in identifying the steps required in implementing the channel model. Simulation results demonstrated the backward compatibility with the existing GSM model. The capacity analysis on the implemented channel model shows that the AS is the primary determinant of the system performance.

An antenna model is then established that incorporates several important parameters such as beampatterns, array geometries, MC, etc. It is demonstrated that different antenna elements and arrays yield different performance which is more favourable in some cases than others. When antenna elements are in close proximity, the effect of MC becomes apparent. It is shown that for all AAs under consideration, MC can decorrelate the received signal. However, the performance gain due to the lowered correlation is compensated for by a signal cancellation effect that reduces the received power. The overall effect of MC is to reduce the system performance. These two effects of the MC shown in our analysis clarify the conflicting results available in the literature.

In order to facilitate the derivation of a closed-form SFC for various AAs, the impact of different types of angular of arrival distributions needs to be clearly understood. As shown in the analysis, the impact of using different typical angular of arrival pdfs for both AOA and EOA

is minimal, at least from the diversity point of view. On the other hand, the standard deviation of the underlying pdf is the key parameter that decides the system performance. Hence, for a system that exploits spatial diversity, the use of a single AOA and EOA pdf are suffice to characterise the SFC for a given AA topology.

Based on the above results, closed-form 3-D SFCs for the ULA, UCA, URA, EVS, ULA-EVS, UCA-EVS and URA-EVS are developed. The closed form expressions are paramaterised by the MAOA, AOA, MEOA, ES, antenna spacing and geometry of the AA. The validity of the derived expressions is achieved by means of computer simulation, where an excellent match is found between the theoretical and simulation results. The derived SFC function allows the study of the importance and dependency of the AOA and EOA parameters, as can be envisaged from the performance patterns. The performance pattern which relates the AA performance as a function of two angular parameters provides a better understanding of how the array responds to the changes of the angular parameters under study. Several important implications can be deduced from the performance patterns that assist in the design of diversity combining algorithms for various AAs topologies. Our analysis shows that in general, the system performance is AS and ES dependent while the impact of the MAOA and MEOA is insignificant but array dependent. Furthermore, the performance gain due to a given increase in AS is greater than the corresponding increase in ES. However, to obtain an accurate AA performance, both AS and ES must be taken into consideration.

Another major application of the developed SFC functions is to determine the correlation matrices at the transmitter and receiver for capacity evaluation of MIMO systems. The capacity results show that the feasibility of deploying EVS and EVS arrays over traditional arrays as a MIMO receiver. The EVS with its small physical size is insensitive to the changes in both MAOA and MEOA which makes it a robust array configuration. By comparing the capacity results, one can observe that the EVS arrays offers several advantages over the traditional arrays in terms of its potential of exploiting multipath richness, reduced dependency on the angular of arrival and capability to yield higher performance for a given increase in antenna spacing.

7.2 Future work

There are number of research areas in this thesis that can be developed through future research as outlined in the following:

- The antenna model considered in this thesis does not take into account implementation issues such as impedance matching, non ideal current distribution, feeding arrangement, polarisation mismatch etc. Therefore, an advanced antenna model needs to be developed and incorporate those practical issues into the system performance. In order to evaluate the validity of the developed theoretical model, extensive measurements need to be carried out. Furthermore, the effect user's hand and head on the performance of handheld AAs is a topic of interest. Use of phantom heads and hands in theoretical and experimental work results in gain imbalance between antenna elements in the array as one of more antennas could be covered by the user's head or hand. This will provide the important design information for AAs such as the use of different antenna elements and positioning of antenna elements on the handset so that the radiation pattern of the element can be directed away from user's head and hand.
- With advances in digital signal processing and faster speed of very large scale integration, implementation of AAs at the subscriber units becomes practical. However, as mentioned in the introductory chapter, the deployment of AAs at the MS requires an appropriate signal processing algorithm to support higher data rates for 3G systems or beyond. Future work aiming to investigate the performance of CAAs on mobile handsets for different spatial and temporal signal processing algorithms is required. A wide range of algorithms including space-time block codes to space-time trellis codes, Bell labs layered space-time schemes, joint transmit-receive techniques, beamforming, etc for MIMO appeared to be possible candidates. Nevertheless, the trade off between the system performance, computational complexity, power consumption and production costs of the above schemes need to be identified. An optimum solution that balances these limitations for practical implementation needs to be explored. This will lead to the practical answer for the required physical size, number of antennas, power requirement, etc for MIMO receivers at the MS.
- In multiple user and multiple BS investigations, effort can also be given to the consideration on how spatial interference cancellation techniques can be used in compact AAs. Such investigation is vital in interference limited scenarios particularly on the cell edges where there is strong interference from adjacent cells.
- Another area of research interest comes from the impact of polarisation diversity on mobile handsets. For wireless local area network applications with high data rate transfer,

a large number of elements for AA could be required. To minimise the requirement for larger MS physical size, the use of co-located dual polarised elements AA can be employed. The use of this type of element can provide lower correlation since it exploits both spatial and polarisation diversity. The work reported in this thesis assumes random polarisation mixing. In practice, there exists power imbalance between the vertical and horizontal polarisations. It is interesting to investigate the performance of EVS and EVS arrays under different cross power discrimination scenarios and to compare these results to the co-located, dual polarised element AA.

- The theoretical capacity analysis of a typical MIMO system employing various AA topologies is investigated in this thesis. The antenna spacing and number of antennas used in this analysis are usually fixed. However, the capacity bound for size constrained AA topologies is not readily available. It is of interest to determine the maximum number of antennas that can be crammed into a given fixed small spacing before the system capacity saturates. Obviously, in such scenarios, the effect of MC will be very significant and must be included in the theoretical analysis.

Appendix A

Generation of correlated Gaussian random variables

This appendix explains how to generate the cluster power, cluster delay spread and cluster azimuth spread as given in (3.14), (3.15) and (3.16) i.e.

$$P_i[dB] = 9X - L_i \quad (\text{A.1})$$

$$S_{\tau,i}[s] = 0.4\mu s \cdot d_i^{0.5} \cdot 10^{\frac{2Z}{10}} \quad (\text{A.2})$$

$$S_{\varphi,i}[\text{deg}] = 10 \cdot 10^{\frac{2Y}{10}} \quad (\text{A.3})$$

where X , Y , Z are normal RVs with zero mean, unit variance and correlation coefficients $\rho_{xy} = -0.75$, $\rho_{yz} = 0.5$ and $\rho_{zx} = -0.75$. This can be performed in four steps:

1. Generate the covariance matrix, \mathbf{K}

$$\mathbf{K} = \begin{bmatrix} \rho_{xx} & \rho_{xy} & \rho_{xz} \\ \rho_{yx} & \rho_{yy} & \rho_{yz} \\ \rho_{zx} & \rho_{zy} & \rho_{zz} \end{bmatrix} = \begin{bmatrix} 1 & -0.75 & -0.75 \\ -0.75 & 1 & 0.5 \\ -0.75 & 0.5 & 1 \end{bmatrix} \quad (\text{A.4})$$

2. Generate also the vector \mathbf{C} which consists of three independent, zero mean and unit variance Gaussian RVs.
3. Find a matrix \mathbf{A} such that $\mathbf{K} = \mathbf{A}\mathbf{A}^T$. This can be done by finding the matrix of eigenvalues, \mathbf{W} , and the matrix of eigenvectors, \mathbf{V} , of the matrix \mathbf{K} . Then, $\mathbf{A} = \mathbf{V}\mathbf{W}^{\frac{1}{2}}$.
4. Finally, the vector of correlated Gaussian RVs, \mathbf{D} is given by $\mathbf{D} = \mathbf{A}\mathbf{C}$ where $\mathbf{D} = [X, Y, Z]^T$.

Appendix B

Computation of path loss of first cluster

To compute the path loss of the first cluster, L_1 , consider the following equation given by [92]:

$$\begin{aligned} L &= L_1 + L_{LOS} \text{ [dB]} \\ &= L_1(1 + K_0) \end{aligned} \tag{B.1}$$

where L is the global path loss predicted by COST Walfisch-Ikegami and L_{LOS} is the attenuation of the LOS component. The term K_0 is given by

$$\begin{aligned} K_0(EPL) &= N\left(\frac{26 - EPL[\text{dB}]}{6}, 6\right) \text{ [dB]} \\ &= \frac{26 - EPL[\text{dB}]}{6} + 6N(0, 1) \end{aligned} \tag{B.2}$$

where EPL is given by

$$EPL(d) = L_1 - 20 \log_{10} \left(\frac{4\pi d_{MS-BS}}{\lambda} \right) \text{ [dB]} \tag{B.3}$$

d_{MS-BS} is the distance between the MS and BS. Substitute (B.3) into (B.2) and converting the log scale to a linear scale gives

$$K_0 = 1.6469 \cdot L_1^{\frac{1}{6}} \left(\frac{4\pi d}{\lambda} \right)^{\frac{1}{6}} 10^{0.3N(0, 1)} \tag{B.4}$$

Substitute (B.4) into (B.1) to give

$$L = L_1 + L_1^{\frac{7}{6}} (1.6469) \cdot \left(\frac{4\pi d}{\lambda} \right)^{\frac{1}{6}} 10^{0.3N(0, 1)} \tag{B.5}$$

Equation (B.5) can be solved to give a single solution, L_1 , that satisfies the following conditions

$$0 < L_1 < L \quad \text{and} \quad \Im(L_1) = 0 \tag{B.6}$$

where $\Im(\cdot)$ represents the imaginary part of the complex number.

Appendix C

Radiation Patterns

C.1 The ULA with isotropic elements

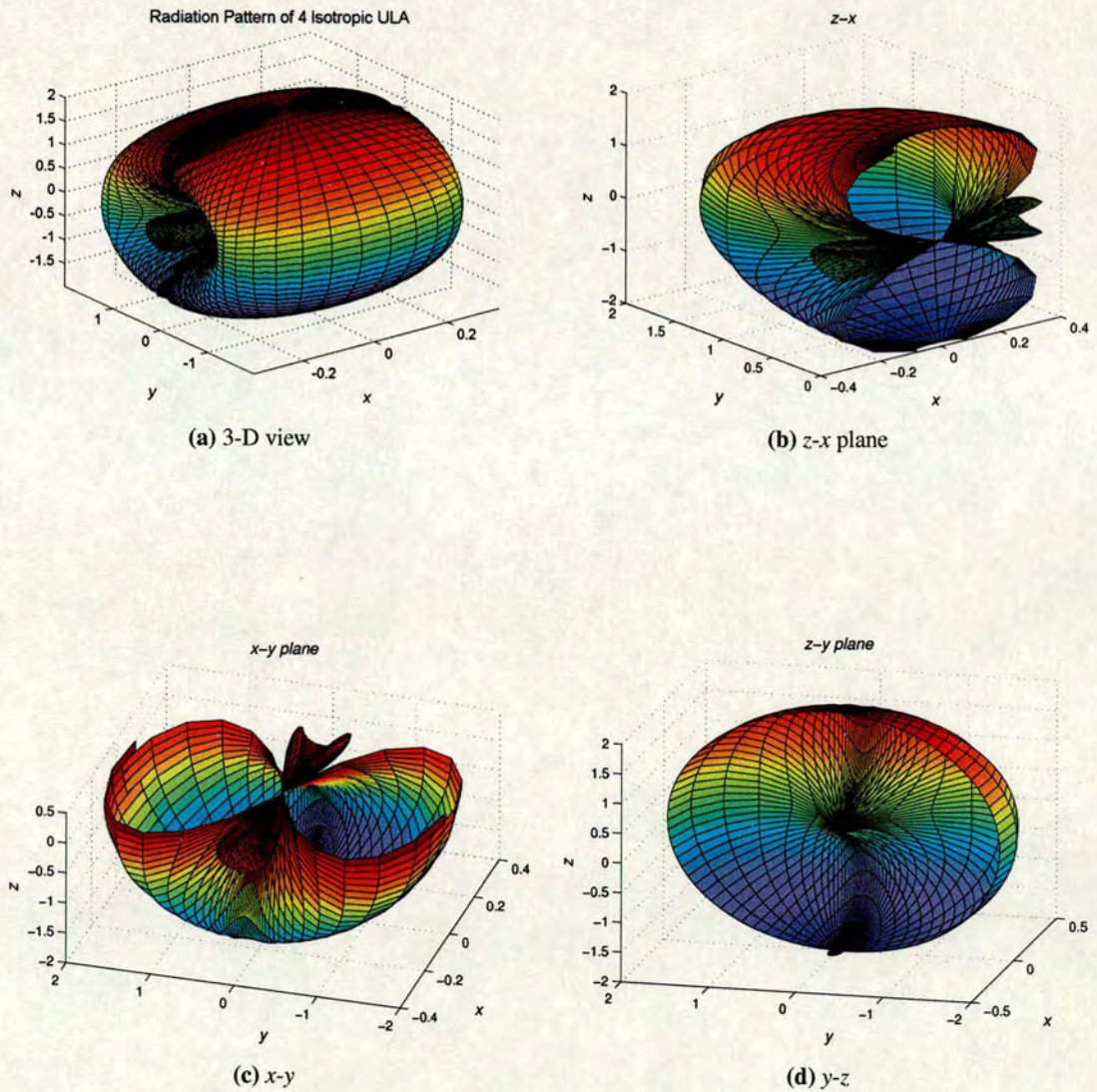


Figure C.1: The radiation pattern for the 4-element isotropic ULA with 0.5λ antenna spacing in 3-D, and with cuts through the z-x plane, x-y plane and y-z plane.

C.2 The UCA with Isotropic

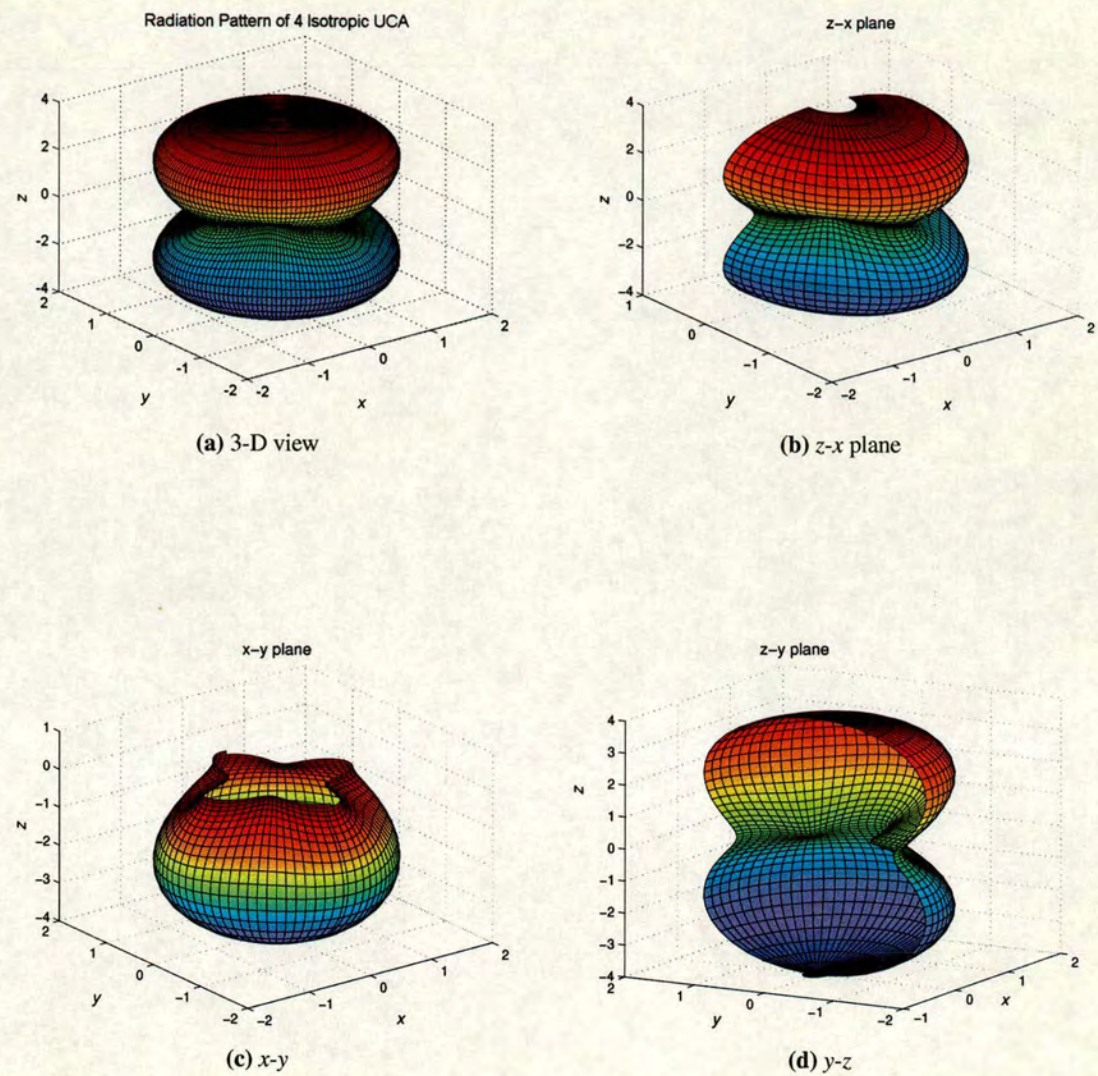


Figure C.2: The radiation pattern for the 4-element isotropic UCA with 0.5λ antenna spacing in 3-D, and with cuts through the z-x plane, x-y plane and y-z plane.

C.3 The URA with isotropic elements

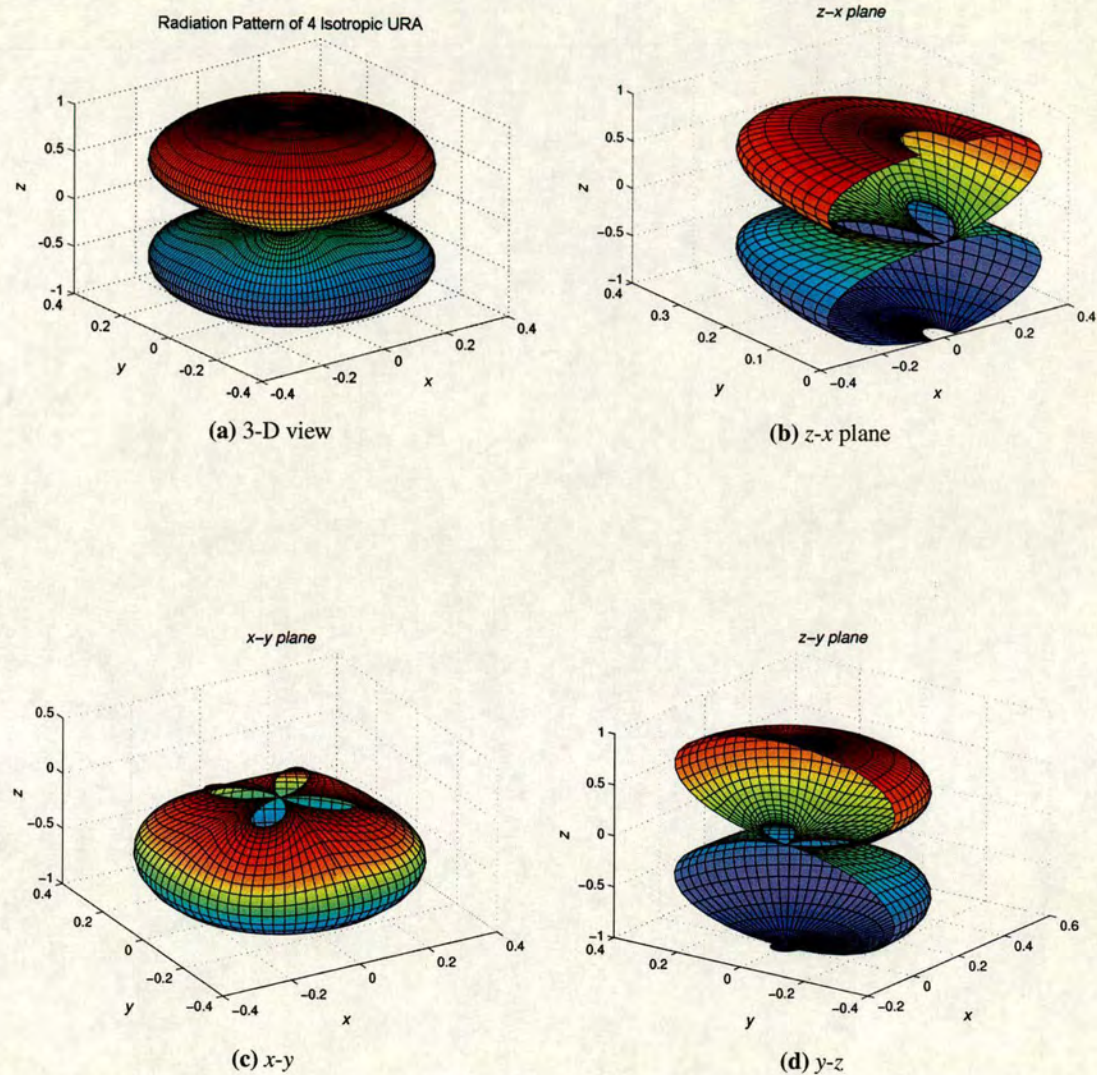


Figure C.3: The radiation pattern for the 4-element isotropic URA with 0.5λ antenna spacing in 3-D and with cuts through the z-x plane, x-y plane and y-z plane.

C.4 The ULA with HW dipoles

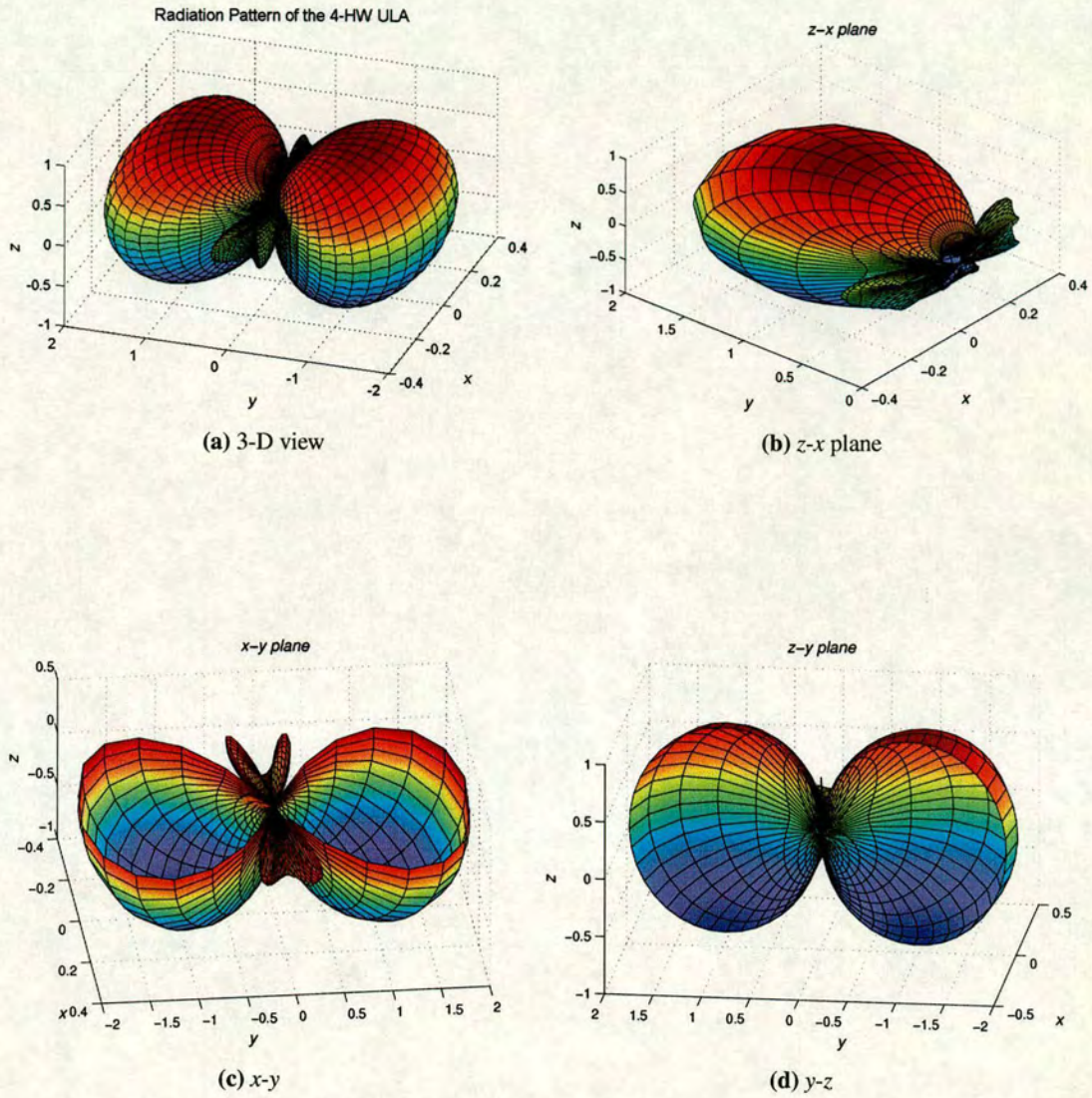


Figure C.4: The radiation pattern for the 4-HW dipoles ULA with 0.5λ antenna spacing in 3-D and with cuts through the z-x plane, x-y plane and y-z plane.

C.5 The UCA with HW dipoles

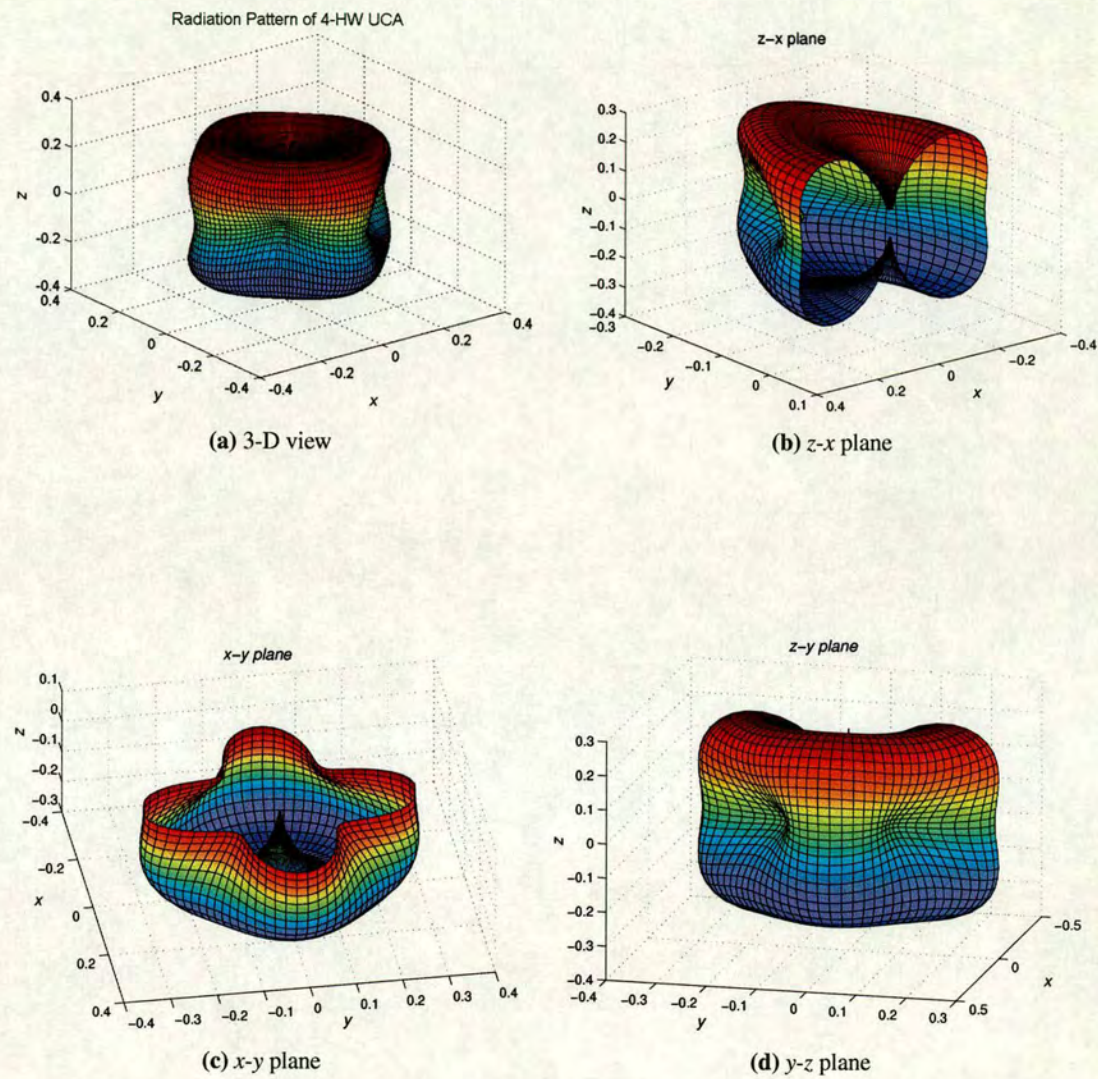


Figure C.5: The radiation pattern for the 4-HW dipoles UCA with 0.5λ circumference antenna spacing in 3-D and with cuts through the z-x plane, x-y plane and y-z plane.

C.6 The URA with HW dipoles

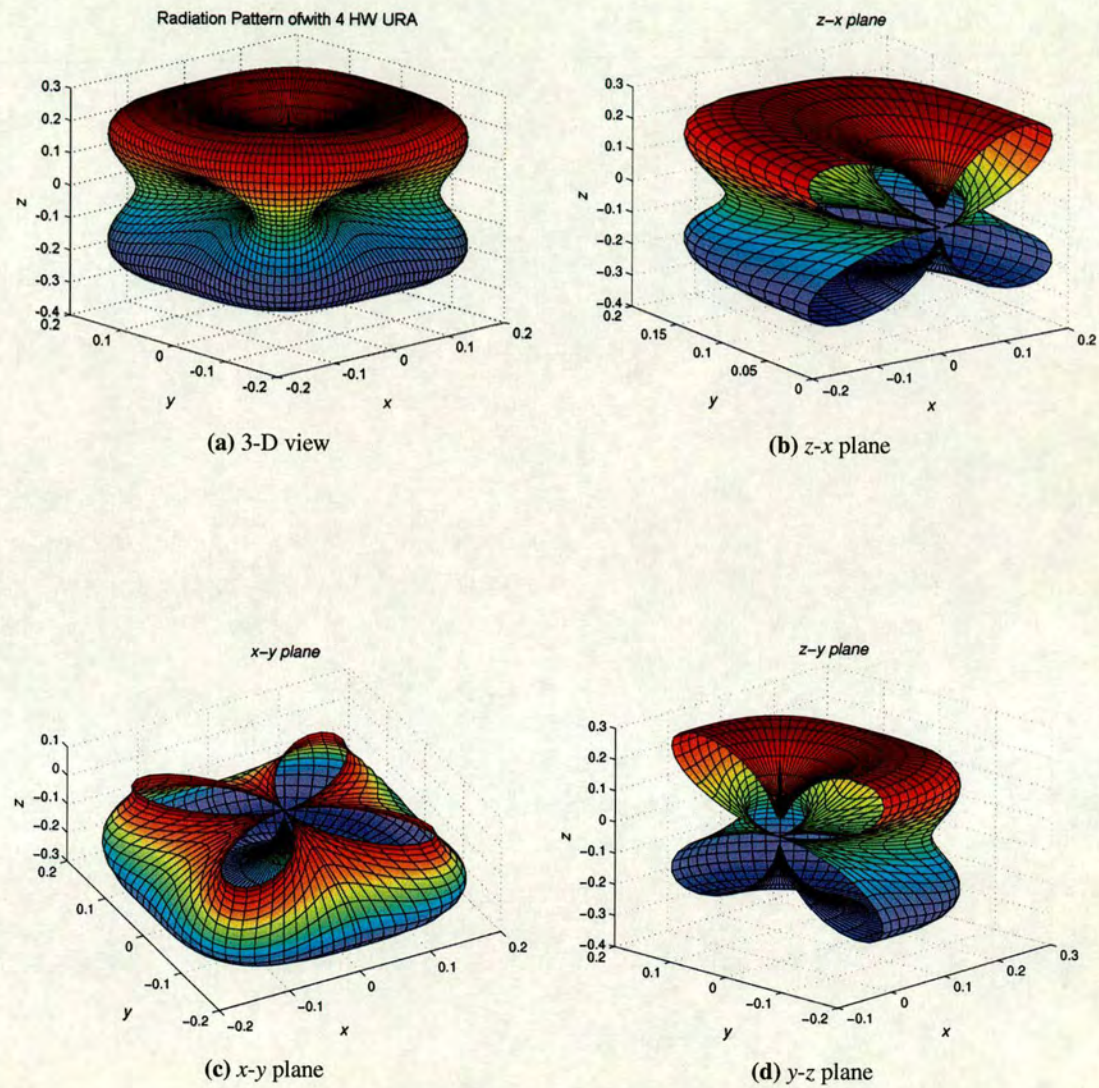


Figure C.6: The radiation pattern for the 4-HW dipoles URA with 0.5λ antenna spacing for d_x and d_y in 3-D and with cuts through the z-x plane, x-y plane and y-z plane.

Appendix D

Derivation of closed-form spatial fading correlation for ULA, UCA and URA

D.1 Closed-form SFC for ULA

From (6.1), the SFC between the antenna elements n and m of the ULA can be expressed as

$$\begin{aligned}
 \rho_{(m,n)} &= \int_{\theta} \int_{\varphi} a_n(\theta, \varphi) a_m^*(\theta, \varphi) p(\theta, \varphi) \sin(\theta) d\theta d\varphi \\
 &= \frac{1}{2\Delta_{\varphi} [\cos(\theta_0 - \Delta_0) - \cos(\theta_0 + \Delta_0)]} \times \\
 &\quad \int_{\varphi_0 - \Delta_{\varphi}}^{\varphi_0 + \Delta_{\varphi}} \int_{\theta_0 - \Delta_{\theta}}^{\theta_0 + \Delta_{\theta}} e^{jk_w(m-n)d \cos(\varphi) \sin(\theta)} \sin(\theta) d\theta d\varphi \\
 &= G_1 \int_{\varphi_0 - \Delta_{\varphi}}^{\varphi_0 + \Delta_{\varphi}} \int_{\theta_0 - \Delta_{\theta}}^{\theta_0 + \Delta_{\theta}} e^{jZ \cos(\varphi) \sin(\theta)} d\theta d\varphi
 \end{aligned} \tag{D.1}$$

where $G_1 = 1/4\Delta_{\varphi} \sin(\theta_0) \sin(\Delta_{\theta})$ and $Z = k_w(m-n)d$. Equation (D.1) can be rewritten as

$$\rho_{(m,n)} = \int_{\varphi_0 - \Delta_{\varphi}}^{\varphi_0 + \Delta_{\varphi}} \int_{\theta_0 - \Delta_{\theta}}^{\theta_0 + \Delta_{\theta}} \left\{ \cos[Z \sin(\theta) \cos(\varphi)] - j \sin[Z \sin(\theta) \cos(\varphi)] \right\} \sin(\theta) d\theta d\varphi \tag{D.2}$$

By making use of the well-known series [143],

$$\cos(z \sin \theta) = J_0(z) + 2 \sum_{k=1}^{\infty} J_{2k}(z) \cos(2k\theta) \tag{D.3}$$

$$\sin(z \sin \theta) = 2 \sum_{k=0}^{\infty} J_{2k+1}(z) \sin \{(2k+1)\theta\} \tag{D.4}$$

$$\cos(z \cos \theta) = J_0(z) + 2 \sum_{k=1}^{\infty} (-1)^k J_{2k}(z) \cos(2k\theta) \tag{D.5}$$

$$\sin(z \cos \theta) = 2 \sum_{k=0}^{\infty} (-1)^k J_{2k+1}(z) \cos \{(2k+1)\theta\} \tag{D.6}$$

The real and imaginary parts of $\rho_{(m,n)}$ can be further expressed as

$$\begin{aligned} \Re[\rho_{(m,n)}] = G_1 \int_{\varphi_0 - \Delta_\varphi}^{\varphi_0 + \Delta_\varphi} \int_{\theta_0 - \Delta_\theta}^{\theta_0 + \Delta_\theta} \left\{ J_0(Z \sin(\theta)) + \right. \\ \left. 2 \sum_{k=1}^{\infty} (-1)^k J_{2k}(Z \sin(\theta)) \cos(2k\varphi) \right\} \sin(\theta) d\theta d\varphi \end{aligned} \quad (\text{D.7})$$

$$\Im[\rho_{(m,n)}] = G_1 \int_{\varphi_0 - \Delta_\varphi}^{\varphi_0 + \Delta_\varphi} \int_{\theta_0 - \Delta_\theta}^{\theta_0 + \Delta_\theta} 2 \sum_{k=1}^{\infty} (-1)^k J_{2k+1}(Z \sin(\theta)) \sin[(2k+1)\varphi] \sin(\theta) d\theta d\varphi \quad (\text{D.8})$$

where J_k is the Bessel function of k^{th} order. In order to evaluate these double integrals we first substitute for the Bessel functions in (D.7) and (D.8), using the following infinite series [144]:

$$J_0(Z) = \sum_{k=0}^{\infty} (-1)^k \frac{Z^{2k}}{2^{2k} (k!)^2} \quad (\text{D.9})$$

$$J_v(Z) = \left(\frac{Z}{2}\right)^v \sum_{k=0}^{\infty} \frac{(-1)^k}{(k!) \Gamma(v+k+1)} \left(\frac{Z}{2}\right)^{2k} \quad (\text{D.10})$$

These series converge rapidly for small values of Z . The use of these series should be satisfactory when considering antenna spacings of practical interest, i.e. up to several carrier wavelengths. Secondly, we use the following indefinite integrals for power of trigonometric functions in (D.11) and (D.12) to obtain the closed-form expressions of (6.2) and (6.3).

$$\int \sin^{2n} x dx = \frac{1}{2^{2n}} \binom{2n}{n} x + \frac{(-1)^n}{2^{2n-1}} \sum_{k=0}^{n-1} (-1)^k \binom{2n}{k} \frac{\sin(2n-2k)x}{2n-2k} \quad (\text{D.11})$$

$$\int \sin^{2n+1} x dx = \frac{(-1)^{n+1}}{2^{2n}} \sum_{k=0}^n (-1)^k \binom{2n+1}{k} \frac{\cos(2n+1-2k)x}{2n+1-2k} \quad (\text{D.12})$$

D.2 Closed-form SFC for UCA

From (6.1), the SFC between the antenna elements n and m of the UCA can be expressed as

$$\begin{aligned}
 \rho_{(m,n)} &= \int_{\varphi_0 - \Delta_\varphi}^{\varphi_0 + \Delta_\varphi} \int_{\theta_0 - \Delta_\theta}^{\theta_0 + \Delta_\theta} e^{j\xi[\cos(\varphi - \psi_m) - \cos(\varphi - \psi_n)]} \sin(\theta) d\theta d\varphi \\
 &= \int_{\varphi_0 - \Delta_\varphi}^{\varphi_0 + \Delta_\varphi} \int_{\theta_0 - \Delta_\theta}^{\theta_0 + \Delta_\theta} e^{j \sin(\theta)[Z_1 \cos(\varphi) + Z_2 \sin(\varphi)]} \sin(\theta) d\theta d\varphi \\
 &= \int_{\varphi_0 + \xi - \Delta_\varphi}^{\varphi_0 + \xi + \Delta_\varphi} \int_{\theta_0 - \Delta_\theta}^{\theta_0 + \Delta_\theta} e^{jZ \sin(\theta) \sin(\beta)} \sin(\theta) d\theta d\beta
 \end{aligned} \tag{D.13}$$

where $\beta = \varphi + \xi$, $Z_1 = k_w r [\cos \psi_m - \cos \psi_n]$ and $Z_2 = k_w r [\sin \psi_m - \sin \psi_n]$ with $Z = \sqrt{Z_1^2 + Z_2^2}$ and $\xi = \tan^{-1}(Z_1/Z_2)$. We can further simplify (D.13) by making use of the well-known series [143] and substituting $\alpha = \xi + \varphi_0$, the real and imaginary parts of $\rho_{(m,n)}$ can be expressed as

$$\begin{aligned}
 \Re[\rho_{(m,n)}] &= G_1 \int_{\alpha - \Delta_\varphi}^{\alpha + \Delta_\varphi} \int_{\theta_0 - \Delta_\theta}^{\theta_0 + \Delta_\theta} \left\{ J_0(Z \sin(\theta)) + \right. \\
 &\quad \left. 2 \sum_{k=1}^{\infty} J_{2k}(Z \sin(\theta)) \cos(2k\beta) \right\} \sin(\theta) d\theta d\beta
 \end{aligned} \tag{D.14}$$

$$\Im[\rho_{(m,n)}] = G_1 \int_{\alpha - \Delta_\varphi}^{\alpha + \Delta_\varphi} \int_{\theta_0 - \Delta_\theta}^{\theta_0 + \Delta_\theta} 2 \sum_{k=1}^{\infty} J_{2k+1}(Z \sin(\theta)) \sin[(2k+1)\beta] \sin(\theta) d\theta d\beta \tag{D.15}$$

Again, we substitute (D.9) and (D.10) into (D.14) and (D.15) and perform the double integration using (D.11) and (D.12) to obtain the closed-form expressions of (6.2) and (6.3).

D.3 Closed-form SFC for URA

From (6.1), the SFC between the antenna elements (n, p) and (m, q) of the URA can be expressed as

$$\begin{aligned}
 \rho_{[(n,p),(m,q)]} &= \int_{\varphi_0 - \Delta_\varphi}^{\varphi_0 + \Delta_\varphi} \int_{\theta_0 - \Delta_\theta}^{\theta_0 + \Delta_\theta} e^{jk_w \sin(\theta)[(p-q)d_y \sin(\varphi) + (n-m)d_x \cos(\varphi)]} \sin(\theta) d\theta d\varphi \\
 &= \int_{\varphi_0 - \Delta_\varphi}^{\varphi_0 + \Delta_\varphi} \int_{\theta_0 - \Delta_\theta}^{\theta_0 + \Delta_\theta} e^{j \sin(\theta)[Z_y \sin(\varphi) + Z_x \cos(\varphi)]} \sin(\theta) d\theta d\varphi \\
 &= \int_{\varphi_0 + \xi - \Delta_\varphi}^{\varphi_0 + \xi + \Delta_\varphi} \int_{\theta_0 - \Delta_\theta}^{\theta_0 + \Delta_\theta} e^{jZ \sin(\theta) \sin(\beta)} \sin(\theta) d\theta d\beta
 \end{aligned} \tag{D.16}$$

where $Z_x = k_w d_x(n - m)$ and $Z_y = k_w d_y(p - q)$ with $Z = \sqrt{Z_x^2 + Z_y^2}$ and $\xi = \tan^{-1}(Z_x/Z_y)$. Note that (D.16) is in fact identical to (D.13) which yields the same closed-form expression as in (6.2) and (6.3) with Z taking different values according to the geometry of the UCA and URA.

Appendix E

Derivation of closed-form spatial fading correlation for EVS

From (6.4), let us define vectors Ψ_1 and Ψ_2 to be the first and second columns of 6×2 matrix $\Psi(\theta, \varphi)$ in (4.12). Thus, the SV of the EVS can be expressed in a compact form in terms of vectors Ψ_1 and Ψ_2 as

$$a(\Theta) = \Psi_1 \sin \gamma e^{j\eta} + \Psi_2 \cos \gamma \quad (\text{E.1})$$

Thus,

$$\begin{aligned} a(\Theta)a^*(\Theta) &= \Psi_1 \Psi_1 \sin^2 \gamma + \Psi_1 \Psi_2 \cos \gamma \sin \gamma e^{jn} + \\ &\quad \Psi_1 \Psi_2 \cos \gamma \sin \gamma e^{-jn} + \Psi_2 \Psi_2 \cos^2 \gamma \end{aligned} \quad (\text{E.2})$$

Following the assumptions prescribed in Chapter 6 i.e.

1. $p(\Theta)$ comprises four statistical independent parameters whereby $p(\Theta)$ can be decomposed to $p(\Theta) = p(\theta)p(\varphi)p(\gamma)p(\eta)$.
2. Both $p(\theta)$ and $p(\varphi)$ are uniformly distributed over the $[\theta_0 - \Delta_\theta, \theta_0 + \Delta_\theta]$ and $[\varphi_0 - \Delta_\varphi, \varphi_0 + \Delta_\varphi]$ respectively.
3. $p(\gamma)$ and $p(\eta)$ are uniformly distributed over the range $[0, \pi/2]$ and $[-\pi, \pi]$ respectively which is referred as random polarization mixing.

Then, the SFC between components (m, n) of an EVS in (6.4) can be simplified to

$$\begin{aligned} \rho_{(m,n)} &= \frac{\int_\varphi \int_\theta a_n(\Theta) a_m^*(\Theta) p(\theta) p(\varphi) \sin(\theta) d\theta d\varphi}{\sqrt{\int_\varphi \int_\theta |a_n(\Theta)|^2 p(\theta) p(\varphi) \sin(\theta) d\theta d\varphi \int_\varphi \int_\theta |a_m(\Theta)|^2 p(\theta) p(\varphi) \sin(\theta) d\theta d\varphi}} \\ &= \frac{\Upsilon_{(m,n)}}{\sqrt{N_{(m,n)}}} \end{aligned} \quad (\text{E.3})$$

where

$$\begin{aligned}\Upsilon_{(m,n)} &= C \int_{\varphi_0-\Delta_\varphi}^{\varphi_0+\Delta_\varphi} \int_{\theta_0-\Delta_\theta}^{\theta_0+\Delta_\theta} (\Psi_{1,m}\Psi_{1,n} + \Psi_{2,m}\Psi_{2,n}) \sin(\theta) d\theta d\varphi \\ &= C(\mathbf{M}_1(m,n) + \mathbf{M}_2(m,n))\end{aligned}\quad (\text{E.4})$$

where $C = 1/8\Delta_\varphi \sin(\theta_0) \sin(\Delta_\theta)$, $\mathbf{M}_1(m,n)$ and $\mathbf{M}_2(m,n)$ are the result of the integration of the terms $\Psi_{1,m}\Psi_{1,n}$ and $\Psi_{2,m}\Psi_{2,n}$ over spherical coordinates. The scalars $\Psi_{1,m}$ and $\Psi_{2,m}$ are the m^{th} entries of the first and second columns of 6×2 matrix $\Psi(\theta, \varphi)$. Since there exists no general expression for the EVS SV i.e. $a_m(\Theta)$ cannot be represented by a single formula for all values of m , we consider all the possible combinations involving $a_m(\Theta)$ for the six EVS components to completely develop the closed-form expression. To do this, let us define the 6×6 matrix \mathbf{M}_1 and \mathbf{M}_2 as the result of integrating all combinations of $\Psi_1\Psi_1^H$ and $\Psi_2\Psi_2^H$ respectively. Note that \mathbf{M}_1 and \mathbf{M}_2 can be completely specified by the integral of a function involving $\cos^a(x) \sin^b(x)$ where a and b are integers. Hence, the closed-form expression of 6×6 matrix \mathbf{M}_1 can be determined as follows

$$\mathbf{M}_1 = \begin{pmatrix} I_{20}K_{21} & I_{11}K_{21} & -I_{10}K_{12} & -I_{11}K_{12} & I_{20}K_{11} & 0 \\ I_{11}K_{21} & I_{02}K_{21} & -I_{01}K_{12} & -I_{02}K_{11} & I_{11}K_{11} & 0 \\ -I_{10}K_{21} & -I_{01}K_{21} & I_{00}K_{03} & I_{01}K_{02} & -I_{10}K_{02} & 0 \\ -I_{11}K_{11} & -I_{02}K_{11} & I_{01}K_{02} & I_{02}K_{01} & -I_{11}K_{01} & 0 \\ I_{20}K_{11} & I_{11}K_{11} & -I_{10}K_{02} & -I_{11}K_{01} & I_{20}K_{01} & 0 \\ 0 & 0 & 0 & 0 & 0 & 0 \end{pmatrix} = \begin{pmatrix} \mathbf{M}_{11} & \mathbf{M}_{12} \\ \mathbf{M}_{13} & \mathbf{M}_{14} \end{pmatrix}\quad (\text{E.5})$$

where

$$I_{ab} = \int_{\varphi_0-\Delta_\varphi}^{\varphi_0+\Delta_\varphi} \cos^a(\varphi) \sin^b(\varphi) d\varphi = f_{ab}(\varphi) \quad (\text{E.6})$$

$$K_{ab} = \int_{\theta_0-\Delta_\theta}^{\theta_0+\Delta_\theta} \cos^a(\theta) \sin^b(\theta) d\theta = f_{ab}(\theta) \quad (\text{E.7})$$

and the 3×3 matrices \mathbf{M}_{11} , \mathbf{M}_{12} , \mathbf{M}_{13} and \mathbf{M}_{14} are the submatrices of \mathbf{M}_1 . The solutions for the I_{ab} and K_{ab} for all possible values of a and b are listed in Table 1 where Δ and μ represent angle spread and mean angle of arrival respectively. Note that, $C(\mathbf{M}_1 + \mathbf{M}_2)$ is in fact a 6×6 covariance matrix. Furthermore, \mathbf{M}_2 can be determined from \mathbf{M}_1 due to symmetrical properties as

a	b	$f_{ab}(x) = \int_{\Delta-\mu}^{\Delta+\mu} \cos^a x \sin^b x dx$
0	0	2Δ
0	1	$2 \sin(\Delta) \sin(\mu)$
0	2	$2 \cos(\Delta) \cos^2(\mu) \sin(\Delta) + \cos(\Delta) \sin(\Delta) + \Delta$
0	3	$-(2 \sin(\Delta) \sin(\mu)/3)[4 \cos^2(\mu) \cos^2(\Delta) - \cos^2(\mu) - \cos^2(\Delta) - 2]$
1	0	$2 \sin(\Delta) \cos(\mu)$
1	1	$2 \sin(\Delta) \cos(\mu) \cos(\Delta) \sin(\mu)$
1	2	$2 \sin^3(\Delta) \cos^3(\Delta)/3 + 2 \sin(\Delta) \cos(\mu) \sin^2(\mu) \cos^2(\Delta)$
2	0	$2 \cos(\Delta) \cos^2(\mu) \sin(\Delta) - \cos(\Delta) \sin(\Delta) + \Delta$
2	1	$2 \sin(\Delta) \cos^2(\mu) \cos^2(\Delta) \sin(\mu) + 2 \sin^3(\mu) \sin^3(\Delta)/3$

Table E.1: Result of integration for I_{ab} and K_{ab} .

$$\mathbf{M}_2 = \begin{pmatrix} \mathbf{M}_{14} & -\mathbf{M}_{13} \\ -\mathbf{M}_{12} & \mathbf{M}_{11} \end{pmatrix} \quad (\text{E.8})$$

Similarly, the denominator of (E.3), $N(m, n)$ can be simplified to

$$\begin{aligned} N_{(m,n)} &= C \int_{\varphi_0-\Delta\varphi}^{\varphi_0+\Delta\varphi} \int_{\theta_0-\Delta\theta}^{\theta_0+\Delta\theta} (\Psi_{1,m}^2 + \Psi_{2,m}^2) \sin(\theta) d\theta d\varphi \times \\ &\quad C \int_{\varphi_0-\Delta\varphi}^{\varphi_0+\Delta\varphi} \int_{\theta_0-\Delta\theta}^{\theta_0+\Delta\theta} (\Psi_{1,n}^2 + \Psi_{2,n}^2) \sin(\theta) d\theta d\varphi \\ &= C^2 \Phi_m \Phi_n \end{aligned} \quad (\text{E.9})$$

where Φ_m and Φ_n are the results of integrating of $\Psi_{1,m}^2 + \Psi_{2,m}^2$ and $\Psi_{1,n}^2 + \Psi_{2,n}^2$ respectively.

The quantities Φ_m and Φ_n are the elements of the vector Φ which can be written as

$$\Phi = \begin{pmatrix} \Phi_1 \\ \Phi_2 \\ \Phi_3 \\ \Phi_4 \\ \Phi_5 \\ \Phi_6 \end{pmatrix} = \begin{pmatrix} I_{20}K_{21} + I_{02}K_{01} \\ I_{02}K_{21} + I_{20}K_{01} \\ I_{00}K_{03} \\ I_{02}K_{01} + I_{20}K_{21} \\ I_{20}K_{01} + I_{02}K_{21} \\ I_{00}K_{03} \end{pmatrix} \quad (\text{E.10})$$

Thus, to completely specify the possible combinations for the denominator, a total of 36 combinations involving the integration given by $\Phi\Phi^H$ are required. The closed-form expression for the denominator of the SFC between the components (m, n) of the EVS is then given by the m^{th} and n^{th} elements of $\Phi\Phi^H$.

Appendix F

Derivation of closed-form spatial fading correlation for EVS arrays

Using the approach in [45] and from (4.13), $a_{EAA(m,p)}(\Theta)$ can be expressed in compact form as

$$\begin{aligned} a_{EAA(m,p)}(\Theta) &= a_{EVS_p}(\Theta) a_{UAA_m}(\theta, \varphi) \\ &= [\Psi_{1,p} \sin(\gamma) e^{j\eta} + \Psi_{2,p} \cos(\gamma)] a_{UAA_m}(\theta, \varphi) \end{aligned} \quad (F.1)$$

where $a_{UAA_m}(\theta, \varphi)$ is the m^{th} element of the ULA, UCA or URA given in (4.4), (4.5) and (4.10) respectively. Similarly, the term $a_{EAA(m,p)}(\Theta) a_{EAA(m,p)}^*(\Theta)$ is then can be represented by

$$\begin{aligned} a_{EAA(m,p)}(\Theta) a_{EAA(m,p)}^*(\Theta) &= [\Psi_1 \Psi_1 \sin^2(\gamma) + \Psi_1 \Psi_1 \cos(\gamma) \sin(\gamma) e^{j\eta} + \\ &\quad \Psi_1 \Psi_1 \cos(\gamma) \sin(\gamma) e^{-j\eta} + \Psi_1 \Psi_1 \sin^2(\gamma)] \times \\ &\quad a_m(\theta, \varphi)_{UAA} a_p^*(\theta, \varphi)_{UAA} \end{aligned} \quad (F.2)$$

Following the assumptions in Chapter 6 and reemphasised in Appendix E, the SFC between element p of the m EVS and element q of the n EVS can be simplified to

$$\begin{aligned} \rho_{(m,n,p,q)} &= \frac{\int_{\varphi} \int_{\theta} a_{EAA(m,p)}(\Theta) a_{EAA(n,q)}^*(\Theta) p(\theta) p(\varphi) \sin(\theta) d\theta d\varphi}{\sqrt{\int_{\varphi} \int_{\theta} |a_{EAA(m,p)}(\Theta)|^2 \sin(\theta) p(\theta) p(\varphi) d\theta d\varphi}} \times \\ &\quad \frac{1}{\sqrt{\int_{\varphi} \int_{\theta} |a_{EAA(n,q)}(\Theta)|^2 \sin(\theta) p(\theta) p(\varphi) d\theta d\varphi}} \\ &= \frac{\Upsilon_{(m,n,p,q)}}{\sqrt{N_{m,n,p,q}}} \end{aligned} \quad (F.3)$$

F.1 Closed-form SFC for ULA-EVS

For the ULA-EVS, $\Upsilon_{(m,n,p,q)}$ is given by

$$\Upsilon_{(m,n,p,q)} = G_2 \int_{\varphi_0 - \Delta_\varphi}^{\varphi_0 + \Delta_\varphi} \int_{\theta_0 - \Delta_\theta}^{\theta_0 + \Delta_\theta} \left(\Psi_{1,p} \Psi_{1,q} + \Psi_{2,p} \Psi_{2,q} \right) e^{jk_w d(m-n) \sin(\theta) \cos(\varphi)} \sin(\theta) d\theta d\varphi \quad (\text{F.4})$$

where $G_2 = 1/8\Delta_\varphi \sin(\theta_0) \sin(\Delta_\theta)$. Let us define $\mathbf{Q}_1(p, q) = \Psi_{1,p} \Psi_{1,q}$, $\mathbf{Q}_2(p, q) = \Psi_{2,p} \Psi_{2,q}$ and $\mathbf{Q} = \mathbf{Q}_1 + \mathbf{Q}_2$ where \mathbf{Q}_1 and \mathbf{Q}_2 are given respectively by

$$\mathbf{Q}_1 = \begin{pmatrix} C^{22}S^{00} & C^{12}S^{10} & -C^{11}S^{01} & -C^{11}S^{11} & C^{21}S^{00} & 0 \\ C^{12}S^{10} & C^{02}S^{20} & -C^{01}S^{11} & -C^{01}S^{20} & C^{11}S^{10} & 0 \\ -C^{12}S^{00} & -C^{02}S^{10} & C^{00}S^{02} & C^{00}S^{11} & -C^{10}S^{01} & 0 \\ -C^{11}S^{10} & -C^{01}S^{20} & C^{00}S^{11} & C^{00}S^{20} & -C^{10}S^{10} & 0 \\ C^{21}S^{00} & C^{11}S^{10} & -C^{10}S^{01} & -C^{10}S^{10} & C^{20}S^{00} & 0 \\ 0 & 0 & 0 & 0 & 0 & 0 \end{pmatrix} = \begin{pmatrix} \mathbf{Q}_{11} & \mathbf{Q}_{12} \\ \mathbf{Q}_{13} & \mathbf{Q}_{14} \end{pmatrix} \quad (\text{F.5})$$

$$\mathbf{Q}_2 = \begin{pmatrix} \mathbf{Q}_{14} & -\mathbf{Q}_{13} \\ -\mathbf{Q}_{12} & \mathbf{Q}_{11} \end{pmatrix} \quad (\text{F.6})$$

where C^{ab} and S^{ab} signify $\cos^a(\varphi) \cos^b(\theta)$ and $\sin^a(\varphi) \sin^b(\theta)$ respectively. Taking the real part of (F.4) and making use of the well-known series, $\Re [\Upsilon_{(m,n,p,q)}]$ is given by

$$\begin{aligned} \Re [\Upsilon_{(m,n,p,q)}] &= G_2 \int_{\varphi_0 - \Delta_\varphi}^{\varphi_0 + \Delta_\varphi} \int_{\theta_0 - \Delta_\theta}^{\theta_0 + \Delta_\theta} \mathbf{Q}(p, q) \sin(\theta) \times \\ &\quad \left\{ J_0(Z \sin(\theta)) + 2 \sum_{k=1}^{\infty} (-1)^k J_{2k}(Z \sin(\theta)) \cos(2k\varphi) \right\} d\theta d\varphi \quad (\text{F.7}) \end{aligned}$$

In the case of $\mathbf{Q}(p, q) \neq 0$, the first term of (F.7), $\Re [\Upsilon_{(m,n,p,q)_1}]$ can be simplified by substituting the Bessel functions in (F.7) using the infinite series in (D.9) and (D.10) i.e.

$$\begin{aligned} \Re [\Upsilon_{(m,n,p,q)_1}]_1 &= G_2 \sum_{k=0}^{\infty} \frac{(-1)^k}{(k!)^2} \left(\frac{Z}{2}\right)^{2k} \int_{\varphi_0-\Delta_\varphi}^{\varphi_0+\Delta_\varphi} \int_{\theta_0-\Delta_\theta}^{\theta_0+\Delta_\theta} \mathbf{Q}(p, q) \sin^{2k+1}(\theta) d\theta d\varphi \\ &= G_2 \sum_{k=0}^{\infty} \frac{(-1)^k}{(k!)^2} \left(\frac{Z}{2}\right)^{2k} \int_{\varphi_0-\Delta_\varphi}^{\varphi_0+\Delta_\varphi} \int_{\theta_0-\Delta_\theta}^{\theta_0+\Delta_\theta} \left\{ \cos^{a_1}(\varphi) \sin^{a_2}(\varphi) \times \right. \\ &\quad \left. \cos^{b_1}(\theta) \sin^{b_2}(\theta) + \cos^{c_1}(\varphi) \sin^{c_2}(\varphi) \cos^{d_1}(\theta) \sin^{d_2}(\theta) \right\} \sin^{2k+1}(\theta) d\theta d\varphi \\ &= G_2 \sum_{k=0}^{\infty} \frac{(-1)^k}{(k!)^2} \left(\frac{Z}{2}\right)^{2k} \left\{ R_{a_1 a_2 00} S_{b_1 b_2 b_3 00} + R_{c_1 c_2 00} S_{d_1 d_2 d_3 00} \right\} \end{aligned} \quad (\text{F.8})$$

where $b_3 = d_3 = 1$ and the functions R and S are the results of integration of

$$R_{tuvw} = \int_{\varphi_0-\Delta_\varphi}^{\varphi_0+\Delta_\varphi} \cos^t(\varphi) \sin^u(\varphi) \cos^v(2k\varphi) \cos^w[(2k+1)\varphi] d\varphi \quad (\text{F.9})$$

$$S_{tuvwx} = \int_{\theta_0-\Delta_\theta}^{\theta_0+\Delta_\theta} \cos^t(\theta) \sin^u(\theta) \sin^{v(2k+1)}(\theta) \sin^{w[2(k+l)+1]}(\theta) \sin^{x[2(k+l+1)]}(\theta) d\theta \quad (\text{F.10})$$

Note that the functions in (F.9) and (F.10) can be reduced to integral functions involving $\cos^a(x) \sin^b(x)$ as in (E.6) for a given set of arguments using the expansions of multiple angle sinusoids into power series (see [144] 1.332, pp. 34). Taking a simple case for illustration, the function R_{tu01} can be simplified to the form of $\cos^a(x) \sin^b(x)$ by first expanding the term $\cos[(2k+1)]$ using the trigonometric identity i.e. $R_{tu01} = \int_{\varphi_0-\Delta_\varphi}^{\varphi_0+\Delta_\varphi} \left\{ \cos^{t+1}(\varphi) \sin^u(\varphi) \cos(2k\varphi) - \cos^t(\varphi) \sin^{u+1}(\varphi) \sin(2k\varphi) \right\} d\varphi$. Further we can expand the $\cos(2k\varphi)$ and $\sin(2k\varphi)$ terms into power series of $\sin(\varphi)$ and $\cos(\varphi)$ through

$$\cos(2kx) = 1 - \frac{4n^2}{2!} \sin^2(x) + \frac{4n^2(4n^2 - 2^2)}{4!} \sin^4(x) + \frac{4n^2(4n^2)(4n^2 - 4^2)}{6!} \sin^6(x) + \dots \quad (\text{F.11})$$

$$\sin(2kx) = 2n \cos(x) \left\{ \sin(x) - \frac{4n^2 - 2^2}{3!} \sin^3(x) + \frac{(4n^2 - 2^2)(4n^2 - 4^2)}{5!} \sin^5(x) + \dots \right\} \quad (\text{F.12})$$

Hence, the integral function of that in E.6 can be obtained.

Similarly, the second term of (F.7), $\Re [\Upsilon_{(m,n,p,q)_2}]$ turns out to be

$$\begin{aligned}
 \Re [\Upsilon_{(m,n,p,q)_2}] &= G_2 \sum_{k=1}^{\infty} \sum_{l=0}^{\infty} \frac{(-1)^{k+1}}{l! \Gamma(2k+l+1)} \left(\frac{Z}{2}\right)^{2(k+l)} \times \\
 &\quad \int_{\varphi_0-\Delta_\varphi}^{\varphi_0+\Delta_\varphi} \int_{\theta_0-\Delta_\theta}^{\theta_0+\Delta_\theta} \left\{ \cos^{a_1}(\varphi) \sin^{a_2}(\varphi) \cos^{b_1}(\theta) \sin^{b_2}(\theta) + \right. \\
 &\quad \left. \cos^{c_1}(\varphi) \sin^{c_2}(\varphi) \cos^{d_1}(\theta) \sin^{d_2}(\theta) \right\} \cos(2k\varphi) \sin^{2(k+l)+1}(\theta) d\theta d\varphi \\
 &= G_2 \sum_{k=1}^{\infty} \sum_{l=0}^{\infty} \frac{(-1)^{k+1}}{l! \Gamma(2k+l+1)} \left(\frac{Z}{2}\right)^{2(k+l)} \times \\
 &\quad \left\{ R_{a_1 a_2 a_3 0} S_{b_1 b_2 0 b_4 0} + R_{c_1 c_2 c_3 0} S_{d_1 d_2 0 d_4 0} \right\}
 \end{aligned} \tag{F.13}$$

where $a_3 = c_3 = b_4 = d_4 = 1$. Also, the imaginary part of (F.4) can be expressed as

$$\begin{aligned}
 \Im [\Upsilon_{(m,n,p,q)}] &= 2G_2 \sum_{k=1}^{\infty} \sum_{l=0}^{\infty} \frac{(-1)^{k+1}}{l! \Gamma(2k+l+1)} \left(\frac{Z}{2}\right)^{2(k+l)+1} \times \\
 &\quad \int_{\varphi_0-\Delta_\varphi}^{\varphi_0+\Delta_\varphi} \int_{\theta_0-\Delta_\theta}^{\theta_0+\Delta_\theta} \left\{ \cos^{a_1}(\varphi) \sin^{a_2}(\varphi) \cos^{b_1}(\theta) \sin^{b_2}(\theta) \right. \\
 &\quad \left. + \cos^{c_1}(\varphi) \sin^{c_2}(\varphi) \cos^{d_1}(\theta) \sin^{d_2}(\theta) \right\} \sin^{2(k+l)+1}(\theta) \cos[(2k+1)\varphi] d\theta d\varphi \times \\
 &= G_2 \sum_{k=0}^{\infty} \sum_{l=0}^{\infty} \frac{(-1)^{k+1}}{l! \Gamma(2k+l+2)} \left(\frac{Z}{2}\right)^{2(k+l)+1} \\
 &\quad \left\{ R_{a_1 a_2 0 a_4} S_{b_1 b_2 0 0 b_5} + R_{c_1 c_2 0 c_4} S_{d_1 d_2 0 0 d_5} \right\}
 \end{aligned} \tag{F.14}$$

where $a_4 = c_4 = b_5 = d_5 = 1$. Similarly, the denominator of (F.3) for the ULA-EVS configuration can be simplified to give the same closed-form expression as that of the denominator of (E.3).

F.2 Closed-form SFC for UCA-EVS and URA-EVS

As shown in Appendix D the closed-form SFC expressions for the UCA and URA are identical. Since using a six-element EVS at each array position does not introduce an additional spatial factor into the SV equation, the SFC of the EVS in UCA and URA would result in the same

closed-form expressions. For the UCA, $\Upsilon_{(m,n,p,q)}$ is given by

$$\Upsilon_{(m,n,p,q)} = G_2 \int_{\varphi_0 - \Delta_\varphi}^{\varphi_0 + \Delta_\varphi} \int_{\theta_0 - \Delta_\theta}^{\theta_0 + \Delta_\theta} \left(\Psi_{1,p} \Psi_{1,q} + \Phi_{2,p} \Phi_{2,q} \right) e^{j\xi [\cos(\varphi - \psi_m) - \cos(\varphi - \psi_n)]} d\theta d\varphi \quad (\text{F.15})$$

Again defining \mathbf{Q}_1 , \mathbf{Q}_2 and \mathbf{Q} and performing the similar steps as in the case of ULA-EVS in Appendix C.2, it can be shown that the real and imaginary parts of (F.15) are given by

$$\begin{aligned} \Upsilon_{(m,n,p,q)} = G_2 \Bigg\{ & \sum_{k=0}^{\infty} \frac{(-1)^k}{(k!)^2} \left(\frac{Z}{2} \right)^{2k} \left(U_{a_1 a_2 00} S_{b_1 b_2 b_3 00} + U_{c_1 c_2 00} S_{d_1 d_2 d_3 00} \right) + \\ & 2 \sum_{k=1}^{\infty} \sum_{l=0}^{\infty} \frac{(-1)^l}{l! \Gamma(2k + l + 1)} \left(\frac{Z}{2} \right)^{2(k+l)} \left(U_{a_1 a_2 a_3 0} S_{b_1 b_2 0 b_4 0} + U_{c_1 c_2 c_3 0} S_{d_1 d_2 0 d_4 0} \right) + \\ & j 2 \sum_{k=0}^{\infty} \sum_{l=0}^{\infty} \frac{(-1)^l}{l! \Gamma(2k + l + 2)} \left(\frac{Z}{2} \right)^{2(k+l)+1} \left(U_{a_1 a_2 0 a_4} S_{b_1 b_2 00 b_5} + \right. \\ & \left. U_{c_1 c_2 0 c_4} S_{d_1 d_2 00 d_5} \right) \Bigg\} \quad (\text{F.16}) \end{aligned}$$

where

$$U_{tuvw} = \int_{\varphi_0 - \Delta_\varphi}^{\varphi_0 + \Delta_\varphi} \cos^t(\varphi) \sin^u(\varphi) \cos^v[(2k(\varphi + \xi))] \sin^w[(2k + 1)(\varphi + \xi)] d\varphi \quad (\text{F.17})$$

Similarly, (F.17) can be reduced to integral functions involving $\cos^a(x) \sin^b(x)$ using the functions of multiples angle in terms of power of the functions. Again, the denominator of (F.2) for the UCA-EVS and URA-EVS configurations is given by the same closed-form expression as that of the denominator of (E.3). For the URA-EVS, $\Upsilon_{(m,n,p,q)}$ is given exactly by (F.17) but with Z takes the value for the URA geometry.

Appendix G

Original publications

G.1 Journal papers

- [J1] [†]**S. K. Yong** and J. S. Thompson, "A 3-Dimensional spatial fading correlation model for uniform rectangular arrays," *IEEE Antennas and Wireless Propagation Letters*, vol. 2, no. 12, pp. 182-185, 2003.
- [J2] **S. K. Yong** and J. S. Thompson, "3-Dimensional spatial fading correlation models for compact MIMO receivers," *IEEE Transactions on Wireless Communications*, submitted in October 2003.
- [J3] **S. K. Yong** and J. S. Thompson, "The effect of channel conditions and antenna parameters on the performance analysis of compact antenna arrays," *IEE Proceedings on Communications*, submitted in July 2003, revised in January 2004.

G.2 Conference papers

- [C1] **S. K. Yong**, J. S. Thompson and S. McLaughlin, "The Performance of Diversity Combining Techniques for Antenna Arrays," in *Proceedings of 6th London Communication Symposium (LCS'01)*, pp. 95-98, London, UK, September 2001.
- [C2] [†]**S. K. Yong**, J. S. Thompson and S. McLaughlin, "Implementation of COST259 channel models using tapped delay line for multiple antenna receivers," in *Proceedings of IEE 3rd International Conference on 3G 2002 Mobile Communication Technologies (3G'02)*, pp. 165-169, London, UK, May 2002.
- [C3] **S. K. Yong**, J. S. Thompson and S. McLaughlin, "Capacity evaluation for multiple antennas using wideband directional channel model for different channel conditions," in *Proceedings of IEE Conference on Getting the Most Out of the Radio Spectrum*, pp. 27/1-27/4, London, UK, October 2002.

[†]These papers are reprinted in this appendix.

- [C4] [†]**S. K. Yong** and J. S. Thompson, "The impact of angle of arrival distribution on the performance analysis of different antenna arrays architectures," in *Proceedings of 12th IEEE International Conference on Antennas and Propagation (ICAP 2003)*, vol. 2, pp. 840-843, Exeter, UK, March 2003.
- [C5] [†]**S. K. Yong** and J. S. Thompson, "The impact of antenna parameters on the performance of different antenna arrays architectures," in *Proceedings of 5th European Personal Mobile Communications Conference (EPMCC 2003)*, vol. 1, pp. 5-10, Glasgow, UK, April 2003.
- [C6] [†]**S. K. Yong** and J. S. Thompson, "The effect of various channel conditions on the performance of various antenna arrays architectures," in *Proceedings of 58th IEEE Vehicular Technology Conference (VTC 2003-Fall)*, vol. 1, pp. 6-10, Orlando, USA, October 2003.
- [C7] P. M. Grant, J. S. Thompson, C. C. Chong, Y. Lee and **S. K. Yong**, "Mobile communications activities in wireless access," in *Proceedings of 14th IEEE International Symposium on Personal, Indoor and Mobile Radio Communications (PIMRC 2003)*, vol. 3, pp. 2650-2654, Beijing, China, September 2003.
- [C8] **S. K. Yong** and J. S. Thompson, "On the analysis of spatial fading correlation for electromagnetic vector sensor in uniform circular arrays," in *Proceedings of 9th IEEE International Symposium on Wireless Personal Multimedia Communications (WPMC 2003)*, Yokosuka, Kanagawa, Japan, October 2003, in press.
- [C9] **S. K. Yong** and J. S. Thompson, "A 3-Dimensional spatial fading correlation model for electromagnetic vector sensors," in *Proceedings of IEEE 6th International Symposium on Antenna, Propagation and EM Theory (ISAPE'03)*, pp. 843-846, Beijing, China, October 2003.

G.3 MVCE internal reports

- [R1] **S. K. Yong**, J. S. Thompson and S. McLaughlin, "Overview of diversity combining techniques," *Mobile VCE Core 2 Research Programme, WP 3.3.2, Internal Report I*, January 2001.
- [R2] **S. K. Yong**, J. S. Thompson and S. McLaughlin, "On the implementation of COST259 channel models," *Mobile VCE Core 2 Research Programme, WP 3.3.2, Internal Report*

II, July 2001.

- [R3] **S. K. Yong** and J. S. Thompson, "Antenna and channel models," *Mobile VCE Core 2 Research Programme, WP 3.3.2, Internal Report III (Deliverable)*, January 2002.
- [R4] **S. K. Yong** and J. S. Thompson, "On the effect of channel conditions and antenna parameter to the performance of antenna arrays," *Mobile VCE Core 2 Research Programme, WP 3.3.2, Internal Report IV*, July 2002.
- [R5] **S. K. Yong** and J. S. Thompson, "3-Dimensional spatial fading correlation models for antenna arrays," *Mobile VCE Core 2 Research Programme, WP 3.3.2, Internal Report V*, March 2003.

G.4 COST 273 submissions

- [TD1] **S. K. Yong** and J. S. Thompson, "A closed-form spatial fading correlation model for electromagnetic vector sensors," COST 273 Temporary Documents TD(03)106, Paris, France, May 2003.

A Three-Dimensional Spatial Fading Correlation Model for Uniform Rectangular Arrays

S. K. Yong, *Student Member, IEEE*, and J. S. Thompson, *Member, IEEE*

Abstract—In this letter, a closed-form expression for the spatial fading correlation function of a uniform rectangular array (URA) in a three-dimensional (3-D) multipath channel is derived. The fading correlation function is expressed in terms of both the azimuth and elevation angle of arrival as well as the antenna spacing and geometry of the URA. Verification is achieved by means of computer simulation where the theoretical and simulation results are shown to be in good agreement. Our results demonstrate that azimuth spread (AS) is the primary determinant of the antenna correlation and the impact of the elevation spread is mainly noticeable at low AS values. The results obtained in this letter are vital for capacity analysis in multiple-input multiple-output systems, as well as for sensitivity analysis of the antenna array under study.

Index Terms—Azimuth spread, elevation spread, radio propagation, spatial fading correlation, uniform rectangular arrays (URA).

I. INTRODUCTION

ANTENNA arrays (AAs) are one of the most promising candidates for capacity and signal quality enhancement in wireless communications systems. Since the functionality of the AA is mainly based on the exploitation of the spatial properties of the multipath channel, it is imperative to gain a good understanding of the influence of angular parameters on the performance of AAs. In general, the angular domain comprises both the azimuth-of-arrival (AOA) and elevation-of-arrival (EOA). One investigation that incorporates a three-dimensional (3-D) approach has been reported in [1], where the author assumed that AOA is uniformly distributed over $[0, 2\pi]$, while the EOA is nonuniformly distributed around the horizontal plane. The spatial correlation (SC) is expressed in terms of an integral of a Bessel function of first kind of zero order. However, no closed-form expression is given in [1] to relate different parameters associated with AOA, EOA, and the geometry of the AA so that the SC can be easily evaluated. Such a closed-form expression is needed to simplify the analyses of the impact of these parameters on the system performance. Recent results in [2], [3] demonstrate that it is not always true to assume isotropic scattering, particularly in dense urban areas with street dominated environments where the *canyon effect* is significant. Moreover, in AA terminal receivers, the beamforming algorithm itself will determine the effective angle spread that is being observed.

Prior works such as [4] and [5] expressed the SC functions for the case of uniform linear arrays and uniform circular arrays under uniform and Laplacian AOA probability density functions (pdfs). While the results in these works are important for diversity studies, they are limited to the azimuth plane only. Here, we consider the impact of both the AOA and the EOA on the SC for uniform rectangular arrays (URA). Our analysis is important as the performance of the handset AAs is also dependent on the effect of EOA since the handset could be randomly oriented [6]. Furthermore, recent measurement results have also demonstrated the significance of the EOA where [2] reported that about 65% of the energy was incident with elevation larger than 10° with respect to azimuth plane. Interestingly, [3] reported an average elevation spread (ES) of 9° for several environments ranging from indoor to outdoor. The major applications of our work are twofold. First, for capacity analysis in multiple-input multiple-output (MIMO) systems as the developed SC function can be applied to determine the correlation matrix at both the base station (BS) and mobile station (MS) [7]. Second, to study the sensitivity of the AA under various channel conditions as demonstrated in [8]. These applications further emphasize the importance of our work. This letter is organized as follows: Section II describes the directional channel model and the steering vector (SV) of the URA; Section III derives the closed-form expression for the spatial fading correlation function in terms of AOA, EOA, antenna spacing, and antenna geometry; Section IV presents some analytical and simulation results to highlight the impact of both the AOA and EOA on the SC. Finally, in Section V, some concluding remarks are drawn.

II. DIRECTIONAL CHANNEL MODEL

In this letter, the performance analysis is done by using a frequency nonselective directional Rayleigh fading channel model. The channel impulse response, $h(t)$ can be expressed as

$$h(t) = \sum_{l=1}^L \alpha_l(t) \cdot \mathbf{a}(\varphi_l, \theta_l) \quad (1)$$

where L is the total number of multipath components (MPCs), $\alpha_l(t)$ is the complex amplitude of the l^{th} MPC, $\mathbf{a}(\varphi_l, \theta_l)$ is the SV of the URA, where the scalars $0 \leq \varphi_l < 2\pi$ and $0 \leq \theta_l < \pi$ are the azimuth and elevation angles of the l^{th} MPC defined with respect to the positive x - and z -axis, respectively, as illustrated in Fig. 1. For a size $N \times P$ URA located in the x - y plane with

Manuscript received June 30, 2003; revised August 22, 2003. This work was supported by Virtual Centre of Excellence in Mobile and Personal Communications (Mobile VCE).

The authors are with the Institute for Digital Communications, University of Edinburgh, Edinburgh EH9 3JL, U.K. (e-mail: ysk@ieee.org).
Digital Object Identifier 10.1109/LAWP.2003.819666

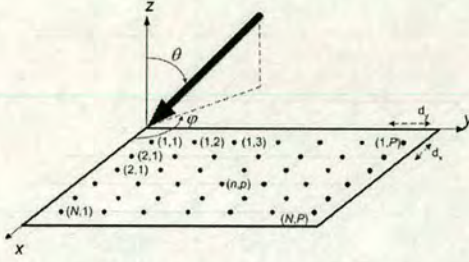


Fig. 1. Plane wave propagation where the incoming signal paths are at a discrete MAOA, AS, MEOA, and ES.

the phase reference at the origin, the SV for the azimuth, φ and elevation, θ is given by

$$\begin{aligned} \mathbf{a}(\varphi, \theta) &= \text{vec}(\mathbf{a}_N(\mu) \mathbf{a}_P^T(v)) \\ &= \begin{bmatrix} 1, e^{jv}, \dots, e^{j(P-1)v}, e^{j\mu}, e^{j(\mu+v)}, \dots, \\ e^{j[\mu+(P-1)v]}, \dots, e^{j(N-1)\mu}, \dots, e^{j[(N-1)\mu+(P-1)v]} \end{bmatrix}^T \end{aligned} \quad (2)$$

where $\mu = 2\pi d_x \cos \varphi \sin \theta / \lambda$, $v = 2\pi d_y \sin \varphi \sin \theta / \lambda$, $\mathbf{a}_N(\mu) = [1, e^{j\mu}, \dots, e^{j(N-1)\mu}]^T$, and $\mathbf{a}_P(v) = [1, e^{jv}, \dots, e^{j(P-1)v}]^T$. The notation $[\cdot]^T$ denotes the transpose and λ is the wavelength. The scalars d_x and d_y are the spacings between the array elements parallel to the x - and y -axis, respectively. The operator $\text{vec}(\cdot)$ maps the $N \times P$ matrix to an $NP \times 1$ vector by stacking the columns of the matrix. The index n and p refer to the antenna element located at n^{th} row and p^{th} column of the URA, denoted as (n, p) .

III. SPATIAL FADING CORRELATION

The spatial fading correlation between antennas at positions (n, p) and (m, q) is defined as

$$\begin{aligned} \rho_{[(n,p),(m,q)]} &= E[a_{np}(\varphi, \theta) a_{mq}^*(\varphi, \theta)] \\ &= \int_{\varphi} \int_{\theta} a_{np}(\varphi, \theta) a_{mq}^*(\varphi, \theta) p(\varphi, \theta) \sin(\theta) d\theta d\varphi \end{aligned} \quad (3)$$

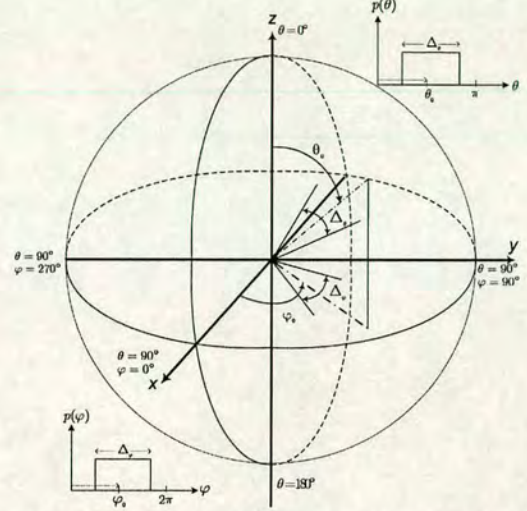


Fig. 2. Illustration of the MAOA, AS, MEOA, and ES used throughout the analysis.

where $E[\cdot]$ denotes expectation, the superscript $*$ denotes the complex conjugate and $a_{np}(\varphi, \theta)$ is the (n, p) entry of $\mathbf{a}(\varphi, \theta)$. The scalar $p(\varphi, \theta)$ is the joint pdf of the angles of arrival of the MPC. Assuming that the AOA and EOA are independent of each other, the function $p(\varphi, \theta)$ can be decomposed to $p(\varphi)p(\theta)$. We concentrate our analysis on uniform AOA and EOA distributions since [9] shows that the key parameter to the system performance is the spread of the MPC and not the type of pdf under investigation. As shown in the Appendix, the real and imaginary part of the $\rho_{[(n,p),(m,q)]}$ can be expressed as (4) and (5), respectively, shown at the bottom of the page, where Δ_θ , Δ_φ , θ_o and φ_o are the ES, azimuth spread (AS), mean elevation-of-arrival (MEOA), and mean azimuth-of-arrival (MAOA), respectively. The scalars $\alpha = \varphi_o + \gamma$ and Z are defined in the Appendix. Throughout our analysis, the AS and ES are defined as the maximum deviation of the angle spread from the MAOA and MEOA, respectively, as depicted in Fig. 2. Using

$$\begin{aligned} \text{Re} \{ \rho_{[(n,p),(m,q)]} \} &= \frac{-1}{\sin c(\Delta_\theta) \sin(\theta_o)} \left\{ \sum_{k=0}^{\infty} \sum_{l=0}^k \frac{(-1)^{2k+1+l} Z^{2k}}{2^4 (k!)^2} \binom{2k+1}{l} \text{sinc}[(2k+1-2l)\Delta_\theta] \sin[(2k+1-2l)\theta_o] \right. \\ &\quad \left. + 2 \sum_{k=1}^{\infty} \sum_{l=0}^k \sum_{p=0}^{k+l} \frac{(-1)^{k+2l+1+p}}{l! \Gamma(2k+l+1)} \left(\frac{Z^{2(k+l)}}{2^4 (k+l)!} \right) \text{sinc}(2k\Delta_\varphi) \cos(2k\alpha) \text{sinc}[[2(k+l-p)+1]\Delta_\theta] \sin[[2(k+l-p)+1]\theta_o] \binom{2(k+l)+1}{p} \right\} \end{aligned} \quad (4)$$

$$\begin{aligned} \text{Im} \{ \rho_{[(n,p),(m,q)]} \} &= \frac{2}{\sin c(\Delta_\theta) \sin(\theta_o)} \sum_{k=0}^{\infty} \sum_{l=0}^k \sum_{p=0}^{k+l} \frac{(-1)^l}{l! \Gamma(2k+l+2)} \times \left(\frac{Z}{2} \right)^{2(k+l)+1} \text{sinc}[(2k+1)\Delta_\varphi] \sin[(2k+1)\alpha] \\ &\quad \times \left\{ \frac{1}{2^{2(k+l+1)}} \binom{2(k+l+1)}{l+k+1} + \frac{(-1)^{k+l+1+p}}{2^{2(k+l+1)}} \binom{2(k+l+1)}{p} \text{sinc}[2(k+l+1-p)\Delta_\theta] \cos[2(k+l+1-p)\theta_o] \right\} \end{aligned} \quad (5)$$

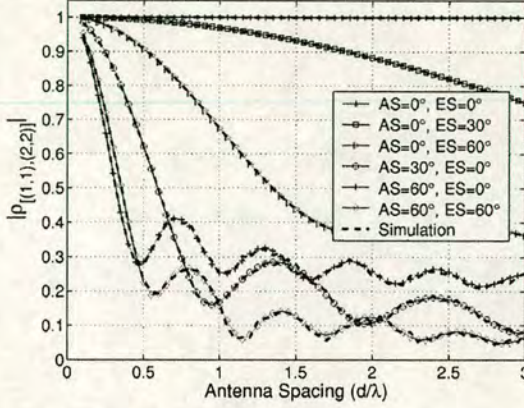


Fig. 3. SC at various AS and ES values with 90° MEOA and MAOA.

the definition in [4], the AOAs of the MPCs are uniformly distributed over the range of angles $[\varphi_0 - \Delta\varphi, \varphi_0 + \Delta\varphi]$. Similarly, the EOAs of the MPCs are also uniformly distributed over $[\theta_0 - \Delta\theta, \theta_0 + \Delta\theta]$. Note that the developed SC function is computationally efficient: summation over 50 terms for k and l is sufficient to achieve accuracy up to six decimal places when comparing (4) and (5) with numerical integration of (8) and (9), respectively.

IV. ANALYTICAL RESULTS

In this section, some analytical results are presented and compared with simulation results. For all cases, simulation has been performed over 3 000 000 channel realizations to calculate the correlation values and these results validate the derived expression. Furthermore, the impact of both the AOA and the EOA is compared to identify the importance of these two parameters to the system performance. Fig. 3 shows the SC, $|\rho_{[(n,p),(m,q)]}|$ between antennas (1,1) and (2,2) as a function of antenna spacing with $d = d_x = d_y$ for different AS and ES values, at 90° MAOA and MEOA. It can be observed that as the AS and ES increase, the SC decreases. For the same increment in both AS and ES, the SC reduces more rapidly in the case of the AS. This suggests that the impact of AS on the SC is more significant than that of ES. To account for the joint contribution of both parameters on SC, we present theoretical results for the SC at 0.5λ spacing, 90° MAOA and MEOA with varying AS and ES values as illustrated in Fig. 4. It can

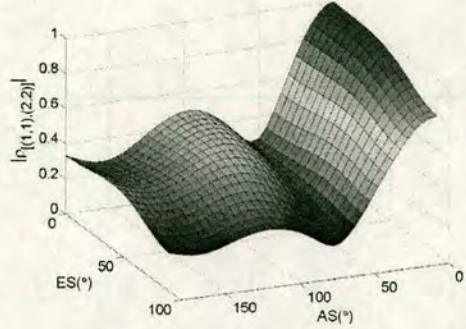


Fig. 4. SC as a function of both AS and ES at 90° MAOA and MEOA with 0.5λ spacing.

be noted that the rate at which the SC drops with respect to the ES is somewhat less than the AS case.

V. CONCLUSION

In this letter, a closed-form expression for the spatial fading correlation function in terms of MAOA, AS, MEOA, ES, antenna spacing, and geometry of the URA is derived. The theoretical results are verified by means of computer simulation, where both results show excellent agreement. The developed SC is useful for capacity analysis in MIMO systems as it can be used to determine the covariance matrix at both the BS and MS. Furthermore, the closed-form SC can also be used to study the array sensitivity under various channel conditions. While our results demonstrate that AS is the primary determinant of the SC, the SC is reduced somewhat as the ES increases, an effect that will impact the performance most dramatically when AS is small. Therefore, we emphasize that for an accurate system performance analysis, both AOA and EOA must be taken into consideration.

APPENDIX

From (3), the SC between the antenna elements (n,p) and (m,q) of the URA can be expressed as shown in (6) at the bottom of the page, where $C = 1/4\Delta\varphi \sin(\theta_0) \sin(\Delta\theta) Z_x = 2\pi d_x(n-m)/\lambda$ and $Z_y = 2\pi d_y(p-q)/\lambda$. Let $Z = \sqrt{Z_x^2 + Z_y^2}$ and $\gamma = \tan^{-1}(Z_x/Z_y)$, then (6) can be rewritten as (7), shown at the top of the next page, where $\psi = \varphi + \gamma$. By making use of the well-known series [1], the real part and imaginary part of $\rho_{[(n,p),(m,q)]}$ can be further expressed as (8) and (9), shown at the top of the next page.

$$\begin{aligned}
 \rho_{[(n,p),(m,q)]} &= \int_{\varphi_0 - \Delta\varphi}^{\varphi_0 + \Delta\varphi} \int_{\theta_0 - \Delta\theta}^{\theta_0 + \Delta\theta} a_{np}(\varphi, \theta) a_{mq}^*(\varphi, \theta) p(\varphi, \theta) \sin(\theta) d\theta d\varphi \\
 &= C \int_{\varphi_0 - \Delta\varphi}^{\varphi_0 + \Delta\varphi} \int_{\theta_0 - \Delta\theta}^{\theta_0 + \Delta\theta} \left\{ e^{j2\pi/\lambda[(p-q)d_y \sin \varphi \sin \theta]} e^{j2\pi/\lambda[(n-m)d_x \cos \varphi \sin \theta]} \sin(\theta) \right\} d\theta d\varphi \\
 &= C \int_{\varphi_0 - \Delta\varphi}^{\varphi_0 + \Delta\varphi} \int_{\theta_0 - \Delta\theta}^{\theta_0 + \Delta\theta} \left\{ e^{jZ_y \sin \theta \sin \varphi} e^{jZ_x \sin \theta \cos \varphi} \sin(\theta) \right\} d\theta d\varphi
 \end{aligned} \tag{6}$$

$$\begin{aligned}
\rho_{[(n,p),(m,q)]} &= C \int_{\varphi_0-\Delta\varphi}^{\varphi_0+\Delta\varphi} \int_{\theta_0-\Delta\theta}^{\theta_0+\Delta\theta} e^{jZ \sin \theta \sin(\gamma+\varphi)} \sin(\theta) d\theta d\varphi \\
&= C \int_{\varphi_0+\gamma-\Delta\varphi}^{\varphi_0+\gamma+\Delta\varphi} \int_{\theta_0-\Delta\theta}^{\theta_0+\Delta\theta} e^{jZ \sin \theta \sin(\psi)} \sin(\theta) d\theta d\varphi \\
&= C \int_{\varphi_0+\gamma-\Delta\varphi}^{\varphi_0+\gamma+\Delta\varphi} \int_{\theta_0-\Delta\theta}^{\theta_0+\Delta\theta} \{\cos[Z \sin \theta \cos \psi] + j \sin[Z \sin \theta \sin(\psi)]\} \sin(\theta) d\theta d\varphi
\end{aligned} \quad (7)$$

$$\operatorname{Re} \{\rho_{[(n,p),(m,q)]}\} = C \int_{\varphi_0+\gamma-\Delta\varphi}^{\varphi_0+\gamma+\Delta\varphi} \int_{\theta_0-\Delta\theta}^{\theta_0+\Delta\theta} \left\{ J_0(Z \sin \theta) + 2 \sum_{k=1}^{\infty} J_{2k}(Z \sin \theta) \cos(2k\psi) \sin(\theta) d\theta d\varphi \right\} \quad (8)$$

$$\operatorname{Im} \{\rho_{[(n,p),(m,q)]}\} = C \int_{\varphi_0+\gamma-\Delta\varphi}^{\varphi_0+\gamma+\Delta\varphi} \int_{\theta_0-\Delta\theta}^{\theta_0+\Delta\theta} 2 \sum_{k=1}^{\infty} J_{2k+1}(Z \sin \theta) \sin[(2k+1)\psi] \sin(\theta) d\theta d\varphi. \quad (9)$$

In order to evaluate these double integrals we first substitute for the Bessel functions in (8) and (9), using the following infinite series [10]

$$J_0(Z) = \sum_{k=0}^{\infty} (-1)^k \frac{Z^{2k}}{2^{2k}(k!)^2} \quad (10)$$

$$J_v(Z) = \left(\frac{Z}{2}\right)^v \sum_{k=0}^{\infty} \frac{(-1)^k}{(k!)\Gamma(v+k+1)} \left(\frac{Z}{2}\right)^{2k} \quad (11)$$

where $\Gamma(\cdot)$ is a gamma function. These series converge rapidly for small values of Z . The use of these series should be satisfactory when considering antenna spacings of practical interest, i.e., up to several carrier wavelengths. Second, we use the following indefinite integrals for power of trigonometric functions in (12) and (13) [10] to obtain the closed-form expressions of (4) and (5)

$$\begin{aligned}
\int \sin^{2n} x dx &= \frac{1}{2^{2n}} \binom{2n}{n} x + \frac{(-1)^n}{2^{2n-1}} \\
&\times \sum_{k=0}^{n-1} (-1)^k \binom{2n}{k} \frac{\sin(2n-2k)x}{2n-2k}
\end{aligned} \quad (12)$$

$$\begin{aligned}
\int \sin^{2n+1} x dx &= \frac{1}{2^{2n}} (-1)^{n+1} \sum_{k=0}^n (-1)^k \\
&\times \binom{2n+1}{k} \frac{\cos(2n+1-2k)x}{2n+1-2k}.
\end{aligned} \quad (13)$$

REFERENCES

- [1] T. Aulin, "A modified model for the fading signal at the mobile radio channel," *IEEE Trans. Veh. Technol.*, vol. 28, pp. 182–202, Aug. 1979.
- [2] A. Kuchar, J. P. Rossi, and E. Bonek, "Directional macro-cell channel characterization from urban measurements," *IEEE Trans. Antennas Propagat.*, vol. 48, pp. 137–146, Feb. 2000.
- [3] K. Kalliola, K. Sulonen, H. Laitinen, O. Kivekas, J. Krogerus, and P. Vainikainen, "Angular power distribution and mean effective gain of mobile antenna in different propagation environments," *IEEE Trans. Veh. Technol.*, vol. 51, pp. 823–838, Sept. 2002.
- [4] J. Salz and J. H. Winters, "Effect of fading correlation on adaptive arrays in digital mobile radio," *IEEE Trans. Veh. Technol.*, vol. 43, pp. 1049–1057, Nov. 1994.
- [5] J.-A. Tsai, R. B. Buehrer, and B. D. Woerner, "Spatial fading correlation function of circular antenna arrays with Laplacian distribution energy," *IEEE Commun. Lett.*, vol. 6, pp. 178–180, May 2002.
- [6] P. C. F. Eggers, I. Z. Kováč, and K. Olesen, "Penetration effects on XPD with GSM 1800 handset antennas, relevant for BS polarization diversity for indoor coverage," *Proc. IEEE Vehicular Technology Conf.—Spring*, vol. 13, pp. 1959–1963, May 1998.
- [7] J. P. Kermoal, L. Schumacher, K. I. Pedersen, P. E. Mogensen, and F. Frederiksen, "A stochastic MIMO radio channel model with experiment validation," *IEEE J. Select. Areas Commun.*, vol. 20, pp. 1211–1226, Aug. 2002.
- [8] S. K. Yong and J. S. Thompson, "The effect of various channel conditions on the performance of different antenna arrays architectures," in *Proc. IEEE Vehicular Technology Conf.—Fall 2003*, to be published.
- [9] J. B. Andersen and K. I. Pedersen, "Angle-of-arrival statistics for low resolution antenna," *IEEE Trans. Antennas Propagat.*, vol. 50, pp. 391–395, Mar. 2002.
- [10] I. S. Gradshteyn and I. M. Ryzhik, *Table of Integrals, Series and Products*, 5th ed. New York: Academic, 1994.

IMPLEMENTATION OF COST259 CHANNEL MODELS USING TAPPED DELAY LINE FOR MULTIPLE ANTENNA RECEIVERS

S. K. Yong, J. S. Thompson and S. McLaughlin

SASG, University of Edinburgh, United Kingdom

Abstract: In this paper, the implementation of COST 259 channel models in macrocells, using a stochastic approach in terms of tapped delay line (TDL) models is presented. The implementation of this wideband channel is very important for link level simulation in future wireless systems that exploit space-time processing techniques using multiple antenna elements. Major channel effects are discussed and incorporated into existing channel models. The temporal correlation is realised by using a power spectrum shaping filter whereas the spatial correlation is achieved by invoking a canonical Gaussian approach. Furthermore, antenna effects as well as array geometries can be taken into consideration for the development of compact antenna arrays at the user's terminal. The array implementation is focused at the mobile station (MS) point of view.

1 INTRODUCTION

A reliable wireless system design and system performance evaluation requires a realistic channel model which closely resembles real propagation environments. Recently, directional antenna arrays have received significant attention for capacity improvement. The ability of the directional antenna arrays to exploit the spatial property of the channel offers a new dimension to improve the overall system performance. Hence, directional channel models will help in developing and optimising the concept of antenna arrays for future wireless systems. In this regard, COST259 channel models extend the well known COST207 channel models with directional information as well as clustering of the multipath components. Unlike the COST207 model which is limited to macrocells and omni-directional antennas, COST259 can be considered as one of the most "complete" wideband directional models to date. It is topographically dependent, as it covers all three cell types, macro, micro and pico-cell. The COST207 model is treated as a special propagation scenario that can be found in the COST259 models. COST259 does not specify a particular implementation method. To the best knowledge of the authors, only the implementation in terms of geometric stochastic channel models has been published [1].

The TDL models are characterised by the approaches and concepts used in COST259 [2] with some modifications and assumptions. In this implementation, we ignore the effect of large scale fading, user mobility and thus the transition between radio environments (RE) and cell types. The channel model described here is only valid for short time interval or small mobile displacement. In section 2, the COST259 channel

models will be described in terms of a single input multiple output (SIMO) system. In the next section, parameter settings are presented which form the basis of simulation flow in section 6. This is done by randomly locating the geometrical positions of the MS, base station (BS), local and distant cluster. Hence, various parameters which describe the characteristic of the clusters of the radio environment under study can be determined. In section 4, the temporal correlation of the channel is characterised. This is achieved by filtering complex Gaussian white noise with the frequency response of the required Doppler spectrum. The spatial correlation of the channel is realised by invoking the canonical Gaussian approach as will be shown in section 5. Simulation flow and results are discussed in section 6 and 7 respectively. Finally, conclusions are drawn.

2 CHANNEL MODEL: MATHEMATICAL VIEW

In the mobile radio channel, the signal from the transmitter impinges at the receiver with multiple copies due to multipath propagation. Hence, the dispersion of the channel in the temporal and angular domain can be described by the time variant – directional vector channel impulse response (TV-DVCIR) given by

$$\mathbf{h}(t, \tau, \Omega) = [\mathbf{h}_1(t, \tau, \Omega) \dots \mathbf{h}_M(t, \tau, \Omega)]^T \quad (1)$$

Where $[\cdot]^T$ denotes the transposition, M is number of receive antennas, t is the time, τ is the time delay and Ω is the direction of arrival in both azimuth and elevation angle. $\mathbf{h}_m(t, \tau, \Omega)$ is the TV-DVCIR as "seen" at the m^{th} antenna and can be expressed [1] as

$$\begin{aligned} h_m(t, \tau, \Omega) &= \sum_{j=1}^J h_{mj}(t, \tau, \Omega) \\ &= \sum_{c=1}^C \sum_{j \in C_c} h_{mj}(t, \tau, \Omega) \\ &= \sum_{c=1}^C \sum_{j \in C_c} \alpha_j \delta(\tau - \tau_j) \delta(\Omega - \Omega_j) \end{aligned} \quad (2)$$

Where J is the total number of multipath components (MPC) and C is the total number of clusters. This means that \mathbf{h}_m comprises the superposition of large number of MPCs with amplitude α_j , delay τ_j and angle Ω_j . Equation (2) can be further written to include clustering when these multipath components (MPC) arrive at about the same delay or angle. Theoretically, the channel impulse response (CIR) $\mathbf{h}(t, \tau)$ is obtained by integrating equation (1) weighted by antenna pattern over direction i.e.

$$\mathbf{h}(t, \tau) = \int_{\Omega} G(\Omega) \mathbf{h}(t, \tau, \Omega) d\Omega \quad (3)$$

The evaluation of this CIR will be shown in the later section and the CIR can be used as the time variant coefficients of a multiple TDL model as shown in the Fig 1.

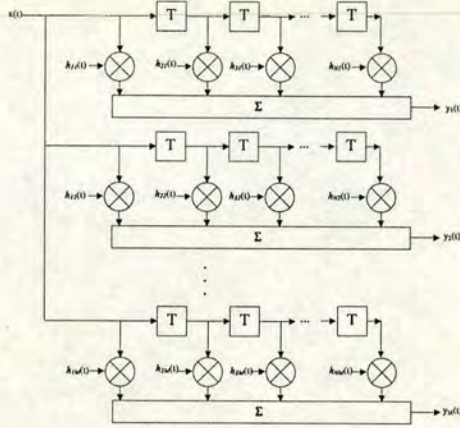


Fig. 1. Multiple tapped delay line model.

3 BACKGROUND OF MODELLING CONCEPT

Radio propagation is highly dependent on the environment under consideration. To generalise this, the COST 259 directional channel model (DCM) has defined a 3-level structure consists of cell types, radio environment (RE) and propagation scenarios. This three level structure can be fully characterised by three types of parameter called External Parameter (EP), Global Parameter (GP) and Local Parameter (LP). A set of EPs, GPs can be obtained from [2]. For an excellent descriptions of the modelling concept adapted in COST259, interested readers are referred to [2]. The random realisations which represent propagation scenarios are important to generate realistic versions of the channel impulse response for Monte Carlo simulations. For simulation purposes, we look at the simulation flow in section 6, taking the Macro-cells general typical urban (GTU) case as a specific example, and identify the steps involved to generate these random realisations (LPs). This process can be extended to any other RE.

4 TEMPORAL CORRELATION

In this section, the generation of the fading signal is discussed. This can be realised by filtering complex white Gaussian noise with infinite impulse response (IIR) or finite impulse response (FIR) filters. To obtain a reasonable result with low computation effort, a fourth order IIR filter is chosen which consists of two cascade second order filters. A more accurate higher order filter

can be found in [3]. The transfer function of the fourth order IIR filter is given by

$$H(s) = \frac{1}{s^2 + \sqrt{2}s + 1} \frac{1}{s^2 + 0.02s + 1} \quad (4)$$

The filter is then transformed to the z-domain by using the bilinear transformation with the appropriate sampling frequency f_s . The choice of f_s must be at least twice of the Doppler frequency of the channel under consideration to ensure the Nyquist criterion is met. Since the Doppler frequency of the channel would be expected to be much lower than that of the channel bandwidth, the fading signal can be assumed to be stationary over a number of transmitted symbols. Fig 2 depicts the generation of the fading signal.

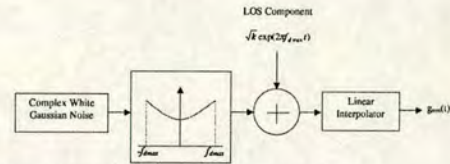


Fig. 2. The generation of fading signal

First, the complex Gaussian white noise is passed through this filter before the dominant coherent path (if any) with Rice factor K is added to the filter output. The sum of these components is then linearly interpolated at a simulation rate to increase the rate to match that of the time resolution of the tap, T the inverse of the system bandwidth. The final output, $g_{nm}(t)$ is applied to the spatial shaping filter described in section 5. Note that, for each of the taps, a new independent set of fading signals is generated. This gives a matrix g of size $N \times M$ whose entries correspond to the outputs g_{nm} . Also, the line of sight (LOS) component K can be modelled using probability of occurrence of LOS [4] given as

$$P_{LOS} = \begin{cases} \frac{(h_{BS} - h_B)}{h_{BS}} \cdot \frac{d_{CO} - d}{d_{CO}} & d < d_{CO} \text{ \& } h_{BS} > h_B \\ 0 & d > d_{CO} \text{ or } h_{BS} < h_B \end{cases} \quad (5)$$

Where h_{BS} , h_B and d_{CO} are the BS height, average building height and cut off distance respectively. With equation (5), we can characterise how often the LOS component occurs in a given RE and for a given distance between BS and MS. For the LOS scenario, the K-factor is obtained by computing the power of the direct component for the first cluster. Note that, this direct path will be a scaled steering vector $\mathbf{a}(\Omega_{LOS})$ where Ω_{LOS} is the LOS path azimuth/elevation.

5 SPATIAL CORRELATION

The directional information of the channel is incorporated into the model by using the canonical

Gaussian approach as proposed in [5],[6]. According to this approach, the spatial property of the channel at a particular delay can be described by specifying the spatial correlation matrix \mathbf{R}_n which is calculated using the steering vector $\mathbf{a}(\Omega_i)$ of the array under study. This approach assumes Rayleigh fading at each antenna and is approximately valid in Ricean fading case [5]. Hence, at a particular delay tap, a spatial correlation matrix is generated according to [5]

$$\mathbf{R}_n = \sum_{i=1}^L \alpha_i^2 \mathbf{a}(\Omega_i) \mathbf{a}^H(\Omega_i) \quad (6)$$

Where n = tap index, L is the total number of multipaths in that tap and α_i is the amplitude of the multipath. \mathbf{R}_n represents the mean power and cross correlations at each tap. Furthermore, by studying \mathbf{R}_n , the envelope correlation given by the squared magnitude of the complex signal correlation can be explicitly formed [9]. Observing the envelope correlation enables us to determine the possible benefit of applying diversity combining techniques at the MS. \mathbf{R}_n is then further decomposed into its unitary eigenvectors and diagonal matrix of eigenvalues using eigenvalue decomposition as shown in section 6. The application of the canonical Gaussian approach not only simplifies the channel implementation but also enables us to use different antenna array geometries in the design of compact antenna arrays. This allows us to include the impact of antenna effects in the system performance analysis.

6 SIMULATION FLOW

In this section, the fundamental steps involved to generate random realisations (LPs) of the channel based on the EPs and GPs are presented. This is supported by the assumptions we made in the implementation.

1. Firstly, the number of clusters, N_{cl} is determined

$$N_{cl} = N_{cl,min} + P(m) \quad (7)$$

Where $P(m)$ is the Poisson distribution with m the mean number of additional clusters. For macrocell, the minimum number of cluster $N_{cl,min}$ is always one.

2. The additional clusters (if $N_{cl} > 1$) determined in step 1 are placed uniformly in space with maximum cell radius 3km. So, the position of additional clusters (coordinates) can be determined assuming the BS is at the (0,0) point.
3. The position of the MS is randomly placed with MS-BS distance, d_{MS-BS} is uniformly distributed between 50m and 1000m.
4. For the cluster local to MS, we place local scatterers, $N_{LS}=50$ uniformly distributed within the local cluster circle with radius 100m centred at MS position [7] determined in step 3. This is to distinguish the location of MS and the scatterers local to the MS.

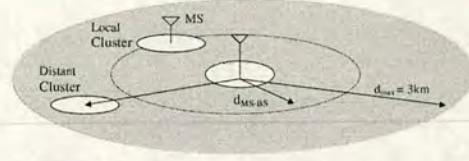


Fig. 3. The location of the local and distance cluster.

5. Assuming single bounce, we then compute the delay and direction of arrival (azimuth) due to each cluster by using a simple geometry. The average cluster delay and average cluster azimuth are then calculated. This gives τ_i and ϕ_i for $i=1$, i.e. local cluster delay and azimuth respectively. Similarly, with the position of the additional clusters obtained in step 2, the average cluster delay and azimuth for any additional clusters can be computed.
6. With the data obtained in step 5, the shadowing, P_i [dB], delay spread, $S_{\tau,i}$ [s] and azimuth spread of each cluster $S_{\phi,i}$ [deg] can be computed using the following equations [2]

$$\begin{aligned} P_i [\text{dB}] &= 9X - L_i \\ S_{\tau,i} [\text{s}] &= 0.4\mu\text{s} \cdot d_i^{0.5} \cdot 10^{\frac{2Z}{10}} \\ S_{\phi,i} [\text{deg}] &= 10 \cdot 10^{\frac{2Y}{10}} \end{aligned} \quad (8)$$

Where X , Y and Z are normal random variables with zero mean, unit variance, and correlation coefficients $\rho_{xy} = -0.75$, $\rho_{yz} = 0.5$ and $\rho_{xz} = -0.75$. The generation of these random variables is discussed in [1]. Also $d_i = \tau_i c$ and is expressed in km. The quantity L_i is cluster path loss¹ and can be written as follows

$$\begin{aligned} L_i &= L_1 + L_{add} [\text{dB}] \\ L_{add} &= U(0,20) + (\tau_i - \tau_0) / \mu\text{s} [\text{dB}] \end{aligned} \quad (9)$$

Where L_1 is the path loss of the first cluster and L_{add} is the path loss of additional cluster(s). Also, $U(a,b)$ signifies a random variable uniformly distributed between a and b . The delay, τ_0 is given by d_{MS-BS} divided by c (speed of light).

7. With the set of data $\{P_i, S_{\tau,i} \text{ and } S_{\phi,i}\}$ and $\{\tau_i, \phi_i\}$ determined from above, the characteristics of the clusters in terms of their position, delay and azimuth spread, power delay spectrum (PDS) and power azimuth spectrum (PAS) can be obtained.
8. For the first cluster, we assume the joint power azimuth-delay spectrum (ADPS) is given by

$$P_{i=1}(\tau, \phi) = \frac{1}{2\pi} e^{\frac{-\tau}{S_{\tau,1}}} \quad (10)$$

¹ L_i is valid for $i = 2, \dots, N_{cl}$.

while for additional clusters, the joint ADPS with elevation, $\theta_i=0$ can be expressed as

$$P_i(\tau, \varphi) = \frac{1}{1 - e^{-\frac{\tau}{S_{\tau,i}}}} \cdot \frac{1}{\sqrt{2} S_{\tau,i} S_{\varphi,i} S_{\theta,i}} e^{-\frac{\tau}{S_{\tau,i}}} e^{-\sqrt{2} \left| \frac{\varphi}{S_{\varphi,i}} \right|} \quad (11)$$

This is because [8] found that $P(\varphi, \tau)$ can be decomposed to $P(\varphi, \tau) \propto P(\varphi)P(\tau)$ where $P(\varphi)$ is the PAS and $P(\tau)$ is the PDS. Thus, the joint ADPS of each cluster, $P_i(\varphi, \tau)$ can be decomposed as $P_i(\varphi, \tau) = P_i(\varphi)P_i(\tau)$. This relation is important in channel modelling with the clustering effect taking into account.

9. The probability density functions (PDF) of the delay and azimuth are found to be negative exponential and uniform for the first cluster and exponential and Gaussian distributed for far clusters [8]. Hence, random variables for delay and azimuth can be generated. With the relation in step 8 coupled with the random variables generated in 9, a joint ADPS can be obtained for each cluster.
10. With these parameters, we set the dynamic range D_R (dB) say 20dB below the strongest path and determine the number of delay taps required

$$Power_i(\tau) = \exp\left(\frac{\tau_i - \tau}{S_{\tau,i}}\right) \quad (12)$$

Let τ_{1,D_RdB} = the delay when the power level drops below D_R dB for cluster 1 and $Power_i(\tau) = -D_R$ dB. Rearranging terms to give

$$\tau_{1,D_RdB} = \tau_1 - S_{\tau,1} \ln(10^{-D_R/10}) \quad (13)$$

11. Thus the maximum numbers of taps required are given by

$$Total \text{ taps for cluster } 1 = \tau_{1,D_RdB} \times BW \quad (14)$$

Where BW is the bandwidth of the system. For example, we may use the UMTS system bandwidth. Similarly, this is done to cluster 2, 3 and so on depending on their occurrences.

12. For each cluster, we generate a sufficiently large number of MPCs L to ensure the regeneration of the statistics of the channel. Each MPC is associated with its corresponding power, AOA and delay generated according to their PDFs. This can be envisaged as shown in the Fig 4. The MPCs that arrive within T secs of each other are grouped into one tap. Hence, each of the taps has different number of MPCs and some may have no MPCs.
13. For each of the delay taps, a spatial correlation matrix is generated according to equation (6). This is followed by factorising R_n into matrix Q_n of its eigenvectors and diagonal matrix Λ_n of its eigenvalues by

$$R_n = Q_n \Lambda_n Q_n^H \quad (15)$$

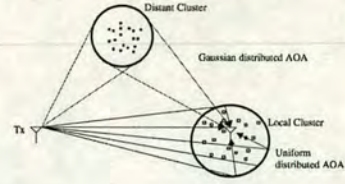


Fig. 4. Distinction between local and distance cluster and their effects in the received signal.

14. Finally, the discrete TV-CIR, $h[n, k]$ is given by

$$h[n, k] = \sqrt{P_i} Q_n \Lambda_n^{\frac{1}{2}} g_n[k] \quad (16)$$

Where P_i is shadowing of the corresponding cluster and $g_n[k]$ is fading signal as discussed in section 4. The scalar n represents the discrete time and $g_n[k]$ is of the size $1 \times M$ vector of independent complex Gaussian samples. The $h[n, k]$ obtained can be used as time variant coefficients of the multiple TDL.

7 SIMULATION RESULTS

In this section, some of the simulation results are analysed. Fig 5 shows the channel responses of antenna one in a macrocell GTU environment with carrier frequency 2GHz.

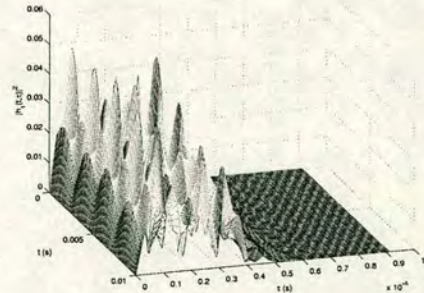


Fig. 5. Channel response of an omni-directional antenna 1 in the GTU at velocity 100km/h and antenna spacing $\lambda/2$.

The speed of the mobile is approximately 100km/h, which corresponds to maximum Doppler frequency 200Hz. Due to the spatial separation between the two antennas, the TV-CIR of the two antennas are different even though they share the same joint ADPS. This suggests the use of the diversity techniques at the receiver where we observe that there are times when the

signal at antenna one fades whilst the signal at antenna two is at an acceptable level. In addition, fading with several deep fades occurring within 10ms can be clearly identified. Fig 6 shows the average power delay profile for the GTU where it is dominated by the first cluster corresponding to the scattering around the MS. A comparison is made with the COST207 TU model where both curves show some degree of agreement. Note that COST207 only represents an average propagation condition of that found in COST259 directional channel model.

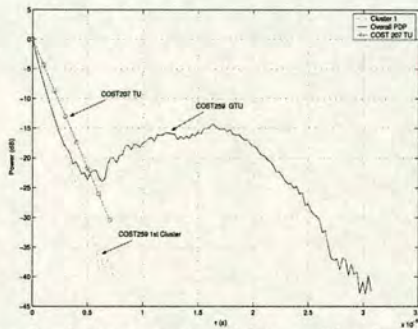


Fig. 6. Average power delay profile for GTU normalised by the first arrival path.

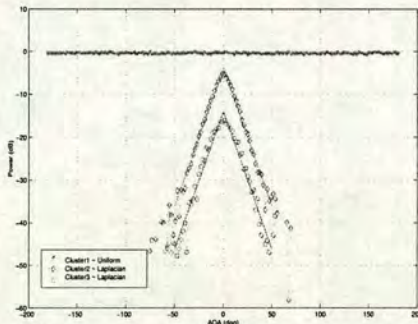


Fig. 7. Average power azimuth spectrum normalised to the mean AOA of the cluster.

Fig 7 shows the average power azimuth spectrum normalised with respect to mean AOA of the cluster. It can be seen that the first cluster is uniform and the additional clusters are Laplacian in shape. Both figure 6 and 7 match the PDS and PAS as described in section 6 and thus ensure the correct regeneration of the channel impulse response.

CONCLUSION

This paper describes the implementation of COST259 channel models in macrocells using a TDM. This realistic COST259 channel model is implemented to facilitate the development of appropriate link level simulations for multiple antennas at the receiver. The

impact of antenna effects can be integrated into the channel through the canonical Gaussian approach. This is particularly important to create realistic scenarios for link level simulation to investigate the system performance using multiple antennas at the user terminal. Though it is described in GTU RE, it can be extended to other REs as well as to MIMO systems. Furthermore, the simulation results shown that certain degree of compatibility with COST207 model as one of the main objectives of the COST259 modelling framework[2].

ACKNOWLEDGEMENTS

The work reported here has formed part of the Wireless Access area of the Core 2 Research Programme of the Virtual Centre of Excellence in Mobile & Personal Communications, Mobile VCE (www.mobilevce.com) whose funding support, including that of EPSRC, is gratefully acknowledged. The author would like to acknowledge H. Asplund, and M. Steinbauer for their helpful clarification.

REFERENCES

- [1] Hofstetter H., Molisch A. F. & Steinbauer M., 2001, "Implementation of COST259 geometry based stochastic channel model for macro- and microcells," *EPMCC 2001*.
- [2] Correia L. M. (editor), 2001, "Wireless flexible personalised communications," John Wiley and Sons.
- [3] Baltersee J., 1998, "Modeling and simulating fading channels for systems with smart antennas," *Proc. of IEEE PIMRC 98*, 2, 957-961.
- [4] Asplund H., 1999, "An empirical model for the probability of line of sight in urban macrocell," TD(99)107.
- [5] Hammerschmidt J. S. & Hutter A. A., 2000, "Spatio-temporal channel models for mobile station: concept, parameters and canonical implementation," *Proc. of IEEE VTC'2000*, 3, 1641-1645.
- [6] Siemens, 2000, "Channel models for Tx diversity simulations using correlated antennas," 3GPP document TSGR#15 R1-00-1067.
- [7] Description of modelling methods, technical report, METAMORP-Report C-2/1, 1999.
- [8] Pedersen K. I., Mogensen P. E. & Fluery B. H., 2000, "A stochastic model of the temporal and azimuthal dispersion seen at the base station in outdoor propagation environments," *IEEE Trans. on vehicular technology*, 49, no 2, 437-447.
- [9] A. Stéphenne & B. Champagne, 2000, "Effective multi-path vector channel simulator for antenna array systems," *IEEE Trans. on vehicular technology*, 49, no.6, 2370-2381.

THE IMPACT OF ANGLE OF ARRIVAL DISTRIBUTION ON THE PERFORMANCE ANALYSIS OF DIFFERENT ANTENNA ARRAY ARCHITECTURES

S. K. Yong and J. S. Thompson

Institute for Digital Communications,
University of Edinburgh, United Kingdom

Abstract: In this paper, the effect of both azimuth-of-arrival (AOA) and elevation-of-arrival (EOA) on the system performance using different type of antenna array (AA) architectures are investigated. This includes uniform linear array (ULA), uniform circular array (UCA) and uniform rectangular array (URA) configurations. The spatial correlation (SC) of the AA under study for different statistical probability density functions (PDFs) for the azimuth and elevation angles are examined and analysed. The results show that the impact of using different AOA and EOA PDFs on SC is insignificant. The key parameter for system performance is the standard deviation of the underlying PDFs.

1 INTRODUCTION

Different statistical PDFs have been deployed to model the multipath components (MPCs) AOA and EOA in the mobile station. For the AOA, uniform, Gaussian and Laplacian PDFs have been proposed in [1], [2] and [3] respectively. One other hand, the EOA is usually modelled as a uniform or Laplacian PDF as suggested in [4]. Preliminary results of [5] expressed the SC between antenna elements in terms of antenna spacing, azimuth spread (AS) and mean azimuth of arrival (MAOA) while [6] extended to work to the UCA with Laplacian energy distribution in azimuth. To the best of the authors' knowledge, no researchers have considered the effect of both AOA and EOA on the system performance using different types of AA architectures.

The aims of this paper are two fold. Firstly, to study in more detail the impact of using different AOA PDFs on the SCs of the ULA, UCA and URA. Secondly, to study the SC of the AAs under the effect of EOA. This investigation is important as the system performance of the handset AAs are highly dependent on the effect of the multipath elevation since the handset could be oriented in any direction [7]. Furthermore, measurement results have also shown that about 65% of the energy was incident with elevation larger than 10° [8]. The above two investigations allow us to deduce the significance the AOA PDFs as well as its associated parameters i.e. the effect of azimuth and elevation spread (ES) on the system performance.

By studying the SCs which serve as a figure of merit in the performance analysis of AAs, they can provide a useful measure of the required antenna spacing for a diversity system to work in a given channel condition

and a given AA configuration. This paper is organised as follows, Section 2 describes the directional channel model and the steering vector (SV) of the AA under consideration. The impact of AOA and EOA distributions on the SC for different AAs are discussed in section 3 and 4 respectively. In section 5, the joint contribution of AOA and EOA on the SC is highlighted. Finally, some concluding remarks will be made.

2 DIRECTIONAL CHANNEL MODEL

In this paper, the performance analyses are done by using a frequency non selective directional Rayleigh fading channel model. The channel impulse response, $h(t)$ can be expressed as

$$h(t) = \sum_{l=1}^L \alpha_l(t) \mathbf{a}(\varphi_l, \theta_l) \quad (2)$$

α_l is the complex amplitude, $\mathbf{a}(\varphi, \theta)$ is the SV of the AA under study and L is the total number of MPCs. The scalars φ and θ are the azimuth and elevation angles defined with respect to the positive x and z-axis respectively. The above description can be illustrated as shown in Fig. 1. For the ULA, the SV is given by

$$\mathbf{a}(\varphi, \theta)_{ULA} = [1, e^{j2\pi d \cos \varphi \sin \theta / \lambda}, \dots, e^{j2\pi d(M-1) \cos \varphi \sin \theta / \lambda}]^T \quad (3)$$

where M is the number of antennas, d is the antenna spacing, λ is the wavelength, and $[\cdot]^T$ denotes the transpose. The SV of the UCA with the centre as a reference point is given by

$$\mathbf{a}(\varphi, \theta)_{UCA} = [e^{j\zeta \cos(\varphi - \varphi_s)}, e^{j\zeta \cos(\varphi - \varphi_{s+1})}, \dots, e^{j\zeta \cos(\varphi - \varphi_{s+M-1})}]^T \quad (4)$$

where $\varphi_s = 2\pi n / M$ and $\zeta = 2\pi r \sin \theta / \lambda$. The scalar r is the radius of the UCA. In addition, the SV of the URA with $N \times P$ elements located in the x-y plane with the phase reference at the origin is given by

$$\mathbf{a}(\mu, \nu)_{URA} = \text{vec}(\mathbf{a}_N(\mu) \mathbf{a}_P^T(\nu)) \quad (5)$$

where $\mu = 2\pi d_x \cos \varphi \sin \theta / \lambda$, $\nu = 2\pi d_y \sin \varphi \sin \theta / \lambda$, $\mathbf{a}_N(\mu) = [1, e^{j\mu}, \dots, e^{j(N-1)\mu}]^T$, $\mathbf{a}_P(\nu) = [1, e^{j\nu}, \dots, e^{j(P-1)\nu}]^T$ and d_x, d_y are the spacings between the array elements parallel to the x and y-axis respectively. The operator $\text{vec}(\cdot)$ maps the a $N \times P$ matrix to an $NP \times 1$ vector by stacking the column of the matrix.

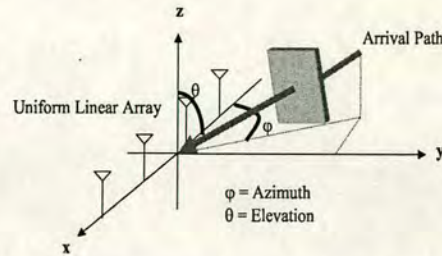


Fig. 1: Plane wave propagation where the incoming signal path is at a discrete azimuth and elevation.

3 THE IMPACT OF AOA DISTRIBUTION

In this paper, three AOA PDFs are considered. The uniform, Gaussian and Laplacian AOA PDFs can be expressed as in equations (6), (7) and (8) respectively.

$$f(\varphi)_u = \frac{1}{2\Delta_{\varphi,u}} \quad (6)$$

$$f(\varphi)_g = \frac{\kappa_g}{\sqrt{2\pi}\sigma_g} e^{-\frac{(\varphi-\varphi_0)^2}{2\sigma_g^2}}, (-\pi+\varphi_0 \leq \varphi \leq \pi+\varphi_0) \quad (7)$$

$$f(\varphi)_l = \frac{\kappa_l}{\sqrt{2}\sigma_l} e^{-\frac{\sqrt{2}|\varphi-\varphi_0|}{\sigma_l}}, (-\pi+\varphi_0 \leq \varphi \leq \pi+\varphi_0) \quad (8)$$

where $2\Delta_{\varphi,u}$ is the maximum deviation of the AS from the MAOA, φ_0 . The scalars σ_g and σ_l are the standard deviations while κ_g and κ_l are the normalizing constants to make (7) and (8) PDFs. To allow a consistent comparison, the AS is assumed equal to the standard deviation of the underlying PDFs. Unless otherwise specified, the SC is computed between antenna elements (1,2) for the cases of the ULA and UCA, while (1,4) for the case of the URA is used.

Fig. 2 shows the SCs for different arrays using the three AOA PDFs at MAOA=90°. By studying Fig. 2, we observe that for a given AS, the SCs for the three AOA PDFs have a similar pattern. Furthermore, as the AS increases, the SC decreases very rapidly from 2°, 10° to 90° respectively. This suggests that the important parameter of the SC as a function of antenna spacing is the standard deviation of the PDF and not the type of

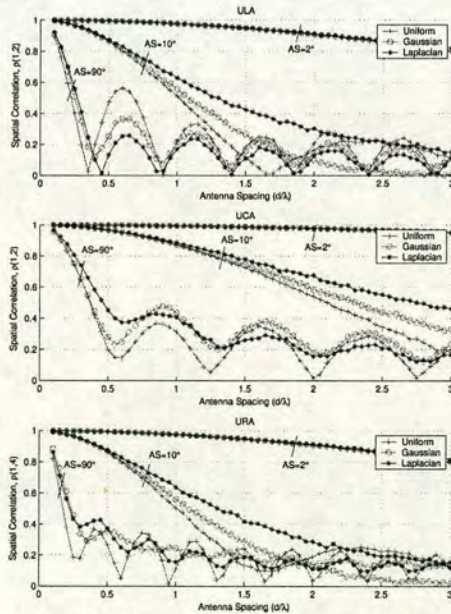


Fig. 2: SC for the ULA, UCA and URA at 90° MAOA, 0° ES and MEOA=90° for different AS.

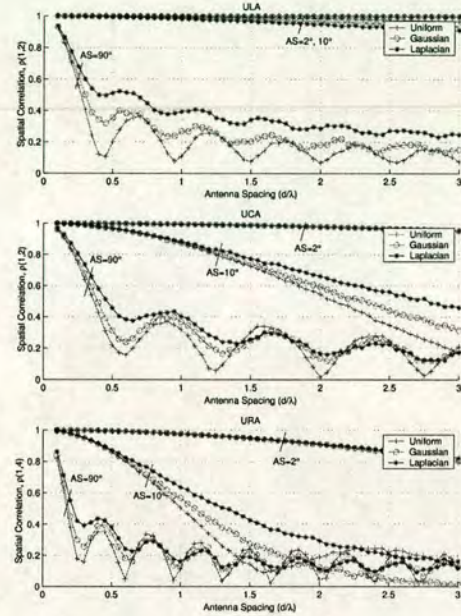


Fig. 3: SC for the ULA, UCA and URA at 0° MAOA, 0° ES and MEOA=90° for different AS.

PDF under consideration. Although, the impact of different PDFs on the SC can be regarded as negligible, it is observed that the uniform and Laplacian PDFs have the lowest and highest SCs respectively while the Gaussian case in the intermediate one. The uniform PDF has more paths located further away from the MAOA than the case of Laplacian and Gaussian PDFs where most of the paths are incident close to the MAOA. Similarly, the small SC difference between Gaussian and Laplacian can be justified from their symmetrical properties. The main discrepancy between them is the much heavier tail and higher density at the peak of the Laplacian as compared to the Gaussian PDF. To demonstrate the impact of using different arrays, we change the MAOA from 90° to 0° as illustrated in Fig. 3. For the ULA case, significant changes in SC can be observed for a given AS. Since the MAOA is in the endfire condition, the SC is expected to be very high (≈ 1) for a small AS values and only increases gradually with the AS. Comparing both Fig. 2 and Fig. 3 for the UCA and URA cases, the SC for 0° and 90° MAOA are similar. This is due to the orientation of the arrays which make them in general insensitive to changes in MAOA [9].

4 THE IMPACT OF EOA DISTRIBUTION

In this section, we extend our analysis to the case of EOA which has not been reported in the literature. For the case of EOA, similar analyses are performed to investigate the impact of using different EOA PDFs on

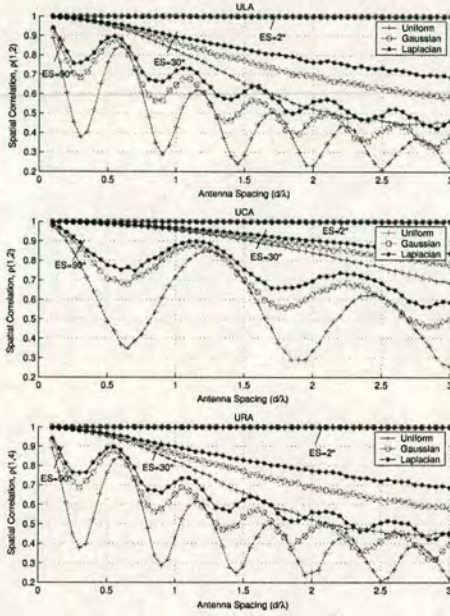


Fig. 4: SC for the ULA, UCA and URA at 0° MAOA, 0° AS and MEOA=90° for different ES.

the SC. Fig. 4. shows the SC of different arrays under three EOA PDFs at 0° MAOA. Under this specific condition, the impact of the EOA and AOA on the SC can be compared by observing Fig. 3 and Fig. 4 where the AS and ES are the only changing variables. Our analysis demonstrates that in general, higher AS values lead to lower SC. In addition, the reduction in SC due to increasing ES is less rapid than that for the AS. If the MAOA is changed to 90°, similar observations are expected for the case of the UCA and URA. Nevertheless, the SC of the ULA will be at value one. To enumerate the impact of the mean elevation of arrival (MEOA), the SC at 0° MEOA is evaluated as shown in Fig. 5. At 0° MEOA, the SC at a given ES for all the arrays reduces very rapidly with element spacing but the oscillation dies off very slowly as compared to the case of 90° MEOA.

5. THE IMPACT OF BOTH AOA AND EOA

Fig. 6. shows the impact of the AS, ES and MAOA on the system performance. We use the uniform PDF for both AOA and EOA in this analysis since it has been shown previously that the actual PDF of the MPC angle of arrival is not a key issue. By examining closely this figure, we see that for all the MAOAs considered, the lowest SC for all the antenna spacings is obtained when both the AS and ES are at their maximum. Nevertheless, the impact of the AS is more significant than the corresponding ES. For example, the SC for the case of

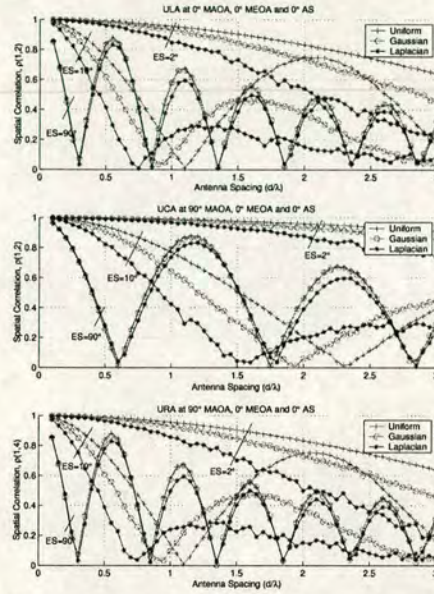


Fig. 5: SC for the ULA, UCA and URA at 0° MAOA, 0° MEOA and 0° AS for different ES.

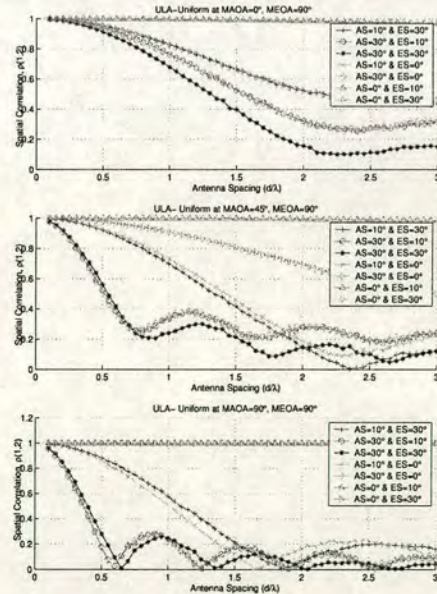


Fig. 6: The impact of AS, ES and MAOA on the SC as a function of antenna spacing for the ULA.

30° AS and 0° ES is always lower than the case of 0° AS and 30° ES. For a given AS and antenna spacing, the impact of the ES on the SC in all the cases is

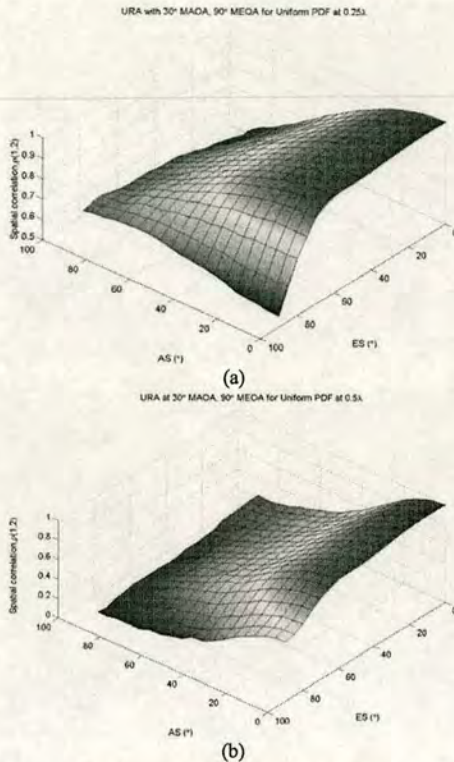


Fig. 7: The impact of both the AOA and EOA on the SC of the URA at antenna spacing (a) 0.25λ and (b) 0.5λ .

negligible. This is clearly illustrated when one looks, for example the SC for different ES values with AS set to 30° . It can be seen that the SC only reduces for large values of ES (80° – 90°). To analyse the joint contribution of both the AOA and EOA on the SC, we perform simulation results for the SC of the URA with varying AS and ES values. This is illustrated in Fig. 7(a) and (b) for 0.25λ and 0.5λ spacing respectively. It can be observed that the highest and lowest achievable SCs are obtained when the AS and ES are at their minimum and maximum values. In general, the contribution of the ES is relatively small as compared to the AS. At spacing of 0.25λ , the SC reduces very rapidly as the AS increases. However for the case of increasing ES, the SC reduces fairly slowly before it drops significantly at the 80° to 90° ES region. At spacing 0.5λ , the impact of the AS becomes more apparent as the SC drops from sharply for a given ES value. The rate at which SC drops with respect to ES is somewhat less than that of the AS case.

5 CONCLUSIONS

This paper has investigated the impact of both the AOA and EOA on the SC of different AA architectures. As

shown in our analysis, the impact of using different AOA and EOA PDFs on SC is insignificant. On the other hand, the key parameter to the system performance is the standard deviation of the underlying PDFs. Our results also demonstrate that the effect of AS on SC is more significant than that of ES. It must be emphasised that in evaluating the performance of AA, both AOA and EOA must be taken into consideration.

ACKNOWLEDGEMENTS

The work reported here has formed part of the Wireless Access area of the Core 2 Research Programme of the Virtual Centre of Excellence in Mobile & Personal Communications, Mobile VCE (www.mobilevce.com) whose funding support, including that of EPSRC, is gratefully acknowledged.

REFERENCES

- [1] Description of the modelling methods, Technical report, METAMORP-Report C-2/1, 1999.
- [2] Luo J., Zeidler J. R. and McLaughlin S., January 2001 "Performance Analysis of Compact Antenna Arrays with MRC in Correlated Nakagami Fading Channels," *IEEE Trans. Veh. Technol.*, vol. 50, no. 1, 267-277.
- [3] Q. H. Spencer, B. D. Jeffs, M. A. Jensen and A. L. Swindlehurst, March 2000, "Modeling the statistical time and angle of arrival characteristics of an indoor multipath channel," *IEEE J. Select Areas Commun.*, vol. 18, no. 3, 347-360.
- [4] Correia Luis M., 2001, "Wireless Flexible Personalised Communications," John Wiley and Sons.
- [5] Salz J. and Winters J. H., Nov 1994, "Effect of fading correlation on adaptive arrays in digital mobile radio," *IEEE Trans. Veh. Technol.*, vol. 43, no. 4, 1049-1057.
- [6] Tsai Jann-An, Buehrer R. B. and Woerner B. D., May 2000, "Spatial fading correlation function of circular antenna arrays with Laplacian energy distribution," *IEEE Commun. Lett.*, vol. 6, no. 5.
- [7] Eggers P. C. F., Kováč I. Z. and Olesen K., May 1998 "Penetration effects on XPD with GSM 1800 handset antennas, relevant for BS polarization diversity for indoor coverage," *Proc. IEEE VTC*, Ottawa, vol. 13, 1959-1963.
- [8] Kuchar A., Rossi J.-P. and Bonek E., Feb 2000, "Directional Macro-Cell channel characterization from urban measurements," *IEEE Trans. Antennas Propagat.*, vol. 48, 137-146.
- [9] Yong S. K., Thompson J. S. and McLaughlin S., 2002, "The impact of channel conditions and antenna parameters on the performance analysis of antenna array architectures," *Mobile VCE core 2 Research Programme, Internal Report*.

The Effect of Antenna Parameters on the Performance Analysis of Different Antenna Array Architectures

S. K. Yong & J. S. Thompson

Institute of Digital Communications

School of Engineering and Electronics, University of Edinburgh,
Edinburgh EH9 3JL, UK.

[†]E-Mail: sky@ee.ed.ac.uk

Abstract

An extensive investigation involving many different antenna parameters on handset antenna arrays is described. The antenna parameters under study include types of antenna arrays, type of antenna elements, mutual coupling, antenna spacing and number of received antennas. These investigations provide invaluable insight to the feasibility of introducing compact antenna arrays on the mobile terminal. Results show that, the application of compact antenna arrays is practical in both indoor and outdoor environments except in strong street canyon effect scenario.

1 Introduction

Antenna arrays (AA) are one of the most promising candidates for capacity and signal quality enhancement in wireless communications systems. The use of multiple antennas at the base station (BS) has been actively investigated by many researchers for many years. Only recently, the introduction of AA at mobile terminals (MT) has gain significant attention due to the huge capacity improvement using multiple input-multiple output configurations. However, the use of multiple antennas at the MT imposes several constraints that need to be taken into consideration. One of the major challenges is due to the limitation in the physical sizes of the MT that limits the number of antenna elements. Ideally, correlation should be zero but the performance loss with correlation as high as 0.7 is not significant [1]. This figure yields an antenna spacing of approximately half a wavelength at the MT. However, when the antenna elements are in close proximity, the effect of mutual coupling (MC) becomes significant. MC arises from the complex interaction between antenna elements in which the voltage at each antenna element is different from the theoretical value when they are isolated in space. Hence, to accurately evaluate the system performance of AA, the effect of MC must be adequately modelled. A number of conflicting studies have been reported that examine the impact of MC. It was shown that the performance of adaptive AA in the presence of MC degraded significantly as compared to the case of no MC [2]. However, [3] reveals that MC improves the performance of AA in term of bit error ratio (BER) in Nakagami fading channel whilst [4] shows that MC decreases the correlation of the received signal between antenna elements. In this paper, we extend the model of MC for uniform linear array (ULA) in [1-4] to the case of uniform circular array (UCA) and uniform rectangular array (URA) by assuming the AA as a linear bilateral network. In addition, the effect of different antenna elements on the system performance is also evaluated using isotropic, halfwave dipole (HD) and patch antennas. In order to study the practicability of handset AA, issues such as antenna spacing and number of receiver antennas are also included in our analysis.

The aims of this paper are two fold. Firstly, to study in details the main constraints in the application of compact antenna arrays (CAA) and describes how such constraints can be modelled and incorporated into the system performance evaluation. This is particularly important as little work has been reported that comprehensively investigates the system performance from the perspective of antenna parameters. Secondly, to study the trade-offs between these parameters in the development of handset AA by considering a 3 dimensional multipath propagation models that permitting both azimuth and elevation angles of arrival to be taken into account. This paper is organised as follows, Section 2 briefly describes the directional channel model used in the simulation. Section 3 outlines the antenna model and approaches adopted in our investigation to analyse the impact of antenna effects on the system performance. This is followed by the performance analysis of the various antenna parameters in Section 4. Simulation results are discussed under specific scenarios. Finally some concluding remarks will be drawn.

2 Directional Vector Channel Model

In this paper, the performance analyses are done by using a frequency non selective directional Rayleigh fading channel model, in a single input-multiple output configuration. The $M \times 1$ received signal vector $\mathbf{y}(t)$, $M \times 1$ channel impulse response $\mathbf{h}(t)$, transmitted BPSK signal $x(t)$ and $M \times 1$ additive white Gaussian noise vector $\mathbf{n}(t)$ are related by

$$\mathbf{y}(t) = \mathbf{h}(t) x(t) + \mathbf{n}(t) \quad (1)$$

where $\mathbf{h}(t)$ is given by

$$\mathbf{h}(t) = \sum_{l=1}^L \alpha_l(t) \mathbf{a}(\varphi_l, \theta_l) \quad (2)$$

α_l is the complex amplitude, $\mathbf{a}(\varphi, \theta)$ is the array factor (AF), M is the number of antennas and L is the total number of MPCs. The scalars φ and θ are the azimuth and elevation angles defined with respect to the positive x and z -axis respectively. The distribution of angles of arrival in both azimuth and elevation angle of arrivals

are modelled by uniform/Gaussian distribution. The AS and ES values are the maximum deviation of the angle spread from the mean direction of arrival. The signals arrive at the AA are processed using maximum ratio combining over 3 million channel realisations and assuming perfect channel knowledge at the receiver.

$$BER = \frac{1}{2} \sum_{k=1}^M \pi_k \left[1 - \sqrt{\frac{\bar{\lambda}_k}{1 + \bar{\lambda}_k}} \right] \quad (3)$$

$$\pi_k = \prod_{i=1}^M \frac{\bar{\lambda}_k}{\bar{\lambda}_k - \bar{\lambda}_i} \quad (4)$$

The theoretical BER can be calculated by [5] where λ_k is the diagonal matrix of eigenvalues obtained using eigenvalue decomposition of covariance matrix $R = E[h(t)h(t)^H] = U\Lambda U^H$ and U is the unitary matrix of eigenvectors. This formula assumes the variance of each entry of $n(t)$ is one.

3 Modelling of Antenna Effect

Apart from the channel effects, to enable a complete performance evaluation of CAA, the impact of the antenna effects on the system performance must be adequately characterised. This section is devoted to how to develop such an antenna model, a topic which is ignored by most of the researchers in studying the performance of AA.

3.1 Types of Antenna Element

Most of the work reported in the literatures assume that the elements of the antenna array are isotropic. This type of element is unrealistic but provides benchmark for more practical antennas to be assessed. In this paper we consider two types of antenna element that are commonly used in wireless communications namely HD and patch antenna. The normalised radiation pattern of HD and patch antenna are given by [6]

$$f(\theta)_{HD} = \cos\left(\frac{\pi}{2} \cos\theta\right) / \sin\theta \quad (5)$$

$$f(\theta, \phi)_{Patch} = \{\sin\theta \sin(X) \sin(Z) / (XZ)\} \times \cos(kL \sin\theta \sin\phi / 2) \quad (6)$$

where $X = 0.5kh \sin\theta \cos\phi$, $Z = 0.5kW \cos\theta$, while L , W and h are the length, width and thickness of the patch antenna respectively. In our case, $L=3\text{cm}$, $W=3\text{cm}$ with negligible h .

3.2 Types of Antenna Array

When the antenna elements are arranged to form an AA, the overall radiation pattern of an array is determined by the type of element used, the spatial positions and orientation of the elements as well as the current that feeds the elements. For an AA with identical elements, the overall radiation pattern can be derived from the principle of pattern multiplication [6] given by $f(\theta, \phi)_{overall} = \text{elemental pattern} \times \text{AF}$. The AF is a function of the array geometry, inter-element spacing,

number of antenna elements as well as the relative magnitude and phase between the elements. In our analysis, we assume the elements are fed with equal amplitude, phases and spacing. Thus, for a given spacing, magnitude and phase shift, the radiation pattern will solely depend on the geometry / configuration of the array. Three types of array are considered in this paper. For the ULA, the AF is given by

$$a(\varphi, \theta)_{ULA} = [1, e^{j2\pi d \cos\varphi \sin\theta / \lambda}, \dots, e^{j2\pi d(M-1) \cos\varphi \sin\theta / \lambda}]^T \quad (7)$$

where d is the antenna spacing, λ is the wavelength, $[\cdot]^T$ denotes the transpose. The AF of the UCA with the centre as a reference point is given by

$$a(\varphi, \theta)_{UCA} = [e^{j\zeta \cos(\varphi - \varphi_1)}, e^{j\zeta \cos(\varphi - \varphi_2)}, \dots, e^{j\zeta \cos(\varphi - \varphi_{M-1})}]^T \quad (8)$$

where $\varphi_n = 2\pi n / M$ and $\zeta = 2\pi r \sin\theta / \lambda$. The scalar r is the circumference distance between antenna elements. In addition, the AF of the URA with $P \times N$ elements located in the x-y plane with reference at the origin is given by

$$a(\mu, \nu)_{URA} = \text{vec}(a_n(\mu) a_p^T(\nu)) \quad (9)$$

where $\mu = 2\pi d_x \cos\varphi \sin\theta / \lambda$, $\nu = 2\pi d_y \sin\varphi \sin\theta / \lambda$,

$a_n(\mu) = [1, e^{j\mu}, \dots, e^{j(N-1)\mu}]^T$, $a_p(\nu) = [1, e^{j\nu}, \dots, e^{j(P-1)\nu}]^T$ and d_x , d_y are the spacings between the array elements parallel to the x and y-axis respectively. The operator $\text{vec}(\cdot)$ maps the a $N \times P$ matrix to an $NP \times 1$ vector by stacking the column of the matrix. Fig. 1. shows the radiation patterns of various arrays using different antenna elements. It can be clearly seen that the pattern gain changes drastically for different arrays as well as for the same array but different antenna elements.

3.3 Mutual Coupling

The modelling of MC in ULA has been discussed in detail in [2]-[4] where an expression that relates the output voltages, current and mutual impedance of the elements is first developed. By treating the M antenna elements as an $M+1$ terminal linear bilateral network, an impedance matrix Z that consists of self and mutual impedance is formed. This approach is valid for any antenna provided the corresponding impedances can be calculated. For instance, the self and mutual impedance

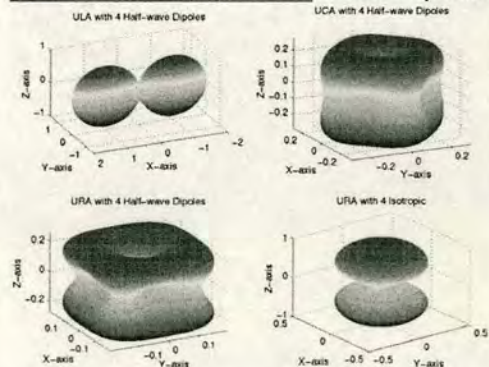


Fig. 1. The radiation pattern of various arrays and elements.

of a thin centre fed dipole can be computed from induced EMF methods. The relationship that governed the received signal with and without coupling, V_m and S_m can be expressed as

$$\begin{bmatrix} 1 + \frac{Z_{11}}{Z_L} & \frac{Z_{12}}{Z_L} & \dots & \frac{Z_{1M}}{Z_L} \\ \frac{Z_{21}}{Z_L} & 1 + \frac{Z_{22}}{Z_L} & \dots & \frac{Z_{2M}}{Z_L} \\ \vdots & \vdots & \ddots & \vdots \\ \frac{Z_{M1}}{Z_L} & \frac{Z_{M2}}{Z_L} & \dots & 1 + \frac{Z_{MM}}{Z_L} \end{bmatrix} \begin{bmatrix} V_1 \\ V_2 \\ \vdots \\ V_M \end{bmatrix} = \begin{bmatrix} S_1 \\ S_2 \\ \vdots \\ S_M \end{bmatrix} \quad (10)$$

Z_{mm} and Z_{mn} are the self and mutual impedances. Written in matrix form, the received signal with MC taken into account can be obtained by matrix inversion as Z is always non-singular i.e. $V=Z^{-1}S$. Note that most of the analysis of adaptive AA assumes the element spacing is such that the MC is negligible and the matrix Z becomes diagonal. The matrix Z characterises the array and is independent of the channel in which the arrays operates. We extend the same modelling approach to the case of the UCA and URA by assuming that the antennas have been relocated into circular and rectangular positions respectively. Fig. 2. shows the magnitude of the coupling matrix elements for HD elements of the UCA and URA case. Notice that the density of the coupling matrix is mostly concentrated at the most adjacent elements corresponding to the nearest elements on the main diagonal. As the distance between successive adjacent elements increases, the magnitude of coupling matrix decreases. In addition, the matrix entries along each subdiagonal are symmetrical about the main diagonal. By incorporating all of the above antenna parameters, the received signal vector, $y(t)$ given by equation (1) is now modified to

$$y(t) = Z^{-1} \sum_{i=1}^L f(\theta_i, \phi_i) a(\theta_i, \phi_i) x(t) + n(t) \quad (11)$$

3.4 Number of Antenna Elements and Inter-element Spacing

In order to optimise the performance gain, a large diversity order is generally required. However, for a given terminal size, increasing the number of antenna elements will reduce the spacing and increase the fading correlation. Thus, the best compromise between spacing and number of elements must be found.

4 Performance Analysis

4.1 The Effect of Type of Antenna Element

To demonstrate the impact of the type of antenna element used in the AA on the system performance, simulations are performed in the 3D multipath propagation model under 2 specific channel conditions associated with azimuth and elevation angles. Firstly, the performance of the ULA with different elements under the channel conditions of MEOA=60°, AS=0° and MAOA=0° with varying ES values is investigated and shown in Fig. . At low SNR, the performance difference between ES values of 5° and 60° for the patch and HD are negligible. Nevertheless, the BER improves

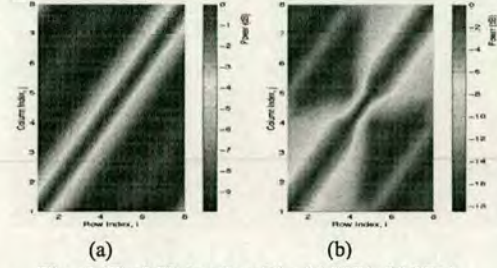


Fig. 2. The MC density of the (a) UCA (b) URA

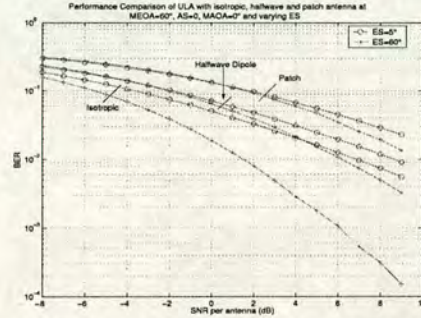


Fig. 3. The BER performance comparison of ULA with different antenna elements associated with the ES.

gradually from low to high ES values at higher SNR. The HD outperforms the patch antenna by approximately 4 dB for both ES values. It is also evident that the BER improves for higher ES values for all types of antenna element. For comparison purposes, the isotropic elements which have the best achievable performance is also plotted. The above observations can be explained by computing the directivity of the ULA for various antenna elements given by

$$D(\theta, \phi) = \frac{4\pi |f(\theta, \phi)|^2}{\int_{\phi=0}^{2\pi} \int_{\theta=0}^{\pi} |f(\theta, \phi)|^2 \sin \theta d\theta d\phi} \quad (12)$$

The directivity for the isotropic, HD and patch elements of the ULA are 4, 8.4 and 20.3 respectively. Since directivity represents the ability of the antennas to focus energy in a particular direction, the antennas corresponding to higher directivity with AOA off the target direction will have low performance gain. On the other hand, low directivity antennas perform well even under large AOA as the energy is distributed over a larger range of angles of arrival. In the second case, the system performance is evaluated at varying the AS values with fixed MAOA=30°, ES=30° and MEOA=45°. The corresponding result is plotted in Fig. 2. where it is observed that the performance improve more drastically as the AS increases as compared to the ES in Fig. . This suggests that both antenna elements perform better under AS rich than ES rich environments. In all the cases, the performance of isotropic element is superior while the patch has performance that is poorest of the 3 types of element. Again, we observe that the HD performs better than the patch antenna by about 4dB.

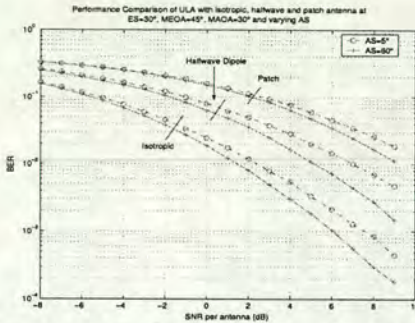


Fig. 2. The BER performance comparison of ULA with different antenna elements associated with the AS.

4.2 The Effect of Types of Antenna Array

In order to illustrate the impact of the type of AA on the system performance, we consider two specific scenarios in which one array performs better from one to another. Fig. 5 (a) shows performance comparison of the three AAs as a function of AS and MAOA. For all the arrays, the performance improves as the AS increases. It can be identified that the UCA and URA outperform the ULA in the endfire (0°) condition and vice versa in the broadside condition (90°). At a very low MAOA, the elements of the ULA are parallel to the direction of the incoming signals and thereby increase the correlation of the received signal at each of the antenna elements. In contrast, for the UCA and URA, only two of the antenna elements are in parallel to the incoming signals while the other two are perpendicular. Thus, the UCA and URA perform better than ULA in this case. As the MAOA increases, the performance of ULA improves to the maximum as the MAOA moves from endfire (0°) to broadside 90° . It is also observed that the UCA and URA are in general insensitive to the MAOA of the incoming signal [7]. Fig. 5 (b) shows the performance comparison of the ULA, UCA and URA as a function of AS and ES. The performance of the three arrays improves as the ES and AS of the incoming signals

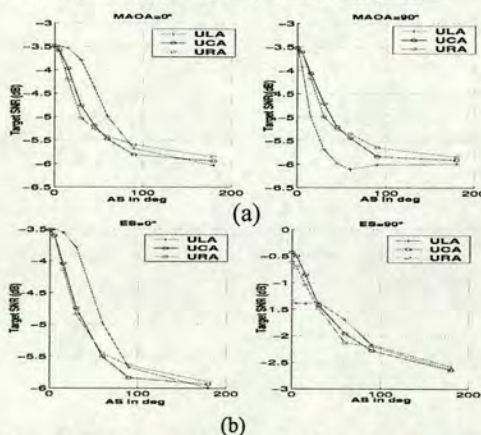


Fig. 3. The effect of type of AA as a function of (a) AS-MAOA (b) AS-ES

increase. This makes the required target SNR drop accordingly. At low ES ($<30^\circ$), the UCA and URA outperform the ULA. For higher ES values, the ULA outperforms the UCA and URA at AS values up to 50° . Beyond this AS value, the performance of these arrays converges.

4.3 The Effect of MC

In all types of AA under consideration, it is apparent that the effects of MC are significant when the antenna separation is small i.e., 0.1λ . The curves of spatial correlation (between element 1 and 2) versus AS with and without MC can be clearly distinguished as shown in Fig. 4. As the antenna spacing increases to 0.5λ , the effects of MC decreases drastically, so that the curves correspond to the case of with and without MC are almost overlapping each other. This suggests that the effect of MC can in fact decorrelate the received signal between the antenna elements due to pattern diversity which has dominant effect over the spatial diversity at low antenna spacing [8]. Furthermore, the spatial correlation also decreases as the MAOA switches from endfire to broadside conditions for the ULA and URA. However, for the UCA, the spatial correlation remains approximately the same for the two extreme MAOA values as UCA are in general insensitive to changes in MAOA values [7]. The reason for the ULA and URA curves looking the same is that the spatial positions of the element 1 and 2 of both arrays are identical.

4.4 The Effect of Number of Antenna Element and Antenna Spacing

Fig. 5. shows the target SNR as a function of antenna spacing for the three AA with a uniform AOA distribution. At low AS, large antenna spacing is necessary to achieve the required target SNR. This is due to the insufficient spatial diversity for the combining techniques to operate efficiently. Hence, under low AS conditions, a large antenna spacing is required to obtain an acceptable result. It is observed that the system performance saturates as the antenna

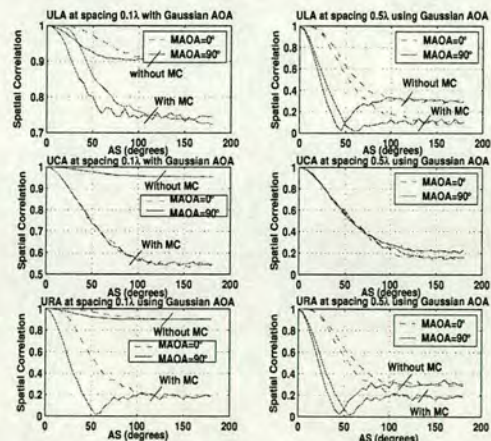


Fig. 4. Spatial correlation versus AS with spacing 0.1 and 0.5λ in Gaussian AOA for ULA, UCA and URA.

spacing goes beyond at least 4λ which signifies that the application of CAA becomes difficult in metropolitan area with narrow streets that causes canyon effect and strong scatterers without line of sight to the MT [9]. Under this scenario, the angles of arrival are confined to two opposite directions with low AS. As the AS increases, more uncorrelated paths arrive from many different directions and thus permitting the combining techniques to work well even at low antenna spacing. An additional 2dB in SNR is needed to achieve the target BER as the antenna spacing is reduced from 0.5 to 0.1λ . Increasing in antenna spacing beyond 0.5λ under large AS does not provide further improvement which indicates that the concept of CAA can be well applied in indoor environment where the AS is expected to be high. Fig. 6. shows the BER comparison for 2, 4 and 8 antennas for the ULA and URA at AS=30° in endfire and broadside conditions. As the MAOA varied from 0° to 90° in a 4 element ULA, the system performance improves considerably. Since the URA is in general not sensitive to the changes in the MAOA, there is no improvement that can be noted in the case URA/URA. However, a small performance difference can be observed in the case of 8 antenna URA. This is due to the orientation of the URA which essentially consists of two four-receiver antennas ULA located parallel to the x-axis. A diversity gain of 4dB can be achieved by doubling the number of antennas used. The use of large diversity order may not be justified in practice. Implementation and marketing issues such as complexity, weight, battery life and size of the MT need to be taken into account.

5 Conclusion

This paper investigates the impact of different antenna parameters associated with the type of antenna elements and arrays, MC, inter-element spacing and number of antennas in the development of CAA. These parameters are modelled and incorporated into the system performance evaluation under some specific channel conditions to demonstrate the efficacy of the antenna parameters. It is found that different antenna elements and arrays yield different performance which is favourable in some cases over another. In addition, we also shown that the presence of the MC can decorrelate

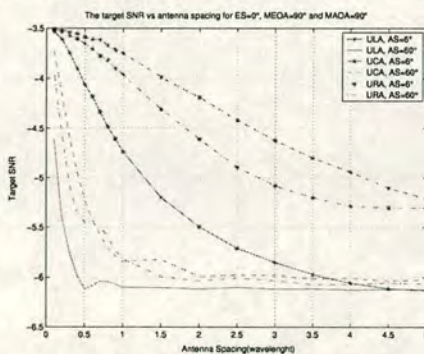


Fig. 5. The target SNR versus antenna spacing for ULA, UCA and URA in uniform AOA distribution.

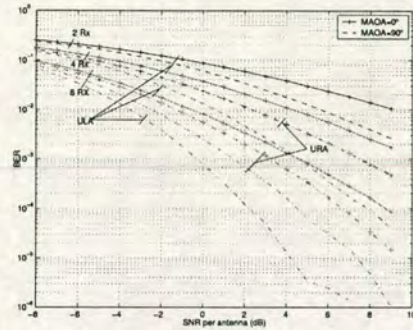


Fig. 6. BER comparison for 2, 4 and 8 diversity branches using HD.

the spatial correlation between antenna elements and is particularly significant at low antenna spacing in all of the AA under considered. The application of CAA is shown to be practical in both indoor and outdoor environments except in scenario where the canyon effect is significant. This in turn requires a lower antenna spacing to achieve the target BER and thus more antenna elements can be crammed into the MT to give better performance.

6 Acknowledgement

The work reported here has formed part of the Wireless Access area of the Core 2 Research Programme of the Virtual Centre of Excellence in Mobile & Personal Communications, Mobile VCE (www.mobilevce.com) whose funding support, including that of EPSRC, is grateful acknowledged.

7 References

- [1] J. Salz and J. H. Winters, "Effect of fading correlation on adaptive arrays in digital mobile radio," *IEEE Trans. Veh. Technol.*, vol. 43, no. 4, pp. 1049-1057, Nov 1994.
- [2] I. D. Gupta, A. A. Ksienski, "Effect of MC on the performance of adaptive arrays," *IEEE Trans. Antennas Propagat.*, Sept 1983, vol. 31, no. 5, pp. 785-791.
- [3] J. Luo, J. R. Zeidler, S. McLaughlin, "Performance analysis of compact antenna arrays with MRC in correlated Nakagami fading channels," *IEEE Trans. Veh. Technol.*, Jan 2001, vol. 50, no. 1, pp. 267-277.
- [4] T. Sventesson, "Antennas and Propagation from a Signal Processing Perspective," PhD Thesis, 2001.
- [5] J. G. Proakis, "Digital Communications," 4th ed. McGraw Hill, 2000.
- [6] C. A. Balanis, "Antenna Theory: Analysis and Design, 2nd Edition," John Wiley and Sons, 1997.
- [7] S. K. Yong, J. S. Thompson and S. McLaughlin, "The impact of channel conditions and antenna parameters on the performance analysis of antenna architectures," Mobile VCE core 2 Research Programme, Internal Report, June 2002.
- [8] J. F. Diouris, S. McLaughlin and J. Zeidler, "Sensitivity analysis of the performance of a diversity receiver," *IEEE 48th ICC, Vancouver*, vol. 3, pp. 1598-1602, June 1999.
- [9] A. Kuchar, J. P. Rossi and E. Bonck, "Directional Macro-Cell channel characterization from urban measurements," *IEEE Trans. Antennas Propagat.* Vol. 48, No. 2, Feb 2000.

The Effect of Various Channel Conditions on the Performance of Different Antenna Array Architectures

S. K. Yong[†] and J. S. Thompson

Institute for Digital Communications, School of Engineering and Electronics,
University of Edinburgh, King's Buildings, Mayfield Road, Edinburgh EH9 3JL, UK.
Telephone: +44 131 650 5655, Fax: +44 131 650 6554
E-Mail: yysk@ieee.org

Abstract—An extensive investigation into the effect of many different channel conditions on the performance of handset antenna arrays is studied. In this paper, we concentrate our analysis to investigate the impact of angular parameters associated with mean azimuth-of-arrival (MAOA), azimuth spread (AS), mean elevation-of-arrival (MEOA) and elevation spread (ES) of the propagation channel under study. The performance analysis is done by comprehensive simulations that incorporate various channel conditions ranging from outdoor to indoor environments on three types of antenna array architectures i.e. uniform linear array, uniform circular array and uniform rectangular array. A theoretical probability of error is also developed which shows excellent agreement with the simulation results. The importance and dependency of the above parameters on the system performance are examined. Results show that the system performance is always dependent on AS and ES while the impact of MAOA and MEOA is array dependent.

Keywords—antenna arrays; radio propagation; sensitivity analysis; spatial correlation

I. INTRODUCTION

Antenna arrays (AAs) are one of the most promising candidates for capacity and signal quality enhancement in wireless communications systems. Since the functionality of the AA is mainly based on the exploitation of the spatial properties of the multipath channel, it is imperative to gain a better understanding of the effect of angular parameters on the performance of AAs. A number of studies have been reported that examine this impact on the system performance. In particular, [1] and [2] studied the effect of mean azimuth-of-arrival (MAOA), azimuth spread (AS) and antenna spacing on the fading correlation for the uniform linear array (ULA) using uniform and Gaussian distributions for the azimuth angle of arrival. However, most of the studies are mainly focused on azimuth plane only, parameterized by the AS and MAOA of the impinging signals. The introduction of handset AAs motivates an investigation into the effect of multipath elevation since the handset could be orientated in any direction [3]. Furthermore, measurement results have also shown that about 65% of the energy was incident with elevation angles larger than 10° with respect to azimuth plane [4]. Thus, it is important to consider a 3-dimensional multipath propagation model that

permits different azimuth-of-arrival (AOA) and elevation-of-arrival (EOA) at the user terminals

The aims of this paper are two fold. Firstly, to study in detail the importance and dependency of the four angular parameters to the system performance. By evaluating the performance patterns as a function of two of the parameters, the sensitivity of these parameters on the system performance can be determined. Secondly, to compare the performance of different AAs under the same channel conditions. This is crucial in selecting types of AAs used in different applications and radio environments. The paper is organized as follows; Section II describes the directional channel model and the steering vector (SV) of the AAs under study. The simulation assumptions are also described. Section III explains the channel parameters sets which form the major part of the analysis in this paper. Analysis on the system performance under various channel parameters sets are also explained and quantified. In section IV, the performance of the AA architectures under study is compared. Finally, in Section V some concluding remarks are drawn.

II. DIRECTIONAL VECTOR CHANNEL MODEL

The performance analyses are done by using a frequency non selective directional Rayleigh fading channel model, in a single input-multiple output configuration. The $M \times 1$ received signal vector $y(t)$, $M \times 1$ channel impulse response $h(t)$, transmitted BPSK signal $x(t)$ and $M \times 1$ additive white Gaussian noise vector $n(t)$ are related by $y(t) = h(t) \cdot x(t) + n(t)$ where $h(t)$ is given by

$$h(t) = \sum_{l=1}^L \alpha_l(t) \cdot a(\varphi_l, \theta_l) \quad (1)$$

where $\alpha_l(t)$ is the complex amplitude, $a(\varphi, \theta)$ is the steering vector (SV), M is the number of antennas and L is the total number of multipath components (MPCs). The scalars $0 \leq \varphi < 2\pi$ and $0 \leq \theta < \pi$ are the AOA and EOA defined with respect to the positive x- and z-axis respectively. For the ULA, the SV is given by

$$a(\varphi, \theta) = [1, e^{j2\pi d \cos \varphi \sin \theta / \lambda}, \dots, e^{j2\pi d (M-1) \cos \varphi \sin \theta / \lambda}]^T \quad (2)$$

[†] This work is supported by Virtual Centre Excellence in Mobile & Personal Communications (Mobile VCE).

where d is the antenna spacing, λ is the wavelength and $[\cdot]^T$ denotes the transpose. The SV of a uniform circular array (UCA) with the centre as a reference point is given by

$$\mathbf{a}(\varphi, \theta) = [e^{j\zeta \cos(\varphi - \psi_1)}, e^{j\zeta \cos(\varphi - \psi_2)}, \dots, e^{j\zeta \cos(\varphi - \psi_{M-1})}]^T \quad (3)$$

where $\psi_n = 2\pi n / M$ and $\zeta = 2\pi r \sin \theta / \lambda$. r is the radius of the UCA. In addition, the SV of a uniform rectangular array (URA) with $P \times N$ elements located in the x - y plane with reference at the origin is given by

$$\mathbf{a}(\varphi, \theta) = \mathbf{a}_N(\mu) \mathbf{a}_P^T(\nu) \quad (4)$$

where $\mu = 2\pi d_x \cos \varphi \sin \theta / \lambda$, $\nu = 2\pi d_y \sin \varphi \sin \theta / \lambda$,

$$\mathbf{a}_N(\mu) = [1, e^{j\mu}, \dots, e^{j(N-1)\mu}]^T \quad \text{and} \quad \mathbf{a}_P(\nu) = [1, e^{j\nu}, \dots, e^{j(P-1)\nu}]^T.$$

Also, d_x and d_y are spacings between the array elements parallel to the x - and y -axis. The signals that arrive at the AA are processed using maximum ratio combining assuming perfect channel knowledge at the receiver. We derive a theoretical bit-error-rate (BER) by first calculating the $M \times M$ covariance matrix as

$$\mathbf{R} = E[\mathbf{h}\mathbf{h}^H] = \int_0^\pi \int_0^{2\pi} \mathbf{a}(\varphi, \theta) \mathbf{a}^H(\varphi, \theta) p(\varphi, \theta) \sin(\theta) d\varphi d\theta \quad (5)$$

where $p(\varphi, \theta)$ is the joint probability density function (pdf) of the AOA and EOA. It is assumed that the AOA and EOA are

independent of each other i.e. $p(\varphi, \theta)$ can be decomposed to $p(\varphi)p(\theta)$. We concentrate our analysis on uniform AOA and EOA distributions since [5] shows that the key parameter to the system performance is the spread of the MPC and not the type of pdf under investigation. The AS and elevation spread (ES) values are defined as the maximum deviation of the angle spread from the MAOA and mean elevation-of-arrival (MEOA) respectively.

As shown in [6], the real and imaginary parts of the element $R_{(m,n)}$ can be expressed in closed-form in (6) and (7) for the case of ULA and (8) and (9) for the both cases of UCA and URA, respectively. The scalars Δ_θ , Δ_φ , θ_0 and φ_0 denotes the ES, AS, MEOA and MAOA respectively. $\Gamma(x)$ is the gamma function and $C = 1/\text{sinc}(\theta_0)\text{sinc}(\Delta_\theta)$. The scalar Z takes different values according to the geometry of the AA. For the ULA, $Z = 2\pi d(m-n)/\lambda$. For the UCA, $Z = \sqrt{Z_1^2 + Z_2^2}$ where $Z_1 = k[\cos \psi_m - \cos \psi_n]$ and $Z_2 = k[\sin \psi_m - \sin \psi_n]$. Similarly, for the case of URA, $Z = \sqrt{Z_x^2 + Z_y^2}$ with $Z_y = k(p-q)k_y$ and $Z_x = k(n-m)k_x$. The BER is then calculated using [7]

$$\begin{aligned} \text{Re}[R_{(m,n)}] = & -C \left\{ \sum_{k=0}^{\infty} \sum_{l=0}^k \frac{(-1)^{2k+1+l} Z^{2k}}{2^{4k} (k!)^2} \binom{2k+1}{l} \text{sinc}[\Delta_\theta(2k+1-2l)] \sin[\theta_0(2k+1-2l)] \right. \\ & \left. + 2 \sum_{k=1}^{\infty} \sum_{l=0}^{\infty} \sum_{p=0}^{k+l} \frac{(-1)^{2k+2l+1+p}}{l! \Gamma(2k+l+1)} \right. \\ & \left. \times \left(\frac{Z^{2(k+l)}}{2^{4(k+l)}} \right) \binom{2(k+l)+1}{p} \cos(2k\varphi_0) \text{sinc}(2k\Delta_\varphi) \text{sinc}[(2k+l-p)+1]\Delta_\theta \sin[(2k+l-p)+1]\theta_0 \right\} \quad (6) \end{aligned}$$

$$\begin{aligned} \text{Im}[R_{(m,n)}] = & 2C \sum_{k=0}^{\infty} \sum_{l=0}^{\infty} \sum_{p=0}^{k+l} \frac{(-1)^{k+l+p}}{l! \Gamma(2k+l+2)} \left(\frac{Z}{2} \right)^{2(k+l)+1} \text{sinc}[(2k+1)\Delta_\varphi] \cos[(2k+1)\varphi_0] \times \\ & \left[\frac{1}{2^{2(k+l+1)}} \binom{2(k+l+1)}{k+l+1} + \frac{(-1)^{k+l+1}}{2^{2(k+l+1)}} \binom{2(k+l+1)}{p} \text{sinc}[2(k+l+1-p)\Delta_\theta] \cos[2(k+l+1-p)\theta_0] \right] \quad (7) \end{aligned}$$

$$\begin{aligned} \text{Re}[R_{(m,n)}] = & -C \left\{ \sum_{k=0}^{\infty} \sum_{l=0}^k \frac{(-1)^{2k+1+l} Z^{2k}}{2^{4k} (k!)^2} \binom{2k+1}{l} \text{sinc}[\Delta_\theta(2k+1-2l)] \sin[(2k+1-2l)\theta_0] \right. \\ & \left. + 2 \sum_{k=1}^{\infty} \sum_{l=0}^{\infty} \sum_{p=0}^{k+l} \frac{(-1)^{k+2l+1+p}}{l! \Gamma(2k+l+1)} \right. \\ & \left. \times \left(\frac{Z^{2(k+l)}}{2^{4(k+l)}} \right) \binom{2(k+l)+1}{p} \text{sinc}(2k\Delta_\varphi) \cos(2k\alpha) \text{sinc}[(2k+l-p)+1]\Delta_\theta \sin[(2k+l-p)+1]\theta_0 \right\} \quad (8) \end{aligned}$$

$$\begin{aligned} \text{Im}[R_{(m,n)}] = & 2C \sum_{k=0}^{\infty} \sum_{l=0}^{\infty} \sum_{p=0}^{k+l} \frac{(-1)^{l+p}}{l! \Gamma(2k+l+2)} \left(\frac{Z}{2} \right)^{2(k+l)+1} \text{sinc}[(2k+1)\Delta_\varphi] \sin[(2k+1)\alpha] \\ & \left[\frac{1}{2^{2(k+l+1)}} \binom{2(k+l+1)}{l+k+1} + \frac{(-1)^{k+l+1}}{2^{2(k+l+1)}} \binom{2(k+l+1)}{p} \text{sinc}[2(k+l+1-p)\Delta_\theta] \cos[2(k+l+1-p)\theta_0] \right] \quad (9) \end{aligned}$$

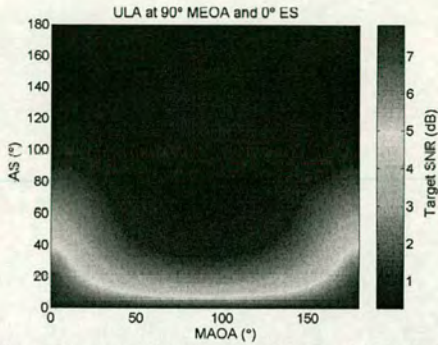


Figure 1: The target SNR as function of MAOA and AS for ULA.

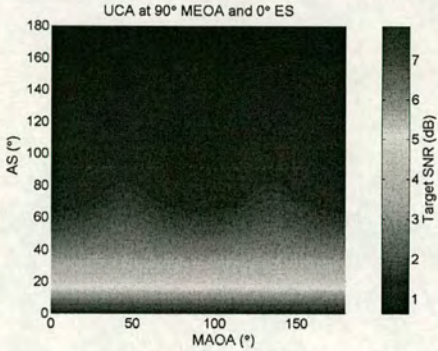


Figure 2: The target SNR as function of MAOA and AS for UCA.

$$BER = \frac{1}{2} \sum_{k=1}^M \pi_k \left[1 - \sqrt{\frac{\bar{\lambda}_k}{1 + \bar{\lambda}_k}} \right] \quad (10)$$

$$\pi_k = \prod_{i=1}^M \frac{\bar{\lambda}_k}{(\bar{\lambda}_k - \bar{\lambda}_i)} \quad (11)$$

where $\bar{\lambda}_k$ is the diagonal matrix of eigenvalues obtained using eigenvalue decomposition of covariance matrix $R = U\Lambda U^H$ and U is the unitary matrix of eigenvectors.

III. PERFORMANCE ANALYSIS

The performance of the ULA, UCA and URA can be vastly different under different channel conditions especially, depending on the angles of arrival of the MPCs. The angles of arrival are governed by several parameters in terms of the MAOA, AS, MEOA and ES of the MPCs. In order to examine the importance and dependency of the above parameters to the system performance, two of the above parameters are examined at a time while keeping the other two fixed. In our analysis, the performance is measured in terms of required target signal-to-ratio (SNR) to achieve a given target BER. Unless otherwise specified, the number of received antennas (with isotropic elements) and target BER are fixed at 4 and 0.01. Note that the

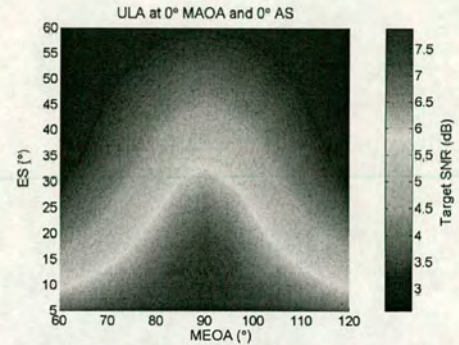


Figure 3: The target SNR as function of MEOA and ES for ULA.

four element UCA and URA have a similar geometry but the former is 0.1λ less than the latter in spacing. Four parameter sets are investigated to study their impact on the system performance. The investigation on parameter set in subsection A has also been reported such as in [1] and [2]. We then discuss three additional parameter sets in subsection B, C and D, which to the best of authors' knowledge have yet to be reported in the literature.

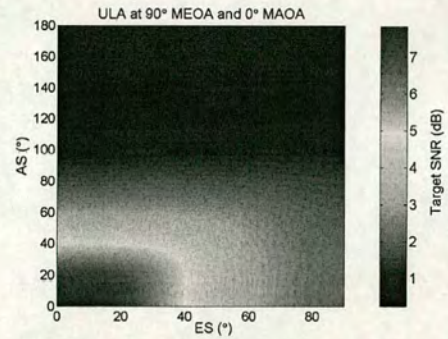


Figure 4: The target SNR as function of AS and ES for ULA.

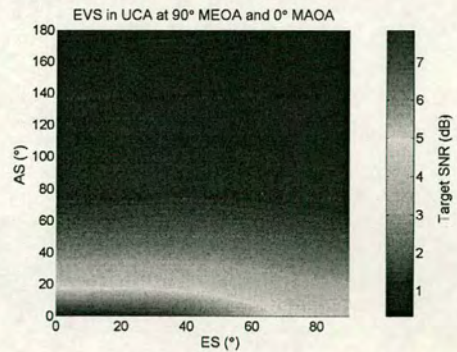


Figure 5: The target SNR as function of AS and ES for UCA.

A. Effect of MAOA and AS at 0° ES and 90° MEOA

Fig. 1 and 2 show the target SNR as a function of AS and MAOA with the ULA and UCA configurations. For the ULA, at low AS ($<5^\circ$), the required target SNR is high irrespective of the MAOA values. However, as the AS increases, the reduction of the target SNR is more rapid in the broadside region (around 90°) than in the endfire region (around 0° and 180°). For large AS values ($>80^\circ$), the performance of the ULA is approximately equal irrespective of the MAOA [2]. Unlike the ULA, the performance of the UCA or URA is relatively insensitive to changes of MAOA. Nonetheless, their performance is highly sensitive to the AS of the incoming signal. By studying Fig. 1, we note that as the AS increases, significant improvements occur in target SNR. On the other hand, only small changes can be observed in target SNR as the MAOA changes. This suggests that the system performance is AS dependent while the effect of MAOA is array dependent

B. Effect of MEOA and ES at 0° AS and 0° MAOA

In this scenario, the performance of the three arrays have a similar pattern. As shown in Fig. 3 for the case of the ULA, the higher target SNR values are concentrated at the horizontal plane corresponding to 90° MEOA. In addition, the performance is symmetrical about this MEOA value because the SVs for MEOAs below/above 90° are mirror images to each other. For a given ES, the performance improves slightly as the MEOA deviates from the 90° . For a given MEOA, the performance improves significantly as the ES increases. The above observations highlight the importance of ES as compared to MEOA in system performance. Unlike the MAOA, the behaviour of all the three array types is similar when the MEOA is changed. Only slight performance differences between the ULA and UCA/URA can be observed. This is due to a slightly higher pattern gain in elevation of the ULA over the UCA and URA.

C. Effect of AS and ES at 0° MAOA and 90° MEOA

Fig. 4 and 5 show the target SNR as a function of AS and ES for the ULA and UCA respectively. The performance of both arrays has a very similar pattern. However, in the case of the ULA, it can be seen that the changes in target SNR is equal in both directions of AS and ES which suggests that the impact of both parameters for the ULA is equally important for this MAOA (0°). On the other hand, the impact of AS is more significant than ES in the case of the UCA and URA as their performance improves considerably as the AS increases. Only little performance gain can be obtained at low AS even with high ES values. This condition holds up to AS about 50° and then performance starts to saturate even with increasing ES. Hence, we can conclude that the sensitivity of the UCA and URA to changes in AS is higher than to changes in ES.

D. Effect of MAOA and MEOA at 30° AS and 30° ES

Fig. 6 and 7 show the impact of the MAOA and MEOA on the ULA and UCA. For the ULA, highest and lowest target

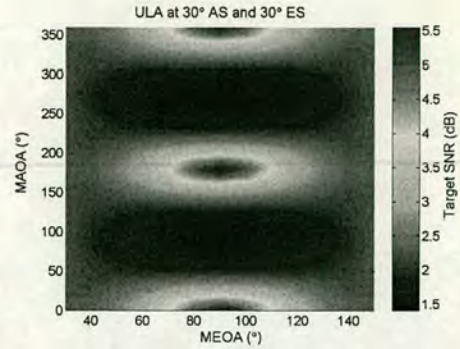


Figure 6. The target SNR as function of MAOA and MEOA for ULA

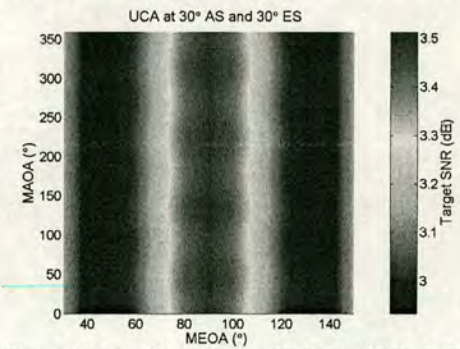


Figure 7. The target SNR as function of MAOA and MEOA for UCA

SNR regions can be identified in endfire (0° and 180° MAOA) and broadside (90° and 270° MAOA) conditions respectively, with 90° MEOA. As the MEOA deviates from 90° , the target SNR decreases and increases by a fraction of a dB in the endfire and broadside regions respectively. The performance of the UCA and URA has a similar pattern (the latter is not shown) with higher target SNR values concentrated at the horizontal plane (90° MEOA) and independent of the MAOA values. Notice that the changes in target SNRs under this parameter set is comparatively small. Hence, we conclude that the effect of the MEOA and MAOA on the system performance is negligible. In addition, we found that the ULA is sensitive to both parameters while the UCA and URA are relatively insensitive to both parameters (though the effect of MEOA is more significant, than MAOA).

IV. PERFORMANCE COMPARISON

In general, the performance of the three arrays improves as the AS increases. For most of the cases, the ULA outperforms the UCA and URA except at very low MAOA values. At a very low MAOA, the elements of the ULA are parallel to the direction of the incoming signals and thereby increasing the correlation of the received signal at each of the antenna elements. In contrast, for the UCA and URA, only two of the antenna elements are in parallel to the incoming signals while

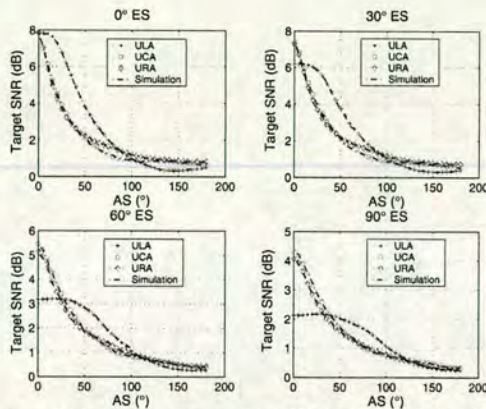


Figure 8. The performance comparison of ULA, UCA and URA under different ES at varying AS with 0° MAOA and 90° MEOA.

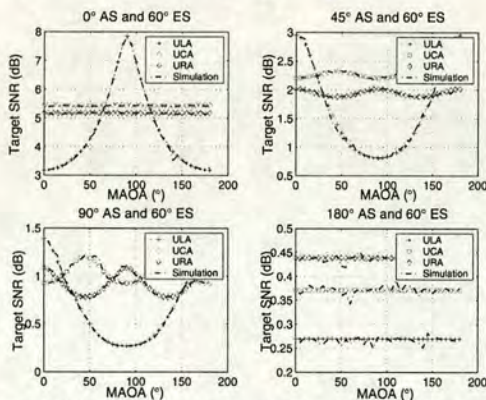


Figure 9. The performance comparison of ULA, UCA and URA under different AS at varying MAOA with the 60° ES and 90° MEOA

the other two are perpendicular. Thus, the UCA and URA perform better than ULA in this case. The performance of ULA improves to the maximum as the MAOA moves from endfire (0°) to broadside (90°). Fig. 8 shows the performance comparison between the three arrays for different ES again with varying AS. In general, the performance of the three arrays improves as the ES increases. This makes the required target SNR drop accordingly. Also, for a given ES, the performance of the array improves as the AS of the incoming signal increases. At an ES less than or equal to 30°, the UCA and URA outperform the ULA. For higher ES values, the ULA outperforms the UCA and URA at low AS values up to 40° and beyond this AS value, the performance of these arrays converges. Fig. 9 shows the performance comparison versus MAOA under different AS with ES at 60°. In this specific instance of the ULA, we note that at zero AS, the performance

gets worse as MAOA goes from 0° to 90°. However, as the AS increases, the performance now improves as MAOA goes from 0° to 90°. Thus, the AS effect is more important than that of the MAOA. For a very large AS value, the ULA performance turns out to be insensitive to the MAOA. In all the cases, the performance of the UCA and URA are relatively insensitive to the MAOA parameter. Also, the performance of the UCA and URA are comparable to each other under many scenarios as the pattern gain for both arrays with four antennas looks very similar. Furthermore, verification is achieved by means of computer simulation over 3 million channel realizations to calculate the BER performance.

V. CONCLUSION

This paper investigates the impact of different channel conditions on the system performance parameterized by the MAOA, AS, MEOA and ES of the impinging signals. Three types of AA are examined under four parameter sets. As shown in our analysis, the performance of the arrays can be vastly different in different channel conditions. The importance and dependency of the parameters under study can be seen from the performance patterns. We found that the impact of AS and ES are of particular interest. On the other hand, the impact of MAOA and MEOA are generally insignificant to the system performance but it does depend on the type of array under investigation. The four element URA and UCA are insensitive to the MAOA and MEOA but the ULA is very much affected by the MAOA of the MPCs - it usually performs much better in broadside than in endfire conditions. There are also trade-offs of ES with MAOA and AS for the ULA. Furthermore, theoretical results are also presented which agree very well with the simulation results.

REFERENCES

- [1] J. Salz and J. H. Winters, "Effect of fading correlation on adaptive arrays in digital mobile radio," *IEEE Trans. on Veh. Technol.*, vol. 43, no. 4, pp. 1049-1057, Nov. 1994.
- [2] J. Luo, J. R. Zeidler and S. McLaughlin, "Performance analysis of compact antenna arrays with MRC in correlated Nakagami fading channels," *IEEE Trans. on Veh. Technol.*, vol. 50, no. 1, pp. 267-277, Jan. 2001.
- [3] P. C. F. Eggers, I. Z. Kováč and K. Olesen, "Penetration effects on XPD with GSM 1800 handset antennas, relevant for BS polarization diversity for indoor coverage," *IEEE 48th Veh. Technol. Conference*, vol. 13, pp. 1959-1963, Ottawa, May 1998.
- [4] A. Kuchar, J.-P. Rossi and E. Bonek, "Directional Macro-Cell channel characterization from urban measurements," *IEEE Trans. Antennas Propagat.*, vol. 48, pp. 137-146, Feb 2000.
- [5] J. B. Andersen and K. I. Pedersen, "Angle-of-arrival statistics for low resolution antenna," *IEEE Trans. Antennas Propagat.* Vol. 50, No. 3, pp. 391-395, Mar. 2002.
- [6] S. K. Yong and J. S. Thompson S. McLaughlin, "3-dimensional spatial fading correlation models for antenna arrays," Mobile VCE core 2 Research Programme, *Internal Report*, Mar 2003.
- [7] J. G. Proakis, "Digital communications," 4th ed., McGraw Hill, 2000.
- [8] I. S. Gradshteyn and I. M. Ryzhik, "Table of integrals, series and products," 5th ed., Academic press, 1994.

References

- [1] T. S. Rappaport, A. Annamalai, R. M. Buehrer, and W. H. Tranter, "Wireless communications: past events and a future perspective," *IEEE Communications Magazine*, vol. 40, no. 5, pp. 148–161, May 2002.
- [2] Y. Kim, B. J. Jeong, J. Chung, C. S. Hwang, J. S. Ryu, K. H. Kim, and Y. K. Kim, "Beyond 3G: vision, requirements, and enabling technologies," *IEEE Communications Magazine*, vol. 41, no. 3, pp. 120–124, March 2003.
- [3] P. H. Lehne and M. Pettersen, "An overview of smart antenna technology for mobile communications systems," *IEEE Communications Surveys*, vol. 2, no. 4, pp. 2–13, Forth Quarter 1999.
- [4] S. Ponnekanti, "An overview of smart antenna technology for heterogeneous networks," *IEEE Communications Surveys*, vol. 2, no. 4, pp. 14–23, Fourth Quarter 1999.
- [5] J. H. Winters, "Smart antenna for wireless systems," *IEEE Personal Communications*, pp. 23–35, February 1998.
- [6] J. S. Thompson, P. M. Grant, and B. Mulgrew, "Smart antenna arrays for CDMA systems," *IEEE Personal Communications*, vol. 3, no. 5, pp. 16–25, October 1996.
- [7] T. S. Rappaport, *Smart Antenna: Adaptive Arrays, Algorithms, and Wireless Position Location*, IEEE press, Virginia, USA, 1999.
- [8] C. B. Dietrich, K. Dietze, J. R. Neally, and W. L. Stutzman, "Spatial, polarization and pattern diversity for wireless handheld terminals," *IEEE Transactions on Antennas and Propagation*, vol. 49, no. 9, pp. 1271–1281, September 2001.
- [9] G. F. Pedersen, J. O. Nielsen, and J. B. Andersen, "Antennas for mobile terminals; size, measurements and performance," in *Proceedings of URSI General Assembly (URSI'02)*, Maastricht, Netherlands, August 2002, invited paper, no. 1742.
- [10] G. F. Pedersen and J. Bach Andersen, "Handset antennas for mobile communications: Integration, diversity, and performance," *Review of Radio Science 1996-1999*, pp. 119–138, August 1999.
- [11] L. M. Correia, *Wireless Flexible Personalised Communications: COST 259: European Co-operation in Mobile Radio Research*, John Wiley and Sons Ltd., West Sussex, 2001.
- [12] I. D. Gupta and A. A. Ksienski, "Effect of mutual coupling on the performance of adaptive arrays," *IEEE Transactions on Antennas and Propagation*, vol. 31, no. 5, pp. 785–791, September 1983.
- [13] E. M. Freil and K. M. Pasala, "Effect of mutual coupling on the performance of STAP antenna arrays," *IEEE Transactions on Aerospace and Electronic Systems*, vol. 36, no. 2, pp. 518–527, April 2000.

- [14] T. Svantesson, *Antennas and propagation from a signal processing perspective*, Ph.D. thesis, Chalmers University of Technology, Göteborg, Sweden, May 2001.
- [15] J. Luo, J. R. Zeidler, and S. McLaughlin, "Performance analysis of compact antenna arrays with MRC in correlated Nakagami fading channels," *IEEE Transactions on Vehicular Technology*, vol. 50, no. 1, pp. 267–277, January 2001.
- [16] "Description of the modelling methods," Tech. Rep., METAMORP Technical Report C-2/1, 1999.
- [17] Q. H. Spencer, B. D. Jeffs, M. A. Jensen, and A. L. Swindlehurst, "Modelling the statistical time and angle of arrival characteristics of an indoor multipath channel," *IEEE Journal on Selected Areas in Communications*, vol. 18, no. 3, pp. 347–360, March 2000.
- [18] J. Salz and J. H. Winters, "Effect of fading correlation on adaptive arrays in digital mobile radio," *IEEE Transactions on Vehicular Technology*, vol. 43, no. 4, pp. 1049–1057, November 1994.
- [19] Jann-An. Tsai and B. D. Woerner, "Spatial fading correlation function of circular antenna arrays with Lapalcian distribution energy," *IEEE Communications Letters*, vol. 6, no. 5, pp. 178–180, May 2002.
- [20] J. Fulh, A. F. Molisch, and E. Bonek, "A unified channel model for mobile radio systems with smart antennas," *IEE Proceedings on Radar, Sonar and Navigation*, vol. 145, pp. 32–41, February 1998.
- [21] G. D. Durgin and T. S. Rappaport, "Theory of multipath shape factors for small-scale fading wireless channels," *IEEE Transactions on Antennas and Propagation*, vol. 48, no. 5, pp. 682–693, May 2000.
- [22] R. M. Buehrer, "The impact of angular energy distribution on the spatial correlation," in *Proceedings of IEEE 56th Vehicular Technology Conference (VTC'02-Fall)*, Vancouver, Canada, September 2002, vol. 2, pp. 1173–1177.
- [23] L. Schumacher, K. I. Pedersen, and P. E. Mogensen, "From antenna spacings to theoretical capacities-guidelines for simulating MIMO systems," Lisbon, Portugal, September 2002, vol. 2, pp. 587–592.
- [24] J. B. Andersen and K. I. Pedersen, "Angle-of-arrival statistics for low resolution antennas," *IEEE Journal on Selected Areas in Communications*, vol. 50, no. 3, pp. 391–394, March 2002.
- [25] T. Aulin, "A modified model for the fading signal at the mobile radio channel," *IEEE Transactions on Vehicular Technology*, vol. 28, no. 3, pp. 182–202, August 1979.
- [26] R. H. Clarke, "A statistical theory of mobile-radio reception," *Bell System Technical Journal*, vol. 47, pp. 957–1000, July-August 1968.
- [27] P. D. Teal, D. Abhayapala, and R. D. Kennedy, "Spatial correlation for general distributions of scatterers," *IEEE Signal Processing Letters*, vol. 9, no. 10, pp. 305–308, October 2002.

- [28] Y. Z. Mohasseb and M. P. Fitz, "A 3-D spatio-temporal simulation model for wireless channels," *IEEE Journal on Selected Areas in Communications*, vol. 20, no. 6, pp. 1193–1203, August 2002.
- [29] R. G. Vaughan and J. B. Andersen, *Channels, Propagation and Antennas for Mobile Communications*, IEE Electromagnetic Waves Series 50, London, UK, 2003.
- [30] A. Kuchar, J. P. Rossi, and E. Bonek, "Directional macro-cell channel characterization from urban measurements," *IEEE Transactions on Antennas and Propagation*, vol. 48, no. 2, pp. 137–146, February 2000.
- [31] J. Fuhl, J. P. Rossi, and E. Bonek, "High-resolution 3-D direction-of-arrival determination for urban mobile radio," *IEEE Transactions on Antennas and Propagation*, vol. 45, no. 4, pp. 672–682, April 1997.
- [32] K. Kalliola, K. Sulonen, H. Laitinen, O. Kivekas, J. Krogerus, and P. Vainikainen, "Angular power distribution and mean effective gain of mobile antenna in different propagation environments," *IEEE Transactions on Vehicular Technology*, vol. 51, no. 5, pp. 823–838, September 2002.
- [33] M. B. Knudsen and G. F. Pedersen, "Spherical outdoor to indoor power spectrum model at the mobile terminal," *IEEE Journal on Selected Areas in Communications*, vol. 20, no. 6, pp. 1156–1169, August 2002.
- [34] M. Toeltsch, J. Laurila, K. Kalliola, A. F. Molisch, P. Vainikainen, and E. Bonek, "Statistical characterization of urban spatial radio channels," *IEEE Journal on Selected Areas in Communications*, vol. 20, no. 3, pp. 539–549, April 2002.
- [35] J. Laurila, K. Kalliola, M. Toeltsch, K. Hugl, P. Vainikainen, and E. Bonek, "Wide-band 3-D characterization of mobile radio channels in urban environment," *IEEE Transactions on Antennas and Propagation*, vol. 50, no. 2, pp. 233–243, February 2002.
- [36] J. C. Liberti and T. S. Rappaport, *Smart Antennas for Wireless Communications: IS-95 and Third Generation CDMA Applications*, Prentice Hall, Upper Saddle River, NJ, USA, 1999.
- [37] S. K. Yong, J. S. Thompson, and S. McLaughlin, "Implementation of COST259 channel models using tapped delay line for multiple antenna receivers," in *Proceedings of IEE 3rd International Conference on 3G 2002 Mobile Communication Technologies (3G'02)*, London, United Kingdom, May 2002, pp. 165–169.
- [38] S. K. Yong, J. S. Thompson, and S. McLaughlin, "Capacity evaluation for multiple antennas using wideband directional channel model for different channel conditions," in *Proceedings of IEE Conference on Getting the Most Out of the Radio Spectrum*, London, UK, October 2002, pp. 27/1–27/4.
- [39] S. K. Yong and J. S. Thompson, "The impact of antenna parameters on the performance of different antenna arrays architectures," in *Proceedings of 5th European Personal Mobile Communications Conference (EPMCC'03)*, Glasgow, United Kingdom, April 2003, pp. 5–10.

- [40] S. K. Yong and J. S. Thompson, "The effect of channel conditions and antenna parameters on the performance analysis of compact antenna arrays," submitted to *IEE Proceedings on Communications*, July 2003, revised January 2004,.
- [41] S. K. Yong and J. S. Thompson, "The impact of angle of arrival distribution on the performance analysis of different antenna arrays architectures," in *Proceedings of IEE 11th International Conference on Antennas and Propagation (ICAP'03)*, Exeter, United Kingdom, March 2003, vol. 2, pp. 840–843.
- [42] S. K. Yong and J. S. Thompson, "The effect of various channel conditions on the performance of various antenna arrays architectures," in *Proceedings of IEEE 58th Vehicular Technology Conference (VTC'03-Fall)*, Orlando, USA, October 2003, vol. 1, pp. 6–10.
- [43] S. K. Yong and J. S. Thompson, "A 3-Dimensional spatial fading correlation model for uniform rectangular arrays," *IEEE Antennas and Wireless Propagation Letters*, vol. 2, no. 12, pp. 182–185, 2003.
- [44] S. K. Yong, "A closed-form spatial fading correlation model for electromagnetic vector sensors," Tech. Rep., COST273 Temporary Documents TD(03)106, Paris, France, May 2003.
- [45] S. K. Yong and J. S. Thompson, "A 3-dimensional spatial fading correlation model for electromagnetic vector sensors," in *Proceedings of IEEE 6th International Symposium on Antenna, Propagation and EM Theory (ISAPE'03)*, Beijing, China, October 2003, in press, pp. 843–846.
- [46] S. K. Yong and J. S. Thompson, "3-Dimensional spatial fading correlation models for compact MIMO receivers," submitted to *IEEE Transactions on Wireless Communications*, October 2003.
- [47] C. A. Balanis, *Antenna Theory: Analysis and Design*, John Wiley & Son, Inc., New York, USA, 2nd edition, 1997.
- [48] W. L. Stutzman and G. A. Thiele, *Antenna Theory and Design*, John Wiley & Son, Inc., New York, USA, 2nd edition, 1998.
- [49] J. D. Kraus and R. Marhefka, *Antennas for all applications*, McGraw Hill, New York, 3rd edition, 2001.
- [50] R. S. Elliot, *Antenna Theory and Design, Revised Edition*, IEEE Press Series on Electromagnetic Wave Theory, New York, USA, classical edition, 2003.
- [51] J. D. Kraus and D. A. Fleisch, *Electromagnetics with applications*, McGraw Hill, Singapore, 5th edition, 1999.
- [52] W. L. Stutzman, *Polarization in electromagnetic systems*, Artech House, Boston, USA, 1992.
- [53] R. C. Johnson and H. Jasik, *Antenna engineering handbook*, McGraw Hill, New York, 3rd edition, 1991.

-
- [54] K. Fujimoto and J.R. James (Editor), *Mobile Antenna Systems Handbook*, Artech House, Boston, USA, 2nd edition, 2000.
- [55] R. Janaswamy, *Radiowave propagation and smart antennas*, Kluwer academic publishers, Norwell, Massachusetts, USA, 2001.
- [56] K. R. Dandekar, H. Ling, and G. Xu, "Experimental study of mutual coupling compensation in smart antenna applications," *IEEE Transactions on Wireless Communications*, vol. 1, no. 3, pp. 480–487, July 2002.
- [57] R. F. Harrington, *Field Computation by Moment Methods*, IEEE Press, Piscataway, New Jersey, USA, 1993.
- [58] G. J. Burke and A. J. Poggio, "Numerical electromagnetics code (NEC)-method of moments," Technical document 11,, Naval Ocean System Center, San Diego, USA, January 1981.
- [59] A. J. Julian, J. M. Logan, and J. W. Rockway, "MININEC: A mini-numerical electromagnetics code," Technical document 516, Naval Ocean System Center, San Diego, USA, September 1982.
- [60] J. Rockway, J. Logan, D. Tam, and S. Li, *The MININEC SYSTEM: Microcomputer analysis of wire antennas*, Artech House, Boston, USA, 1988.
- [61] C. See, "Sensor array calibration in the presence of mutual coupling and unknown sensor gains and phases," *IEE Electronics Letters*, vol. 30, pp. 373–374, March 1994.
- [62] D. P. McNamara, M. A. Beach, and P. N. Flescher, "Experimental investigation into the impact of mutual coupling on MIMO communication systems," in *Proceedings of 5th International Symposium on Wireless Personal Multimedia Communications (WPMC'01)*, Aalborg, Denmark, September 2001, pp. 169–173.
- [63] B. H. Fleury and P. E. Leuthold, "Radiowave propagation in mobile communications: An overview of European research," *IEEE Communications Magazine*, vol. 34, no. 2, pp. 70–81, February 1996.
- [64] J. D. Parsons, *The mobile radio propagation channel*, Pentech press, London, United Kingdom, 1992.
- [65] T. S. Rappaport, *Wireless Communications: Principles and Practice*, Prentice Hall PTR, New Jersey, USA, 2nd edition, 2002.
- [66] B. H. Fleury, "First- and second-order characterization of direction dispersion and space selectivity in the radio channel," *IEEE Transactions on Information Theory*, vol. 46, no. 6, pp. 2027–2044, September 2000.
- [67] J. G. Proakis, *Digital Communications*, McGraw-Hill, New York, 4th edition, 2000.
- [68] B. Sklar, "Rayleigh fading channel in mobile digital communication systems part 1: Characterization," *IEEE Communications Magazine*, vol. 35, no. 9, pp. 136–146, September 1997.

-
- [69] M. C. Vanderveen, *Estimation of parametric channel models in wireless communication networks*, Ph.D. thesis, Stanford University, Stanford, USA, November 1997.
- [70] W. Jakes, *Microwave Mobile Communications*, Wiley Interscience, New York, USA, 1974.
- [71] M. J. Gans, "A power-spectra theory of propagation in the mobile radio environment," *IEEE Transactions on Vehicular Technology*, vol. 21, no. 1, pp. 27–38, February 1972.
- [72] S. Saunders, *Antenna and propagation for wireless communications systems*, John Wiley and Sons Ltd., London, United Kingdom, 1999.
- [73] S. K. Yong, J. S. Thompson, and S. McLaughlin, "On the implementation of COST259 channel models," Mobile VCE Core 2 Research Programme, WP 3.3.2, internal report II, MVCE, July 2001.
- [74] K. I. Pedersen, P. E. Mogensen, and B. H. Fleury, "A stochastic model of the temporal and azimuthal dispersion seen at the base station in outdoor propagation environments," *IEEE Transactions on Vehicular Technology*, vol. 49, no. 2, pp. 437–447, March 2000.
- [75] W. Lee, "Effects on correlation between two mobile radio base station antennas," *IEEE Transactions on Communications*, vol. 21, no. 11, pp. 1214–1224, November 1973.
- [76] M. Steinbauer, H. Asplund, I. de Coster, D. Hampicke, R. Heddergott, N. Lohse, and A. F. Molisch, "Mission report – modelling unification workshop," Tech. Rep., COST 259 Temporary Documents TD(61), Vienna, Austria, April 1999.
- [77] S. Kozono, T. Tsuruhara, and M. Sakamoto, "Base station polarization diversity reception for mobile radio," *IEEE Transactions on Vehicular Technology*, vol. 33, no. 4, pp. 301–305, November 1984.
- [78] P. C. F. Eggers, J. Toftgard, and A. M. Oprea, "Antenna systems for base station diversity in urban small and micro cells," *IEEE Journal on Selected Areas in Communications*, vol. 11, no. 7, pp. 1046–1057, September 1993.
- [79] A. M. D. Turkmani, A. A. Arowojolu, P. A. Jefford, and C. J. Kellett, "An experimental evaluation of the performance of two-branch space and polarization diversity schemes at 1800MHz," *IEEE Transactions on Vehicular Technology*, vol. 44, no. 2, pp. 318–326, May 1995.
- [80] H. Sano, M. Miyake, and T. Fujino, "Performance of diversity combining scheme using simplified weighting factor," *IEICE Transactions on Communications*, vol. E80-B, no. 8, pp. 1160–1165, August 1997.
- [81] J. H. Winters, "The impact of antenna diversity on the capacity of wireless communication systems," *IEEE Transactions on Communications*, vol. 42, no. 2/3/4, pp. 1740–1751, February/March/April 1994.
- [82] J. H. Winters, "Optimum combining in digital mobile radio with cochannel interference," *IEEE Journal on Selected Areas in Communications*, vol. 2, pp. 528–539, July 1984.

-
- [83] R. D. Vaughan, "On optimum combining at the mobile," *IEEE Transactions on Vehicular Technology*, vol. 37, no. 4, pp. 181–188, Nov 1988.
- [84] J. H. Winters, "Signal acquisition and tracking with adaptive antenna arrays in the digital mobile radio systems IS-54 with flat fading," *IEEE Transactions on Vehicular Technology*, vol. 42, no. 4, pp. 377–384, Nov 1993.
- [85] R. A. Monzingo and T. W. Miller, *Introduction to Adaptive Array*, John Wiley & Sons, Inc., New York, USA, 1980.
- [86] S. Haykin, *Adaptive Filter Theory*, Prentice Hall, New York, USA, 4th edition, 2001.
- [87] S. J. Grant and J. K. Cavers, "Performance enhancement through joint detection of co-channel signals using diversity arrays," *IEEE Transactions on Communications*, vol. 46, no. 8, pp. 1038–1049, August 1998.
- [88] S. D. Gray, M. Kocic, and D. Brady, "Multiuser detection in mismatched multiple access channels," *IEEE Transactions on Communications*, vol. 43, no. 12, pp. 3080–3089, December 1995.
- [89] R. Khono, "Spatial and temporal communication theory using adaptive antenna array," *IEEE Personal Communications*, pp. 28–35, February 1998.
- [90] M. Failli, "Digital land mobile radio communications-cost207 final report," Tech. Rep., Comission of the European Communities, 1989.
- [91] A. F. Molisch, M. Steinbauer, H. Asplund, and N. B. Mehta, "Backward compatibility of the COST259 directional channel model," in *Proceedings of 5th International Symposium on Wireless Personal Multimedia Communications (WPMC'02)*, Hawaii, USA, October 2002, vol. 2, pp. 27–30.
- [92] H. Hofstetter, A. F. Molisch, and M. Steinbauer, "Implementation of COST259 geometry based stochastic channel model for macro- and microcells," in *Proceedings of 4th European Personal Mobile Communications Conference (EPMCC'01)*, Vienna, Austria, February 2001.
- [93] M. Steinbauer, *The radio propagation channel – a non-directional, directional, and double-directional point-of-view*, Ph.D. thesis, Vienna University of Technology, Vienna, Austria, November 2001.
- [94] A. Stéphenne and B. Champagne, "Effective multi-path vector channel simulator for antenna array systems," *IEEE Transactions on Vehicular Technology*, vol. 49, no. 6, pp. 2370–2375, November 2000.
- [95] M. F. Pop and N. C. Beaulieu, "Limitation of sum of sinusoids fading channel simulators," *IEEE Transactions on Communications*, vol. 49, no. 4, pp. 699–708, April 2001.
- [96] J. S. Hammerschmidt and A. A. Hunter, "Spatio-temporal channel models for mobile station: concept, parameter and canonical implementation," in *Proceedings of IEEE 51th Vehicular Technology Conference (VTC'00-Spring)*, Tokyo, Japan, May 2000, pp. 1641–1645.

-
- [97] 3GPP, "Channel model for Tx diversity simulations using correlated antennas," 3GPP documents TSRG1/15 R1-00-1067, August 2000.
- [98] D. I. Laurenson, D. G. M. Cruickhank, and G. Povey, "A computationally efficient channel simulator for the COST207 channel models," in *IEE Colloquium on Computer Modelling of Communications Systems*, United Kingdom, May 1994, pp. 8/1–8/6.
- [99] J. Baltersee, "Modelling and simulating fading channels for systems with smart antennas," in *Proceedings of IEEE 10th International Symposium on Personal, Indoor and Mobile Radio Communications (PIMRC'98)*, Boston, USA, September 1998, vol. 2, pp. 957–961.
- [100] H. Asplund, "Bandwidth-independent fading characterization," Tech. Rep., COST 259 Temporary Documents TD(99)103, Leidsendam, Netherlands, September 1999.
- [101] G. H. Golub and C. F. Van Loan, *Matrix Computations*, The Jonh Hopkins University Press, 3rd edition, 1996.
- [102] A. F. Molisch, H. Asplund, R. Heddergott, M. Steinbauer, and T. Zwick, "The COST259 directional channel model I-philosophy and general aspects," submitted to IEEE Transactions on Wireless Communications 2001.
- [103] H. Asplund, A. A. Glazunov, A. F. Molisch, R. Heddergott, M. Steinbauer, and T. Zwick, "The COST 259 directional channel model II-macrocell and general aspects," submitted to IEEE Transactions on Wireless Communications 2001.
- [104] H. Asplund and J. E. Berg, "Parameter distributions for the COST259 directional channel model," Tech. Rep., COST259 Temporary Documents TD(99)108, Leidsendam, Netherlands, September 1999.
- [105] A. F. Molisch, M. Steinbauer, and H. Asplund, "Virtual cell deployment areas and cluster tracing-new methods for directional channel modelling in macrocells," in *Proceedings of IEEE 55th Vehicular Technology Conference (VTC'02-Spring)*, Alabama, USA, May 2002, pp. 1279–1283.
- [106] L. J. Greenstien, V. Erceg, Y. S. Yeh, and M. V. Clark, "A new path-gain/delay spread propagation model for digital cellular channels," *IEEE Transactions on Vehicular Technology*, vol. 66, no. 2, pp. 477–485, May 1997.
- [107] H. Asplund, P. Lunqvist, and J. E. Berg, "A channel model for positioning," Tech. Rep., COST259 Temporary Documents TD(98)020, Bern, Switzerland, February 1998.
- [108] G. J. Foschini and M. J. Gans, "On limits of wireless communications in a fading environment when using multiple antennas," *Kluwer Wireless Personal Communications*, vol. 6, no. 3, pp. 311–335, March 1998.
- [109] J. B. Andersen, "Array gain and capacity for known random channels with multiple element arrays at both ends," *IEEE Journal on Selected Areas in Communications*, vol. 18, no. 11, pp. 2172–2178, November 2000.

-
- [110] J. P. Kermoal, L. Schumacher, K. I. Pedersen, P. E. Mogensen, and F. Frederiksen, "A stochastic MIMO radio channel model with experiment validation," *IEEE Journal on Selected Areas in Communications*, vol. 18, no. 6, pp. 1211–1226, August 2002.
- [111] D. P. Palomar, J. R. Fonollosa, and M. A. Lagunas, "Capacity results on frequency-selective rayleigh MIMO channels," in *Proceedings of IST Mobile Communications Summit (IST'00)*, Galway, Ireland, October 2000, pp. 491–496.
- [112] L. Schumacher, J. P. Kermoal, F. Frederiksen, K. I. Pedersen, A. Algans, and P. E. Mogensen, "Mimo channel characterisation," Tech. Rep., IST METRA, IST-1999-11719/AAU-WP2-D2-V1.1, Aalborg, Denmark, February 2001.
- [113] D. Gesbert, H. Bolcskei, D. Gore, and A. Paulraj, "Outdoor wireless MIMO channels: Models and performance prediction," *IEEE Transactions on Communications*, vol. 50, no. 12, pp. 1926–1934, December 2002.
- [114] D. Chizhik, G. J. Foschini, M. J. Gans, and R. A. Valenzuela, "Keyholes, correlations, and capacities of multielement transmit and receive antennas," *IEEE Transactions on Wireless Communications*, vol. 1, no. 2, pp. 361–368, April 2002.
- [115] M. Shafi, D. Gesbert, D. S. Shiu, P.J. Smith, and W.H. Tranter, "Guest editorial: MIMO systems and applications I," *IEEE Journal on Selected Areas in Communications*, vol. 21, no. 3, pp. 277–280, April 2003.
- [116] M. D. Zoltowski, C. P. Mathews, and M. Haardt, "Eigenstructures techniques for 2-D angle estimation with uniform circular arrays," *IEEE Transactions on Signal Processing*, vol. 44, no. 2, pp. 316–328, February 1996.
- [117] C. P. Mathews and M. D. Zoltowski, "Eigenstructures techniques for 2-D angle estimation with uniform circular arrays," *IEEE Transactions on Signal Processing*, vol. 42, no. 9, pp. 2395–2407, September 1994.
- [118] L. C. Godara (editor), *Handbook of antennas in wireless communications*, CRC Press LLC, Boca Raton, Florida, 2002.
- [119] A. Nehorai and E. Paldi, "Vector-sensor array processing for electromagnetic source localization," *IEEE Transactions on Signal Processing*, vol. 42, pp. 376–378, February 1994.
- [120] K. T. Wong and M. D. Zoltowski, "Closed-form direction finding and polarization estimation with arbitrary spaced electromagnetic vector-sensors at unknown locations," *IEEE Transactions on Antennas and Propagation*, vol. 48, no. 5, pp. 671–681, May 2000.
- [121] M. R. Andrew, P. P. Mitra, and R. deCarvalho, "Tripling the capacity of wireless communications using electromagnetic polarization," *Nature*, vol. 409, pp. 316–318, January 2001.
- [122] K. T. Wong and M. D. Zoltowski, "Self initiating MUSIC-based direction finding and polarization estimation in spatio-polarizational beamspace," *IEEE Transactions on Antennas and Propagation*, vol. 48, no. 8, pp. 1235–1245, August 2000.

- [123] M. D. Zoltowski and K. T. Wong, "Closed-form eigenstructure-based direction finding using arbitrary but identical subarrays on a sparse uniform cartesian arrays grid," *IEEE Transactions on Signal Processing*, vol. 48, no. 8, pp. 2205–2210, August 1998.
- [124] G. Sommerkorn, D. Hampicke, R. Klukas, A. Richter, A. Schneider, and R. Thoma, "Uniform rectangular antenna array calibration issues for 2-D ESPRIT application," in *Proceedings of 4th European Personal Mobile Communications Conference (EPMCC'01)*, Vienna, Austria, February 2001.
- [125] R. Thoma, D. Hampicke, A. Richter, and G. Sommerkorn, "Measurement and identification of mobile radio propagation channels," in *Proceedings of IEEE Instrumentation and Measurement Technology Conference (IMTC'01)*, Budapest, Hungary, May 2001, pp. 1163–1170.
- [126] E. H. Van Lil and A. R. Van De Capella, "Transmission line model for mutual coupling between microstrip antennas," *IEEE Transactions on Antennas and Propagation*, vol. 32, no. 8, pp. 816–821, August 1984.
- [127] F. Adachi, M. T. Feeney, A. G. Williamson, and J. D. Parsons, "Cross-correlation between envelopes of 900 MHz signals received at a mobile radio base station site," *IEEE Proceedings on Radar, Sonar and Navigation*, vol. 133, no. 6, pp. 506–512, 1986.
- [128] M. T. Feeney and J. D. Parsons, "Cross-correlation between 900 MHz signals received on vertically separated antennas in small-cell mobile radio systems," *IEEE Proceedings on Communications, Speech and Vision*, vol. 138, no. 2, pp. 81–86, April 1991.
- [129] Y. Ebine and Y. Yamada, "A vehicular-mounted vertical space diversity antenna for a land mobile radio," *IEEE Transactions on Vehicular Technology*, vol. 40, no. 2, pp. 420–425, May 1991.
- [130] Spatial Channel Model AHG (combined ad-hoc from 3GPP and 3GPP2), "Spatial channel model text description," Tech. Rep. SCM-134, April 2003.
- [131] J. F. Diouris, S. McLaughlin, and J. Zeidler, "Sensitivity analysis of the performance of the diversity receiver," in *Proceedings of IEEE International Conference on Communications (ICC'99)*, Vancouver, Canada, June 1998, vol. 3, pp. 1598–1602.
- [132] R. Janaswamy, "Effect of mutual coupling on the capacity of fixed length linear arrays," *IEEE Antennas and Wireless Propagation Letters*, vol. 1, no. 8, pp. 157–160, August 2002.
- [133] L. Caccavale, T. Isernai, and F. Soldovieri, "Methods for optimal focusing of microstrip array antennas including mutual coupling," *IEEE Proceedings on Microwave, Antennas and Propagation*, vol. 147, no. 3, pp. 199–202, June 2000.
- [134] D. F. Kelley and W. L. Stutzman, "Array antenna pattern modelling methods that include mutual coupling effects," *IEEE Transactions on Antennas and Propagation*, vol. 41, pp. 1625–1632, December 1993.
- [135] C. C. Chong, C. M. Tan, D. I. Laurenson, S. McLaughlin, M. A. Beach, and A. R. Nix, "A new statistical wideband spatio-temporal channel model for 5-GHz band WLAN

- systems,” *IEEE Journal on Selected Areas in Communications*, vol. 21, no. 2, pp. 139–150, February 2003.
- [136] L. Leijten, *Design of antenna-diversity transceivers for wireless consumer products*, Ph.D. thesis, Eindhoven University of Technology, Eindhoven, Netherlands, September 2001.
- [137] P. C. F. Eggers, I. Z. Kovác, and K. Olesen, “Penetration effect on the XPD with GSM 1800 handset antenna relevant for BS polarization diversity for indoor coverage,” in *Proceedings of IEEE 49th Vehicular Technology Conference (VTC’99-Spring)*, Ottawa, Canada, May 1998, vol. 13, pp. 1959–1963.
- [138] M. Evans, N. Hastings, and B. Peacock, *Statistical distributions*, John Wiley & Son, Inc., New York, USA, 3rd edition, 2000.
- [139] R. D. Vaughan and J. B. Andersen, “Antenna diversity in mobile communications,” *IEEE Transactions on Vehicular Technology*, vol. 36, no. 4, pp. 149–172, Nov 1987.
- [140] S. K. Yong and J. S. Thompson, “On the effect of channel conditions and antenna parameter to the performance of antenna arrays,” MVCE core 2 research programme, WP 3.3.2, internal report IV, Mobile VCE, July 2002.
- [141] D. S. Shiu, G. J. Foschini, M. J. Gans, and J. N. Kahn, “Fading correlation and its effect on the capacity of multielement systems,” *IEEE Transactions on Communications*, vol. 48, no. 3, pp. 502–513, March 2000.
- [142] D. Chizhik, F. R. Farrokhi, J. Ling, and A. Lozano, “Effect of antenna separation on the capacity of BLAST in correlated channels,” *IEEE Communications Letters*, vol. 4, no. 11, pp. 337–339, November 2000.
- [143] M. Abramowitz and I. A. Stegun, *Handbook of mathematical functions with formula, graphs and mathematical tables*, Dover publications, Inc., New York, USA, 10th edition, 1972.
- [144] I. S. Gradshteyn and I. M. Ryzhik, *Table of integrals, series and products*, Academic Press Inc., London, UK, 5th edition, 1994.